UC Irvine

UC Irvine Electronic Theses and Dissertations

Title

Synthetic Considerations for Tuning Ligand-Centered Proton-Coupled Electron Transfer Reactions

Permalink

https://escholarship.org/uc/item/59f3c716

Author

Alvelais, Rachel Emilia

Publication Date

2023

Copyright Information

This work is made available under the terms of a Creative Commons Attribution License, available at https://creativecommons.org/licenses/by/4.0/

Peer reviewed|Thesis/dissertation

eScholarship.org Powered by the California Digital Library
University of California

UNIVERSITY OF CALIFORNIA,
IRVINE

Synthetic Considerations for Tuning Ligand-Centered Proton-Coupled Electron Transfer Reactions

DISSERTATION

submitted in partial satisfaction of the requirements
for the degree of

DOCTOR OF PHILOSOPHY

in Chemistry

by

Rachel Emilia Alvelais

Dissertation Committee:
Professor Alan F. Heyduk, Chair
Professor Jenny Y. Yang
Professor Michael T. Green

2023

© 2023 Rachel Emilia Alvelais

Dedication

Many people would undoubtedly consider it foolish and superstitious to go on believing in a change for the better.

It is sometimes so bitterly cold in the winter that one says, *'The cold is too awful for me to care whether summer is coming or not; the harm outdoes the good.'* But with or without our approval, the severe weather does come to an end eventually and one fine morning the wind changes and there is the thaw. When I compare the state of the weather to our state of mind and our circumstances, subject to change and fluctuation like the weather, then I still have some hope that things may get better.

– Vincent van Gogh to Theo van Gogh

August 1879

Table of Contents

	Page
LIST OF FIGURES	v
LIST OF TABLES	x
LIST OF SCHEMES	xii
LIST OF EQUATIONS	xiv
ACKNOWLEDGEMENTS	xv
VITA	xvii
ABSTRACT OF THE DISSERTATION	xix
CHAPTER 1: Introduction	1
1.1. Redox-active ligands on transition metal complexes.	1
1.2. Determining charge distribution in redox-active ligand complexes.	5
1.3. Parameterizing ligand influence on metal-based reduction potentials.	11
1.4. Ancillary ligand influence over redox-active ligand electron transfer behavior.	12
1.5. Measuring PCET in transition metal complexes.	13
1.6. Ligand-based proton-coupled electron transfer in coordination complexes.	16
1.7. Synthetic handles and trends in tridentate redox active ligand PCET.	19
1.8. Contributions of this work.	21
1.9. References.	23
CHAPTER 2: Ancillary ligand influence on tridentate redox active ligand electronics	29
2.1. Introduction.	29
2.1.1. Tuning metal reduction potentials in coordination complexes.	29
2.1.2. Tuning redox-active ligand reduction potentials when bound to metal ions.	29
2.2. Results.	31
2.2.1. Synthesis.	31
2.2.2. Structural characterization.	32
2.2.3. Spectroscopic characterization.	36
2.2.4. Electrochemical characterization.	37
2.2.5. Density functional theory comparison.	38
2.3. Discussion.	40
2.3.1. Oxidation state assignment of Ni and [ONO] fragments in $\{[ONO]Ni(L)\}^{-}$ complexes.	40

2.3.2. Orbital energy estimations and experimental comparisons. 43
2.4. Conclusion. 45
2.5. Experimental. 46
2.6. References. 59

CHAPTER 3: Characterization of [ON(H)O]Co(DMAP)$_n$ proton-coupled electron transfer and ligand equilibria 62
3.1. Introduction. 62
3.2. Results. 66
3.2.1. Structural characterization. 66
3.2.2. Electrochemical characterization. 70
3.2.3. Electronic absorption spectroscopy. 72
3.2.4. Electron paramagnetic resonance spectroscopy. 75
3.2.5. Proton transfer reactivity. 78
3.2.6. PCET reactivity. 79
3.2.7. Density Functional Theory models of five-coordinate {[ONO]Co(DMAP)$_2$}^{y} isomers. 80
3.2.8. Computational models of {[ONO]Co(DMAP)$_n$}^{y} isomers. 84
3.3. Discussion. 85
3.3.1. Evidence of ligand lability. 85
3.3.2. Estimating pK_a, BDFE, and hydricity of [ON(H)O]Co(DMAP)$_2$. 89
3.3.3. Charge distribution in {[ONO]Co(L)$_n$}^{y} complexes and geometry changes. 90
3.4. Conclusions. 100
3.5. Experimental. 102
3.6. References. 115

CHAPTER 4: Attempts to protonate a {[ONO]TaCl$_3$}$^-$ monomer 121
4.1. Introduction. 121
4.2. Results and discussion. 126
4.2.1. Attempted synthesis of [ON(H)O]TaCl$_3$. 126
4.2.2. Isolation of a {[ONO]TaCl$_3$}$^-$ anion. 130
4.2.3. Attempted protonation of the {[ONO]TaCl$_3$}$^-$ anion. 133
4.2.4. Isolation of a monomeric tantalum complex containing the *fac*-[ON(H)O] ligand. 137
4.3. Conclusion. 142
4.4. Experimental. 144
4.5. References. 152

APPENDIX 155

List of Figures

Page

Figure 1.1. Common motifs in redox-active ligands. From these building blocks, many bespoke ligands can be built. 1

Figure 1.2. An example cyclic voltammogram of a generic catecholate-type ligand isolated in three oxidation states, illustrating the shift in open circuit potential despite the otherwise identical electrochemistry. The top voltammogram (red trace) was taken for a catecholate species, and the open circuit potential (red arrow box) lies to the left of the semiquinonate/catecholate reduction, E_1. The middle trace (purple) was produced by the singly-oxidized semiquinonate species, and the open circuit potential (purple arrow box) lies between E_1 and the quinonate/semiquinonate reduction, E_2. The bottom voltammogram (green trace) was obtained from a doubly-oxidized species with a quinonate redox-active ligand, and the open circuit potential lies positive of E_2 (green arrow box). Open circuit potential measurements can be vital evidence of solution state oxidation states in redox-active ligand complexes. 8

Figure 1.3. Tridentate redox-active [ENE] ligands studied in the Heyduk lab. 19

Figure 2.1. Isostructural Ni complexes of the [ONO] ligand studied in this work. 30

Figure 2.2. ORTEP diagrams of {[ONO]NiL}$^-$ complexes discussed in this work (L = DMAP (a), ^{OMe}py (b), py (c)). Hydrogen atoms, counter ions, chelating agents, and solvent molecules have been omitted for clarity. In the case of (a), a crystallographically unique molecule has been omitted here, and in (b), a water-bridged potassium dimer has also been omitted, for clarity. They are reproduced elsewhere in this manuscript. 34

Figure 2.3. ORTEP diagrams of {[ONO]NiL}$^-$ (L = DMAP (a), ^{OMe}py (b)). In (a), potassium ions and 2.2.2.-cryptand have been excluded for clarity. In one molecular unit, L is rotated out of the plane of the redox-active ligand and metal (a, top), and in the other, L is canted up out of the plane (a, bottom). In crystal structure (b), the potassium counter ions of one molecular unit sits closely above the Ni, O, and redox-active backbone of its [ONO] ligand, and the aromatic backbone of a second unit above it; the potassium ions are bridged by one molecule of water each. 35

Figure 2.4. UV-visible spectra in THF of {[ONO]Ni(L)}K (L = DMAP, ^{OMe}py, ^{CN}py) showing main charge transfer bands between 300-900 nm. 36

Figure 2.5. Cyclic voltammograms of {K}{[ONO]Ni(L)} complexes in THF at 200 mV/s. Green trace, L = DMAP; yellow trace, L = ^{OMe}py; red trace, L = py; blue trace, L = ^{4CN}py. Voltammetry was performed in solutions containing 0.1 M {Bu_4N}{PF_6} using a glassy carbon

working electrode, Pt-wire counter electrode, an $Ag^{+/0}$ pseudo-reference electrode, and $[FeCp_2]^{+/0}$ as an internal standard. Star indicates the location of the open circuit potential. 38

Figure 2.6. Kohn-Sham representations of the HOMO (left) and LUMO (right) of {[ONO]Ni(L)K series (L = py shown with iso = 0.045). 40

Figure 2.7. ^{1}H NMR of {[ONO]Ni(DMAP)}K. in d8-THF at 298K. 51

Figure 2.8. Scan rate dependence of {[ONO]Ni(DMAP)}K in THF. 52

Figure 2.9. ^{1}H NMR of {[ONO]Ni(^{OMe}py)}K. in CD_3CN at 298K. 53

Figure 2.10. Scan rate dependence of {[ONO]Ni(^{OMe}py)}K in THF. 54

Figure 2.11. ^{1}H NMR of {[ONO]Ni(py)}K. in CD_3CN at 298K. 55

Figure 2.12. Scan rate dependence of {[ONO]Ni(py)}K in THF. 56

Figure 2.13. ^{1}H NMR of {[ONO]Ni(^{CN}py)}K. in CD_3CN at 298K. 57

Figure 2.14. Scan rate dependence of {[ONO]Ni(^{CN}py)}K in THF. 58

Figure 3.1. ORTEP diagrams of $[ONO]Co(L)_n$ (L = DMAP (a, b, c) n = 1 (b), 2 (a, c); L = py (d, e) n = 2 (d), 3 (e)). Hydrogen atoms, counter ions, chelating agents, and solvent molecules have been omitted for clarity. Bonds relevant to metrical oxidation state analysis have been labeled in the diagram (left). 69

Figure 3.2. Cyclic voltammograms of {K}{[ONO]Co(DMAP)} (orange trace), $[ONO]Co(DMAP)_2$ (blue trace), and $\{[ONO]Co(DMAP)_3\}\{PF_6\}$. The orange stars marks the open circuit potential, and black arrows show forward scan direction. Cyclic voltammograms were taken at 100 mV/s in 0.001 M analyte with 0.1 M $[TBA][PF_6]$ using a glassy carbon working electrode, Ag wire pseudoreference electrode, and a Pt wire counter electrode. All potentials referenced to $[FeCp_2]^{+/0}$ internal standard. 70

Figure 3.3. Cyclic voltammetry of the redox event centered at −0.77 V belonging to $[ONO]Co(DMAP)_n$ in acetonitrile, in the presence of 0-2.0 equivalents of excess DMAP. 71

Figure 3.4. Electronic absorbance spectra of $\{[ONO]Co(DMAP)_n\}^m$ complexes in acetonitrile. Extinction coefficients of $[ONO]Co(DMAP)_n$ (blue), {[ONO]Co(DMAP)}K (red), $[ON(H)O]Co(DMAP)_2$ (pink), and $\{[ONO]Co(L)_3\}\{PF_6\}$ (purple) in acetonitrile. 72

Figure 3.5. Normalized electronic absorption spectra of acetonitrile solutions of oxidized species, $\{[ONO]Co(L)_3\}\{PF_6\}$ (L = DMAP, bright purple trace; L = py, orange trace), and a sample of $[ON(H)O]Co(DMAP)_2$ that was exposed to air. 72

Figure 3.6. Absorbance spectra of [ON(H)O]Co(DMAP)$_2$ (pink trace), and the same sample exposed to air (purple trace). 75

Figure 3.7. Electron paramagnetic spectrum of [ON(H)O]Co(DMAP)$_2$ at 77 K in a 1:1 solution of THF:toluene. 76

Figure 3.8. EPR spectra of cationic {[ONO]Co(L)$_3$}{PF$_6$} species in 1:1 THF:toluene solutions. Spectra taken for L = py at 298 K (a) and 77 K (b) exhibit a large shift in field. Spectra taken for L = DMAP at 298 K (c) and 77 K (d) show a more dramatic difference in field shift, with the room temperature solution yielding a narrower spectrum. Red stars and red bars indicate hyperfine features. 77

Figure 3.9. Spin-density plots (a, c-g) and Kohn-Sham highest-occupied molecular orbital (b) for five-coordinate {[ONO]Co(DMAP)$_2$}^{m} (m = −1, 0, +1) and [ON(H)O]Co(DMAP)$_2$, in high- and low-spin configurations. Spin-density plots are shown with an iso = + 0.0015, and the HOMO is shown with an iso = 0.045. 84

Figure 3.10. Plot of equilibrium measurements of [ONO]Co(DMAP)$_n$ in the presence of varying concentrations of DMAP ([L]). In lieu of equilibrium concentrations, the peak currents i_{pa} corresponding to −0.79 V and −0.63 V were used to measure [(ONO)Co(L)$_3$] and [(ONO)Co(L)$_2$]. 87

Figure 3.11. ^{1}H NMR of [ONO]Co(DMAP)$_n$ in C$_6$D$_6$ at 298 K, 400 MHz. 107

Figure 3.12. Scan rate dependence for putative ligand-based redox events in [ONO]Co(DMAP)$_2$. 108

Figure 3.13. Cyclic voltammograms taken at 100 mV/s in acetonitrile of [ONO]Co(DMAP)n before (blue trace) and after (green trace) addition of 2.0 equivalents of excess DMAP. 109

Figure 3.14. Electronic absorption spectra in acetonitrile of [ON(H)O]Co(DMAP)$_2$ in the absence and presence of 10 equivalents of DMAP. 109

Figure 3.15. Electronic absorption spectra in acetonitrile of {K}{[ONO]Co(DMAP)} in the absence and presence of 10 equivalents of DMAP. 110

Figure 3.16. Cyclic voltammogram of {K}{[ONO]Co(DMAP)} dissolved in acetonitrile, recorded at 100 mV/s. Star indicates open circuit potential determined by a separate measurement, and arrow indicates scan direction. 111

Figure 3.17. ORTEP diagram of [ON(H)O]Co(DMAP)(DBU). Hydrogen atoms, counter ions, chelating agents, and solvent molecules have been omitted for clarity. 112

Figure 3.18. Cyclic voltammogram of {[ONO]Co(DMAP)$_3$}{PF$_6$} dissolved in acetonitrile, recorded at 100 mV/s. Star indicates open circuit

potential determined by a separate measurement, and arrow indicates scan direction. 113

Figure 4.1. Multidentate ligands have been shown to stabilize early transition metal ions in high oxidation states. From left to right: a hafnium (IV) hydride stabilized by a tetradentate ligand; a tantalum (V) trialkyl complex with a tridentate ligand with phenol- and pyridine- motifs; a zirconium (IV) complex supported by two tridentate ligands with pyridine dipyrrolide backbones. 122

Figure 4.2. Stacked ^{1}H NMRs comparing triethylammonium chloride (bottom, CD_3CN; peak at 2.19 ppm is a hexamethylbenzene standard) to the putative $\{HNEt_3\}\{[ONO]TaCl_3\}$ in both CD_3CN and C_6D_6 for comparison. 127

Figure 4.3. Cyclic voltammograms of tantalum complexes (yellow trace = $\{HNEt_3\}\{[ONO]TaCl_3\}$; orange trace = $\{Fc^*\}\{[ONO]TaCl_3\}$)dissolved in acetonitrile, recorded at 3200 mV/s. Star indicates open circuit potential determined by a separate measurement, and black arrows indicates scan direction. Voltammetry was performed in solutions containing 0.1 M $\{Bu_4N\}\{Cl\}$ using a glassy carbon working electrode, Pt-wire counter electrode, an $Ag^{+/0}$ pseudo-reference electrode, and $[FeCp_2]^{+/0}$ as an internal standard. 129

Figure 4.4. ORTEP diagram of $\{Fc^*\}\{[ONO]TaCl_3\}$. Co-crystallized solvent molecules have been removed for clarity. 131

Figure 4.5. Electronic absorption spectra of $\{Fc^*\}\{[ONO]TaCl_3\}$ in acetonitrile. 132

Figure 4.6. Addition of one (middle) and ten (top) equivalents of $\{HNEt_3\}^{+}$ to a solution of $\{Fc^*\}\{[ONO]TaCl_3\}$ was monitored by ^{1}H NMR in CD_3CN. No protonation of the redox-active ligand was observed, and peaks corresponding with the anion did not shift even after several days. 134

Figure 4.7. ORTEP diagram of $[ONO]TaCl_2(OH_2)$. Co-crystallized solvent molecules have been removed for clarity. Protons on the aqua ligand were located in the difference map. 135

Figure 4.8. Comparison of ^{1}H NMR spectra obtained from the reaction of $[ONO]H_3$ and $TaCl_5$. Spectra taken in C_6D_6. Top: suspected $[ONO]TaCl_2$ complex with an impurity of suspected $[ON(H)O]TaCl_3$ (middle). The free $[ONO]H_3$ ligand is included (bottom) for comparison. 138

Figure 4.9. Electronic absorption spectra of the suspected *fac*-$[ON(H)O]TaCl_3$ isomer, produced from the reaction of $[ONO]H_3$ and $TaCl_5$. Spectra taken in acetonitrile. 140

Figure 4.10. Addition of acid (green spectra, d) and base (red spectra, b) to the putative *fac*-[ON(H)O]TaCl3 (orange spectra, a) resulted in the formation of species similar to $\{Fc^*\}\{[ONO]TaCl_3\}$ (brown spectra,

c), and {$HNEt_3$}{[ONO]$TaCl_3$} (black spectra, e). Peak labels were excluded for clarity, see Experimental section. 141

Figure 4.11. ^1H NMR of {Fc*}{[ONO]$TaCl_3$} taken in CD_3CN at 298 K 149

List of Tables

Page

Table 1.1. Metal Ion Substitution Effects on Ligand PCET 20

Table 2.1. Selected bond distances (Å) and τ_4 values of {K}{[ONO]Ni(L)} solid-state structures (L = DMAP, ^{OMe}py, py, PPh_3). 33

Table 2.2. Extinction coefficients and λ_{max} of each UV-visible transition for {K}{[ONO]Ni(L)} complexes in THF. 36

Table 2.3. Reduction potentials observed in cyclic voltammetry experiments for {K}{[ONO]Ni(L)}, performed in THF at 200 mV/s. All values referenced to the $[FeCp_2]^{+/0}$ internal standard redox couple. 38

Table 2.4. Relative frontier orbital energies for complexes of $\{[ONO]Ni(L)\}^-$ (L = DMAP, ^{OMe}py, py, ^{CN}py), as well as their Mulliken charge distributions. 39

Table 2.5. HOMO/LUMO and HOMO/LUMO+2 transition energies of $\{[ONO]Ni(L)\}^-$ complexes from excited state TD-DFT, compared to experimental absorption bands in THF. 40

Table 2.6. Literature p*K*a, and E_L for four para-substituted py ligands. 41

Table 2.7 X-ray diffraction data collection and refinement parameters for {K(2.2.2.-crypt)}, {[ONO]Ni(DMAP)}, {K}{[ONO]Ni(^{OMe}py)}, and {K(2.2.2.-crypt)}{[ONO]Ni(py)}. 49

Table 3.1 Selected bond distances (Å) and τ_5 values of $[ON(H)O]Co(DMAP)_2$, {K(2.2.2.-crypt)}{[ONO]Co(DMAP)}, $[ONO]Co(L)_2$ (L = DMAP, py), and $\{[ONO]Co(py)_3\}\{PF_6\}$ solid-state structures. 67

Table 3.2. Reduction potentials associated with $[ONO]Co(L)_n$ in acetonitrile at 100 mV/s. 70

Table 3.3. Extinction coefficients and λ_{max} of each UV-visible transition for acetonitrile solutions of $[ONO]Co(DMAP)_n$, {K}{[ONO]Co(DMAP)}, $[ON(H)O]Co(DMAP)_2$, and $\{[ONO]Co(L)_3\}\{PF_6\}$ (L = DMAP, py). 73

Table 3.4. Experimentally observed parameters of the EPR spectra for $\{[ONO]Co(L)_3\}\{PF_6\}$ cations. 78

Table 3.5. Mulliken charge distribution in $[ONO]Co(DMAP)_2$, and population analysis of the HOMO when S = 0. 81

Table 3.6. Spin density, calculated bond angles, and τ_5 indices from calculated bond angles of complexes $\{[ONO]Co(DMAP)_2\}^m$ for m = 0, −1, +1, and $[ON(H)O]Co(DMAP)_2$, in both high- and low-spin configurations. 82

Table 3.7. Spin density calculated for {[ONO]Co(DMAP)}$^{-}$ and {[ONO]Co(DMAP)$_3$}$^{+}$ and [ONO]Co(DMAP)$_3$ 83

Table 4.1. Reduction potentials of {X}{[ONO]TaCl$_3$} complexes in acetonitrile reported at 100 mV/s scan rates. 129

Table 4.2. Selected bond distances (Å) of solid-state structures obtained for {Fc*}{[ONO]TaCl$_3$}, [ONO]TaCl$_2$(OH$_2$), and previously-reported [ONO]TaCl$_2$(OEt$_2$). 131

Table 4.3. X-ray diffraction data collection and refinement parameters for [ONO]Ta(OH$_2$) and {Fc*}{[ONO]TaCl$_3$}. 146

List of Schemes

Page

Scheme 1.1. Oxidation states of the redox-active ligand, catecholate (top), each related by transfer of single electrons. Catechol can perform these electron transfers, and exist in the same distinct oxidation states, when bound to the metal center (bottom) without causing oxidation or reduction of the metal ion. Oxidation states from left to right: $[cat]^{2-}$, $[sq\bullet]^{1-}$, [q]. 3

Scheme 1.2. Two-electron oxidation of $Zr(ap)_2(THF)$ and addition of Cl_2 to the metal center, affording "oxidative addition" to a formally d^0 metal (top). "Reductive elimination" of biphenyl via concomitant two-electron reduction of a Zr complex with redox-active [ap] ligands (bottom). In both cases, the electrons were sourced from the bound (ap) ligands. 4

Scheme 1.3. Left: The C–C, C–N, and C–O bonds that contract when redox-active pincer ligand [ONO] is oxidized from its catecholato $[cat]^{3-}$ form to the radical semiquinonato $[sq]^{2-}$ and monoanionic quinonato $[q]^{1-}$ forms. The ligand can exist in and transform between discrete oxidation states even while bound to a metal ion such as nickel(II) without affording a change in metal oxidation state. 6

Scheme 1.4. Valence tautomerization of a cobalt complex studied by Pierpont, in which a Co(III) metal center can be reduced intravalently by a coordinated catecholate-type ligand at equilibrium conditions, resulting in a Co(II) ion and two radical ligands. Ligand backbone R groups omitted for clarity. 9

Scheme 1.5. Proton- and electron-transfer steps that make up the thermodynamic cycle of PCET in an [ENE] ligand complex. Measurement of the individual reduction potentials of the ligand and its pK_a allows the calculation of the free energies associated with homolytic and heterolytic cleavage of the central N–H bond. 15

Scheme 2.1. Two synthesis routes to access {K}{[ONO]NiL} complexes. Stoichiometric deprotonation followed by salt metathesis with a nickel salt (a) has been a fruitful route for most L. Pyridyl ligands can easily displace PPh_3 (b) to obtain the same complexes. 31

Scheme 3.1. Thermodynamic cycle relating $[ONO]Co(L)_2$ species by proton- and electron-transfer steps. 64

Scheme 3.2. Synthetic route to access $[ONO]Co(L)_n$ species and derivatives. 66

Scheme 3.3. Thermodynamic cycle relating $[ONO]Co(L)_n$ species by proton- and electon-transfer steps, amended to include experimentally-observed ligand equilibria. 88

Scheme 4.1. Protonation of [ONO]ZrCl(THF)$_2$ results in a dichloride complex capable of $2H^+/4e^-$ reduction of O_2, forming a hydroxide-bridged dimer. 123

Scheme 4.2. Addition of hydrazine to [ONO]TaMe$_2$ results in the formation of a half-protonated dimer, [ONO^{cat}]TaMe(μ-η^2:η^2–N_2H_2)(μ-η^2:η^1–N_2H_3)TaMe[ON(H)O]. 123

Scheme 4.3. Published [ONO]TaCl$_n$ (n = 2, 3, 4) complexes with the [ONO] ligand bound in the cat, sq, and q states. As the ligand is oxidized, the Ta(V) ion coordinates X-type ligands to maintain a net neutral charge. 124

Scheme 4.4. Proposed thermodynamic scheme of a [ON(H)O]TaCl$_3$ species. Direct measurement of ligand reduction potential and pK_a would afford the bond dissociation free energy of the N–H bond. 125

Scheme 4.5. Bond order changes in ruthenium and vanadium oxo complexes in response to HAT. 136

Scheme 4.6. Proposed reaction to produce the *mer* and *fac* isomers of [ON(H)O]TaCl$_3$. 139

List of Equations

		Page
Eqn. 1.1.	Empirical correlation between the number of carbonyl ligands in a complex and a transition metal ion's oxidation potential as a function of other ancillary ligands.	11
Eqn. 1.2.	Empirical correlation between observed metal reduction potential and the sum of electronic ligand parameters for coordinated ligands.	11
Eqn. 1.3.	Nernst equation relating the Gibbs free energy to standard reduction potentials.	15
Eqn. 1.4.	Gibbs free energy relationship to temperature and equilibrium constant.	15
Eqn. 1.5.	Bond dissociation enthalpy for an H–A bond.	15
Eqn. 1.6.	Bordwell equation for bond dissociation free energy of an H–A bond.	15
Eqn. 2.1.	Bordwell equation for bond dissociation free energy of an H–A bond.	27
Eqn. 3.1.	Equilibrium equation for the association of a ligand to [ONO]CoL_2.	83
Eqn. 3.2.	Ratio of six- and five-coordinate species as a function of ancillary ligand concentration and equilibrium constant.	83
Eqn. 3.3.	Bordwell equation for bond dissociation free energy of an X–H bond.	85
Eqn. 3.4.	Thermodynamic hydricity of an X–H bond.	85
Eqn. 4.1.	Bordwell equation for bond dissociation free energy of an X–H bond.	114

Acknowledgments

A good mentor sees the goals you have and makes it their own to help you get there. They are uniquely positioned to assess your strengths and weaknesses and encourage you to grow in ways that you cannot see for yourself. Coming from a solid-state materials background, I knew I had a long path ahead of me if I joined a synthetic inorganic research group—and Alan knew that, too. From the very moment we met, he made it clear that if I wanted to be the best chemist I could be, he would be there to support me every step of the way. I have been so privileged to work with Alan, and I would not be so critical or resilient as a scientist without his mentorship. His standards for science and personal conduct are high, and they encourage everyone around him to be better, and he will move mountains to help anyone who genuinely wants to meet those standards. I have always felt his faith and support through thick and thin. I am so grateful for the independence he allowed me in his group, hands-off when I needed it but always available to advise, encourage, or ground me. Thanks, Coach.

I have had many other mentors, role models, and support figures who have encouraged me to be the best scientist I can be. At UCI, I have Mike Green and Jenny Yang to thank for a large share of that support. Like Alan, Mike set the bar high in my first year, challenging every one of us to push past whatever our personal knowledge of inorganic chemistry was prior to entering his classroom and to become creative, independent thinkers. I learned so much in my first year of graduate school thanks to the project- and discovery-based learning with Mike, and I am so grateful to have him on my thesis committee now. Jenny was the reason I applied to UCI in the first place, and I am so lucky that even as I pivoted from one field to another, she made herself available as a mentor to me. Her enthusiasm for my projects and the rigorous questions she asked—and the support she offered as I searched for answers—truly made me feel like a colleague. Her feedback throughout my career here, and as a member of my committee, is always something I look forward to. Both Mike and Jenny played a huge part in making me feel like I belonged here in the moments when I doubted my place.

I would not be a synthetic inorganic chemist without *Professor* Bronte Charette. I knew from visit weekend that she was one of the most brilliant and driven scientists I would ever meet—and then she took me under her wing. She taught me the ropes of synthetic inorganic chemistry to such an exacting standard that I rarely see elsewhere, and I am proud to uphold that standard in my future career. Bronte is a kind, patient teacher, a sharp and quick colleague, and a ride-or-die friend. My first three years in graduate school were bearable largely because of her companionship in lab. Everyone who knows her is privileged, and her future students will be incredibly lucky to have her mentorship. I was, and am, indebted to her for my career.

My lab mates, Isis Lee and David Navarro, have been invaluable colleagues and friends. We keep each other sane, make each other laugh, and tackle the most difficult scientific problems together. They have helped make, and maintain, a welcoming and collaborative group culture that I am proud to be part of. The past two years would not have been nearly as enjoyable without them, and I am forever grateful to have such brilliant colleagues. I thank and apologize to them for my rants about cobalt oxidation states, and I look forward to seeing what they accomplish in their own careers.

Our Department is the most collaborative out there. I am so incredibly grateful I can walk into any lab or office and find someone willing and eager to help me with whatever chemical I need, thought experiment I propose, or scientific problem I face. From the user

facilities, and our X-ray crystallographer Dr. Joe Ziller, to the equipment shared by the Borovik and Yang groups, I have benefited immensely from this openness. In particular, I have treasured the scientific knowledge and dear friendship of Dr. Nadia Léonard, Alessandra Zito, and Meghen Goulet.

My research career began at UC Santa Barbara, thanks to the SIMS program just before the start of my freshman year. It was the very first time I considered the *possibility* that I could *do science*—not just learn about other people doing science. The Center for Science and Engineering Partnerships gave me four years of REUs thereafter, as well as a job to feed and house myself, academic support, and—best of all—the most important friends and mentors of my life. Professor Stephanie Mendes, Dr. Arica Lubin, Ofi Aguirre, Dr. Lubi Lenaburg, Wendy Ibsen, and Dr. Ellie Sciacky all became family to me when I needed it most and felt most alone; I would have been absolutely lost without their love and support. They taught me that I *do* look like a scientist, that just because school could be difficult didn't mean that I was *bad* at it, that the things we struggle most with are sometimes the things most worth doing. They taught me what it means to be a good colleague, a good friend, a good teacher, a good mentor… Almost everything I have learned about being a person is because of them. I strive to pay it forward in everything I do in life.

In addition to the great friends and mentorship that aided me, I also had a steadfast companion: my dog, LUMO (Lu). Nothing in life so consistently reminds me of the importance of kindness, patience, and forgiveness—and regular meals. Training a traumatized rescue dog reinforced all the lessons I needed to survive my PhD. Together, we faced the possibility of failure with bravery, and when success eluded us, we commiserated and tried again. Loving LUMO encourages me to celebrate the progress we've made to get here.

And on that note, I must especially thank the rest of the humans in my family for their unwavering support as I pursued this degree. My parents were the first to instill in me lessons of self-improvement, and though their expectations for my conduct and personal growth have always been high, I never doubted their support and love in pursuit of those standards. I am well-aware that not everyone has that certainty, and it is a precious gift to have the absolute trust, friendship, and encouragement of my parents and both of my little sisters, without conditions. I need to specifically thank Tea for her selfless generosity over the past year. The late nights in lab and the writing marathons that generated this thesis would not have been possible without her support—and Lu certainly appreciated her dogsitting on his nap-filled afternoons. I hope I can someday return the favor and relieve some stress while she achieves her goals.

There are few others who've known me through the good and the bad. Dr. Chris Siefe has seen just about everything, starting way back in freshman year of undergrad. He was one of my dearest friends then and remains so now. Watching him in our shared research lab as undergraduates taught me so much about being a scientist, and watching him progress through his own graduate program prepared me so much for what was to come. Through it all, Chris had the kindest words and most hopeful outlook to share. Dr. David Wych knows all sides of me, from the scientist to the artist and everything in-between. Being seen and understood so deeply, so honestly, was integral to feeling like this was all worth something in the end. Work for the sake of work is not enough to make a life worth living; creativity, curiosity, and compassion, are. Thank you for sharing yours with me, and encouraging me to find those values in myself, always.

Vita

RACHEL EMILIA ALVELAIS

EDUCATION

University of California, Irvine (UCI) — Sept. 2023
Ph.D., Chemistry
A. F. Heyduk, Advisor

University of California, Santa Barbara (UCSB) — Jun. 2018
B.S., Chemistry

PUBLICATIONS

In Preparation:

Alvelais, R.E.; Szigethy, G.S.; Ziller, J.W.; Heyduk, A.F. Characterization of $[ON(H)O]Co(L)_n$ proton-coupled electron transfer and ligand equilibria.

Alvelais, R.E.; Ziller, J.W.; Heyduk, A.F. Ancillary ligand influence on tridentate redox active ligand electronics in square-planar complexes of nickel(II).

PRESENTATIONS

Oral:

Synthetic approaches for tuning the thermodynamics of ligand-centered proton-coupled electron transfer reactions. Alvelais, R.E.; Szigethy, G.S.; Ziller, J.W.; Heyduk, A.F. ACS Western Regional Meeting, Las Vegas, NV 2022.

RESEARCH EXPERIENCE

HEYDUK LAB | Graduate Researcher — Irvine, CA
Inorganic Chemistry Ph.D. — 2018–2023

- Identified structure-function relationships in transition metal dyes that contain redox-active pincer ligands.

DANIEL LAB | Research Intern — Cornell University
Cornell LSAMP 2017 REU — Jun–Aug 2017

- Investigated bulk interactions between microvesicles and healthy cell membranes with fluorimetric assays at different ion concentrations and pH.

SOLUTION DEPOSITION SYSTEMS, INC. | Research Intern — Goleta, CA
Jan–Mar 2017

- Developed technology that synthesizes advanced materials from aqueous solution, produces little waste, and performs as well as industry standards.

GORDON LAB | Research Intern UCSB
Sept 2016–Jun 2017

- Deposited crystalline metal oxide thin films and nanostructures with microplasma discharges for battery electrodes, supercapacitors, and antireflective coatings.

MOSKOVITS LAB | Research Intern UCSB
CAMP 2016 REU Jun–Aug 2016

- Electrochemically deposited nickel/cadmium chalcogenide Schottky junctions on silver nanorods to develop nanoscale solar cells.
- Adapted chemical bath and drop-cast depositions for transparent conducting oxide and transparent conducting polymer thin films.

EUREKA 2015 REU Jun 2015–Aug 2016

- Electrochemically deposited cadmium selenide nanorods in anodized alumina templates as solar absorber layer for nanoscale photovoltaics.

Abstract of the Dissertation

Synthetic Considerations for Tuning

Ligand-Centered Proton-Coupled Electron Transfer Reactions

by

Rachel Emilia Alvelais

Doctor of Philosophy in Chemistry

University of California, Irvine, 2023

Professor Alan F. Heyduk, Chair

An attractive feature of tridentate, redox-active [ENE] ligands (E = a heteroatom donor such as O, NR, or S) is their ability to serve as both electron- and proton-reservoirs in coordination complexes. In this dissertation, some of the structural and electronic properties that influence the coupled transfer of protons and electrons from [ENE]-type ligands in transition metal complexes will be explored.

Chapter 2 contains a study of the effect of ancillary donor ligands L on the electron-transfer behavior of the [ONO] tridentate redox-active ligand in complexes {[ONO]Ni(L)}K. ([ONO] = bis(3,5-di-tert-butyl-2-phenoxy)amide). The ancillary ligands L varied in their σ-donor ability, as measured by the pK_a of their conjugate acid, and π-acidity, as indicated by their electrochemical ligand parameter (E_L). Structural, spectroscopic, and electrochemical characterization techniques were employed in conjunction with computational estimates to investigate subtle electronic changes and their effects on reactivity.

Chapter 3 reports the behavior of a [ON(H)O]Co(DMAP)$_2$ complex with respect to proton-coupled electron transfer (PCET). Acid-base titrations indicate that the complex may qualify as a very weak acid and a potent reductant. Reactions with hydrogen atom transfer

(HAT) reagents are reported, placing the ligand-based bond dissociation free energy (BDFE) in a range more typically associated with metal-hydride systems. However, an equilibrium between five- and six-coordinate species was observed upon HAT transfer from the complex, precluding direct spectrophotometric measurement of the BDFE. Experimental evidence and computational investigations indicate that additional equilibria between low- and high-spin species may influence the reactivity of this system.

Chapter 4 contains the attempted protonation of the [ONO] ligand in a complex of tantalum(V). In its monomeric form, {[ONO]$TaCl_3$}{$FeCp_2^*$} appears to be an extremely weak base, contrasting with to a previously-reported {Ta}$_2$ dimer, in which one redox-active ligand is protonated and apparently highly basic. Experimental evidence suggesting the existence of both a *mer*- and *fac*-{[ONO]$TaCl_3$}$^-$ isomer, each with different pK_as, is presented in the form of electrochemical, ^{1}H NMR, and spectroscopic measurements.

CHAPTER 1: Introduction

1.1. Redox-active ligands on transition metal complexes.

Organic molecules capable of performing electron transfer reactivity without experiencing irreversible decomposition have long been studied for applications in electrocatalysis and energy storage. In the human body, reversible electron transfer reactions are necessary for cellular metabolism, enzymatic processes, and other vital biological functions. The nicotinamide adenine dinucleotides NAD^+ and $NADP^+$ store and transfer electrons for these processes, often without the aid of metal cofactors.[1] Enzymes such as glutathione peroxidase perform critical antioxidant functions, such as reducing H_2O_2, a molecule that can cause oxidative stress and disease, to water with electrons sourced from NADP(H) derivatives. Chemists studying electron transfer reactions in nature have identified that several organic cofactors like NAD^+ and $NADP^+$ contain π-conjugated heteroatom motifs[2,3] such as catecholates and benzoquinones,[4] azobenzenes, and heterocyclic pyridyl compounds like pyridine,[5] bipyridine, phenanthroline, and the nitroxyl radical 2,2,6,6-tetramethyl-1-piperidinyloxy ($TEMPO^{\cdot}$) (**Figure 1.1**).[6,7] These redox-active platforms can store and deliver reducing equivalents reversibly in part due to the stabilization of their heteroatom redox centers (often N, O, or S atoms) by larger π- or π*-conjugated orbital systems.

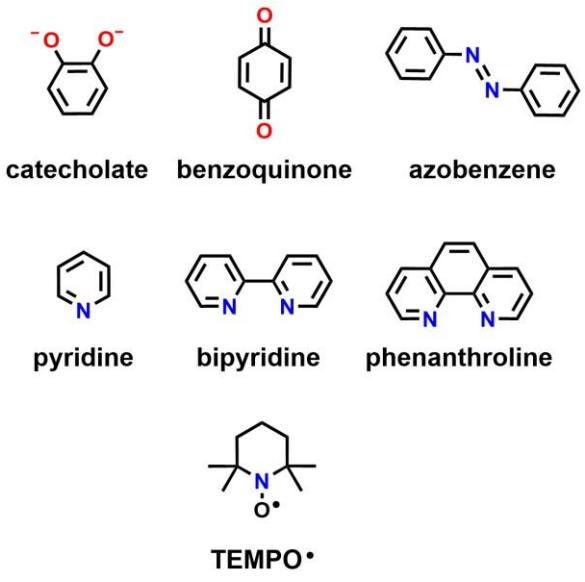

Figure 1.1. Common motifs in redox-active ligands. From these building blocks, many bespoke ligands can be built.

While it is not uncommon for nature to use redox-active molecules in metal-free

electron transfer reactions, they are also used to supplement the reactivity of metalloenzymes. Dioxygen reductases are copper- or iron-based enzymes that catalyze the reduction of atmospheric oxygen to water, a process that requires the transfer of four electrons. However, like many first-row transition metal ions, copper and iron generally only undergo one-electron redox reactions. In a subset of quinol reductases, such as cyt *bo*$_3$, the normally limited metal redox chemistry is aided by organic substrates derived from catechol, which are oxidized to benzoquinones to supply the electrons for this reaction.[8-10] Other enzymes accomplish multi-electron reactivity with ligands bound directly to the catalytic metal, such as the metalloporphyrin motif present in other members of the heme-copper dioxygen reductase superfamily,[11] or the cytochrome P450 hemeprotein that likewise uses a porphyrin radical cation and iron metal center in cooperation to activate C–H bonds of substrates.[12-14]

To replace the expensive rhodium, iridium, and platinum homogenous catalysts used by the chemical industry to perform similar multi-electron reactivity, much attention has been given to the ways in which natural systems use more affordable and abundant first-row transition metals. Research into transition metal complexes with redox-active ligands seeks to impart similar "noble metal" reactivity to first-row transition metal ions, and the prototypical redox-active ligand, catecholate, has served as a model for metal-ligand cooperativity due to its predictable electrochemistry. Catecholate can be oxidized sequentially to initially form the radical, singly-oxidized semiquinonate, and subsequently to form the fully-oxidized quinonate, while the oxidation state of the metal it is bound to remains unchanged (**Scheme 1.1**). As the design and synthesis of redox-active ligands has grown into a field of its own, the catecholate/semiquinonate/quinonate (cat/sq•/q) naming system has been adopted for a larger family of ligands, of which 4,6-di-*tert*-butyl-2-*tert*-butylamidophenolate **[ap]$^{2-}$**, bis(3,5-di-*tert*-butyl-2-phenoxy)amide **[ONO^{cat}]$^{3-}$**, and bis(2-

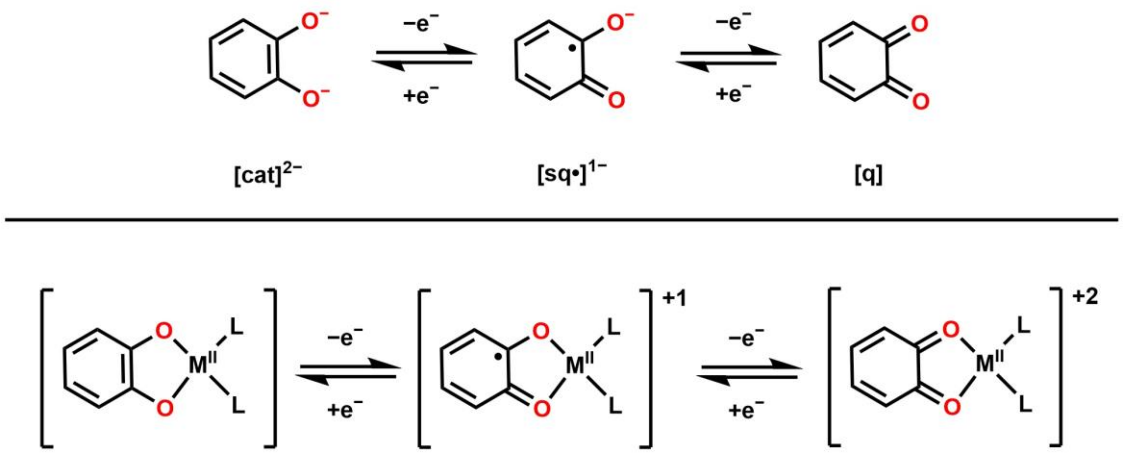

Scheme 1.1. Oxidation states of the redox-active ligand, catecholate (top), each related by transfer of single electrons. Catechol can perform these electron transfers, and exist in the same distinct oxidation states, when bound to the metal center (bottom) without causing oxidation or reduction of the metal ion. Oxidation states from left to right: $[cat]^{2-}$, $[sq\bullet]^{1-}$, [q].

isopropylamino-4-methoxyphenyl)amine **$[NNN^{cat}]^{3-}$** are members.[14-17] Like catecholate, these synthetic ligand platforms are capable of two reversible electrochemical oxidations first to the radical semiquinonate, and secondly to the doubly-oxidized quinonate states, with or without the presence of a coordinated metal. Synthetic inorganic chemists have already leveraged independent ligand-based electron transfers to perform traditional organometallic multi-electron reactions with metal centers that have *no* free metal electrons, such as the $Zr(ap)_2$ complex shown in (**Scheme 1.2**). The zirconium (IV) ion has a d^0 electron count, yet the complex is competent to perform oxidative addition[18] and reductive elimination.[19] Likewise, the $[NNN^{cat}]^{3-}$ molecule has been studied as an organic electrocatalyst in the absence of coordinating metals, as well as a ligand for transition metal ions. As a free molecule, $[NNN^{cat}]^{3-}$ undergoes two reversible oxidations in tetrahydrofuran (THF) at −0.25 V and +0.04 V vs. ferrocenium/ferrocene redox couple ($[FeCp_2]^{+/0}$).[15] When coordinated to a tantalum (V) metal center instead, the ligand-based reduction potentials remain fully-reversible, but shift anodically to +0.02 V and 0.47 V vs. $[FeCp_2]^{+/0}$ in acetonitrile (MeCN).[16]

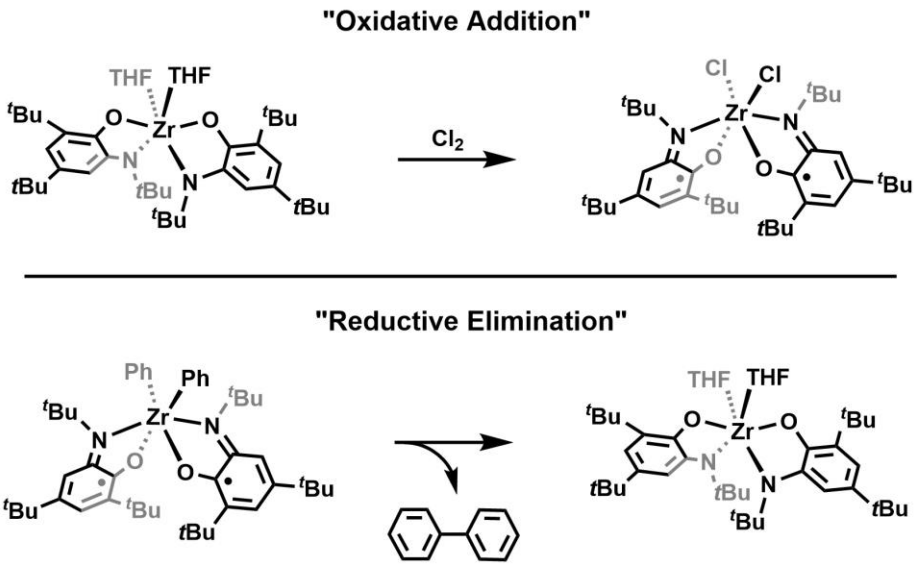

Scheme 1.2. Two-electron oxidation of $Zr(ap)_2(THF)$ and addition of Cl_2 to the metal center, affording "oxidative addition" to a formally d^0 metal (top). "Reductive elimination" of biphenyl via concomitant two-electron reduction of a Zr complex with redox-active [ap] ligands (bottom). In both cases, the electrons were sourced from the bound (ap) ligands.

Both this [NNN]–Ta complex and a similar zirconium(IV) complex were able to perform catalytic nitrene transfer reactivity in which two electrons were sourced from the ligand rather than the d^0 metal ions.

Redox-active ligands are not only active on early transition metals with no *d*-electrons, but also perform separate, ligand-based electron transfer on electron-rich metal ions as well. Wieghardt and coworkers have shown that the aforementioned $[ap]^{2-}$ ligand retains its signature electrochemical behavior when bound to a variety of metals, including copper, nickel, palladium, and cobalt, which are themselves inclined toward one-electron redox events.[17] More recent research has focused on how redox-active ligands can modulate the extant reactivity of late transition metal centers, with the Soper group using a bis-amidophenolate cobalt complex to perform two-electron cross-coupling reactions.[20] The development of new redox-active ligands and more expansive studies of how they can modulate the reactivity of different metal ions, have each become their own active fields with unique challenges.

1.2. Determining charge distribution in redox-active ligand complexes.

When a complex contains redox-active ligands, it becomes more difficult to predict its reactivity compared to the traditional principles of inorganic and organometallic complexes. Usually, knowledge of the number of valence electrons and magnitude of charge localized on a transition metal center in a coordination compound provides insight into the reactivity and stability of a species. Anionic X-type ligands, such as chloride, and neutral L-type ligands, such as phosphines, leave no ambiguity about metal oxidation state assignments and *d*-electron counts; it is clear that in a complex like $ZrCl_4$, the metal exists in the +4 oxidation state. However, some redox-active ligands, such as NO, have the capacity to accept electron density from metal ions into empty ligand-based antibonding orbitals, thus introducing a degree of uncertainty around the formal oxidation state of the metal.[21,22] Ligands that manifest this uncertainty are termed "non-innocent." To date, complexes such as $Cp_2Ti(\eta^2\text{-}C_2H_4)$ still resist oxidation state assignments.[23] By all methods of analysis, the ethylene ligand lies in an oxidation state that is somewhere between $[C_2H_4]$ or $[C_2H_4]^-$. In the solid-state, the C–C bond lengths within the ethylene are far longer than the free alkene, with 1.337(2) Å in free ethylene compared to the 1.438(5) Å in the bound species, due to back-donation from the metal center into intraligand π^* orbitals. However, this bond length is still significantly contracted from typical alkane C–C single bonds, which are generally around 1.54 Å. The titanium ethylene complex likewise does not have similar reactivity to other alkyl complexes of Ti(III) and Ti(IV); rather than undergo migratory insertion with carbon monoxide as they do, the ethylene molecule is simply displaced. Yet $Cp_2Ti(\eta^2\text{-}C_2H_4)$ reacts with hydrogen gas to produce C_2H_6, as might be expected of other dialkyl Ti(IV) complexes. Therefore it does not suffice to say the metal center is in either the +2 or +4 oxidation

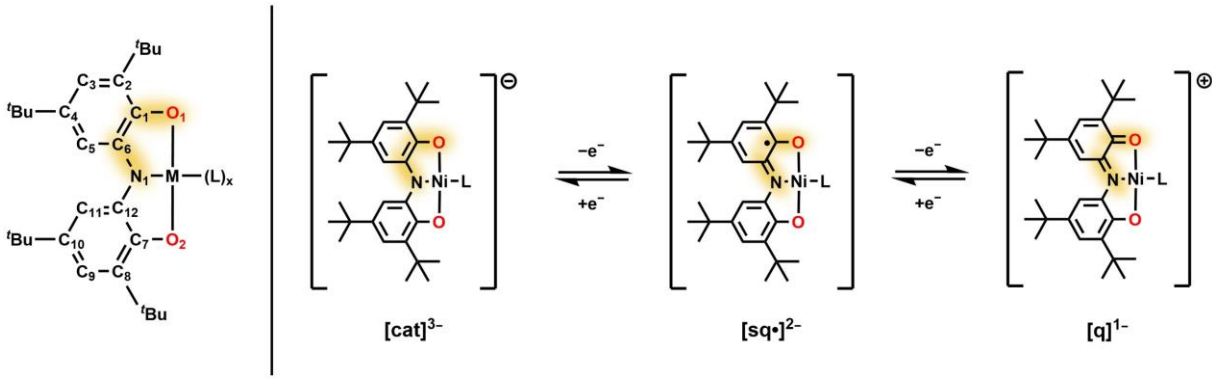

Scheme 1.3. Left: The C–C, C–N, and C–O bonds that contract when redox-active pincer ligand [ONO] is oxidized from its catecholato $[cat]^{3-}$ form to the radical semiquinonato $[sq]^{2-}$ and monoanionic quinonato $[q]^{1-}$ forms. The ligand can exist in and transform between discrete oxidation states even while bound to a metal ion such as nickel(II) without affording a change in metal oxidation state.

state.[23,24] Ligands such as the catecholato-, and amidophenolato-type platforms discussed previously *can* behave non-innocently, depending on what metal they are bound to. Thus, establishing the oxidation state of the ligand and the metal each requires careful spectroscopic, electrochemical, and structural analysis.

Thanks to the proliferation of ligands derived from catecholato-, amidophenolato-, and even thiolato-motifs in literature, several structural metrics can be correlated to each ligand's oxidation state. With some variation due to metal-ligand interactions, the C–C, C–N, and C–E (where E is a donor atom such as O, NR, or S) (**Scheme 1.3,** left) bond lengths will bear evidence of single, double, or aromatic character, depending on whether the ligand is fully-reduced (cat), singly-oxidized (sq•), or fully-oxidized (q) (**Scheme 1.3,** right). For well-studied ligands such as $[ap]^{2-}$ and $[ONO]^{3-}$, there is such a wealth of literature with high-quality structural, spectroscopic, and electrochemical data, that Brown and coworkers developed a "Metrical Oxidation State" (MOS) calculator wherein a given set of bond lengths can be compared to hundreds of other transition metal complexes with ligands in various oxidation states.[25,26] The resulting MOS value indicates how closely the ligand in question is to bearing a given charge.

Structural analysis can be useful in corroborating spectroscopic and electrochemical data to illuminate the extent of non-innocent character in the coordinated ligand. The electronic absorption spectra of redox-active ligands, and coordination complexes that contain them, may be starkly different when the ligand is in one oxidation state or another. Radical species often exhibit intense (ε_0 ~10^4 cm^{-1} M^{-1}) ligand-to-ligand (LL'), ligand-to-metal (LM), or metal-to-ligand (ML) charge transfer (CT) bands. For catecholate-type platforms, the fully-reduced cat form generally produces spectra devoid of transitions between 300-900 nm. Upon single-oxidation to the sq• oxidation state, a distinct transition dominates the visible portion of the spectrum ~ 600 nm, and the q oxidation state has its own characteristic low-energy absorptions.[27] Likewise, the chelate effect of pincer redox-active ligands improves their ability to stay coordinated to a metal center as a complex is oxidized or reduced, resulting in reversible electron transfer events measured in voltametric experiments. If a redox-active ligand complex can be independently prepared *via* chemical oxidation or reduction, the resulting cyclic voltammograms (CVs) of each species should be nearly identical; however, the open circuit potential of the bulk species in solution should shift to opposite sides of the observed electron transfer event, as indicated by the example voltammograms in **Figure 1.2**. Each piece of spectroscopic, electrochemical, and structural data gathered for a coordination complex can be used to build a comprehensive picture of metal-ligand oxidation states in solution and in the solid state.

While the formal oxidation states of some redox-active ligand complexes can be discretely defined based on clear structural and spectroscopic data, and some redox-nonninocent ligands produce genuinely ambiguous bond metrics and spectroscopic transitions such as in the example of $Cp_2Ti(\eta^2\text{-}C_2H_4)$,[28–32] in some cases, external stimuli can induce a complete intravalent charge transfer between ligand and metal fragments. When

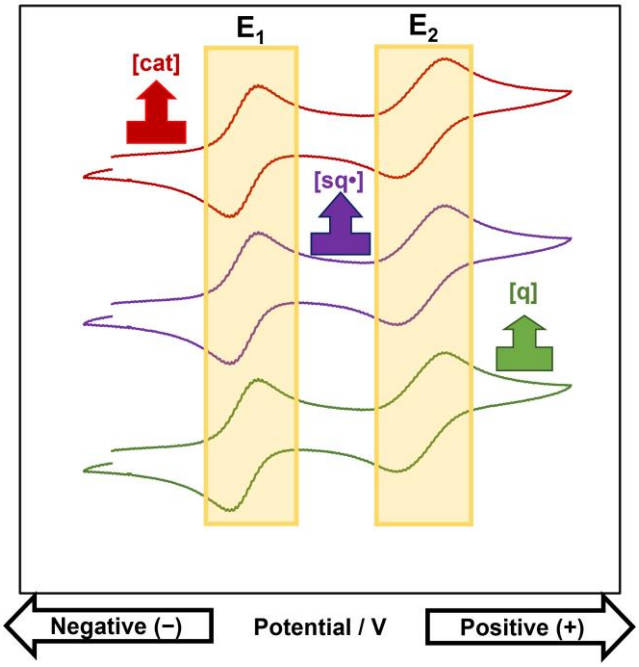

Figure 1.2. An example cyclic voltammogram of a generic catecholate-type ligand isolated in three oxidation states, illustrating the shift in open circuit potential despite the otherwise identical electrochemistry. The top voltammogram (red trace) was taken for a catecholate species, and the open circuit potential (red arrow box) lies to the left of the semiquinonate/catecholate reduction, E_1. The middle trace (purple) was produced by the singly-oxidized semiquinonate species, and the open circuit potential (purple arrow box) lies between E_1 and the quinonate/semiquinonate reduction, E_2. The bottom voltammogram (green trace) was obtained from a doubly-oxidized species with a quinonate redox-active ligand, and the open circuit potential lies positive of E_2 (green arrow box). Open circuit potential measurements can be vital evidence of solution state oxidation states in redox-active ligand complexes.

metal- and ligand-based orbitals are close in energy, changes in temperature, photoexcitation, or even mechanical stress, can cause interconversion between an oxidized ligand and reduced metal or vice versa. This inner-sphere metal-ligand electron transfer, or valence tautomerization, can result in seemingly conflicting evidence for one oxidation state assignment or another between different experiments. For example, a neutral Co(bpy)(3,5-DBQ)$_2$ (bpy = bipyridine, DBQ = dibenzoquinone) (**Scheme 1.4**) studied by Pierpont[33] gave evidence of being a Co(III) ion, with of the two bound "DBQ" ligands in the semiquinonate state and one in the catecholato state. The Co–N and Co–O bond lengths were consistent with other examples of Co(III) low-spin complexes, and the intraligand bond distances were not identical between the two redox-active ligands. Initial magnetic measurements were

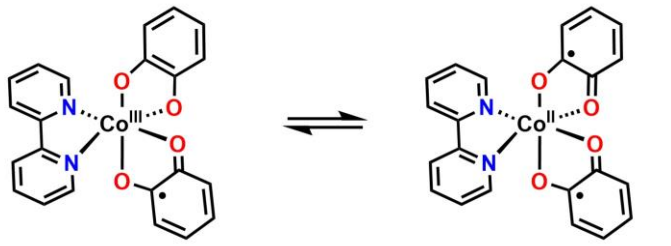

Scheme 1.4. Valence tautomerization of a cobalt complex studied by Pierpont, in which a Co(III) metal center can be reduced intravalently by a coordinated catecholate-type ligand at equilibrium conditions, resulting in a Co(II) ion and two radical ligands. Ligand backbone R groups omitted for clarity.

consistent with this formal oxidation state assignment, with only one unpaired electron present in the sample. However, at higher temperatures the complex converted to a high-spin Co(II) center, with both ligands described as catecholates, as evidenced by a change in the EPR spectra. Variable temperature solution magnetic measurements indicate that the species exist in equilibrium with each other and changes in temperature can control which dominates in solution. Solid-state variable temperature magnetic measurements corroborated the solution findings. However, the structural metrics of the valence tautomer were not obtained; the intravalent metal-ligand charge transfer that separates two valence tautomers can occur due to the conditions used to gather evidence of oxidation state, such as during single-crystal X-ray analysis, making it difficult to characterize the structural changes associated with charge transfer.

Identifying valence tautomers in a variety of ligand and metal systems is therefore a challenging process that requires solid-state, solution, and computational methods. However, the study of strongly coupled diradical redox-active ligand complexes has highlighted the prevalence of valence tautomer species, as well as the closely-related phenomenon of spin-crossover species, that may play important roles in catalysis. In spin-crossover systems, low- and high-spin electronic configurations in metal *d*-orbitals lie close together in energy, and

complexes are often observed to convert between singlet and triplet states.[34] Discerning whether valence tautomerization (between metal and ligand) or spin-crossover (within metal-based orbitals) is occurring can be difficult, and both can occur within the same system. Complexes such as (^{i}PrPDI)$CoCl_2$ (^{i}PrPDI = ^{i}PrPDI = 2,6-(2,6-$^{i}Pr_2C_6H_3N$=CMe)$_2C_5H_3N$) and similar iron compounds have been shown to catalyze olefin polymerization reactions,[35,36] with the active catalytic species forming as a result of ligand-based electron transfer followed by metal-based spin-crossover.[37,38] In a related family of pyridine diimine (PDI) cobalt complexes studied by Budzelaar and co-workers,[39] it was found that low-spin Co(II) antiferromagnetically coupled to oxidized PDI radicals, producing diamagnetic complexes; however, triplet electronic states were accessible at room temperature, separated by only a few kcals mol^{-1}. In this case, the paramagnetic spin-crossover species bore tangible evidence not only in the shifts to the ^{1}H NMR spectra of the complexes, but also in the solid-state bond distortions. It is now known that ligands with nitrogen heteroatoms, such as PDI and ap, are especially susceptible to both valence tautomerization and antiferromagnetic coupling due to the close match between redox-active orbitals and metal *d*-orbitals, especially in the case of metalloradicals such as cobalt.[40]

Transition metal complexes that contain redox-active ligands exist on a continuum of behavior that can be described as non-innocent, in equilibrium with valence tautomers, or as a discrete distribution of charges between metal and ligand. Different chemical applications, from catalysis to quantum computing, favor materials that lie in specific regions of this continuum. A species capable of valence tautomerism under mechanical or thermal stimuli might perform well as a quantum bit or redox switch,[41,42] while a complex with more discrete charge localization may reliably exhibit separate metal- and ligand-based electron-transfer reactivity,[43] and a fully-delocalized non-innocent system might be able to alleviate electron density from a metal center as it undergoes organometallic transformations like reductive

elimination or oxidative addition.[44] Understanding what properties of redox-active ligands, metals, spectator ligands, and counter ions influence electron distribution is therefore key to designing homogenous catalysts and molecular materials for specific applications.

1.3. Parameterizing ligand influence on metal-based reduction potentials.

Empirical models that can predict how metal-based electron transfer is affected by the properties of coordinated ligands have greatly aided the design of bespoke catalysts and electron transfer reagents. For example, it is now well understood that adding more donating ligands to a complex should increase the charge density on the metal ion, rendering it easier to oxidize (lowering its reduction potential) and effectively raising the energy of the *d*-orbitals.[45,46] Substituting donor ligands for more π-accepting carbonyl (CO) alleviates electron density from the metal center, rendering the metal harder to oxidize and lowering the *d*-orbitals in energy.[47,48] This correlation was observed empirically, and eventually the change in a metal ion's oxidation potential (E_{ox}) the number of CO ligands vs. other L ligands (x) was parameterized into **Equation 1.1**:

$$E_{ox} = A + x\left(\frac{dE_{ox}}{dx}\right) + 1.48y \qquad \textbf{(EQN 1.1)}$$

where the oxidation potential also depends on the overall y charge of the complex, and a solvent-dependent constant A.

Since the development of **Equation 1.1,** several other relationships between ancillary ligand identity and metal reduction potential have been proposed, including efforts to find correlations to ligands other than carbonyl.[49-53] Building off of work by Chatt, Pickett, and others, Lever studied hundreds of ligands common to coordination chemistry and how they influenced the ruthenium(III)/ruthenium(II) redox couple when bound to the metal ion.[54] The observed correlations were used to give each ligand an empirically-derived electronic ligand

parameter (E_L), the total sum of which (ΣE_L) could be used to predict changes to other metal reduction potentials (E_{obs}), according to **Equation 1.2:**

$$E_{obs} = S_M\left[\sum E_L\right] + I_M \qquad \textbf{(EQN 1.2)}$$

where S_M and I_M are the experimentally observed slope and intercept for a metal M.

Mathematical relationships such as **Equation 1.1** and **1.2** afford chemists powerful tools in the design of organometallic complexes for electron transfer reactions. However, they are empirical in nature, and the structure-function relationships that underpin the experimentally observed behavior must always be explored. Lever and others have subsequently investigated E_L's correlation to a ligand's σ-donor ability and π-acidity, where a lower E_L corresponds to better σ-donor ability.[54,55] Some have also related E_L to other properties of ligands such as Tolman and Hammett parameters and suggest that E_L can be expanded to beyond six-coordinate systems.[56,57] The ligand electronic parameter E_L is now understood to primarily reflect a given ligand's ability to accept electrons from a metal center *via* back-bonding and influence metal-based reduction potentials associated with t_{2g} orbitals.

1.4. Ancillary ligand influence over redox-active ligand electron transfer behavior.

In addition to shifting metal-based electron transfer behavior, ancillary ligands have also been shown to exert substantial influence over the electrochemical behavior of redox-active ligands in transition metal coordination complexes. However, only a few studies have investigated the extent of this control. Lever[58] demonstrated the linear free energy relationship between the ΣE_L of WXYZ ancillary ligands, the *o*-benzoquinonediimine (bqdi) quinone/semiquinone reduction ($E_{1/2}$[q/sq•]), and the net Mulliken charge on the bqdi backbone in six-coordinate complexes of ruthenium. The bqdi ligand itself is a π-accepting ligand with an empty redox-active orbital, and as such, the charge on the ligand is very

sensitive to electronic changes on the metal it is bound to *via* π-back donation. Binding more σ-donating ancillary ligands (lower ΣE_L) to the Ru center resulted in a decrease in C=N bond order in the bqdi ligand, and a concomitant shift in $E_{1/2}[q/sq^{\bullet}]$ to more negative potentials, both indicative of increased charge on the ligand. A secondary result of this study was the realization that substantial changes to the bqdi reduction potential were not accompanied by a change in its σ-donation to the Ru metal center. Any changes to the $Ru–N_{bqdi}$ bond order seemed to be primarily influenced by the M→bqdi *π*-back bonding interaction; as the Ru center added charge to the bqdi ligand, the charge was delocalized onto the aromatic backbone and did not significantly increase the $Ru–N_{bqdi}$ σ-bond.

In this way the bqdi ligand, and perhaps many other redox-active ligands, may be predictably influenced by ancillary ligands due to metal π-back bonding into empty ligand π^* orbitals. Less research has been done to understand how ancillary ligands can influence the electron transfer behavior of other redox-active ligands, particularly those that have filled ligand π^* orbitals.

1.5. Measuring PCET in transition metal complexes.

The charge distribution in a transition metal complex can inform whether a given electron transfer between the complex and substrate is favorable, and redox-active ligands have helped expand the number of metal complexes capable of organometallic reactivity, such as oxidative addition, reductive elimination, and group transfer. Yet, to transform chemical feedstocks such as hydrocarbons, hydrogen gas, carbon dioxide, carbon monoxide, nitrogen, and nitrous oxide into value-added products, catalysts must deliver electrons *and* protons to their substrates with a fine degree of control. Many biological systems store and transfer H^+, $H^{\bullet}$, and H^- equivalents in the active sites of proteins, where amino acid residues and

transition metal cofactors work in tandem to activate substrates. Accomplishing similar reactivity with homogenous inorganic catalysts requires careful manipulation of the reactant's sterics and electronic environment when bound to a metal center,[59,60] and detailed understanding of the thermodynamic and kinetic factors that govern electron- and proton-transfer to the coordinated substrate. Redox-active ligands may be useful in such reactivity if the ligand is capable of storing both electrons and protons.

While the name "proton-*coupled* electron transfer" (PCET) implies the utterly concerted, or tandem, movement of electrons and protons (as $H^{\cdot}$ or H^{-}), the term is now inclusive of multiple phenomena. Separate electron transfer (ET) and proton transfer (PT) steps may occur in succession to afford net H-atom transfer (HAT) or hydride transfer. Discerning the timescale of such reactivity, and which step comes first, is not simple.[61] Detailed mechanistic and, often, computational studies are required to attain that level of certainty, with additional care taken as to whether electrons and protons originate from the same bond or from separate orbitals. Whether reaction steps or concerted or asynchronous, and on what timescale, may determine a complex's selectivity toward one or more products. When the generation of a reduced substrate occurs much faster than proton transfer, or if the proton and electron transfer from spatially separated sites, the reduced species may have an opportunity to perform unwanted side-reactivity compared to a system in which both proton and electron transfer occur in a concerted fashion.

However, for fundamental consideration of what affects the thermodynamics of these systems, measurement of the individual ET and PT steps *via* pK_a and reduction potential will suffice.[62] In the case of the previously discussed tridentate pincer ligands [ENE] (E = an electrophilic donor atom O, N, S) or a metal ion, each of which are known to undergo reversible electron transfers, the question becomes whether their Brønsted acidity can be measured. Together, these state values directly comprise the X–H bond dissociation free

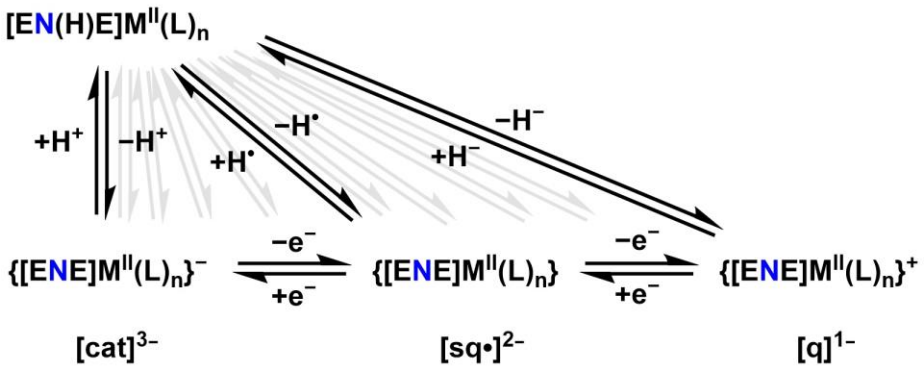

Scheme 1.5. Proton- and electron-transfer steps that make up the thermodynamic cycle of PCET in an [ENE] ligand complex. Measurement of the individual reduction potentials of the ligand and its pK_a allows the calculation of the free energies associated with homolytic and heterolytic cleavage of the central N–H bond.

$$\Delta G = -nFE^\circ = -(23.06 kcal\ mol^{-1}V^{-1})E^\circ \quad \textbf{(EQN 1.3)}$$

$$\Delta G = -RT\ln K = -(1.37\ kcal\ mol^{-1})RT(\mathrm{p}K_a) \quad \textbf{(EQN 1.4)}$$

$$\begin{array}{c} \mathrm{H{-}A} \rightleftarrows \mathrm{H^+ + A^-} \\ \mathrm{A^-} \rightleftarrows \mathrm{A^\bullet + e^-} \\ \mathrm{H^+ + e^-} \rightleftarrows \mathrm{H^\bullet} \\ \hline \mathrm{H{-}A} \rightleftarrows \mathrm{H^\bullet + A^\bullet} \end{array}$$

$$\Delta G(\mathrm{H{-}A}) = 1.37\mathrm{p}K_a + 23.06E^\circ \quad \textbf{(EQN 1.5)}$$

$$\Delta G(\mathrm{H{-}A}) = 1.37\mathrm{p}K_a + 23.06E^\circ + C_{H,sol} \quad \textbf{(EQN 1.6)}$$

energy (BDFE) for homolytic bond cleavage and the thermodynamic hydricity for the heterolytic case. The equilibrium constants of H$^\cdot$ or H$^-$ transfer reactions can likewise be directly measured and used in conjunction with pK_a to calculate a reduction potential, or *vice versa*.

A typical PCET cycle of individual PT and ET steps, and the net acid/base, HAT, and hydride transfer equilibria is shown in (**Scheme 1.5**) for a coordination complex in which an [ENE] ligand serves as both the source of electrons and a proton. In reality, there is no one "central" pathway to afford H$^+$, H$^\cdot$, or H$^-$ transfer, and the truth lies somewhere in between the traditional black reaction arrows (gray arrows).[63] Nevertheless, combining the free energy of electron transfer from the Nernst equation (**Equation 1.3**) and the free energy of proton transfer from the Gibbs-Helmholtz equation (**Equation 1.4**), according to Hess's law,

provides the overall free energy of net H· transfer (**Equation 1.5**) and, when combined with a second reduction potential, affords the free energy of thermodynamic H^- transfer (not shown) of any X–H bond.[62-65]

The Bordwell equation has required several corrections and continues to be the subject of debate.[66,67] The uncertainty surrounding the solvation energy of an H· free in solution, which had previously been assumed to be the same as that of H_2, produced significant enough errors in bond dissociation energy identification and required an additional term to account for it: $\Delta G°_{sol}(H·)$. This constant alone has engendered a number of studies relating to its exact value and solvent dependence, and today, values of $C_{H,sol}$ encompass the $\Delta G_f°$ of H·, its solvation $\Delta G°_{sol}$, and sometimes accounts for the identity of the reference electrode used in electrochemical experiments. Despite the continued debate,[67-69] the amended form is commonly used to calculate bond strengths for HAT (**Equation 1.6**) in what has been termed the "potential-pK_a" method, and these energies remain useful in predicting whether a complex will be a suitable hydrogen atom donor or acceptor in a proposed reaction.

1.6. Ligand-based proton-coupled electron transfer in coordination complexes.

The storage and delivery of protons and reducing equivalents can take many forms. Single-site PCET, where both are sourced from a metal hydride, for example, has been a powerful gateway for hydrogenation and hydroformylation reactivity.[70,71] Metal hydride complexes often behave much better as H-atom donors due to their low BDFE values.[72] The cobalt hydride complex[73] $HCo(dppe)_2$, which is very weakly acidic (pK_a 38.1 in MeCN), has a low BDFE of 59.1 kcal mol^{-1}; in fact, most systems with X–H BDFEs lower than 60 kcal mol^{-1} are metal hydride complexes.[68,72] More recently, studies have focused on multi-site PCET

reactions where a ligand and the metal center it is coordinated to each provide one component of the PCET reaction—usually electrons from the metal, and protons from the ligand.[63] Yet single-site, ligand-based PCET has also been observed. Examples from the groups of Waymouth[73] and Agapie[74,75] demonstrate that ligand-based PCET platforms are generally driven by the restoration of an aromaticity upon removal of a hydrogen atom or hydride.[76] The neutral molybdenum-quinoid complex reported by Agapie can donate $2H^+/2e^-$ from the π-bound ring of the catecholate ligand moiety, with an effective pK_a of 25.89(9) and BDFE below that of TEMPO (66.5 $kcal^{-1}$ mol^{-1}) in MeCN. These ligand-based PCET complexes are characterized by highly acidic protons (pK_a < 20); while that acidity would serve to lower the overall X–H BDFE, it is often counterbalanced by positive reduction potentials. When the same complex, oxidized to an overall dication, was studied by the Agapie group, it was found that the protons of the bound catechol were far more acidic (pK_a = 4.74(9)), though the BDFE remains generally the same. Ligand-based PCET is generally characterized by BDFEs of well above 60 kcal mol^{-1}, rendering them mid- to strong-H-atom acceptors.[77-79] Tuning the reactivity of either metal-hydride or ligand-based PCET systems is difficult, as the synthetic handles used to control the metal reduction potentials—namely, changing donor ligand strength, overall complex charge, and metal coordination environment—also influence pK_a.[80-82] As such, most alterations usually work against one another, resulting in little to no change in BDFE and thermodynamic hydricity.

Redox-active tridentate pincer ligands remain understudied platforms for PCET reactivity. Many redox-active pincer ligand platforms with two electrophilic donor atoms and a central nitrogen, denotated as [ENE] ligands, have been developed and characterized primarily for their electron transfer properties. Complexes with ligands in their different oxidation states can often be prepared independently, with the concomitant shift in open-circuit voltage observed in their voltammetry. However, the basicity of these tridentate

ligands' central nitrogen can be more difficult to measure, especially when coordinated to a metal that can itself be protonated in the form of a metal hydride. Locating the proton *via* ^{1}H NMR can be diagnostic for the presence of a metal-hydride *versus* ligand protonation, as M–H resonances are usually significantly upfield from organic protons. However, a variety of factors can make ^{1}H NMR measurement of these complexes difficult, including the presence of paramagnetic metal ions, or undesired solution equilibria that cause NMR spectra to broaden. In solid-state structures of sufficient quality, N–H protons can sometimes be located in the difference map, though this is not always the case. Evidence of ligand protonation can also be seen in the electronic absorption spectra of redox-active ligand complexes, as the large, conjugated π*-orbital system that spans both aromatic rings of these ligands is interrupted upon N–H protonation. To measure an [EN(H)E] ligand's pK_a requires acid-base titrations with clear end points, which grant equilibrium constants upon analysis, yet it must be considered whether the (often pyridine-based) acid or based titrant used in such reactions can coordinate to the metal itself. Thus, while spectrophotometric titrations or ^{1}H NMR titrations are most often used to extract acidity, these methods require many measurements and identical sample preparation, and are limited by the availability of tabulated pK_as for known acids in the solvent of interest, as well as by the availability of literature C_G values for the potential-pK_a equation, which are also solvent dependent.

Nevertheless, the potential-pK_a method has been successfully applied to coordination complexes of redox- and proton-active [EN(H)E] ligands. The factors that single-site, ligand-based PCET, where all electrons and protons involved in the reaction are sourced from a redox- and proton-active ligand, are still being explored.

1.7. Synthetic handles and trends in tridentate redox active ligand PCET.

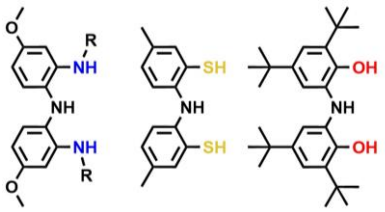

Figure 1.3. Tridentate redox-active [ENE] ligands studied in the Heyduk lab. Left to right: $[NNN]H_3$, $[SNS]H_3$, and $[ONO]H_3$.

In contrast to the aforementioned ligand-based PCET platforms, the Heyduk lab has demonstrated that redox- and proton-active pincer ligands of the [ENE] (E = O, N, S) motif, such as [ONO], [NNN], and [SNS] (bis(2-mercapto-4-methylphenyl)amide) (**Figure 1.3.**), possess thermodynamic properties more similar to metal hydride single-site platforms than to other reported ligand-based PCET systems. These pincer ligands are capable of storing and delivering a proton on the central nitrogen basic site and can additionally transfer one, or in the cases of [ONO] and [NNN], two electrons to affect net $H^{\cdot}$ or H^{-} transfer.

The tridentate redox-active [ENE] ligand platforms have also in some ways provided a workaround to the traditional roadblocks that prevent tuning BDFE and ΔG_{H^-} on metal hydrides in productive directions, and several methods of tuning the electron-transfer behavior of these ligands have been identified. Substitutions of electron withdrawing or electron donating groups on the aromatic backbone of the [NNN] ligand have been shown to shift reduction potentials by up to 270 mV while bound to a given metal center (tantalum(V)).[16] While these modifications demonstrated a large degree of control over [NNN] redox behavior, derivatizing the ligand backbone required drastically different and synthetically challenging routes with low yields. The pK_as of these complexes were not investigated at the time in favor of identifying more accessible routes to tune [ENE] redox activity, such as by simply varying the identity of a metal down one group. A series of $[SN(H)S]M(PR_3)$ complexes were prepared by identical salt metathesis procedures, with M = Ni, Pd, and Pt; metal substitution in this manner resulted in a 100 mV shift in the [sq•/cat] reduction potential (**Table 1.1**).[82] In addition, the pK_a of [SN(H)S] shifted by several units

Table 1.1. Metal Ion Substitution Effects on Ligand PCET

M	E°' / V vs. $[FeCp_2]^{+/0}$ [sq•/cat]	pK_a	BDFE (kcal mol^{-1})
Ni	−0.61	15.9 ± 0.5	62.6 ± 0.8
Pd	−0.58	17.4 ± 0.5	65.4 ± 0.7
Pt	−0.51	22.4 ± 0.4	73.6 ± 0.4

upon substitution of the metal it was coordinated to, as measured by spectrophotometric titrations with a pyridine-derived base. It was found that the aciditiy of [SN(H)S] was the lowest when the ligand was bound to Ni, and the pK_a of the [SN(H)S] proton was higher (became a weaker acid) when bound to Pd. The Pt complex [SN(H)S]Pt(PPh_3) has the highest [SN(H)S] pK_a. Surprisingly, the decrease in acid strength between [SN(H)S]M(PPh_3) species was concomitant with a positive shift in ligand reduction potential, resulting in a significant shift in the BDFE of the central N–H bond. Thus, the [SN(H)S]M(PR_3) system proved that a net 10 kcal^{-1} mol^{-1} shift in BDFE could be obtained without lengthy organic synthesis to derivatize the redox- and proton-active ligand backbone. A third synthetic handle to tune these [ENE] ligand-based PCET systems was discovered to be the identity of the chelating electrophilic donor atom, E, itself. Substituting O[84] for S[85] in isostructural [EN(H)E]NiPPh_3 complexes resulted in a net 300 mV change in the first ligand-based reduction potential, and the BDFE was observed to decrease 63.8 kcal mol^{-1} (E = S) to 54.0 kcal mol^{-1} (E = O). Redox- and proton-active pincer ligands are promising candidates for tunable ligand-based PCET, as there are multiple routes to modify their electron transfer and proton transfer behavior. However, other synthetic handles may exist to tune ligand-based acidity and reduction potentials, and it is unclear at the moment how valence tautomerization between metal-ligand fragments may affect the driving forces behind ligand-based PCET.

1.8. Contributions of this work.

This dissertation contains three studies of the $[ONO^{cat}]^{3-}$ redox- and proton-active ligand as a potential HAT agent when bound to transition metal ions.

Chapter 2 investigates a square-planar $\{[ONO]NiL\}^{-}$ system for linear free energy relationships between the donor strength of ancillary L-type ligands *trans* to the basic site in the tridentate ligand, and $[sq^{\bullet}]^{2-}/[cat]^{3-}$ reduction potential. The work therein demonstrates that the identity of L has minimal influence on the electron-transfer behavior of $[ONO]^{3-}$, compared to the much more tangible effect that ancillary ligand donor strength has on another redox-active ligand: the bidentate *ortho*-benzoquinonediimine (bqdi). What little influence L has on $[ONO]^{3-}$ in the $\{[ONO]NiL\}^{-}$ is in general agreement with understood *trans*-effects, but the electronic disconnect between $[ONO]^{3-}$ and ancillary L molecular orbitals means that this synthetic handle provides only the finest tuning over the overall PCET reactivity of the complex.

Chapter 3 fully describes the equilibria associated with PCET on $[ONO]Co(L)_n$ systems, where L were pyridine and 4-dimethyalminopyridine (n = 1, 2, 3). The [ON(H)O] ligand's acidity and reduction potentials were measured, and some comparative HAT reactivity was performed, to bracket the system's BDFE. However, several ancillary ligand equilibria were observed. The highly covalent nature of the [ONO]–Co fragment demonstrates that close electronic communication between ligand and metal can cause dramatic structural changes around the metal center, even when it may be the ligand that is being oxidized. The same communication and conformational changes result in the complex's very weakly acidic pK_a, which affords a much lower BDFE than seen in most ligand-based PCET systems. A computational investigation of valence tautomerization and accompanying structural changes offers some insight into the inherent barriers and driving forces of the $[ONO]Co(L)_n$ systems.

Chapter 4 of this dissertation demonstrates the opposite extreme, wherein the highly electropositive Ta(V) center of a novel $\{[ONO]TaCl_3\}^-$ may exert such an electronic demand on its coordinated ligands that the barrier to protonation—folding of the otherwise planar [ONO] ligand—nearly prohibits its formation. This results in what may seem like a superacidic ($pK_a < 7$ in MeCN) [ON(H)O] ligand, at least in a monomeric form. The effort to protonate and characterize the acid-base equilibria and the HAT behavior of this system is detailed in this work.

1.9. References.

1. Xiao, W.; Wang, R.S.; Handy, D.E.; Loscalzo, J. NAD(H) and NADP(H) Redox Couples and Cellular Energy Metabolism. *Antioxid Redox Signal.* **2018,** *28* (3), 251-272.
2. Pan, M.; Shao, M.; Jin, Z. Development of organic redox-active materials in aqueous flow batteries: Current strategies and future perspectives. *SmartMat.* **2023,** Early View.
3. Qianru, C.; Li, X. Organic Electrolytes for pH-Neutral Aqueous Organic Redox Flow Batterise. *Adv. Func. Mat.* **2022,** *32* (9), 2108777.
4. Pang, S.; Wang, X.; Wang, P.; Ji, Y. Biomimetic amino acid functionalized phenazine flow batteries with long lifetime at near-neutral pH. *Angew. Chem. Int. Ed.* **2021**, *60* (10), 5289-5298.
5. Xu, J., Pang, S.; Wang, X.; Wang, P. Ji, Y. Ultrastable aqueous phenazine flow batteries with high capacity operated at elevated temperatures. *Joule* **2021,** *5* (9), 2437-2449.
6. Pan, M.; Gao, L.; Liang, J.; Zhang, P.; Lu, S.; Lu, Y.; Ma, J.; Jin, Z. Reversible Redox Chemistry in Pyrrolidinium-Based TEMPO Radical and Extended Viologen for High-Voltage and Long-Life Aqueous Redox Flow Batteries. *Adv. Energy Mater.* **2022,** *12* (13), 2103478.
7. Gao, M.; Salla, M.; Song, Y.; Wang, Q. High-Power Near-Neutral Aqueous All Organic Redox Flow Battery Enabled with a Pair of Anionic Redox Species. *Angew. Chem., Int. Ed.* **2022,** *61* (41), e202208223.
8. Yap, L.L.; Lin, M.T.; Ouyang, H.; Samoilova, R.L.; Dikanov, S.A.; Gennis, R. B. The quinone-binding sites of the cytochrome *bo*$_3$ ubiquinol oxidase from *Escherichia coli. Biochim Biophys Acta Bioenerg* **2010,** *1797* (12), 1924-1932.
9. Choi, S. K.; Schurig-Briccio, L.; Ding, Z.; Hong, S.; Sun, C.; Gennis, R. **B.** Location of the Substrate Binding Site of the Cytochrome *bo*3 Ubiquinol Oxidase from Escherichia coli. *J. Am. Chem. Soc.* **2017**, 139 *(24)*, 8346-8354.
10. McDonald, A.E; Vanlerberghe, G.C. Quinol Oxidases. In *The Structural Basis of Biological Energy Production;* Hohmann-Marriott, M. Ed.; *Advances in Photosynthesis and Respiration,* Vol. 39. Springer, Dordrecht, **2014**.
11. Babcock, G.T.; Wikström, M. Oxygen activation and the conservation of energy in cell respiration. *Nature* **1992,** *356,* 2742-2753.
12. Poulos, T.L. Heme Enzyme Structure and Function. *Chem. Rev.* **2014,** *114* (7), 3919-3962.
13. McDonnell, A.M.; Dang, C.H. Basic Review of the Cytochrome P450 System. *J. Adv. Pract. Oncol.* **2013,** *4*, 263-268.
14. Carter, S.M.; Sia, A.; Shaw, M.J.; Heyduk, A.F. Isolation and Characterization of a Neutral Imino-semiquinone Radical. *J. Am. Chem. Soc.* **2008,** *130* (18), 5838-5839.
15. Singh, V.; Singh, R.; Hazari, A.S.; Adhikari, D. Unexplored Facet of Pincer Ligands: Super-Reductant Behavior Applied to Transition-Metal-Free Catalysis. *JACS Au* **2023,** *3* (4), 1213-1220.

16. Munhá, R. F.; Zarkesh, R.A.; Heyduk, A.F. Tuning the Electronic and Steric Parameters of a Redox-Active Tris(amido) Ligand. *Inorg. Chem.* **2013,** *52* (19), 11244-11255.
17. Chaudhuri, P.; Verani, C.N.; Bill, E.; Bothe, E.; Weyhermüller, T.; Wieghardt, K. Electronic Structure of Bis(o-iminobenzosemiquinonato)metal Complexes (Cu, Ni, Pd). The Art of Establishing Physical Oxidation States in Transition-Metal Complexes Containing Radical Ligands. *J. Am. Chem. Soc.* **2001,** *123* (10), 2213-2223.
18. Blackmore, K.J.; Ziller, J.W.; Heyduk, A.F. "Oxidative Addition" to a Zirconium(IV) Redox-Active Ligand Complex. *Inorg. Chem.* **2005,** *44* (16), 5559-5561.
19. Haneline, M.R.; Heyduk, A.F. C–C Bond-Forming Reductive Elimination from a Zirconium(IV) Redox-Active Ligand Complex. *J. Am. Chem. Soc.* **2006,** *128* (26), 8410-8411.
20. Smith, A. L.; Clapp, L. A.; Hardcastle, K. I.; Soper, J. D. Redox-active ligand-mediated Co–Cl bond-forming reactions at reducing square planar cobalt(III) centers. *Polyhedron*. **2010**, *29* (1), 164-169.
21. Jørgensen, C.K. Differences between the four halide ligands, and discussion remarks on trigonal-bipyramidal complexes, on oxidation states, and on diagonal elements of one-electron energy. *Coord. Chem. Rev.* **1966,** *1* (1-2), 164-178.
22. Enemark. J. H.; Feltham, R. D. Coord. Principles of structure, bonding, and reactivity for metal nitrosyl complexes. *Chem. Rev.* **1974**, *13*, 339–406.
23. Cohen, S.A.; Auburn, P.R.; Bercaw, J.E. Structure and reactivity of bis(pentamethylcyclopentadienyl)(ethylene)titanium(II), a simple olefin adduct of titanium. *J. Am. Chem. Soc.* **1983,** *105* (5), 1136-1143.
24. Luca, O.R.; Crabtree, R.H. Redox-active ligands in catalysis. *Chem. Soc. Rev.* **2013,** *42,* 1440-1459.
25. Brown, S.N. Metrical Oxidation States of 2-Amidophenoxide and Catecholate Ligands: Structural Signatures of Metal–Ligand π Bonding in Potentially Noninnocent Ligands. *Inorg. Chem.* **2012,** *51* (3), 1251-1260.
26. Ranis, L. G.; Werellapatha, K.; Pietrini, N. J.; Bunker, B. A.; Brown, S. N.; Metal and Ligand Effects on Bonding in Group 6 Complexes of Redox-Active Amidodiphenoxides. *Inorg. Chem.* **2014,** *53* (19), 10203-10216.
27. Masui, H.; Dodsworth, E.S..; Lever, A.B.P. Substituent Effects and Bonding Characteristics in o-Benzoquinonediiminebis (bipyridine) ruthenium(II) Complexes. *Inorg. Chem.* **1993,** 32, 258-267.
28. Patra, S.; Sarkar, B.; Mobin, S.M.; Kaim, W.; Lahiri, G.M. Separating Innocence and Non-Innocence of Ligands and Metals in Complexes [(L)Ru(acac)2]n (n = −1, 0, +1; L = o-Iminoquinone or o-Iminothioquinone). *Inorg. Chem.* **2003,** *42* (20), 6469-6473.
29. Remenyi, C.; Kaupp, M. Where Is the Spin? Understanding Electronic Structure and g-Tensors for Ruthenium Complexes with Redox-Active Quinonoid Ligands. *J. Am. Chem. Soc.* **2005,** *127* (32), 11399-11413.
30. Lubitz, W.; Lendzian, F.; Bittl, R. Radicals, Radical Pairs and Triplet States in Photosynthesis. *Acc. Chem. Res.* **2002,** *35 (5),* 313-320.

31. Szigethy, G.; Shaffer, D.W.; Heyduk, A.F. Coordination Effects on Electron Distributions for Rhodium Complexes of the Redox-Active Bis(3,5-di-tert-butyl-2-phenolate)amide Ligand. *Inorg. Chem.* **2012,** *51* (23), 12606-12618.
32. Figgins, P. E.; Busch, D. H. Complexes of iron(II), cobalt(II), and nickel(II) with biacetyl bis(methylimine), 2-pyridinecarboxaldehyde methylimine, and 2,6-pyridinedicarboxaldehyde bis(methylimine). *J. Am. Chem. Soc.* **1960**, *82* (4), 820-824.
33. Pierpont, C.G. Studies on charge distribution and valence tautomerism in transition metal complexes of catecholate and semiquinonate ligands. *Coord. Chem. Rev.* **2001,** *216-217,* 99-125.
34. Stouffer, R. C.; Hadley, W. B.; Busch, D. H. Unusual magnetic properties of some six-coordinate cobalt(II) complexes – electronic isomers. *J. Am. Chem. Soc.* **1961**, 83, 3732-3724.
35. Britovsek, G. J. P.; Gibson, V. C.; Kimberley, B. S>; Maddox, P. J.; McTavish, S. J.; Solan, G. A.; White, A. J. P.; Williams, D. J. Novel olefin polymerization catalysts based on iron and cobalt. *Chem. Commun.* **1998**, 7, 849-850.
36. Bianchini, C.; Giambastiani, G.; Guerrero Rios, I.; Mantovani, G.; Meli, A.; Segarra, A. M. Ethylene oligomerization, homopolymerization and copolymerization by iron and cobalt catalysts with 2,6-(bis-organylimino)pyridyl ligands. *Coord. Chem. Rev.* **2006**, 250 (11-12), 1391-1418.
37. Bowman, A. C.; Milsmann, C.; Bill, E.; Weyhermuller, T.; Wieghardt, K.; Chirik, P. J. Reduced N-Alkyl Substituted Bis(imino)pyridine Cobalt Complexes: Molecular and Electronic Structures for Compounds Varying by Three Oxidation States. *Inorg. Chem.* **2010,** 49 (13), 6110-6123.
38. Bart, S. C.; Chlopek, K.; Bill, E.; Bouwkamp, M. W.; Lobkovsky, E.; Neese, F.; Wieghardt, K.; Chirik, P. J. Electronic Structure of Bis(imino)pyridine Iron Dichloride, Monochloride, and Neutral Ligand Complexes: A Combined Structural, Spectroscopic, and Computational Study. *J. Am. Chem. Soc.* **2006,** *128* (42), 13901-13912.
39. Knijnenburg, Q., Hetterscheid, D., Kooistra, T. M., and Budzelaar, P. H. M. The Electronic Structure of (Diiminopyridine)cobalt(I) Complexes. *Eur. J. Inorg. Chem.* **2004**, 1204-1211.
40. Kruck, M.; Sauer, D.; Enders, M.; Wadepohl, H.; Gade, L. H. Bis(2-pyridylimino)isoindolato iron(ii) and cobalt(ii) complexes: Structural chemistry and paramagnetic NMR spectroscopy. *Dalton Trans.* **2011,** *40*, 10406-10415.
41. Bogani, L.; Werndsorfer, W. Molecular spintronics using single-molecule magnets. *Nature Materials* **2008**, *7* (3), 179-186.
42. Leuenberger, M.N.; Loss, Daniel. Quantum computing in molecular magnets. *Nature*, **2001**, *410* (6830).
43. Hunt, C.; Peterson, M.; Anderson, C.; Chang, T.; Wu, G.; Scheiner, S. Menard, G. Switchable Aromaticity in an Isostructural Mn Phthalocyanine Series Isolated in Five Separate Redox States. *J. Am. Chem. Soc.* **2019,** 141 (6), 2604-2613.
44. Tfouni, E. Krieger, M.; McGarvey, B.R.; Franco, D.W. Structure, chemical and photochemical reactivity and biological activity of some ruthenium amine nitrosyl complexes. *Coord. Chem. Rev.* **2003**, 236 (1-2), 57-69.

45. Chatt, J. Ligand effects. *Coord. Chem. Rev.* **1982**, 43, 337-348.
46. Hussain, W.; Leigh, G. J.; Ali, . M.; Pickett, C. J.; Rankin, D. A. Dinitrogen binding and electrochemistry in complexes of molybdenum and tungsten. *J. Chem. Soc., Dalton Trans.* **1984**, 8, 1131-1136.
47. Pombeiro, A. J. L. Ligand and structural effects on the redox potential of octahedral 18-electron complexes with 14-electron or 12-electron metal centres. *Port. Electrochim. Acta.* **1985**, *3*, 41-66.
48. Pombeiro, A. J. L. Preparation and redox properties of the complexes trans-[ReL2(dppe)2]BF4 (L = CO or isocyanide). Estimate of the oxidation potential of octahedral 18-electron complexes with 14-electron square planar metal centres and of related electrochemical parameters for derived 16-electron sites. *Inorg. Chim. Acta*. **1985,** *103*, 95-103.
49. Pombeiro, A. J. L.; Pickett, C. J.; Richards, R. L. The electronic properties of isocyanides at rhenium—dinitrogen binding sites. Preparation and redox properties of the isocyanide complexes trans-[ReCl(CNR)(Ph2PCH2CH2PPh2)2]. *J. Organomet. Chem.* **1982,** *224*, 285-294.
50. Fernanda, M.; Carvalho, N. N.; Pombeiro, A. J. L. Syntheses and redox properties of mixed isocyanide, carbonyl, or nitrile complexes of rhenium(I)trans-[Re(CNMe)L(Ph2PCH2CH2PPh2)2]X [L = CNR (R = alkyl or aryl), CO, or NCMe; X = Cl, BF4, or PF6]. *J. Chem. Soc., Dalton Trans.* **1989**, 1209-1216.
51. Treichel, P. M.; Dirreen, G. E.; Mueh, H. J. J. Manganese(I) isocyanide complexes. *Organomet. Chem.* **1972**, *44*, 339.
52. Sarapu, A.; Fenske, R. F. The Transition Metal-Isocyanide Bond. An Approximate Molecular Orbital Study. *Inorg. Chem.* **1975**, *14,* 247-253.
53. Chatt, J.; Kan, C. T.; Leigh, G. J.; Pickett, C. J.; Stanley, D. R. J. Transition-metal binding sites and ligand parameters. Chem. Soc., Dalton Trans. 1980, 2032-2038.
54. Lever, A.B.P. Electrochemical parametrization of metal complex redox potentials, using the ruthenium(III)/ruthenium(II) couple to generate a ligand electrochemical series. Inorg. Chem. 1990 29 (6), 1271-1285.
55. Fielder, S.S.; Osborne, M.C.; Lever, A.B.P.; Pietro, W.J. First Principles Interpretation of Ligand Electrochemical (EL(L)) Parameters; Factorization of the sigma and pi Donor and pi-Acceptor Capabilities of a Ligand. J. Am. Chem. Soc., 1995 117 6990-93.
56. Perrin, L.; Clot, E.; Eisenstein, O.; Loch, J.; Crabtree, R. H. Computed Ligand Electronic Parameters from Quantum Chemistry and Their Relation to Tolman Parameters, Lever Parameters, and Hammett Constants. Inorg. Chem 2001, 40, 5806–5811.
57. Masui, H.; Lever, A. B. P. Correlations between the Ligand Electrochemical Parameter, EL(L), and the Hammett Substituent Parameter, .Sigma. Inorg. Chem. 1993, 32 (10), 2199–2201.

58. Lever, A.B.P. Electronic characteristics of an extensive series of ruthenium complexes with the non-innocent o-benzoquinonediimine ligand: A pedagogical approach. *Coord. Chem. Rev.* **2010,** *254* (13-14), 1397-1405.
59. Hill, E.A.; Weitz, A.C.; Onderko, E.; Romero-Riverall, A.; Guo, Y.; Swart, M.; Bominaar, E.L.; Green, M.T.; Hendrich, M.P.; Lacy, D.C.; Borovik, A.S. Reactivity of an FeIV-Oxo Complex with Protons and Oxidants. *J. Am. Chem. Soc.* **2016,** *138* (40), 13143-13146.
60. Borovik, A.S. Bioinspired Hydrogen Bond Motifs in Ligand Design: The Role of Noncovalent Interactions in Metal Ion Mediated Activation of Dioxygen. *Acc. Chem. Res.* **2005,** *38* (1), 54-61.
61. Skone, H. J.; Soudackov, A.V.; Hammes-Schiffer, S. Calculation of Vibronic Couplings for Phenoxyl/Phenol and Benzyl/Toluene Self-Exchange Reactions: Implications for Proton-Coupled Electron Transfer Mechanisms. *J. Am. Chem. Soc.* **2006,** *128* (51), 16655-16663.
62. Tyburski, R.; Liu, T.; Glover, S.D.; Hammarström, L. Proton-Coupled Electron Transfer Guidelines, Fair and Square. *J. Am. Chem. Soc.* **2021,** *143* (2), 560-576.
63. Darcy, J.W.; Koronkiewicz, B.; Parada, G.A.; Mayer, J.M. A Continuum of Proton-Coupled Electron Transfer Reactivity. *Acc. Chem. Res.* **2018,** *51* (10), 2391-2399.
64. Bordwell, F.G.; Cheng, J.P.; Harrelson, J.A. Homolytic bond dissociation energies in solution from equilibrium acidity and electrochemical data. *J. Am. Chem. Soc.* **1988,** *110* (4), 1229-1231.
65. Wayner, D.D.M.; Parker, V.D. Bond energies in solution from electrode potentials and thermochemical cycles. A simplified and general approach. *Acc. Chem. Res.* **1993,** *26* (5), 287-294.
66. Parker, V.D.; Handoo, K.L.; Roness, F.; Tilset, M. Electrode Potentials and the Thermodynamics of Isodesmic Reactions. *J. Am. Chem. Soc.* **1991,** *113,* 7493-7498.
67. Tilset, M.; Parker, V.D. Solution homolytic bond dissociation energies of organotransition-metal hydrides. *J. Am. Chem. Soc.* **1989,** *111* (17), 6711-6717.
68. Warren, J.J.; Tronic, T.A.; Mayer, J.M. Thermochemistry of Proton-Coupled Electron Transfer Reagents and its Implications. *Chem. Rev.,* **2010** *110* (12), 6961-7001.
69. Agarwal, R.G.; Wise, C.F.; Warren, J.J.; Mayer, J.M. Correction to Thermochemistry of Proton-Coupled Electron Transfer Reagents and its Implications. *Chem. Rev.* **2022,** *122* (1), 1482.
70. Schevick, S.L.; Wilson, C.V. Kotesova, S.; Kim, D.; Holland, P.L.; Shenvi, R.A. Catalytic hydrogen atom transfer to alkenes: a roadmap for metal hydrides and radicals. *Chem. Sci.* **2020,** *11* (46), 12401-12422.
71. Bourrez, M.; Steinmetz, R.; Ott, S.; Gloaguen, F.; Hammarström, L. Concerted proton-coupled electron transfer from a metal-hydride complex. *Nature Chem.* **2015,** *7,* 140-145.
72. Wiedner, E.S.; Chambers, M.B.; Pitman, C.L.; Bullock, R.M.; Miller, A.J.M.; Appel, A.M. Thermodynamic Hydricity of Transition Metal Hydrides. *Chem. Rev.* **2016***, 116* (15), 8655-8692.
73. McLoughlin, E.A.; Waldie, K.M.; Ramakrishnan, S.; Waymouth, R.M. Protonation of a Cobalt Phenylazopyridine Complex at the Ligand Yields a Proton, Hydride, and Hydrogen Atom Transfer Reagent. *J. Am. Chem. Soc.* **2018,** *140* (41), 13233-13241.

74. Henthorn, J.T.; Agapie, T. Modulation of Proton-Coupled Electron Transfer through Molybdenum–Quinonoid Interactions. *Inorg. Chem.* **2016,** *55* (11), 5337-5342.
75. Henthorn, J.T. Lin, S.; Agapie, T. Combination of redox-active ligand and lewis acid for dioxygen reduction with π-bound molybdenum-quinonoid complexes. *J. Am. Chem. Soc.* **2015,** *137* (4), 1458-1464.
76. Solis, B.H.; Maher, A.G.; Honda, T.; Powers, D.C.; Nocera, D.G. Theoretical Analysis of Cobalt Hangman Porphyrins: Ligand Dearomatization and Mechanistic Implications for Hydrogen Evolution. *ACS Catal.* **2014,** *4* (12), 4516-4526.
77. Henry, R.M.; Shoemaker, R.K.; DuBois, D.L.; Rakowski DuBois, M. Pendant Bases as Proton Relays in Iron Hydride and Dihydrogen Complexes. *J. Am. Chem. Soc.* **2006,** *128* (9), 3002-3010.
78. Sherbow, T.J.; Fettinger, J.C.; Berben, L.A. Control of Ligand pKa Values Tunes the Electrocatalytic Dihydrogen Evolution Mechanism in a Redox-Active Aluminum(III) Complex. *Inorg. Chem.* **2017,** *56* (15), 8651-8660.
79. Quist, D.A.; Ehudin, M.E.; Schaefer, A.W.; Schneider, G.L.; Solomon, E.I.; Karlin, K.D. Ligand Identity-Induced Generation of Enhanced Oxidative Hydrogen Atom Transfer Reactivity for a $Cu^{II}_2(O_2^{\cdot-})$ Complex Driven by Formation of a Cu^{II}_2(-OOH) Compound with a Strong O-H Bond. *J. Am. Chem. Soc.* **2019,** *141* (32), 12682-12696.
80. Cappellani, E.P.; Drouin, S.D.; Jia, G.; Maltby, P.A.; Morris, R.H.; Schweitzer, C.T. Effect of the Ligand and Metal on the pKa Values of the Dihydrogen Ligand in the Series of Complexes [M(H2)H(L)2]+, M = Fe, Ru, Os, Containing Isosteric Ditertiaryphosphine Ligands, L. *J. Am. Chem. Soc.* **1994,** *116* (8), 3375-3388.
81. Rennie, B.E.; Eleftheriades, R.G.; Morris, R.H. Systematic Trends in the Electrochemical Properties of Transition Metal Hydride Complexes Discovered by Using the Ligand Acidity Constant Equation. *J. Am. Chem. Soc.* **2020** *142* (41), 17607-17629.
82. Bailey, W.D.; Dhar, D.; Cramblitt, A.C.; Tolman, W.B. Mechanistic Dichotomy in Proton-Coupled Electron-Transfer Reactions of Phenols with a Copper Superoxide Complex. *J. Am. Chem. Soc.* **2019,** *141* (13), 5470-5480.
83. Charette, B.J.; Ziller, J.W.; Heyduk, A.F. Metal-Ion Influence on Ligand-Centered Hydrogen-Atom Transfer *Inorg. Chem.* **2021,** *60* (3), 1579-1589.
84. Charette, B.J.; Ziller, J.W.; Heyduk, A.F. Exploring Ligand-Centered Hydride and H-Atom Transfer. *Inorg. Chem.* **2021,** *60* (7), 5367-5375.
85. Rosenkoetter, K.E.; Wojnar, M.K.; Charette, B.J.; Ziller, J.W.; Heyduk, A.F. Hydrogen-Atom Noninnocence of a Tridentate [SNS] Pincer Ligand. *Inorg. Chem.* **2018,** *57* (16), 9728-9737.

CHAPTER 2: Ancillary ligand influence on tridentate redox active ligand electronics

2.1. Introduction.

2.1.1. Tuning metal reduction potentials in coordination complexes.

Designing transition metal catalysts with controlled reactivity for the reduction CO_2 or N_2, and for C–H bond functionalization, requires careful management of proton and electron storage and delivery to and from substrates. Proton-coupled electron transfer (PCET) involving coordination complexes often sources both proton and electrons from a metal hydride (M–H) bond, whose bond dissociation free energy (BDFE) is a state function that, by Hess's law, can be described by its acidity and reduction potential (**Equation 2.1**).[1-9] Tuning the behavior of coordination complexes toward PCET reactions necessitates synthetic control over the system's reduction potential, and the acidity, of metal and bound hydrogen.

$$\Delta G(\mathrm{H-A}) = 1.37\mathrm{p}K_a + 23.06E^{\circ} + C_{H,sol} \qquad \textbf{(EQN 2.1)}$$

Ancillary ligands can influence metal-based reduction potentials associated with t_{2g} orbitals specifically,[10-21] and the electronical ligand parameter (E_L) was empirically derived to predict such shifts.[22] E_L is now understood to primarily reflect the ability of a given ligand to accept electron density from a metal center through π back-bonding, and it is a helpful metric to consider in designing catalysts with specific reduction potentials.[22-25]

2.1.2. Tuning redox-active ligand reduction potentials when bound to metal ions.

A new degree of synthetic control over acidity and reduction potential is introduced when the electron and proton do not originate from the metal center but rather from a coordinated ligand, or some mix of both. Redox-active ligand reduction potentials can be tuned by synthetic modifications on their backbones,[26] but investigations have revealed that

coordinated metal ions can also influence the electron-transfer behavior of coordinated redox-active ligands.[27] Ancillary ligands have also been shown to exert substantial influence over the electrochemical behavior of certain redox-active ligands in coordination complexes.[28-29] Lever demonstrated the linear free energy relationship between the ΣE_L of four ancillary ligands, the *o*-benzoquinonediimine (bqdi) quinone/semiquinone reduction ($E_{1/2}$[q/sq•]), and the net Mulliken charge on the bqdi backbone in six-coordinate complexes of ruthenium.[28] The bqdi ligand itself is *π*-accepting with an empty *π** redox-active orbital, and as such, the electron density on the ligand is very sensitive to electronic changes on the metal it is bound to *via* π-back donation.

It was less clear how much influence ancillary ligands might have on the redox potentials of a fully-reduced ligand such as the bis(3,5-di-*tert*-butyl-2-phenoxy)amide $[ONO^{cat}]^{3-}$ platform, which theoretically cannot accept electron density into its filled redox-active orbital from the metal center.

By tuning the [ONO]→M donation, it might be possible to reduce the charge on the [ONO] backbone and thus raise the $E_{1/2}$ [sq•/cat] potential. The fully-reduced $[ONO^{cat}]^{3-}$ ligand should be a strong π-donor, and increased electron density at a metal center should have an extremely subtle influence, if any, on the [ONO] $E_{1/2}$ [sq•/cat] potential. While increased σ-donation from an ancillary ligand might not be expected to shift $E_{1/2}$ [sq•/cat] much, it was thought that a more π-acidic ancillary ligand might alleviate electron density from the metal center and encourage [ONO]→M donation. To this end, isostructural

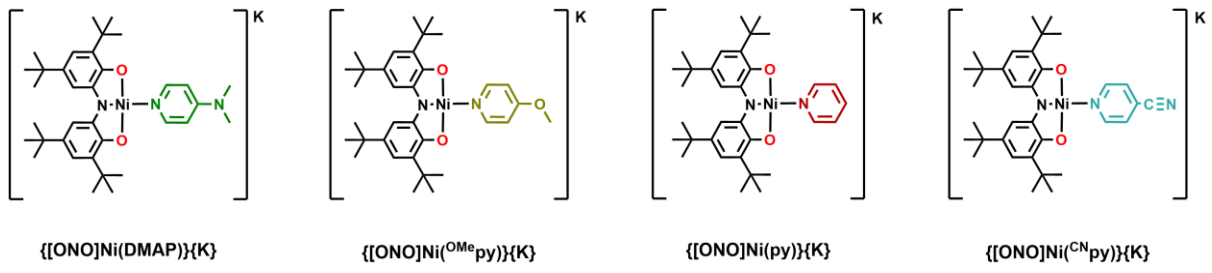

Figure 2.1. Isostructural Ni complexes of the [ONO] ligand studied in this work.

complexes of the form {[ONO]NiL}$^-$ were synthesized (**Figure 2.1**). These four-coordinate complexes were studied spectroscopically, electrochemically, in the solid-state, and computationally to determine changes in redox behavior.

2.2. Results.

2.2.1. Synthesis.

The complexes discussed in this work were synthesized by the stoichiometric deprotonation and salt metathesis previously reported for {[ONO^{cat}]Ni(PPh$_3$)}K and {[ONO^{cat}]Ni(py)}K (**Scheme 2.1, a**). In that study, addition of one equivalent of py to {[ONO^{cat}]Ni(PPh$_3$)}K (**Scheme 2.1, b**) resulted in near quantitative substitution of the PPh$_3$ ligand. The pyridyl ligands DMAP, ^{OMe}py, and ^{CN}py likewise displace PPh$_3$. Electrospray ionization mass spectrometry (ESI-MS) was used to confirm the empirical formula of each anion, with results consistent with {[ONO]Ni(L)}$^-$ fragments.

^{1}H and ^{31}P{^{1}H} NMR spectra were collected for the {[ONO]Ni(L)}K complexes to assess their structure and magnetism in solution. The aromatic region of the spectra when L = ^{OMe}py, py, ^{CN}py, were broad, even at low temperatures (258 K (CD_3CN), or 240 K (d_8-THF)), though sharp [ONO] *t*Bu resonances appeared between 1.2-1.6 ppm in each sample, indicative of bound [ONO] ligands. When L = DMAP, two sets of aromatic and alkyl resonances were found

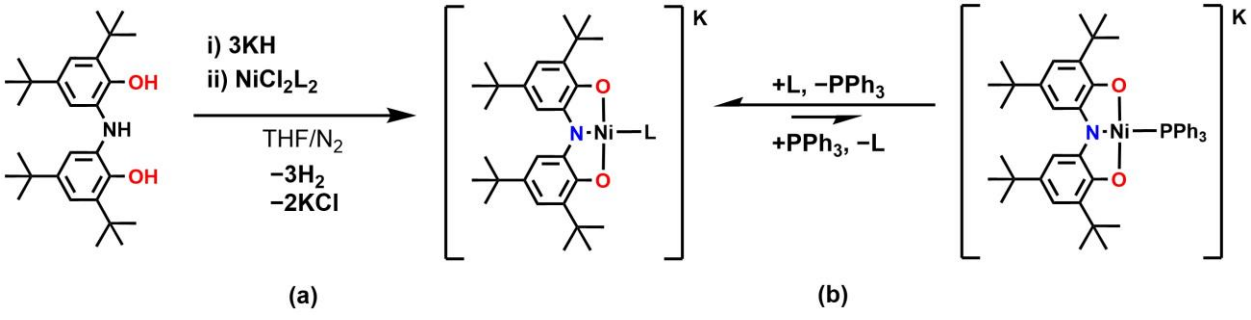

Scheme 2.1. Two synthesis routes to access {K}{[ONO]NiL} complexes. Stoichiometric deprotonation followed by salt metathesis with a nickel salt (a) has been a fruitful route for most L. Pyridyl ligands can easily displace PPh$_3$ (b) to obtain the same complexes.

that could both be attributed to DMAP, but no aromatic [ONO] peaks were resolved. Evans method measurements of the solution effective magnetic moments (μ_{eff}) ranged from 1.0 to 1.5 for these complexes, consistent with S = 0 systems. Titration of excess L into the NMR samples did not sharpen the features of the complex, nor did addition of chelating agent))to {[ONO]Ni(L)}K. Solutions of {[ONO]Ni(L)}K (L = DMAP, ^{OMe}py, ^{CN}py) show minor color changes in coordinating solvents vs. non-coordinating solvents, with minor color changes visible upon addition of 2.2.2-cryptand to sequester the potassium counter ion. Conversely, while {[ONO]Ni(py)}K is red both in coordinating solvents and in benzene, addition of 2.2.2-cryptand to benzene solutions induces a stark color change to vivid purple. No change in solvent resulted in the sharpening of NMR features, however.

2.2.2. Structural characterization.

Crystal structures for L = DMAP and py were obtained from concentrated solutions of the complex dissolved in acetonitrile or pentane stored at –35 °C with 2.2.2-cryptand to sequester the K^+ counter ion (**Figure 2.2 a, b**). For L = ^{OMe}py, crystals were obtained from a concentrated solution of benzene (**Figure 2.2 , c**). In the case of the DMAP complex, the unit cell contained two distinct molecules, one with DMAP tilted up, and one with DMAP rotated out of the [ONO]–Ni plane (**Figure 2.3, a**).

In the structure obtained from concentrated benzene solutions of {K}{[ONO]Ni(^{OMe}py)} (**Figure 2.2, c**), the unit cell consisted of two identical {[ONO]Ni(^{OMe}py)} units (**Figure 2.3, b**). The potassium ion is shared between the aromatic ring of one [ONO] backbone and the N_1, C_6, C_1, and O_1 atoms of the other [ONO]. The potassium ions themselves are bridged by two water molecules, whose protons were located in the difference map. Crystal data from {[ONO^{cat}]Ni(py)}K and {[ONO^{cat}]Ni(PPh_3)}K are reprinted in **Table 2.1** for comparison.[31,32] The

Table 2.1. Selected bond distances (Å) and τ_4 values of {K}{[ONO]Ni(L)} solid-state structures (L = DMAP, ^{OMe}py, py, PPh_3).

L	DMAP	^{OMe}py	py	PPh_3[28]
Bond[a]	**Distance / Å**			
O1-C1	1.3943(3)	1.3535(14)	1.345(19)	1.3490(18)
O2-C7	1.349(3)	1.3526(13)	1.346(2)	1.3490(17)
C6-N1	1.392(3)	1.3825(17)	1.390(2)	1.387(2)
C12-N1	1.385(3)	1.3866(15)	1.387(2)	1.3847(19)
O1-Ni	1.8445(18)	1.8560(8)	1.8435(12)	1.8517(11)
O2-Ni	1.8493(18)	1.8626(8)	1.8433(12)	1.85180 (10)
N1-Ni	1.8193(19)	1.8215(10)	1.8178(14)	1.8552(11)
L-Ni	1.9249(1)	1.9222(10)	1.9210(14)	2.2061(7)
MOS[b]	−2.75 ± 0.196	−2.62 ± 0.175	−2.57 ± 0.174	−2.65 ± 0.097
Bond	**Angle / °**			
O1-Ni-O2	173.67(7)	167.71(4)	173.93(6)	172.08(5)
N1-Ni-L	178.78(8)	176.03(4)	178.18(7)	173.33(5)
O2-Ni-N1	86.91(8)	86.68(4)	86.98(6)	86.52(5)
O1-Ni-N1	86.86(8)	86.29(4)	87.00(6)	86.28(5)
O1-Ni-L	92.82(7)	93.69(4)	92.85(6)	98.04(4)
O2-Ni-L	93.43(7)	94.01(4)	93.19(6)	89.42(4)
τ_4	0.053	0.14	0.056	0.10

(a) In crystals with multiple molecules in the unit cell, reported bonds were taken from just one.
(b) MOS are averaged between two sides of one molecule. In crystals with multiple molecules in the unit cell, MOS is reported for just one.
(c) $\tau_4 = \frac{360°-(\alpha+\beta)}{360°-2\theta}$ where α, ß are the largest angles about the M ion, and θ represents the tetrahedral angle 109.5°.

results of metrical oxidation state (MOS) analysis[33] are reported for {[ONO]Ni(L)}K (L = DMAP, py, and ^{OMe}py) along with relevant bond lengths, bond angles, and the geometric index τ_4; the bonds listed correspond to the labeled diagram (**Figure 2.2**).

The bond lengths within the redox-active ligand reported in Table 2.1. do not vary significantly (< 0.05 Å for most bonds). Accordingly, the MOS of the [ONO] ligand does not vary much from –2.62 ± 0.175 to –2.69 ± 0.196. The X–Ni and Ni–L bond lengths (L = DMAP, ^{OMe}py, py) likewise do not vary much between complexes, ranging from 1.8434(13)-1.863(1) Å for O–Ni bonds, 1.8178(15)-1.822(1) Å for N_{ONO}–Ni bonds, and 1.9209(14)-1.9249(1) Å for L–Ni bonds.

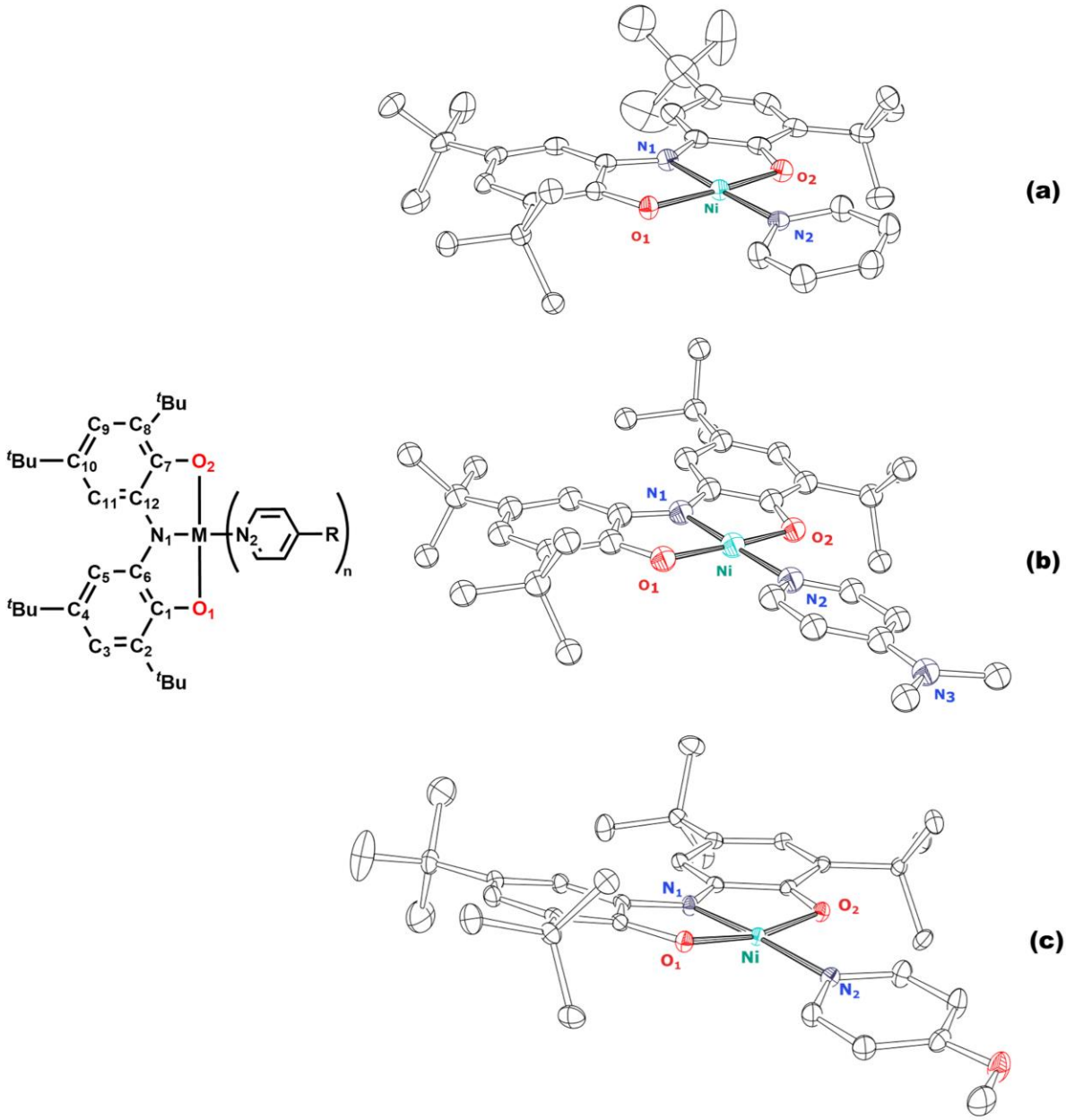

Figure 2.2. ORTEP diagrams of {[ONO]NiL}⁻ complexes discussed in this work (L = DMAP (a), ^{OMe}py (b), py (c)). Hydrogen atoms, counter ions, chelating agents, and solvent molecules have been omitted for clarity. In the case of (a), a crystallographically unique molecule has been omitted here, and in (b), a water-bridged potassium dimer has also been omitted, for clarity. They are reproduced elsewhere in this manuscript.

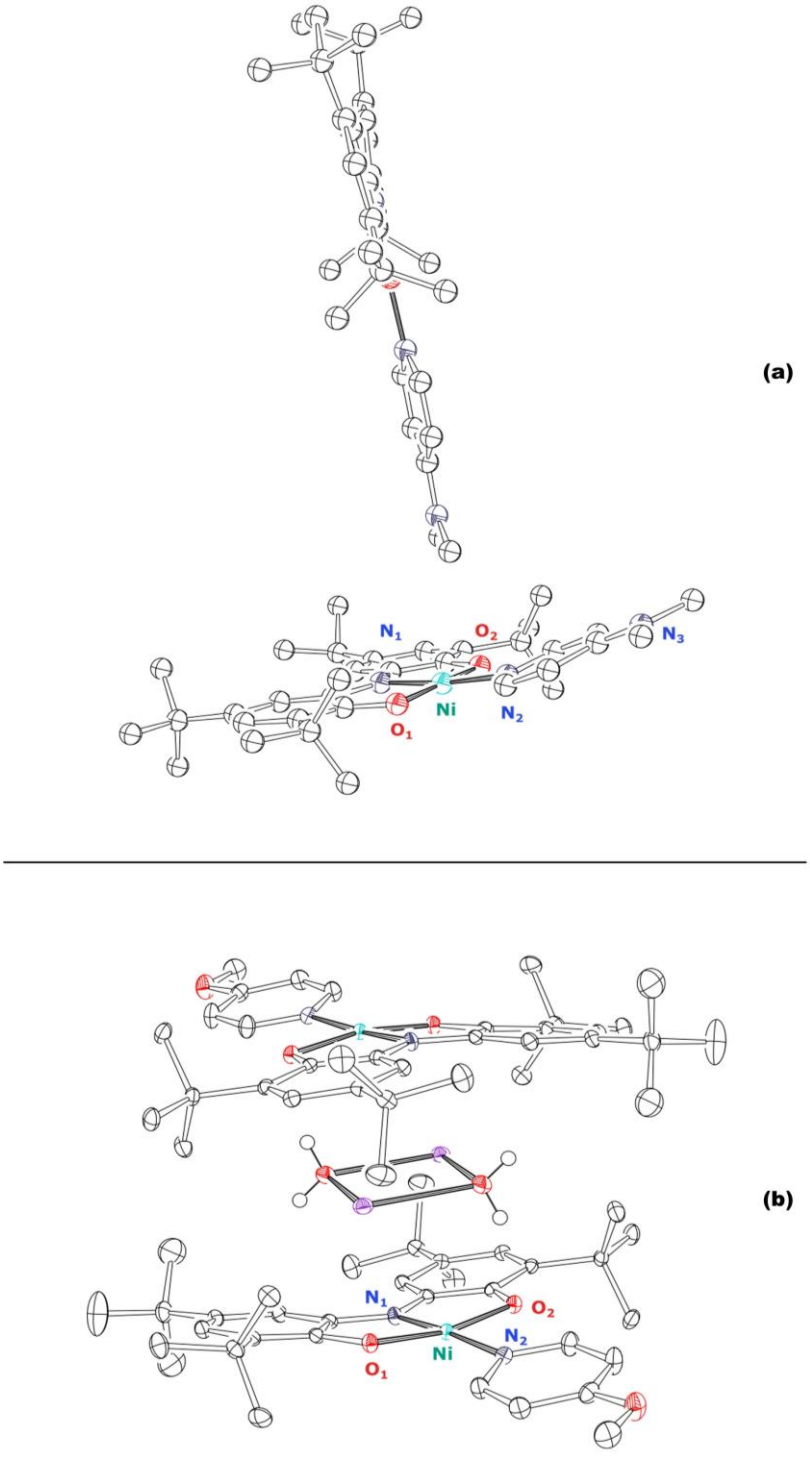

Figure 2.3. ORTEP diagrams of {[ONO]NiL}$^{-}$ (L = DMAP (a), ^{OMe}py (b)). In (a), potassium ions and 2.2.2.-cryptand have been excluded for clarity. In one molecular unit, L is rotated out of the plane of the redox-active ligand and metal (a, top), and in the other, L is canted up out of the plane (a, bottom). In crystal structure (b), the potassium counter ions of one molecular unit sits closely above the Ni, O, and redox-active backbone of its [ONO] ligand, and the aromatic backbone of a second unit above it; the potassium ions are bridged by one molecule of water each.

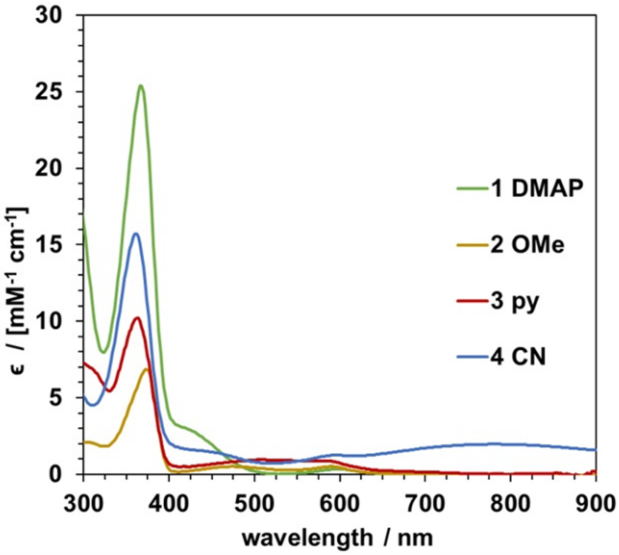

Figure 2.4. UV-visible spectra in THF of {[ONO]Ni(L)}K (L = DMAP, ^{OMe}py, ^{CN}py) showing main charge transfer bands between 300-900 nm.

Table 2.2. Extinction coefficients and λ_{max} of each UV-visible transition for {K}{[ONO]Ni(L)} complexes in THF.

L	DMAP	^{OMe}py	py	^{CN}py
	λ / nm (ε / $M^{-1}cm^{-1}$)			
	366 (23,100)	370 (7,300)	314 (6,900)	362 (16,500)
	443, sh (1,210)	456 (640)	364 (10,300)	444 (1,300)
			555, br (313)	777, br (2,000)

2.2.3. Spectroscopic characterization.

UV-visible spectroscopy was used to further confirm the oxidation state of the [ONO] ligand in these complexes. The main features observed in electronic absorption spectra taken of {[ONO]Ni(L)}K species are summarized in **Table 2.2**. Each of the complexes exhibit a charge-transfer band in the visible region ~360 nm, with extinction coefficients ϵ ranging widely from 700 to 22,000 M^{-1} cm^{-1}. In complexes of L = DMAP and ^{CN}py a mid-intensity absorbance is seen ~445 nm as a shoulder. For L = ^{OMe}py and py, a low-intensity band of absorptions spans 480-550 nm (ϵ = 700 and 1,244 M^{-1} cm^{-1} respectively), and L = ^{CN}py exhibits a broad series of transitions from ~600 nm to 1000 nm. Complexes of $[ONO^{cat}]^{3-}$ are often

green, but complexes of L = ^{OMe}py and py are brown or red in THF, respectively. Solutions of L = py in benzene are purple, and the addition of 2.2.2-cryptand to sequester the potassium counter ion in coordinating solvents induces a change from deep red to dark purple as well.

2.2.4. Electrochemical characterization.

The electrochemistry of the series of complexes is detailed in **Table 2.3. and Figure 2.5.** Voltammetric experiments were performed in THF with 1.0 mM analyte concentration and 0.1 M $\{Bu_4N\}\{PF_6\}$ electrolyte using a glassy carbon working electrode, Pt wire counter electrode, and $Ag^{+/0}$ pseudo-reference electrode at ambient glovebox temperatures. Electrochemistry has been reported in MeCN for L = py and PPh_3,[31,32] but L = DMAP and ^{OMe}py are not well-behaved upon oxidation in MeCN. In THF, species show reversible ($i_{pa}/i_{pc} \cong 1$, $i_{pa} \propto v^{1/2}$) redox couples around −1.1 V and have less reversible events at −0.5 V ($i_{pa}/i_{pc} \neq 1$) with respect to the $[FeCp_2]^{+/0}$ redox couple. Additionally, all have an irreversible reduction between −2.5 and −4.0 V; in L = py, this becomes more reversible at faster scan rates (i_{pa}/i_{pc} approaches unity). In the complex of L = ^{CN}py, two additional reversible features appear between −2.0 and −3.0 V. Scan rate dependence studies are included (**Figure 2.9-Figure 2.15**).

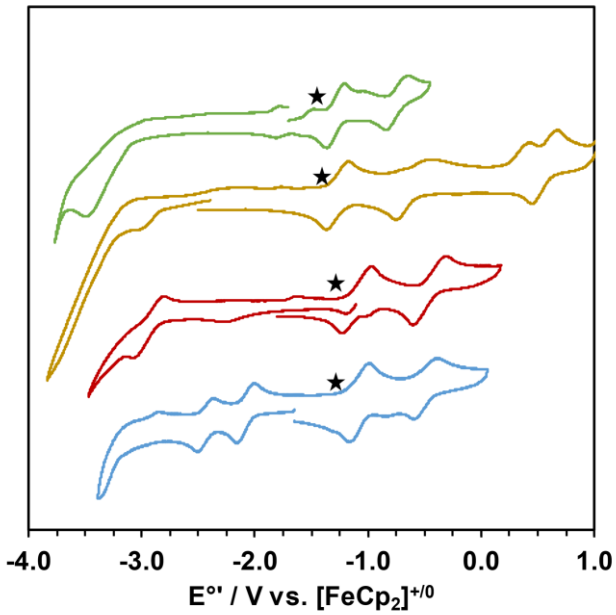

Figure 2.5. Cyclic voltammograms of {K}{[ONO]Ni(L)} complexes in THF at 200 mV/s. Green trace, L = DMAP; yellow trace, L = ^{OMe}py; red trace, L = py; blue trace, L = ^{4CN}py. Voltammetry was performed in solutions containing 0.1 M $\{Bu_4N\}\{PF_6\}$ using a glassy carbon working electrode, Pt-wire counter electrode, an $Ag^{+/0}$ pseudo-reference electrode, and $[FeCp_2]^{+/0}$ as an internal standard. Star indicates the location of the open circuit potential.

Table 2.3. Reduction potentials observed in cyclic voltammetry experiments for {K}{[ONO]Ni(L)}, performed in THF at 200 mV/s. All values referenced to the $[FeCp_2]^{+/0}$ internal standard redox couple.

L	$E^{\circ'}$ / V vs. $[FeCp_2]^{+/0}$ (i_{pa}/i_{pc})			
DMAP	−3.61[a]		−1.28 (0.95)	−0.74 (0.93)
^{OMe}py	−2.74[a]		−1.27 (0.93)	−0.60 (1.04)
py	−2.97 (0.80)[b]		−1.10 (1.16)	−0.46 (0.94)
^{CN}py	−2.47 (1.03)	−2.16 (1.08)	−1.07 (0.98)	−0.50 (0.85)
PPh_3[c]	−2.52		−1.03	−0.46

(a) always reversible
(b) taken at 1600 mV/s
(c) see refs. 28, 29

2.2.5. Density functional theory comparison.

Density functional theory (DFT) calculations were performed using the Gaussian/16 suite to investigate the relative HOMO and LUMO energies (**Table 2.4**) of the complexes. Spin-unrestricted computations used the B3LYP exchange-correlation functional with the LANL2DZ basis set and tight SCF convergence criteria. To obtain the relative energies and population analysis of the $\{[ONO]Ni(py)\}^-$ anions, geometry optimization and vibrational

Table 2.4. Relative frontier orbital energies for complexes of {[ONO]Ni(L)}⁻ (L = DMAP, ^{OMe}py, py, ^{CN}py), as well as their Mulliken charge distributions.

Orbital	Energy / eV			
	DMAP	^{OMe}py	py	^{CN}py
LUMO+2	−0.123	−0.554	−0.614	−0.732
LUMO	−0.418	−1.089	−1.409	−2.473
HOMO	−3.739	−3.924	−3.944	−4.022
L	**Charge** / a.u.			
	Ni	**[ONO]**	**^{x}py**	
DMAP	0.338	−1.569	0.231	
^{OMe}py	0.347	−1.551	0.204	
py	0.353	−1.542	0.189	
^{CN}py	0.372	−1.584	0.348	

frequency calculations were performed to confirm energetic minima had been reached. For L = DMAP, ^{OMe}py, and py geometry optimizations began with solid-state structures whose *tert*-butyl groups were substituted for methyls to minimize computational load. Since no solid-state structure was available for the L = ^{CN}py,complex, geometry optimizations began with the solid-state structure of {[ONO]Ni(py)}⁻ with appropriate substitutions made at the *para*-position of the pyridine backbone. Geometry optimization, energy calculations, population analysis, and time-dependent DFT (TD-DFT) electronic spectra predictions included a correction for solvent dielectric (THF), which resulted in energies much closer in agreement with the experimentally observed electronic absorption spectra (**Table 2.5**). Bond metrics obtained from geometry-optimized structures of L = DMAP, ^{OMe}py, and py were within computational error from the solid-state structures: ΔNi–N<0.04 Å, ΔC–O<0.04 Å, ΔC–N<0.02 Å, and ΔC–C<0.01 Å.

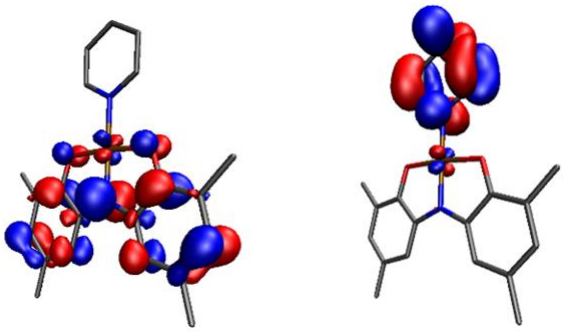

Figure 2.6. Kohn-Sham representations of the HOMO (left) and LUMO (right) of {[ONO]Ni(L)K series (L = py shown with iso = 0.045).

Table 2.5. HOMO/LUMO and HOMO/LUMO+2 transition energies of {[ONO]Ni(L)}⁻ complexes from excited state TD-DFT, compared to experimental absorption bands in THF.

Transition	L			
	DMAP	^{OMe}py	py	^{CN}py
HOMO/LUMO	373 nm	437 nm	489 nm	800 nm
Experimental	*443 nm*	*456 nm*	*555 nm*	*777 nm*
HOMO/LUMO+2	343 nm	369 nm	372 nm	377 nm
Experimental	*366 nm*	*370 nm*	*364 nm*	*362 nm*

Atomic charge distributions were calculated from full population analysis (**Table 2.4**).

The HOMOs of these complexes are primarily composed of the [ONO] aromatic backbone, with small antibonding contributions from the Ni d_{xz} orbital (~7%), in accordance with the ligand-based electrochemistry. The LUMO of these complexes is almost entirely composed of the ancillary L π-system with small antibonding contributions (1-3%) from Ni d_{xz}. The HOMO and LUMO of {[ONO]Ni(py)}⁻ (**Figure 2.6**) illustrate this distribution.

2.3. Discussion.

2.3.1. Oxidation state assignment of Ni and [ONO] fragments in {[ONO]Ni(L)}⁻ complexes.

The small shift in reduction potential between {K}{[ONO]Ni(PPh_3)} and {K}{[ONO]Ni(py)} suggested that ancillary ligand replacement might indeed be a viable synthetic handle to tune the [ONO] redox-active ligand electron transfer behavior in coordination complexes. To quantify the extent of this influence, four isostructural complexes

Table 2.6. Literature p*K*a, and E_L for four para-substituted py ligands.

L	DMAP	^{OMe}py	py	^{CN}py	PPh_3
pK_a (MeCN)	17.96	14.24	12.5	8.0	7.61
E_L / V vs. NHE	0.11	0.22	0.25	0.32	0.39

of Ni(II) and the [ONO] ligand were studied. The ancillary ligands L studied in these complexes range in their σ-donor ability, as measured by the pK_a of their conjugate acid,[34-36] and π-acidity, as indicated by their E_L values (**Table 2.6**).[22] To maintain similar steric profiles across all four complexes, each L was a *para*-substituted pyridine: pyridine, 4-dimethylaminopyridine (DMAP), 4-cyanopyridine (^{CN}py), and 4-methoxypyridine (^{OMe}py). While increased σ-donation from an ancillary ligand might not be expected to shift $E_{1/2}$ [sq•/cat] much, it was thought that a more π-acidic ancillary ligand might remove electron density from the metal center and alter [ONO]→M donation, as was seen in the aforementioned [ONO]RhL_5 system.[30] To investigate the redox properties of the [ONO] ligand in these complexes, it was first necessary to assign the oxidation states of the ligand and metal ion respectively by studying their structural and magnetic properties in solution and the solid-state.

The ^{1}H NMRs of these complexes are broad, and, given that each species is incredibly air-sensitive, the possibility of an oxidized and paramagnetic impurity was examined. However, measurements of the effective solution magnetic moment indicate that all {[ONO]Ni(L)}K complexes studied are diamagnetic (S = 0) systems, and, accordingly, they produce no electron paramagnetic resonance (EPR) spectra. The broadness of the ^{1}H NMR spectra therefore does not seem to be due to paramagnetism, and the [ONO] ligand most likely remains in its fully-reduced form in solution. The solid-state structures of these complexes often feature a potassium counter ion positioned closely to the [ONO] aromatic rings, and a previous study of {[ONO]Ni(py)}K with and without 2.2.2.-cryptand revealed

subtle differences in ligand bond metrics, indicating that the potassium does exert an electrostatic effect on [ONO], at least in the solid state. When 2.2.2.-cryptand is added to ^{1}H NMR samples of these complexes, however, peaks corresponding to the [ONO] backbone do not resolve. In addition, peaks assigned to ancillary ligands do not sharpen. When excess ancillary ligand is added, and when ^{1}H NMR spectra are recorded at low temperatures, it has not been possible to resolve free- and bound-ligand peaks. It is possible then that the equilibrium between free- and bound-ancillary ligands is fast on the ^{1}H NMR timescale, and the equilibrium between {[ONO]Ni(L)}$^{-}$ and {[ONO]Ni(solvent)}$^{-}$ results in peak broadening.

The bond lengths of the aromatic [ONO] backbone and the C–O and C–N bonds are sensitive to changes in the ligand oxidation state. Bond distances in the solid-state structures of {[ONO]Ni(L)}$^{-}$ (L = DMAP, ^{OMe}py, and py) were compared to the compiled metrical data of a series of metal–[ONO] complexes from literature using the metrical oxidation state (MOS) analysis developed by Brown. In the solid-state, these complexes possess bond lengths consistent with a fully-reduced ligand backbone, supporting the assignment of these diamagnetic species as nickel(II) complexes with a [ONO^{cat}]$^{3-}$ ligand coordinated to it. Notably, the C–N bonds within the [ONO] backbone are consistent with single-bonded sp^2-sp^2 atoms (1.370-1.470 Å), whereas in the singly- and doubly-oxidized species these bonds would contract significantly toward double-bonded C=N (1.260-1.350 Å). Accordingly, the MOS of the solid-state structures obtained in this work fall between −2.60 and −2.80, in agreement with previously reported {[ONO^{cat}]Ni(PPh$_3$)}K and within the range of [ONO^{cat}]$^{3-}$ complexes used to develop the MOS database. ESI-MS data collected for solutions of these complexes are consistent with the solid-state structures, yielding M/Z that each correspond to anionic {[ONO]Ni(L)}$^{-}$ fragments.

The electronic absorption spectra of each species are likewise characteristic of metal complexes with fully reduced [ONO^{cat}]$^{3-}$ ligands, with one strong absorption ~ 370 nm (ε =

7,000-20,000 M^{-1} cm^{-1}), with only a few lower energy features, each with molar extinction coefficients < 5,000 M^{-1} cm^{-1}. In literature, spectra of complexes containing the [ONO^{sq}] ligand are dominated by strong absorptions in the 500-900 nm region; these are absent in the spectra of {[ONO]Ni(L)}K. The spectra are likewise not consistent with the [ONO^{q}] electronic state, which not only possess strong transitions in the 500-900 nm range but also absorb in the near-infrared. In the L = py and ^{CN}py complexes, low-intensity transitions are present, but they are not consistent with the excitations of [ONO^{sq}] or [ONO^{q}] ligands. Overall the electronic absorption spectra of {[ONO]Ni(L)}K complexes are consistent with a fully-reduced ligand on an electron rich metal center.

Finally, open circuit potential measurements (OCP) of these pyridyl complexes fall negative of the redox couple at ~ −1.2 V vs. $[FeCp_2]^{+/0}$ in THF (**Figure 2.5**). The presence of two reversible one-electron oxidation events is consistent with a fully-reduced [ONO^{cat}]$^{3-}$ ligand, and agrees with the previously-reported electrochemistry of {[ONO^{cat}]Ni(PPh_3)}K.

Structurally, electrochemically, and spectroscopically, the complexes studied in this work appear to be of the expected form {[ONO]Ni(L)}K, where the redox-active [ONO] ligand is bound in its fully-reduced, fully-deprotonated [ONO^{cat}]$^{3-}$ form to a Ni(II) metal center. Only one ancillary ligand is present and lies *trans* to the chelating N of the [ONO] ligand. These monoanionic complexes are therefore well-described as diamagnetic, closed-shell systems.

2.3.2. Orbital energy estimations and experimental comparisons.

Gas-phase TD-DFT calculations of each of these complexes indicate that the primary excitation responsible for the bands seen ~360-370 nm in electronic absorption spectroscopy is a HOMO-LUMO+2 transition. The LUMO+2 of each of these complexes is characterized as the σ* interaction between the Ni $d_{x^2-y^2}$ orbital and both [ONO] and L fragments. The

energies of these transitions are compared in **Table 2.5.** to the experimentally observed absorptions. According to calculations, the low-intensity broad absorptions seen between 400-800 nm in the case of L = py and ^{CN}py are composed of multiple transitions including a HOMO-LUMO excitation.

In both empirical and calculated data sets, the energy of the putative HOMO-LUMO excitation (LL'CT) shifts linearly with increasing E_L and acidity of L, with L = ^{CN}py being such a strong π-acid that the HOMO-LUMO gap lies over 200 nm lower in energy than L = py. Rather than tune the energy of the [ONO]-based HOMO, however, it is the energy of the LUMO energy that has the largest shift when L is changed (|2.06| eV). The atomic orbital contributions to the HOMO and LUMO reflect this, with the HOMO being dominated by the [ONO] ligand fragment, and the LUMO being almost entirely comprised of L.

Given the solid-state structure, the solution-phase spectroscopic characterization of these species as $\{[ONO^{cat}]Ni^{II}(L)\}^-$ complexes, and OCP measurements, the electrochemical events at ~ −1.1 V and ~ −0.5 V in CV experiments are attributed to the [sq•/cat] and [q/sq•] reductions respectively. Natural orbital population calculations support that these events are primarily based on the redox-active ligand, with [ONO] contributing the most to the HOMO of these complexes. The irreversible reductions ~ −3.0 V are assigned to reductions on the ancillary ligand due to the dominance of L in the composition of the LUMOs, and the low-energy LUMO of {[ONO]Ni(^{CN}py)}K means that it can access two reversible reductions. Despite the evident influence that L has on the overall electrochemistry and electronic absorption spectroscopy of these complexes, the behavior of the [ONO] ligand itself is only subtly affected.

2.4. Conclusion.

The first redox event of these complexes vary from −1.28 to −1.07 V vs. $[FeCp_2]^{+/0}$ in THF, a difference of 210 mV. Conventional thinking suggests that less energy is required to remove an electron from a higher energy HOMO than from a more stabilized, lower energy HOMO. From the calculated frontier orbital energies, it was therefore expected that the complex of L = DMAP would be oxidized from [cat/sq•] at a more negative potential than the other complexes. This is observed experimentally, as the DMAP complex possesses the most negative $E_{1/2}$[sq•/cat], with the same redox event lying at more positive potentials from L = DMAP < ^{OMe}py < py < ^{CN}py. This generally subscribes to the trend in HOMO energies described previously. However, the small variation in the [cat/sq•] oxidation potential suggests that the $[ONO^{cat}]^{3-}$ donation into the Ni metal center is only subtly modulated by increasing π-acidity of the ancillary L in these complexes.

2.5. Experimental.

General Considerations. All manipulations were carried out using standard Schlenk-line techniques or in a dry nitrogen glovebox, except where noted. Trifluoroacetic acid and concentrated ammonium hydroxide were purged of dioxygen with a vigorous nitrogen stream (~1hr) before use in the synthesis of the protoligand. Hydrocarbon and ethereal solvents were sparged with argon and passed through activated Q5 and alumina columns to remove dioxygen and water, as confirmed by a solution of sodium benzophenone ketyl radical in THF. Such solvents were stored over activated molecular sieves in the glovebox. Deuterated solvents were dried over calcium hydride and freeze-pump-thawed to remove dioxygen; they were then stored in a sealed Kontes flask in the glovebox, where small aliquots were removed and stored over molecular sieves. Triphenylphosphine, 4-dimethylaminopyridine, and 2.2.2-cryptand were used as-received from Sigma. Potassium hydride was obtained in mineral oil and washed with pentane prior to use. The other *para*-substituted pyridines used for ligand substitution were purified according to literature procedures and stored in a nitrogen glovebox at −35°C. Tetrabutylammonium hexafluorophosphate ($\{Bu_4N\}\{PF_6\}$) (Acros) was recrystallized from ethanol three times and dried under vacuum before use. Ferrocene and decamethylcobaltocene (Acros) were purified by vacuum sublimation. Nickel salts of PPh_3, py, and DMAP were synthesized by refluxing $NiCl_2$ (anh., Alfa Aesar) and the desired ligand, used as received from Sigma, in methanol overnight before vacuum filtration to collect the bis(L)nickel(II) dichloride salts.

Spectroscopic and Electronic Characterization. All NMR spectroscopy was performed on a Bruker Avance 400, 500, or 600 MHz spectrometer at either 298, 258 (CD_3CN), or 240 K (d_8-THF). ^1H spectra were referenced to residual proteo impurities of the solvents used

(1.72 and 3.58 ppm, d_8-THF; 1.94 ppm, CD_3CN, 7.16 C_6D_6), and $^{31}P\{^1H\}$ NMR were referenced with a phosphoric acid external standard (85%, 0.00 ppm). Electronic absorption spectra were recorded using a Jasco V-670 absorption spectrometer using 10 mm quartz cuvettes at ambient temperatures. Electrospray ionization mass spectrometry (ESI-MS) was performed on a Waters LCT Premier mass spectrometer using dry, degassed benzene.

Cyclic voltammetry and differential pulse voltammetry experiments were performed on a Gamry G300 potentiostat/galvanostat/Zero Resistance Ammeter (Gamry Instruments, Warminster, PA) using a 3.0 mm glassy carbon working electrode, a platinum wire counter electrode, and a silver wire pseudo-reference electrode. Experiments were performed at ambient temperature in a dry nitrogen glovebox with 1 mM analyte and 100 mM $\{Bu_4N\}\{PF_6\}$ supporting electrolyte. All potentials have been referenced to $[FeCp_2]^{+/0}$ using sublimed ferrocene as an internal standard.

Crystallographic Measurements. X-ray diffraction was performed on single crystals coated in Paratone oil and mounted on glass fibers. Data was acquired using a Bruker SMART APEX II diffractometer equipped with a CCD detector. A full sphere of data was collected for each crystal structure, and measurements were carried out using Mo Kα (λ = 0.71073 Å) radiation, which was wavelength selected with a single-crystal graphite monochromator. The SMART program package was used to determine unit-cell parameter and to collect data. The raw frame data were processed using SAINT[43] and SADABS[44] to yield the reflection data files. Subsequent calculations were carried out using the SHELXTL[45] program suite. Structures were solved by direct methods and refined on F^2 by full-matrix least-squares techniques to convergence. Analytical scattering factors for neutral atoms were used throughout the analyses.[46] Hydrogen atoms, though visible in the difference Fourier map, were generated at calculated positions and their positions refined using the riding model. ORTEP diagrams were generated using ORTEP-3 for Windows.

Theoretical Calculations. Density function theory calculations were performed with the Gaussian 16 program. Optimized geometries were calculated using the B3LYP exchange-correlation functional with the LANL2DZ basis set. Tight SCF convergence criteria were used for all calculations. Vibrational frequency calculations were performed as confirmation that the stationary points were minima. Calculations were performed on unrestricted open-shell singlet monoanions, in the absence of counter ions, using geometries obtained from the solid-state crystal data of $\{[ONO]Ni(py)\}^-$ as a starting point. A solvation shell (THF) was included using the polarized continuum model (PCM). Molecular orbital compositions were calculated in the Gaussian 16 program, as were atomic charges (using both Mulliken and Natural Population Analysis methods).

Table 2.7 X-ray diffraction data collection and refinement parameters for {K(2.2.2.-crypt)}, {[ONO]Ni(DMAP)}, {K}{[ONO]Ni(^{OMe}py)}, and {K(2.2.2.-crypt)}{[ONO]Ni(py)}.

Complex	{K(2.2.2.-crypt)}{[ONO]Ni(DMAP)}	{[ONO]Ni(^{OMe}py)}	{[ONO]Ni(py)}
empirical formula	C_{53} H_{86} K N_5 Ni O_8 · 2.5(C_4H_8O)	$C_{68}H_{98}K_2N_4Ni_2O_8$·5($C_6H_6$)	$C_{51}H_{81}KN_4NiO_8$
formula weight	1199.33	1685.66	976.00
crystal system	Triclinic	Triclinic	Orthorhombic
space group	$P\bar{1}$	$P\bar{1}$	*Pbcn*
T(K)	133(2)	133(2)	133(2)
a /Å	13.869(2)	11.9309(5)	18.883(3)
b /Å	22.196(4)	14.6323(7)	19.587(3)
c /Å	22.857(4)	14.9300(7)	28.624(5)
α /deg	89.0428(19)	94.8577(8)	90
β /deg	74.6645(18)	106.5981(7)	90
γ /deg	79.5133(19)	111.7521(7)	90
V /Å^3	6668.5(18)	2266.18(18)	10587(3)
Z	4	1	8
refl. collected	73111	56663	108664
indep. Refl.	27145	13414	13019
R1 ($I > 2\sigma$)[a]	0.0885	0.0329	0.0429
*w*R2 (all data)[b]	0.2657	0.0438	0.1132
GOF	1.028	1.033	1.028

[a] $R1 = \Sigma| |F_o| - |F_c| |/\Sigma|F_o|$; [b] $wR2 = [\Sigma[w(F_o^2 - F_c^2)^2]/\Sigma[w(F_o^2)^2]]^{1/2}$

Synthesis. Complexes of the form {[ONO^{cat}]Ni(L)}K were synthesized via one of two general procedures.

Salt methathesis: A clear amber solution of [ONO^{cat}]H_3 (1.0 equiv.) in THF was added to a THF suspension of KH (3.0 equiv.) in a 20 mL scintillation vial and allowed to stir until effervescence was no longer observed. Solid $NiCl_2(L)_2$ (1.0 equiv.) was then added. The solution was stirred for four hours. The reaction mixture was filtered through a plug of celite on a medium porous glass frit. The filtrate was concentrated, and precipitation of the product was induced with added pentane. The colored powders were collected on a second glass frit, rinsed with cold ether or pentane until the effluent ran clear, and dried under vacuum.

Ligand substitution: Solid {[ONO^{cat}]Ni(PPh_3)}K (1.0 equiv.) was dissolved in THF in a scintillation vial equipped with a stir bar. Separately, a solution of the desired *para*-substituted pyridine (1 equiv.) in THF was prepared. The pyridine was then added to the nickel solution, upon which an immediate Color change could be observed. The solution was stirred for two hours, filtered through a medium porous glass frit, concentrated, and transferred to a scintillation vial. Upon drying, the products were triturated with ether until solids were obtained. The solids were then washed extensively with cold pentane until no more brown filtrate was observed, and no PPh_3 was detected in the ^{1}H NMR.

^{1}H NMR peaks corresponding to the 36H [ONO] *tert*-butyl groups were visible in each complex, though [ONO] aromatic protons are often not visible in ^{1}H NMR especially when other groups, such as those on L, are present in the region.

{[ONO]Ni(DMAP)}K. was obtained as a matcha green powder (190 mg, 73% yield). This complex appears yellow-green in all solvents. In solutions that contain 2.2.2-cryptand, it becomes more yellow. **^{1}H NMR (d_8-THF):** δ/ppm = 8.12 (d, 1H, J = 5.3 Hz, dmap CH(2,6)), 8.07 (d, 2H, J = 6.3 Hz, dmap CH(2,6)), 7.11 (s, 2H, aryl-H), 6.62 (d, 1H, J = 5.3 Hz, dmap CH(3,5)), 6.55 (d, 2H, aryl-H, J = 5.2 Hz), 6.08 (s, 2H, aryl-H), 3.04 (s, 3H, dmap N(CH_3)), 2.97 (s, 6H, dmap N(CH_3)$_2$), 1.32 (s, 18H, C(CH_3)$_3$), 1.25 (s, 18H, C(CH_3)$_3$). **UV-Vis (THF):** λ_{max}/nm (ϵ/M^{-1} cm^{-1}) = 254 (32,000), 303 (10300), 366 (10400), 443 (1210). **MS (ESI+) (C_6H_6):** m/z = 602.1 (MH^+)

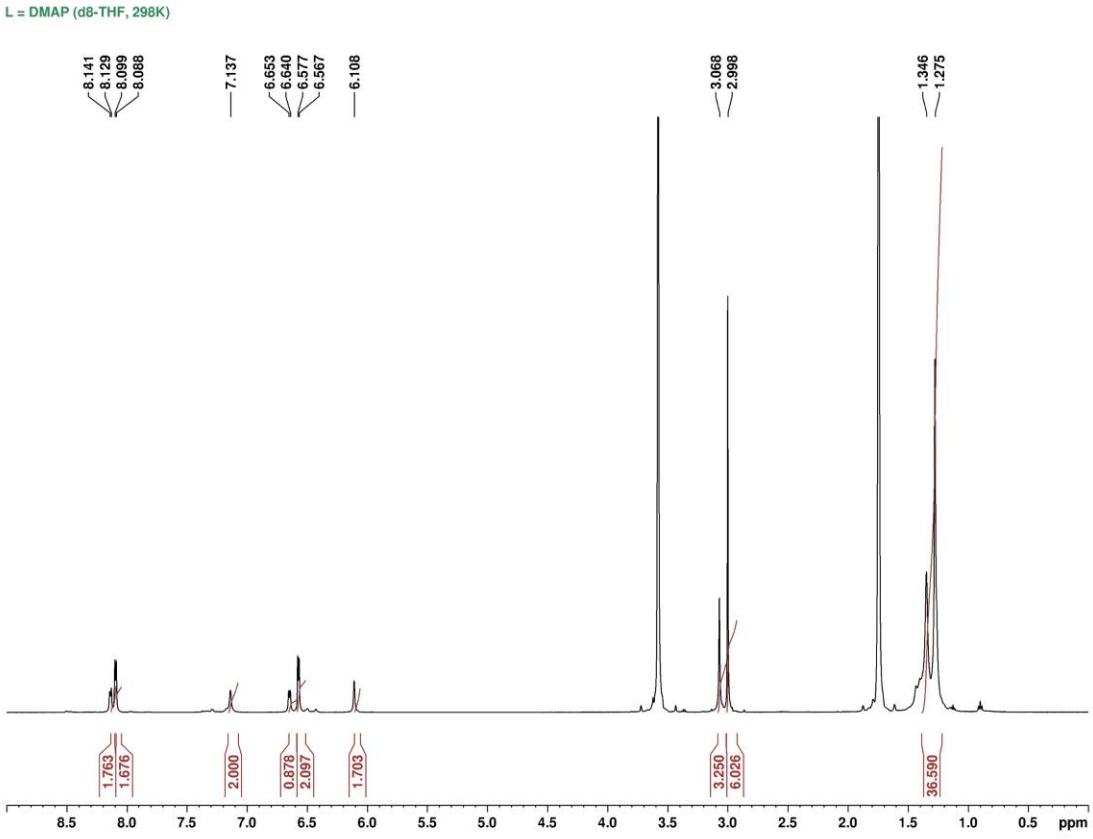

Figure 2.7. ^{1}H NMR of {[ONO]Ni(DMAP)}K in d_8-THF at 298K.

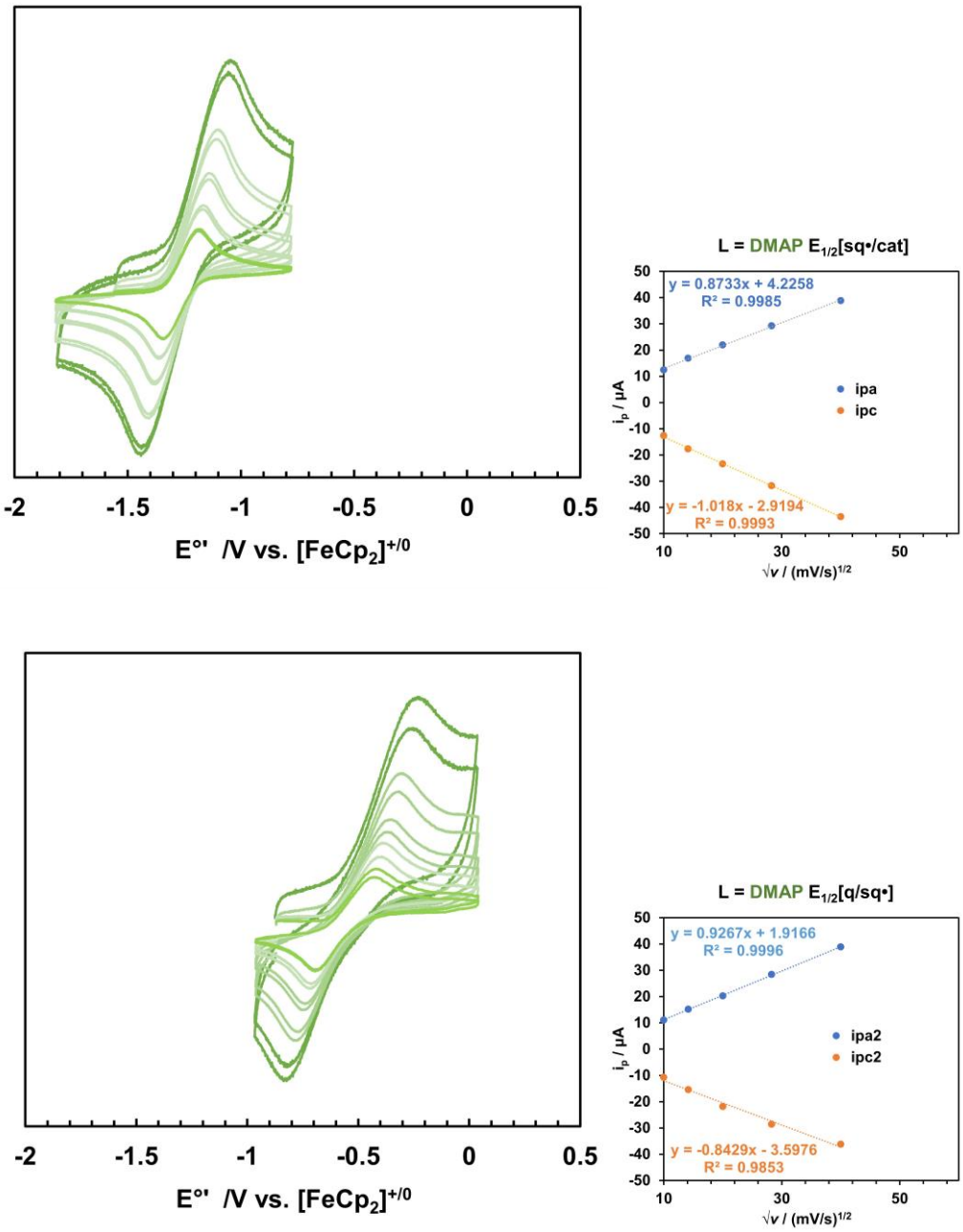

Figure 2.8. Scan rate dependence of {[ONO]Ni(DMAP)}K in THF.

{[ONO]Ni(OMepy)}K was obtained as a yellow-brown powder (145 mg, 76%). This complex appears green-brown in all solvents. In solutions that contain 2.2.2-cryptand, it becomes more yellow. Crystals suitable for structural analysis were obtained from a concentrated solution of benzene stored at ambient glovebox temperature for several weeks. **^{1}H NMR (CD_3CN):** δ/ppm = 8.42 (s, br py CH(2,6)), 6.88 (s, br py CH(3,5)), 3.87 (s, 3H, -OMe), 1.33 (s, 36H, $C(CH_3)_3$) **UV-Vis:** λ_{max}/nm ($\epsilon/M^{-1}\ cm^{-1}$) = 304 (2500), 370 (7300), 456 (640). **MS (ESI$^+$) (C_6H_6):** m/z = 588.9 (MH^+)

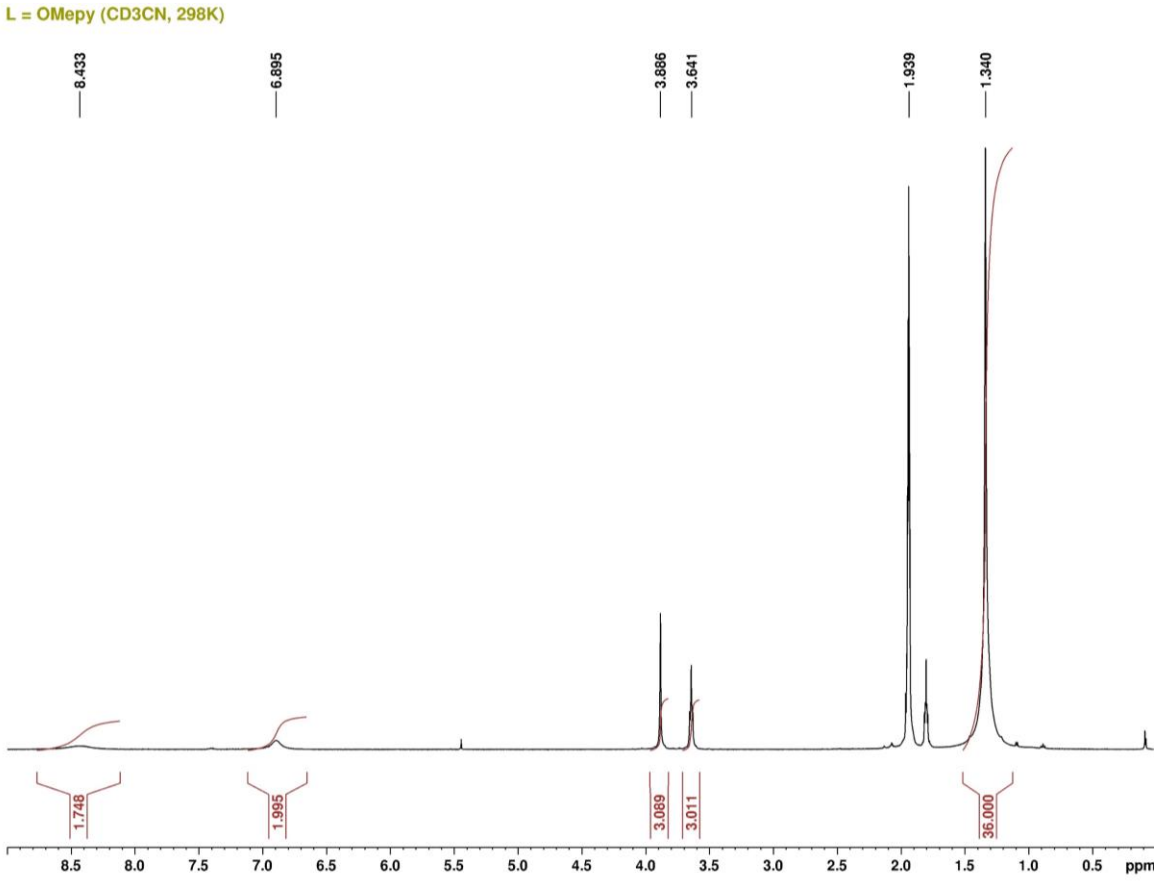

Figure 2.9. ^{1}H NMR of {[ONO]Ni(OMepy)}K. in CD_3CN at 298K.

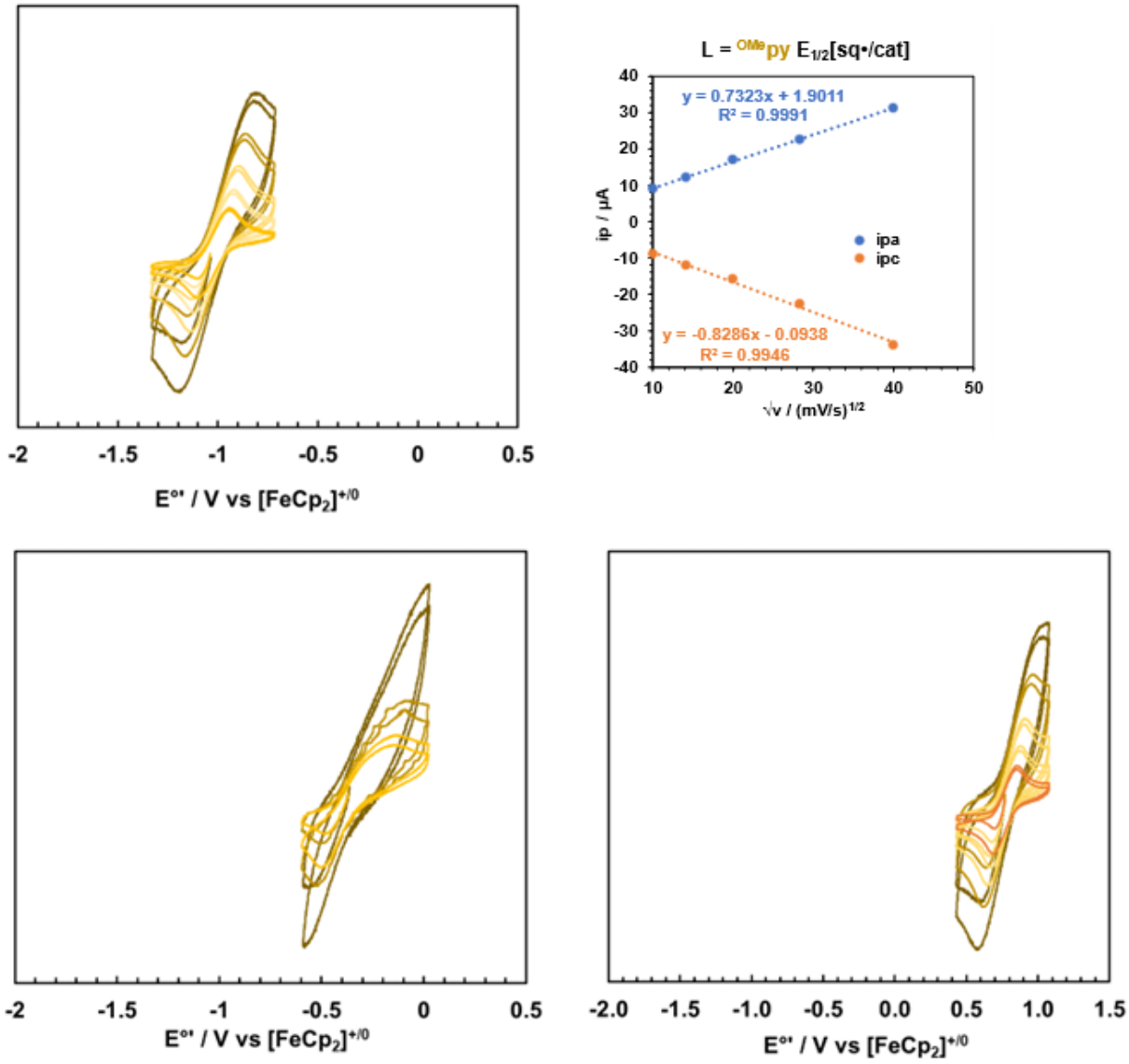

Figure 2.10. Scan rate dependence of {[ONO]Ni(OMepy)}K in THF.

{[ONO^{cat}]Ni(py)}K was obtained as a brick red powder, which became green-brown upon extensive drying (1.580 g, 85.0% yield). Maroon crystals suitable for x-ray diffraction were obtained from concentrated solutions in acetonitrile with 2.2.2-cryptand stored at -35°C overnight. This complex appears red in THF and MeCN and violet in benzene, toluene, and in solutions that contain 2.2.2-cryptand. **Anal. Calcd. for $C_{33}H_{45}N_2NiO_2K(C_5H_5N$, THF):** C, 67.20; H, 7.79; N, 5.60. **Found:** C, 67.17; H, 7.71; N, 5.73. **^{1}H NMR (CD_3CN, 175K):** δ/ppm = 8.69 (d, 2H, py CH(2,6), J=5.28 Hz), 7.76 (t, 1H, py CH(4), J=7.26 Hz), 7.29 (t, 2H, py, CH(3,5), J=6.90 Hz), 7.08 (s, 2H, aryl-H), 6.20 (s, 2H, aryl-H), 1.35 (s, 18H, $C(CH_3)_3$), 1.29 (s, 18H, $C(CH_3)_3$). **UV-Vis (THF):** λ_{max}/nm (ϵ/M^{-1} cm^{-1}) = 246 (20200), 314 (9000), 380 (3000), 513 (555). **MS (ESI$^+$) (C_6H_6):** m/z =559.0 (MH^+)

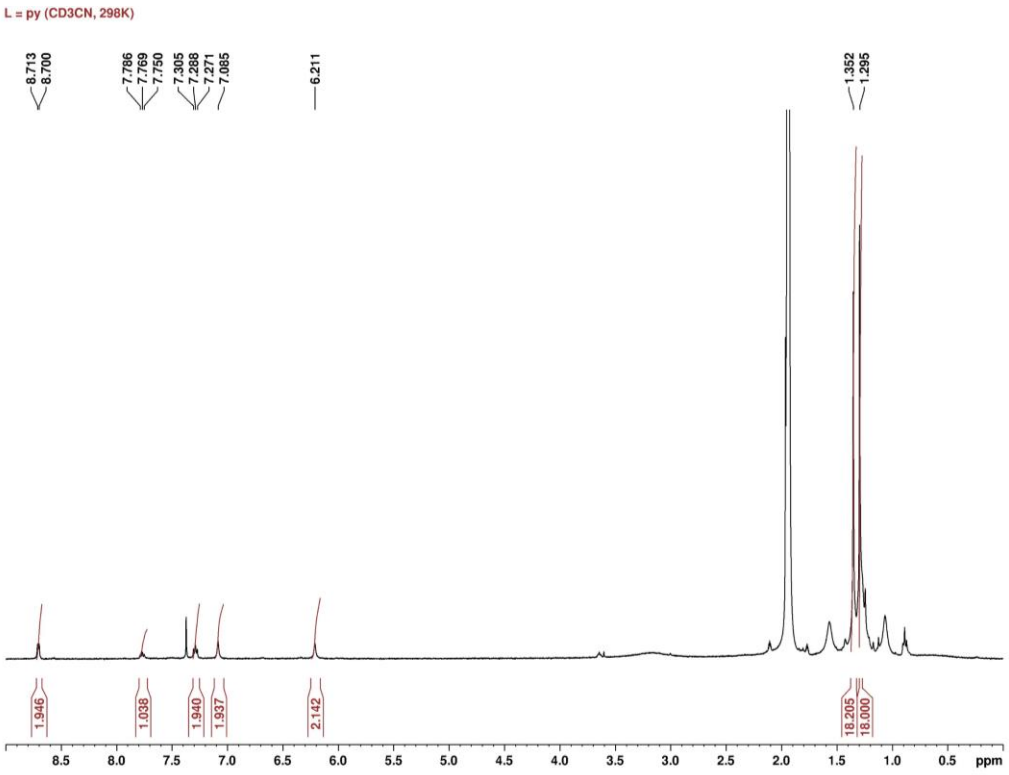

Figure 2.11. ^{1}H NMR of {[ONO]Ni(py)}K. in CD_3CN at 298K.

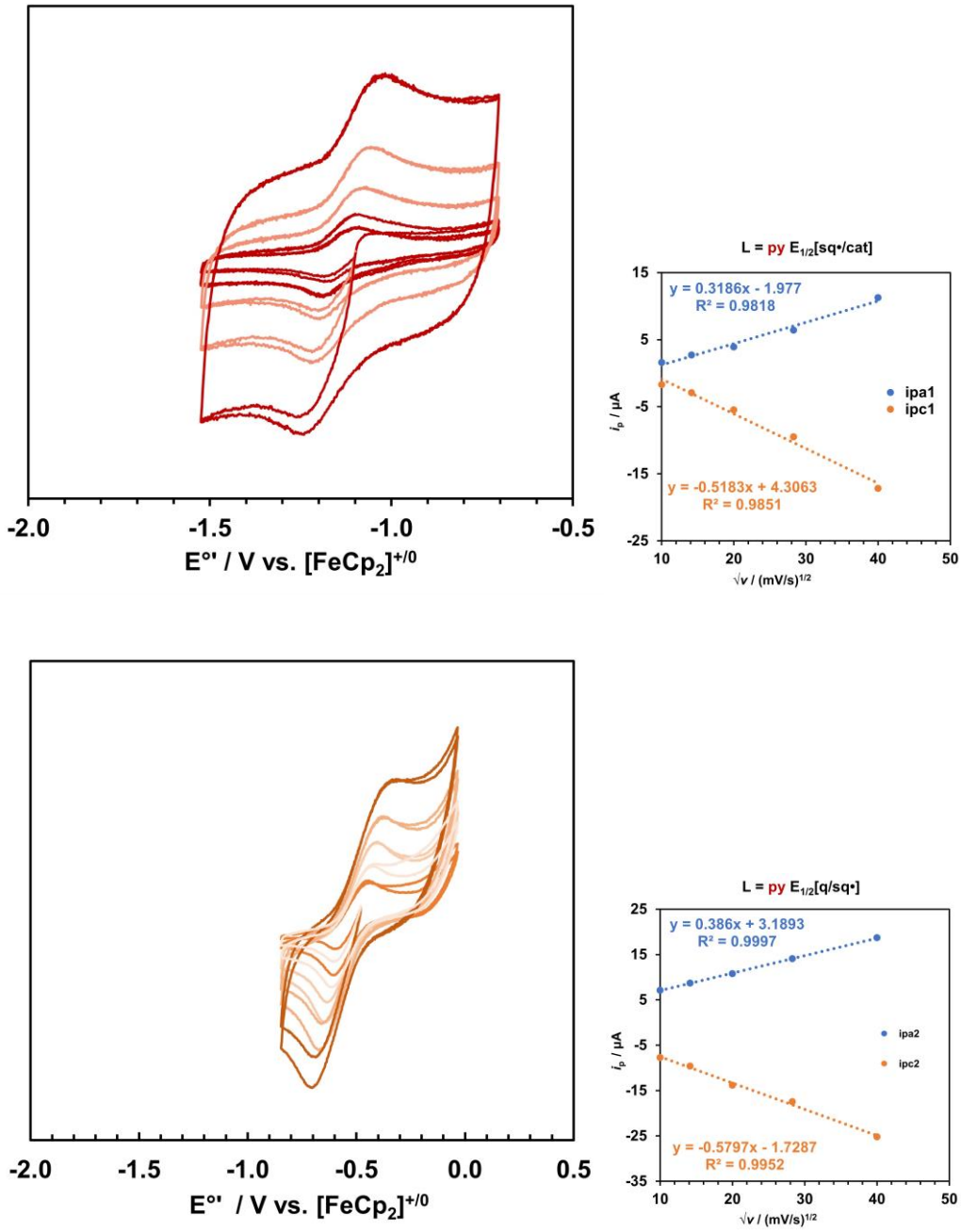

Figure 2.12. Scan rate dependence of {[ONO]Ni(py)}K in THF.

{[ONO^{cat}]Ni(^{CN}py)}K was obtained as a blue-green solid (113 mg, 68%). This complex appears blue-green in all solvents. **^{1}H NMR (CD_3CN):** δ/ppm = 8.97 (s, br, 2H), 7.66 (s, br, 2H), 1.32 (s, 36H, $C(CH_3)_3$). **UV-Vis:** λ_{max}/nm ($\epsilon/M^{-1}\ cm^{-1}$) = 362 (16,500), 444 (1,300), 777 (2,000). **MS (ESI$^+$) (C_6H_6):** m/z = 584.2 (MH^+)

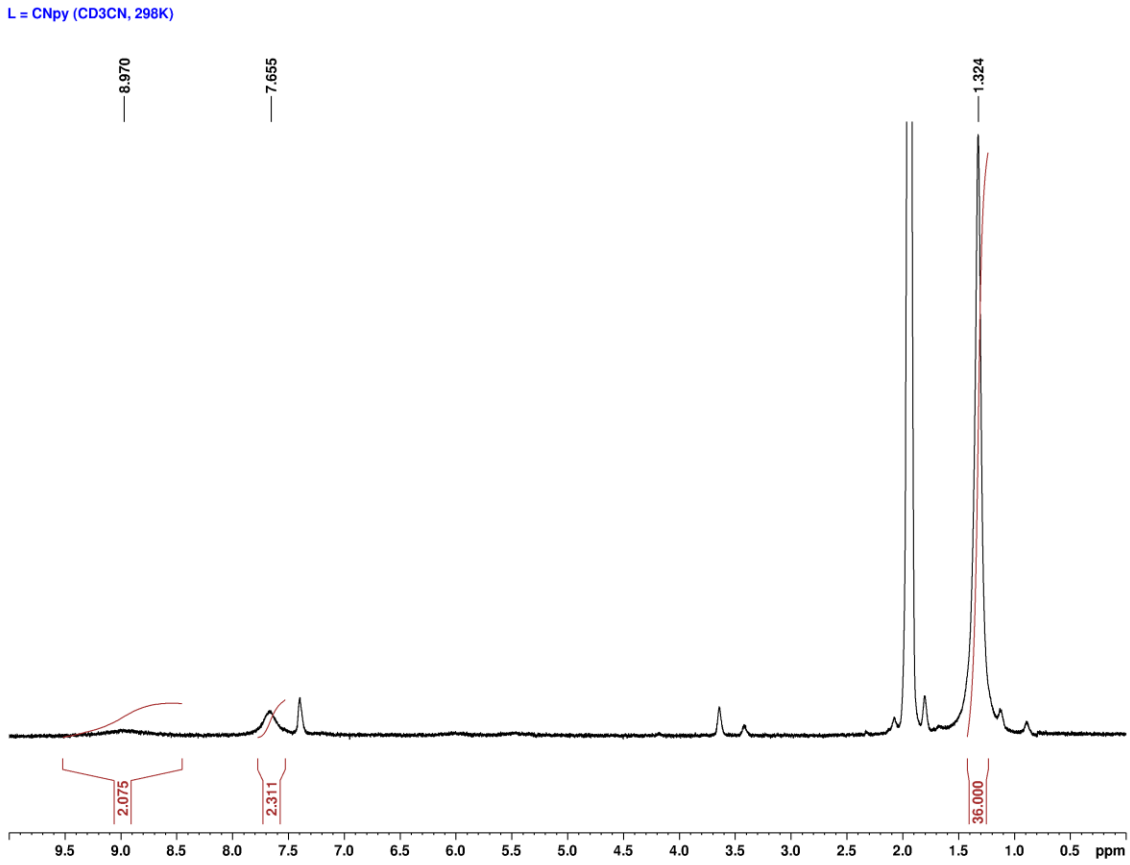

Figure 2.13. ^{1}H NMR of {[ONO]Ni(^{CN}py)}K. in CD_3CN at 298K.

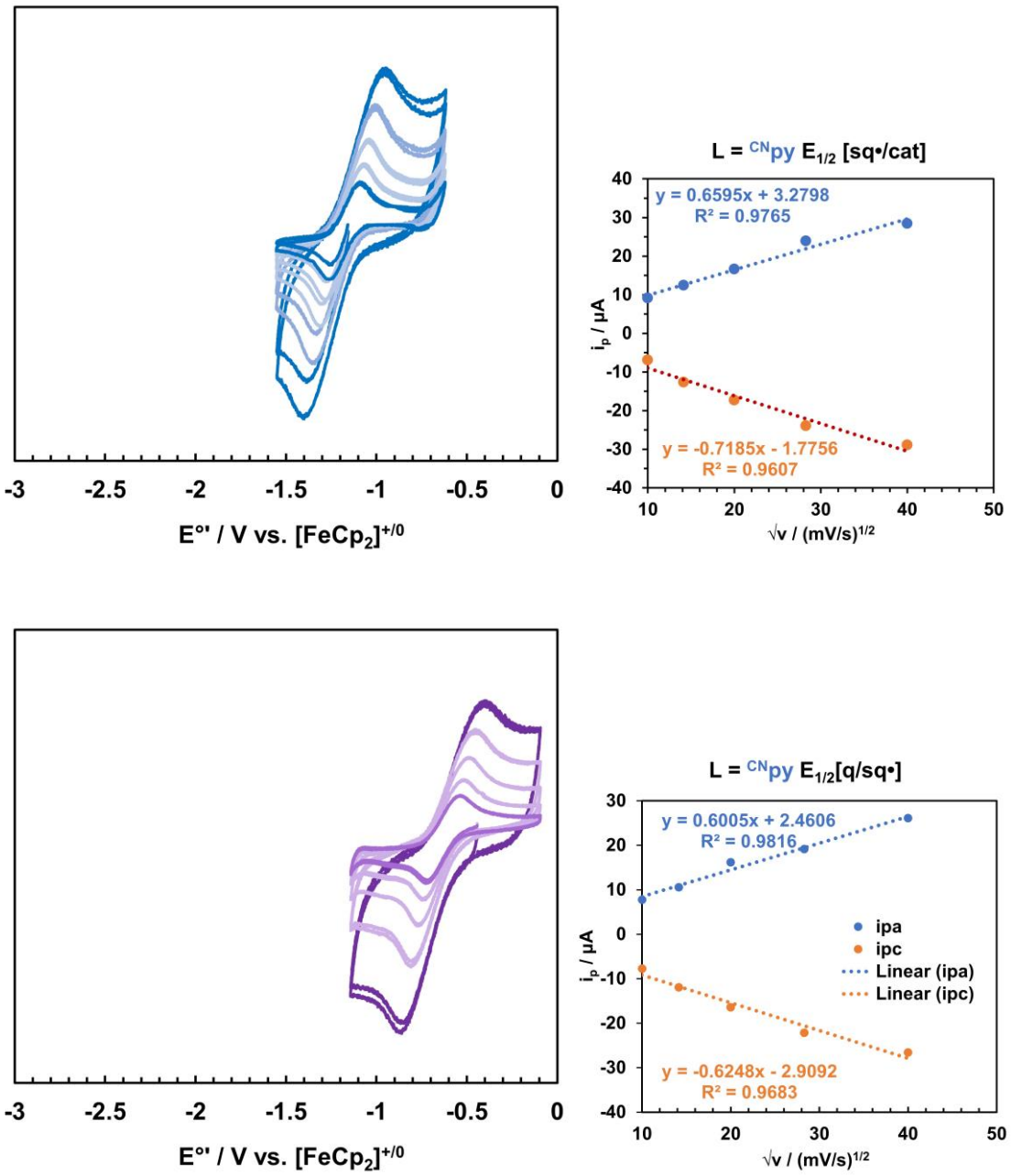

Figure 2.14. Scan rate dependence of {[ONO]Ni(CNpy)}K in THF.

2.6. References.

1. Mayer, J.M. Understanding Hydrogen Atom Transfer: From Bond Strengths to Marcus Theory. *Acc. Chem. Res.* **2011,** *44* (1),36-46.
2. Warren, J.J.; Mayer, J.M. Predicting organic hydrogen atom transfer rate constants using the Marcus cross relation. *Proc. Natl. Acad. Sci. U.S.A.* **2010,** *107* (12), 5282-5287.
3. Bordwell, F.G.; Cheng, J.P.; Harrelson, J.A. Homolytic bond dissociation energies in solution from equilibrium acidity and electrochemical data. *J. Am. Chem. Soc.* **1988,** *110* (4), 1229-1231.
4. Wayner, D.D.M.; Parker, V.D. Bond energies in solution from electrode potentials and thermochemical cycles. A simplified and general approach. *Acc. Chem. Res.* **1993,** *26* (5), 287-294.
5. Parker, V.D.; Handoo, K.L.; Roness, F.; Tilset, M. Electrode Potentials and the Thermodynamics of Isodesmic Reactions. *J. Am. Chem. Soc.* **1991,** *113,* 7493-7498.
6. Tilset, M.; Parker, V.D. Solution homolytic bond dissociation energies of organotransition-metal hydrides. *J. Am. Chem. Soc.* **1989,** *111* (17), 6711-6717.
7. Wiedner, E.S.; Chambers, M.B.; Pitman, C.L.; Bullock, R.M.; Miller, A.J.M.; Appel, A.M. Thermodynamic Hydricity of Transition Metal Hydrides. *Chem. Rev.* **2016***, 116* (15), 8655-8692.
8. Warren, J.J.; Tronic, T.A.; Mayer, J.M. Thermochemistry of Proton-Coupled Electron Transfer Reagents and its Implications. *Chem. Rev.,* **2010** *110* (12), 6961-7001.
9. Berning, D.E.; Noll, B. C.; Dubois, D.L. Relative Hydride, Proton, and Hydrogen Atom Transfer Abilities of [HM(diphosphine)$_2$]PF_6 Complexes (M = Pt, Ni). *J. Am. Chem. Soc.* **1999,** *121* (49), 11432-11447.
10. Treichel, P. M.; Durren, G. E.; Mueh, H. J. Manganese(I) isocyanide complexes. *J. Organomet. Chem.* **1972,** *44* (2), 339-352.
11. Sarapu, A.; Fenske, R. F. The Transition Metal-Isocyanide Bond. An Approximate Molecular Orbital Study. *Inorg. Chem.* **1975**, 14, 247-253.
12. Chatt, J.; Kan, C. T.; Leigh, G. J.; Pickett, C. J.; Stanley, D. R. Transition-metal binding sites and ligand parameters. *J. Chem. Soc., Dalton Trans.* **1980**, 2032-2038.
13. Chatt, J. Coord. Ligand effects. *Chem. Rev.* **1982**, 43, 337-348.
14. Hussain, W.; Leigh, G. J.; Ali, . M.; Pickett, C. J.; Rankin, D. A. Dinitrogen binding and electrochemistry in complexes of molybdenum and tungsten. *J. Chem. Soc., Dalton Trans.* **1984**, 8, 1131-1136.
15. Pombeiro, A. J. L. Ligand and structural effects on the redox potential of octahedral 18-electron complexes with 14-electron or 12-electron metal centres. *Port. Electrochim. Acta.* **1985**, *3*, 41-66.
16. Pombeiro, A. J. L. Preparation and redox properties of the complexes trans-[ReL2(dppe)2]BF4 (L = CO or isocyanide). Estimate of the oxidation potential of octahedral 18-electron complexes with 14-electron square planar metal centres

and of related electrochemical parameters for derived 16-electron sites. *Inorg. Chim. Acta*. **1985,** *103*, 95-103.
17. Pombeiro, A. J. L.; Pickett, C. J.; Richards, R. L. The electronic properties of isocyanides at rhenium—dinitrogen binding sites. Preparation and redox properties of the isocyanide complexes trans-[ReCl(CNR)(Ph2PCH2CH2PPh2)2]. *J. Organomet. Chem.* **1982,** *224*, 285-294.
18. Fernanda, M.; Carvalho, N. N.; Pombeiro, A. J. L. Syntheses and redox properties of mixed isocyanide, carbonyl, or nitrile complexes of rhenium(I)trans-[Re(CNMe)L(Ph2PCH2CH2PPh2)2]X [L = CNR (R = alkyl or aryl), CO, or NCMe; X = Cl, BF4, or PF6]. *J. Chem. Soc., Dalton Trans.* **1989**, 1209-1216.
19. Lever, A.B.P. Electrochemical parametrization of metal complex redox potentials, using the ruthenium(III)/ruthenium(II) couple to generate a ligand electrochemical series. *Inorg. Chem.* **1990** *29* (6), 1271-1285.
20. Fielder, S.S.; Osborne, M.C.; Lever, A.B.P.; Pietro, W.J. First Principles Interpretation of Ligand Electrochemical (EL(L)) Parameters; Factorization of the sigma and pi Donor and pi-Acceptor Capabilities of a Ligand. *J. Am. Chem. Soc.,* **1995** *117* 6990-93.
21. Perrin, L.; Clot, E.; Eisenstein, O.; Loch, J.; Crabtree, R. H. Computed Ligand Electronic Parameters from Quantum Chemistry and Their Relation to Tolman Parameters, Lever Parameters, and Hammett Constants. Inorg. Chem 2001, 40, 5806–5811.
22. Masui, H.; Lever, A. B. P. Correlations between the Ligand Electrochemical Parameter, EL(L), and the Hammett Substituent Parameter, .Sigma. Inorg. Chem. 1993, 32 (10), 2199–2201.
23. Munhá, R. F.; Zarkesh, R.A.; Heyduk, A.F. Tuning the Electronic and Steric Parameters of a Redox-Active Tris(amido) Ligand. *Inorg. Chem.* **2013,** *52* (19), 11244-11255.
24. Charette, B.J.; Ziller, J.W.; Heyduk, A.F. Metal-Ion Influence on Ligand-Centered Hydrogen-Atom Transfer *Inorg. Chem.* **2021,** *60* (3), 1579-1589.
25. Lever, A.B.P. Electronic characteristics of an extensive series of ruthenium complexes with the non-innocent o-benzoquinonediimine ligand: A pedagogical approach. *Coord. Chem. Rev.* **2010,** *254* (13-14), 1397-1405.
26. Alexiou, C.; Lever, A.B.P. Tuning Metalloporphyrin and Metallophthalocyanine Redox Potentials Using Ligand Electrochemical (EL) and Hammett (sp) Parametrization. *Coord. Chem. Rev.* **2001**, 216/217, 45-54.
27. Szigethy, G.; Shaffer, D.W.; Heyduk, A.F. Coordination Effects on Electron Distributions for Rhodium Complexes of the Redox-Active Bis(3,5-di-*tert*-butyl-2-phenolate)amide Ligand. *Inorg. Chem.* **2012,** *51* (23), 12606-12618.
28. Charette, B.J.; Ziller, J.W.; Heyduk, A.F. Exploring Ligand-Centered Hydride and H-Atom Transfer. *Inorg. Chem.* **2021,** *60* (7), 5367-5375.
29. Charette, B.J. Investigations into the Reactivity of Transition Metal Complexes with Redox-Active Ligands for Proton Coupled Electron Transfer and Nitrene Transfer. Ph.D. Dissertation, University of California Irvine, Irvine, CA, **2021.**

30. Brown, S.N. Metrical Oxidation States of 2-Amidophenoxide and Catecholate Ligands: Structural Signatures of Metal–Ligand π Bonding in Potentially Noninnocent Ligands. *Inorg. Chem.* **2012,** *51* (3), 1251-1260.
31. Tshepelevitsh, S.; Kütt, A.; Lõkov, M.; Kaljurand, I.; Saame, J.; Heering, A.; Plieger, P. G.; Vianello, R.; Leito, I. On the Basicity of Organic Bases in Different Media. *European J. Org. Chem.* **2019,** *2019* (40), 6735–6748.
32. Rossi, M. B.; Piro, O. E.; Castellano, E. E.; Alborés, P.; Baraldo, L. M. Reactivity and Spectroscopy of the {Ru(DMAP) 5 } Fragment: An {Ru(NH 3) 5 } Analogue. *Inorg. Chem.* **2008**, *47* (7), 2416–2427.
33. Schlesener, C. J.; Amatore, C.; Kochi, J. K. Metal Catalyzed Oxidation of Organic Compounds; *Academic Press,* **1984**; Vol. 106.
34. Schmidt, M.H.; Miskelly, G.M.; Lewis, N.S. Effects of redox potential, steric configuration, solvent, and alkali metal cations on the binding of carbon dioxide to cobalt(I) and nickel(I) macrocycles. *J. Am. Chem. Soc.* **1990,** *112* (9), 3420-3426.

CHAPTER 3: Characterization of [ON(H)O]Co(DMAP)$_n$ proton-coupled electron transfer and ligand equilibria

3.1. Introduction.

Catalysts based on cobalt possess rich chemistry, in part due to the substitutional lability that characterize Group 9 ions in the +2 oxidation state,[1,2] a feature that increases the reactivity of some systems by allowing them to more easily bind, react with, and release substrates to regenerate active catalysts. Complexes with d^4-d^7 electron counts may also access either high-spin or low-spin configurations, and cobalt(II) complexes are known to exhibit spin-crossover between these configurations under mild stimuli such as small changes in temperature, photoexcitation, or even pressure. It has been shown that low- and high-spin isomers can have dramatically different reactivity toward the same substrates,[3] thus the synthetic handles by which the transition between low- and high-spin configurations can be controlled has been a topic of great interest. Ligand field strength is known to influence the magnitude of the barrier between high- and low-spin states, and as such, the magnetism and reactivity of Co(II) complexes with a variety of ligand types has been studied.

When redox-active ligands are bound to Co(II) metalloradicals, several additional electronic phenomena become possible due to comparable energies between ligand π^*- and metal 3d-orbitals.[4-10] In the case of radical ligands such as the semiquinone and iminosemiquinone platforms, antiferromagnetic coupling can occur. Intramolecular charge transfer (valence tautomerization) from ligand to metal or metal to ligand has also been identified.[11,12] These electronic changes can also be induced by changes in the coordination environment, such as association of an additional ligand, adding an even greater degree of ambiguity to the electronic configuration of Co complexes with redox-active ligands. It is exactly this ligand π^*- and metal d-orbital overlap that makes it difficult to assign the origin

of electron transfer as either the ligand or the metal, which is a distinction that usually helps rationalize a system's driving force or selectivity in reactions. In addition, when a ligand is not only redox-active but also features a basic site, another question is raised about whether it is the metal or ligand that gets protonated during reactivity.[13] While the oxidation- and protonation-state ambiguity might be considered a deterrent, it may have some benefits. For example, increased metal character in frontier orbitals that are usually localized on the redox-active ligand may encourage the binding of substrates to the metal center for inner-sphere reactivity using ligand-based electrons.[14]

Proton-coupled electron transfer (PCET) reagents containing transition metals have largely been limited to two classes of complexes: those in which both electrons and protons are stored on the metal in the form of a metal hydride (M–H) bond,[15-21] or, in fewer instances, those where a proton is stored or shuttled by a coordinated ligand and the electrons are sourced from a metal.[22-29] A third scenario, in which a redox- and proton-active ligand is the single site of PCET,[29-32] has been a focus of our group. In contrast to previous examples of ligand-based PCET platforms, the Heyduk lab has demonstrated that redox-active and proton-active pincer ligands such as bis(3,5-di-*tert*-butyl-2-phenoxy)amide [ONO] and bis(2-mercapta-*p*-tolyl)amide [SNS] have similar thermodynamic properties to many metal hydride single-site PCET reagents, with comparable BDFEs and hydricities.[33-37] The ligands can exist in a fully-reduced, closed-shell catecholato (cat^{3-}) oxidation state, the singly-oxidized radical semiquinonato ($sq^{\cdot 2-}$) oxidation state, or (in the case of [ONO]) a doubly-oxidized quinonato (q^{1-}) oxidation state, and both ligands can be protonated on the central nitrogen basic site. Prior research in the group has focused on using these ligands to grant redox activity to metals that do not themselves undergo electron transfer, such as d^0 or d^{10}

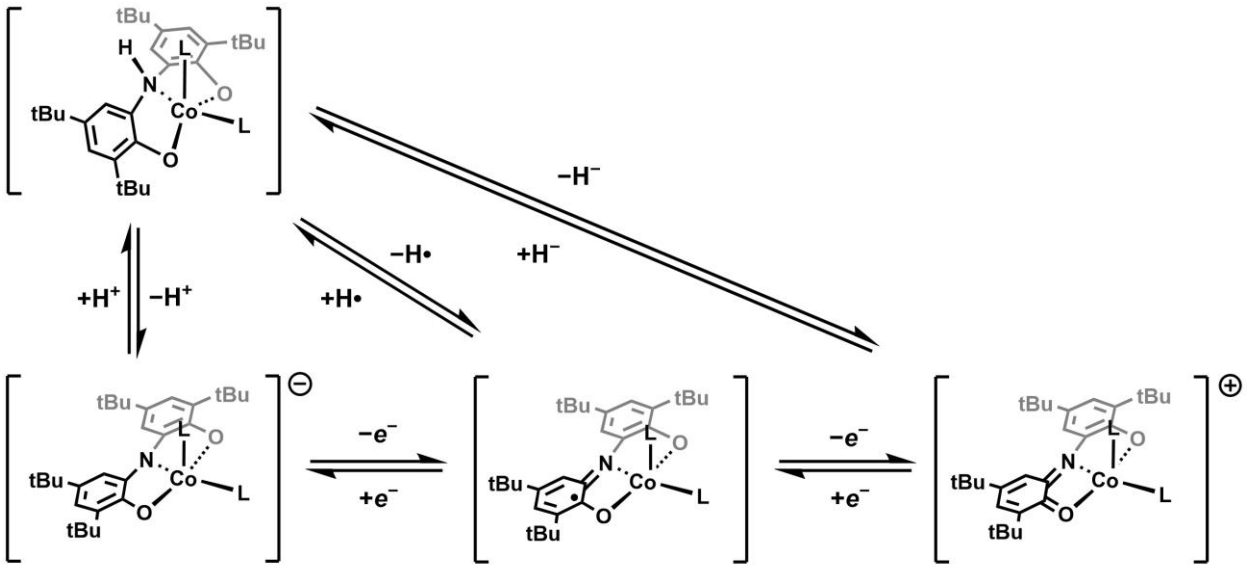

Scheme 3.1. Thermodynamic cycle relating [ONO]Co(L)$_2$ species by proton- and electron-transfer steps.

ions,[33,34] but more recent efforts aim to marry the established electrocatalytic activity of metal ions such as those in Groups 8-10 with the reactivity of a redox-active ligand.[35-37]

We wished to investigate how the Co(II) ion modulated the well-documented PCET behavior of the [ON(H)O] ligand, but we were also interested in understanding how changes in the oxidation and protonation state of a coordinated ligand may influence the electronic preferences of the coordinated Co ion. Therefore, complexes related by direct oxidation and protonation of the [ONO] ligand on Co according to the thermodynamic scheme outlined in **Scheme 3.1** were synthesized and characterized.

The five-coordinate protonated complex, [ON(H)O]Co(DMAP)$_2$, was discovered to be very weakly acidic compared to previous examples of the [ON(H)O]$^{2-}$ ligand coordinated to late transition metals. Proton transfer and H-atom transfer (HAT) from this complex generated cobalt species that appear to be low-spin isomers in the solid-state but show evidence of spin-crossover, valence tautomerization, and lability of innocent ancillary ligands in solution. Association of innocent ancillary ligands resulted in uncertainty regarding pK_a, BDFE, and ΔG°_{H-} measurements, but estimates were obtained from stoichiometric reactivity

with reagents whose thermodynamic values are known in literature. The [ON(H)O]Co(DMAP)$_2$ complex exhibits HAT reactivity comparable to metal-hydride systems, as opposed to many other ligand-based PCET platforms.

While ligand dissociation/association in solution precluded direct measurement of PCET from the protonated complex, it highlighted the important role electronic configuration of the products may have in reactivity. Magnetic, spectroscopic, and electrochemical measurements were performed to identify the spin states of the products in solution. To investigate how spin-crossover and valence tautomerism may influence the stability and reactivity of these complexes, a computational study was performed in both low- and high-spin configurations of the five-coordinate species outlined in **Scheme 3.1**. The charge and spin-density distributions, as well as changes in geometry and bond lengths, were analyzed and compared to behaviors observed in the solid-state and in solution. It was hypothesized that high-spin isomers adopt a distorted trigonal bipyramidal geometry compared to the strictly square pyramidal low-spin isomers, and protonation of the $[ONO]^{3-}$ ligand occurs favorably when the $\{[ONO]Co(DMAP)_2\}^-$ complex is in a high-spin S = 3/2 configuration. The geometric distortions seen in different spin-states were accompanied by changes in spin-density distribution between Co and [ONO] ligand fragments, while changes in coordination number appeared to cause valence tautomerization between the metal and ligand entirely.

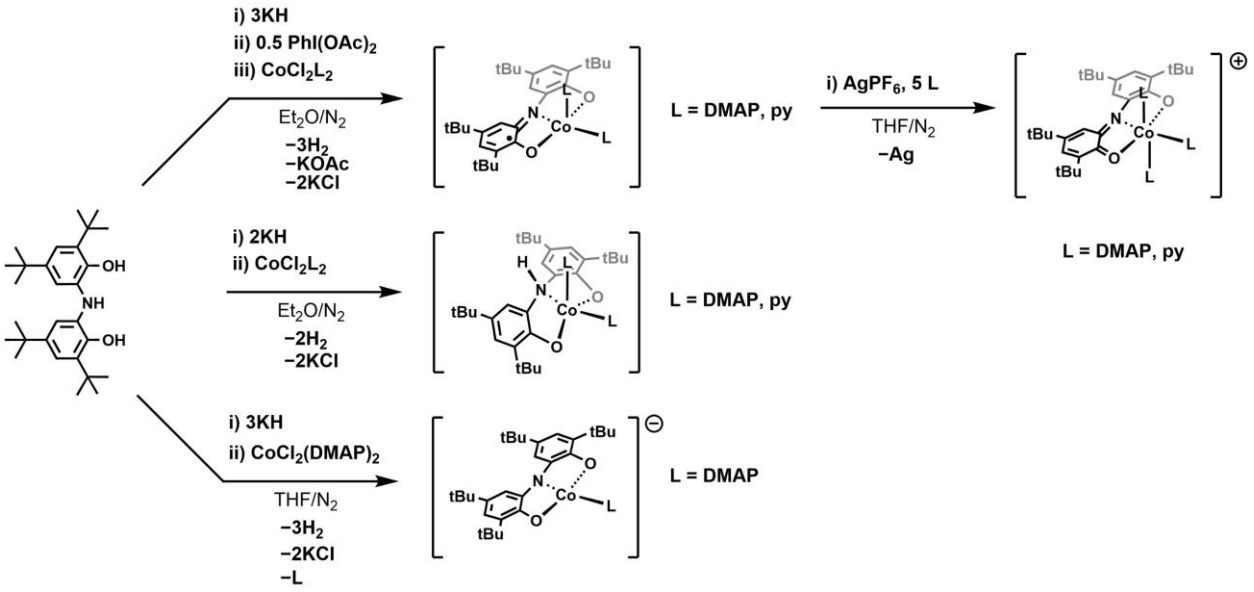

Scheme 3.2. Synthetic route to access $[ONO]Co(L)_n$ species and derivatives.

3.2. Results.

3.2.1. Structural characterization.

Stoichiometric deprotonation of the $[ONO]H_3$ ligand followed by salt metathesis with $CoCl_2L_2$ (L = DMAP, py) was used to prepare $[ON(H)O]Co(L)_2$ and its deprotonated and oxidized analogues (**Scheme 3.2**). Single crystals were obtained, and the intraligand C–O, C–N, and C–C bond lengths of the [ONO] backbone were studied for evidence of ligand-based oxidation (**Table 3.1**).

The isolated protonated $[ON(H)O]Co(L)_2$ complexes were five-coordinate in the solid state. The ligand itself buckles, lifting the sp^3-hybridized nitrogen out of plane and rendering the complexes trigonal bipyramidal, as quantified by a τ_5 value close to 1. The acidic proton was located on the central nitrogen of the [ONO] ligand in both structures (**Figure 3.1, a**).

Loss of one proton and one electron from these complexes would yield a five-coordinate neutral species of the formula $[ONO]Co(L)_2$. Though metallation of the $[ONO^q]K$ proligand has been a fruitful pathway to access highly covalent rhodium species,[38] analogous syntheses with various cobalt (II) salts produced only the known $Co[ONO]_2$, as characterized by ^1H

Table 3.1 Selected bond distances (Å) and τ_5 values of [ON(H)O]Co(DMAP)$_2$, {K(2.2.2.-crypt)}{[ONO]Co(DMAP)}, [ONO]Co(L)$_2$ (L = DMAP, py), and {[ONO]Co(py)$_3$}{PF$_6$} solid-state structures.

Complex	[ON(H)O]Co(DMAP)$_2$	{K(2.2.2.-crypt)}{[ONO]Co(DMAP)}	[ONO]Co(DMAP)$_2$	[ONO]Co(py)$_2$	{[ONO]Co(py)$_3$}{PF$_6$}
Bond			**Distance / Å**		
O1-C1	1.326(2)	1.358(2)	1.324(2)	1.325(2)	1.328(2)
O2-C7	1.3285(19)	1.356(2)	1.330(2)	1.326(2)	1.331(2)
C6-N1	1.462(2)	1.384(2)	1.386(2)	1.382(2)	1.374(3)
C12-N1	1.471(2)	1.386(2)	1.389(2)	1.389(2)	1.374(2)
O1-Co	1.9448(12)	1.8513(12)	1.8913(12)	1.9019(14)	1.8835(13)
O2-Co	1.9420(11)	1.8625(13)	1.8917(12)	1.8958(14)	1.8848(14)
N1-Co	2.2301(14)	1.8373(15)	1.8351(14)	1.8219(16)	1.8570(16)
Co-L	2.0817(14)	1.9420(15)	1.9800(14)	1.9746(16)	1.9659(17)
Co-L'	2.1030(14)	-	1.9764(13)	1.9777(17)	1.9497(16)
MOS[a]	N/A	−2.75 ± 0.19	−2.21 ± 0.087	−2.38 ± 0.15	−2.16 ± 0.086
Bond			**Angle / °**		
O1-Co-O2	119.13(5)	172.15(5)	162.31(5)	166.50(6)	172.65(6)
N1-Co-L	173.55(5)	178.98(7)	167.78(6)	160.38(7)	178.94(7)
N1-Co-L'	92.44(5)	-	100.00(6)	108.85(7)	91.65(7)
O2-Co-N1	81.61(5)	86.35(6)	84.87(6)	85.21(6)	86.63(6)
O1-Co-N1	80.41(5)	86.04(6)	85.45(6)	84.88(6)	86.06(6)
O1-Co-L	111.96(5)	92.72(6)	97.60(5)	93.34(6)	92.90(6)
O1-Co-L'	93.61(5)	-	93.49(6)	97.15(7)	91.03(6)
O2-Co-L	126.49(5)	94.87(6)	98.64(5)	92.91(6)	94.42(6)
O2-Co-L'	98.32(5)	-	92.84(6)	94.72(7)	89.90(6)
τ_n[b,c]	n = 5 0.91	n = 4 0.063	n = 5 0.091	n = 5 0.10	N/A

(a) MOS are averaged between two sides of one molecule. In crystals with multiple molecules in the unit cell, MOS is reported for just one.

(b) $\tau_4 = \frac{360°-(\alpha+\beta)}{360°-2\theta}$ where α, β are the largest angles about the M ion, and θ represents the tetrahedral angle 109.5°.

(c) $\tau_5 = \frac{\beta-\alpha}{60°}$ where α, β are the largest angles about the M ion.

NMR, no matter the stoichiometry. In lieu of direct metallation of $[ONO^{q}]K$, the chemical oxidation of $[ONO]Co(L)_2$ was pursued according to **Scheme 3.2**. Both pyridine and DMAP derivatives were obtained as single crystals suitable for analysis. The $[ONO]^{x-}$ ligands were planar in both structures, and the complexes were rigorously square-pyramidal ($\tau_5 \sim 1$). Analysis of the intraligand bond lengths resulted in metrical oxidation states (MOS)[39] between −2.2 and −2.4.

Hydride transfer from $[ON(H)O]Co(L)_2$ should result in the formation of a cationic $\{[ONO]Co(L)_2\}^{+}$ species. However, only a six-coordinate, octahedral $\{[ONO]Co(py)_3\}^{+}$ complex was characterized in the solid state with a MOS of −2.16 for the [ONO] ligand.

Likewise, proton transfer from $[ON(H)O]Co(L)_2$ should result in the formation of a monoanionic $\{[ONO]Co(L)_2\}^{-}$ species. Electrospray ionization mass spectrometry (ESI-MS) evidence suggested that both a five-coordinate and a four-coordinate anion were produced. It was a four-coordinate square-planar ($\tau_4 \sim 0$) anion that was isolated in the solid-state for L = DMAP, and the MOS of the [ONO] was −2.75. Attempts to crystallize a five-coordinate $\{[ONO]Co(L)_2\}^{-}$ anion or a five-coordinate cation by strictly controlling the amount of ancillary ligand present during synthesis were unsuccessful.

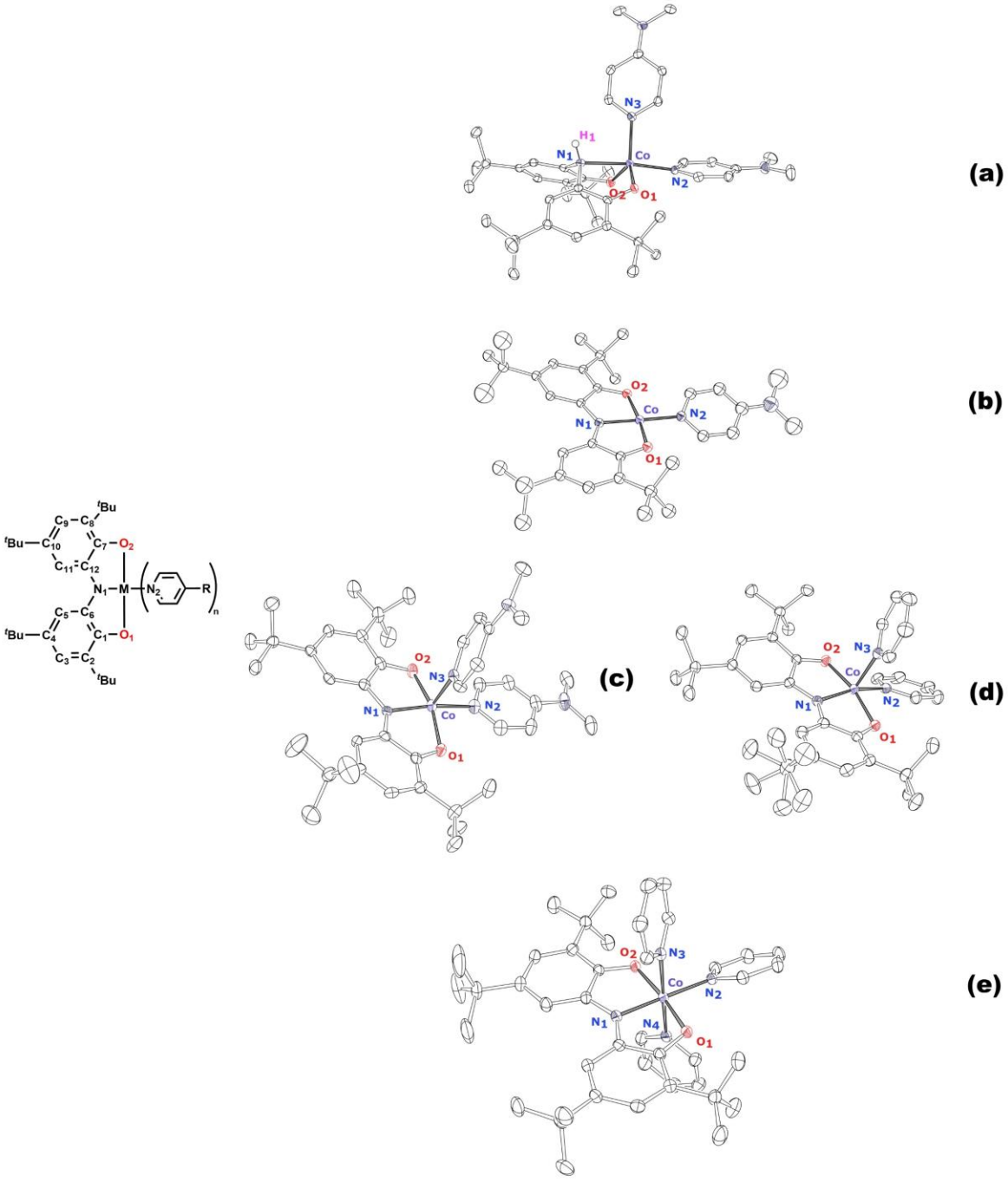

Figure 3.1. ORTEP diagrams of [ONO]Co(L)$_n$ (L = DMAP (a, b, c) n = 1 (b), 2 (a, c); L = py (d, e) n = 2 (d), 3 (e)). Hydrogen atoms, counter ions, chelating agents, and solvent molecules have been omitted for clarity. Bonds relevant to metrical oxidation state analysis have been labeled in the diagram (left).

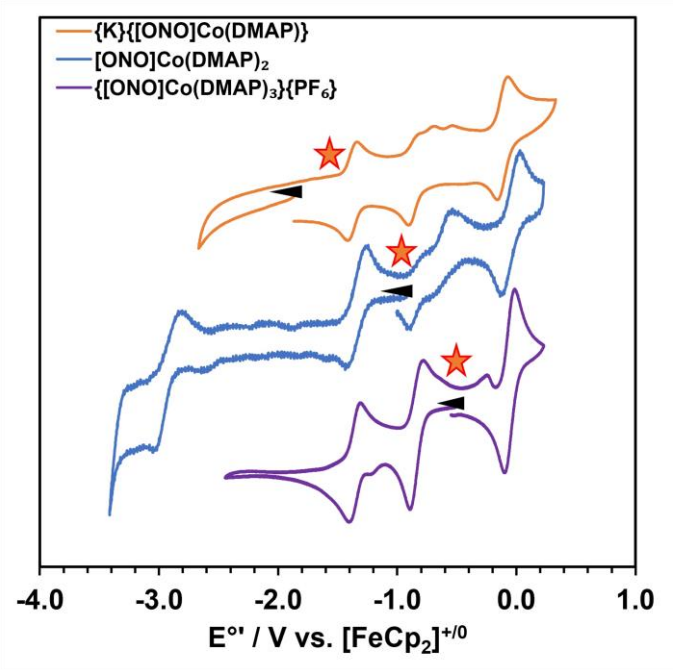

Figure 3.2. Cyclic voltammograms of {K}{[ONO]Co(DMAP)} (orange trace), [ONO]Co(DMAP)$_2$ (blue trace), and {[ONO]Co(DMAP)$_3$}{PF_6}. The orange stars marks the open circuit potential, and black arrows show forward scan direction. Cyclic voltammograms were taken at 100 mV/s in 0.001 M analyte with 0.1 M [TBA][PF_6] using a glassy carbon working electrode, Ag wire pseudoreference electrode, and a Pt wire counter electrode. All potentials referenced to $[FeCp_2]^{+/0}$ internal standard.

Table 3.2. Reduction potentials associated with [ONO]Co(L)$_n$ in acetonitrile at 100 mV/s.

L	E°' / V vs. $[FeCp_2]^{+/0}$ (i_{pa}/i_{pc})				
	$[Co]^{1-/2-}$	$[Co]^{0/1-}$	$[Co]^{1+/0}$	$[Co]^{2+/1+}$	$[Co]^{3+/2+}$
DMAP	−2.95[a]	−1.37 (0.96)	−0.77[b]	−0.09 (1.10)	+0.57[a]
py	−2.80[a]	−1.35 (1.02)	−0.59 (0.94)	+0.10 (1.06)	+0.67[a]

(#) – i_{pa}/i_{pc}. [a] Irreversible. [b] Reversible upon addition of 2.0 equivalents of DMAP.

3.2.2. Electrochemical characterization.

Electrochemistry was performed on the complexes in acetonitrile (**Figure 3.2**). Cyclic voltammetry revealed two redox couples at −0.79 and −0.09 V vs. $[FeCp_2]^{+/0}$, and one couple −1.37 V (**Table 3.2**). An irreversible reduction is seen at very negative potentials in the CV of the neutral [ONO]Co(DMAP)$_2$ complex, and the reversibility of the other redox couples varies with the identity of the bulk complex in solution. The open circuit potential (OCP) of the

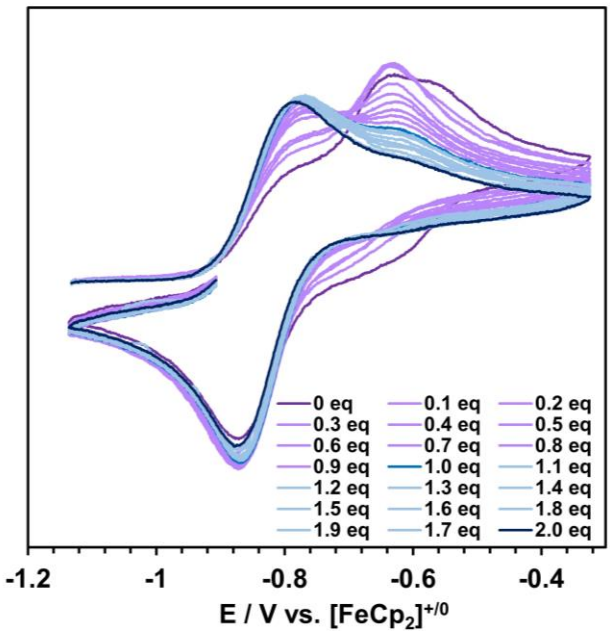

Figure 3.3. Cyclic voltammetry of the redox event centered at −0.77 V belonging to [ONO]Co(DMAP)$_n$ in acetonitrile, in the presence of 0-2.0 equivalents of excess DMAP.

complexes, indicated in **Figure 3.2** by a red star, shifts in relation to their overall charge. The OCP of the monoanionic complex lies at −1.45 V, negative of the reduction at −1.37 V; the OCP of the neutral complex was measured at −0.92 V, between the redox events of −1.37 V and −0.79 V; and the cationic complex has an OCP positive of −0.79 V.

In the anionic and neutral complexes, the oxidation of the complex at −0.79 V appears to be complicated by an overlapping feature at −0.64 V, and the return wave of the neutral complex features two distinct reductions separated by 220 mV. The relative magnitude of these overlapping peaks are dependent on the presence of excess ancillary ligand. Therefore DMAP was titrated into a solution of the neutral [ONO]Co(DMAP)$_2$ complex, and CVs were measured after each addition (**Figure 3.3**). Electrochemical titrations of up to two additional equivalents of DMAP in acetonitrile show the growth of the oxidation at −0.79 V, and the corresponding disappearance of the oxidation at −0.62 V. Likewise, the small reductive event at −0.65 V disappears, while the reduction at −0.87 V appears nearly unchanged throughout the course of the experiment.

3.2.3. Electronic absorption spectroscopy.

The solution stability and the electronic configurations of the complexes were assessed with electronic absorption spectroscopy in dry organic solvents (toluene, benzene, THF, and acetonitrile). No significant changes were observed between coordinating and non-coordinating solvents. Peak wavelengths and molar extinction coefficients are reported for acetonitrile solutions (**Table 3.3** and **Figure 3.4**).

Neon pink solutions of protonated [ON(H)O]Co(DMAP)$_2$ complex (**Figure 3.4,** pink trace) were stable long-term at room temperature in all dry solvents and exhibited a single low-intensity transition at 367 nm. Addition of excess ancillary ligand did not change the intensity or position of the peaks, and no color change was observed.

Moderately intense transitions dominated the spectra of the deep blue neutral [ONO]Co(DMAP)$_2$ complex from 500-700 nm (**Figure 3.4,** blue trace). The relative intensity

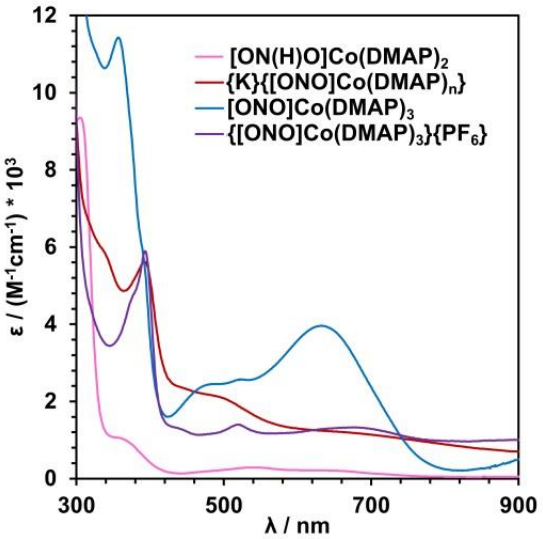

Figure 3.4. Electronic absorbance spectra of {[ONO]Co(DMAP)$_n$}^{m} complexes in acetonitrile. Extinction coefficients of [ONO]Co(DMAP)$_n$ (blue), {[ONO]Co(DMAP)}K (red), [ON(H)O]Co(DMAP)$_2$ (pink), and {[ONO]Co(L)$_3$}{PF$_6$} (purple) in acetonitrile.

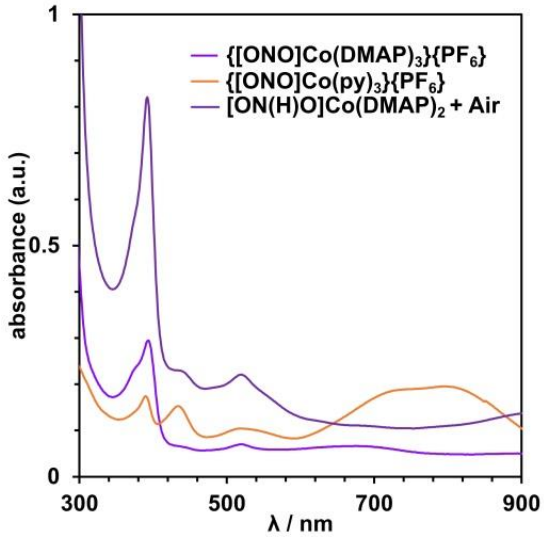

Figure 3.5. Normalized electronic absorption spectra of acetonitrile solutions of oxidized species, {[ONO]Co(L)$_3$}{PF$_6$} (L = DMAP, bright purple trace; L = py, orange trace), and a sample of [ON(H)O]Co(DMAP)$_2$ that was exposed to air.

Table 3.3. Extinction coefficients and λ_{max} of each UV-visible transition for acetonitrile solutions of [ONO]Co(DMAP)$_n$, {K}{[ONO]Co(DMAP)}, [ON(H)O]Co(DMAP)$_2$, and {[ONO]Co(L)$_3$}{PF$_6$} (L = DMAP, py).

Complex	[ON(H)O]Co(DMAP)$_2$	{K}{[ONO]Co(DMAP)}	[ONO]Co(DMAP)$_n$	{[ONO]Co(L)$_3$}{PF$_6$}	
				L = DMAP	L = py
			λ / nm (ε / M^{-1}cm^{-1})		
	364 (990)	393 (5400)	355 (11400)	392 (5800)	387 (3400)
	575	505 (2000)	478 (2400)	374 (4600)	434 (4700)
			631 (3900)	444 (1200)	527 (2400)
				519 (1400)	729 (6300)
				681 (1300)	804 (6800)
				1023 (940)	

of the overlapping features at ~520 nm varied between batches of synthesized [ONO]Co(DMAP)$_2$ and the presence of added DMAP; the blue py [ONO]Co(py)$_2$ complex behaved identically.

The monoanionic {[ONO]Co(DMAP)}$^-$ complex was deep red in solution, and its spectra featured a single sharp transition at ~390 nm with shoulders at ~350 nm and ~500 nm (**Figure 3.4,** red trace). The putative cationic {[ONO]Co(DMAP)$_3$}$^+$ species had the same sharp transition at 390 nm, but only minor features at longer wavelengths (ε_0 < 1500 cm^{-1} M^{-1}) (**Figure 3.4,** purple trace). Surprisingly, the py cation, {[ONO]Co(py)$_3$}$^+$ exhibited a much different spectra (**Figure 3.6,** orange trace), with a prevalent feature at wavelengths > 700 nm.

The protonated [ON(H)O]Co(DMAP)$_2$ complex reacted with both oxygen and water to form products that are spectroscopically distinct from one another. In the presence of even trace amounts water, [ON(H)O]Co(DMAP)$_2$ rapidly and non-stoichiometrically transformed into a vivid blue complex that was spectroscopically identical to [ONO]Co(DMAP)$_2$. Likewise, small amounts of dioxygen (< 5 ppm) induced a color change to deep purple, with spectroscopic characteristics (**Figure 3.6,** purple trace) of the {[ONO]Co(DMAP)$_3$}$^+$ cation. These behaviors have allowed for rapid testing for the presence of water in acetonitrile and dichloromethane solvents, for which ketyl radical solutions cannot be used.

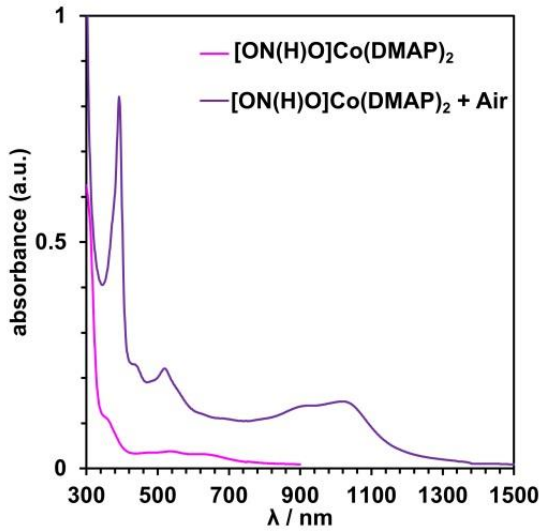

Figure 3.6. Absorbance spectra of [ON(H)O]Co(DMAP)$_2$ (pink trace), and the same sample exposed to air (purple trace).

3.2.4. Electron paramagnetic resonance spectroscopy.

The neutral [ONO]Co(L)$_2$ species exhibited broad ^{1}H NMR spectra, and the chemical shifts associated with aromatic peaks (*ca.* 9.3 and 6.2 ppm) varied from sample to sample at room temperature. Attempts to measure the solution magnetic moment of this complex showed no paramagnetic shift of residual solvent signals, indicating a singlet $S = 0$ ground state for a diamagnetic complex, and the complex was EPR silent.

All other complexes studied were paramagnetic, but their solution magnetic moments and electron paramagnetic resonance (EPR) spectra differed from one another. Evans method measurements of a [ON(H)O]Co(DMAP)$_2$ solution in benzene at room temperature indicate the presence of two unpaired electrons ($\mu_{eff} = 2.96\ \mu_B$), indicating the presence of an S = 1 electronic configuration. An integer spin system would not be visible by perpendicular mode electron paramagnetic resonance, and at room temperature, electron paramagnetic resonance (EPR) spectroscopy resulted in no detected signal. However, upon cooling to 77 K,

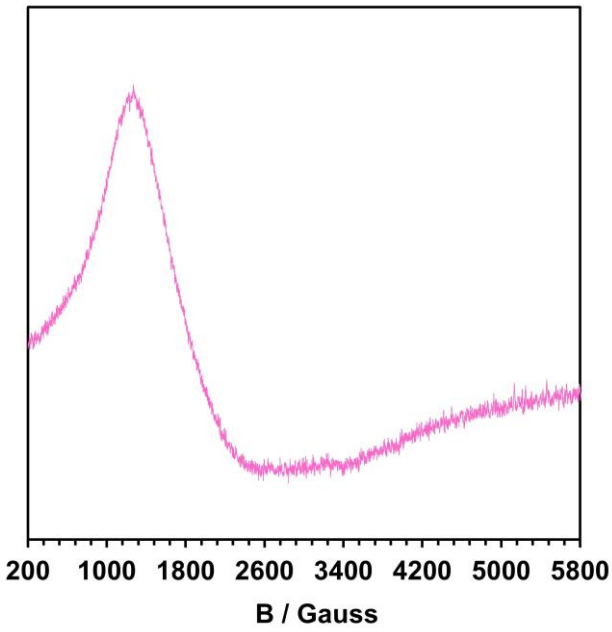

Figure 3.7. Electron paramagnetic spectrum of [ON(H)O]Co(DMAP)$_2$ at 77 K in a 1:1 solution of THF:toluene.

a broad EPR spectra was obtained with g_{eff} = 3.53 (**Figure 3.7**) with no visible hyperfine. No other features were observed at either 77 K or 298 K.

The anionic {K}{[ONO]Co(DMAP)} species was paramagnetic, exhibiting an incredibly weak EPR signal (g = 2.1), and no hyperfine interactions were able to be resolved. A solution magnetic moment μ_{eff} = 3.62 was calculated, indicating the presence of an S = 3/2 quartet spin state.

The EPR taken of the cations in 1:1 THF: toluene solution exhibited significant temperature dependence (**Table 3.4**). A rhombic spectra was obtained (g_z = 2.03, g_y = 1.99, g_x = 1.96) with a distinct nine-line hyperfine pattern (A ~ 40 MHz) for the py cation, {[ONO]Co(py)$_3$}{PF$_6$}, at room temperature (**Figure 3.8,** a). In a 77 K frozen solution, another rhombic spectrum was obtained (**Figure 3.8,** b), but with g factors greatly shifted from what was observed at room temperature.

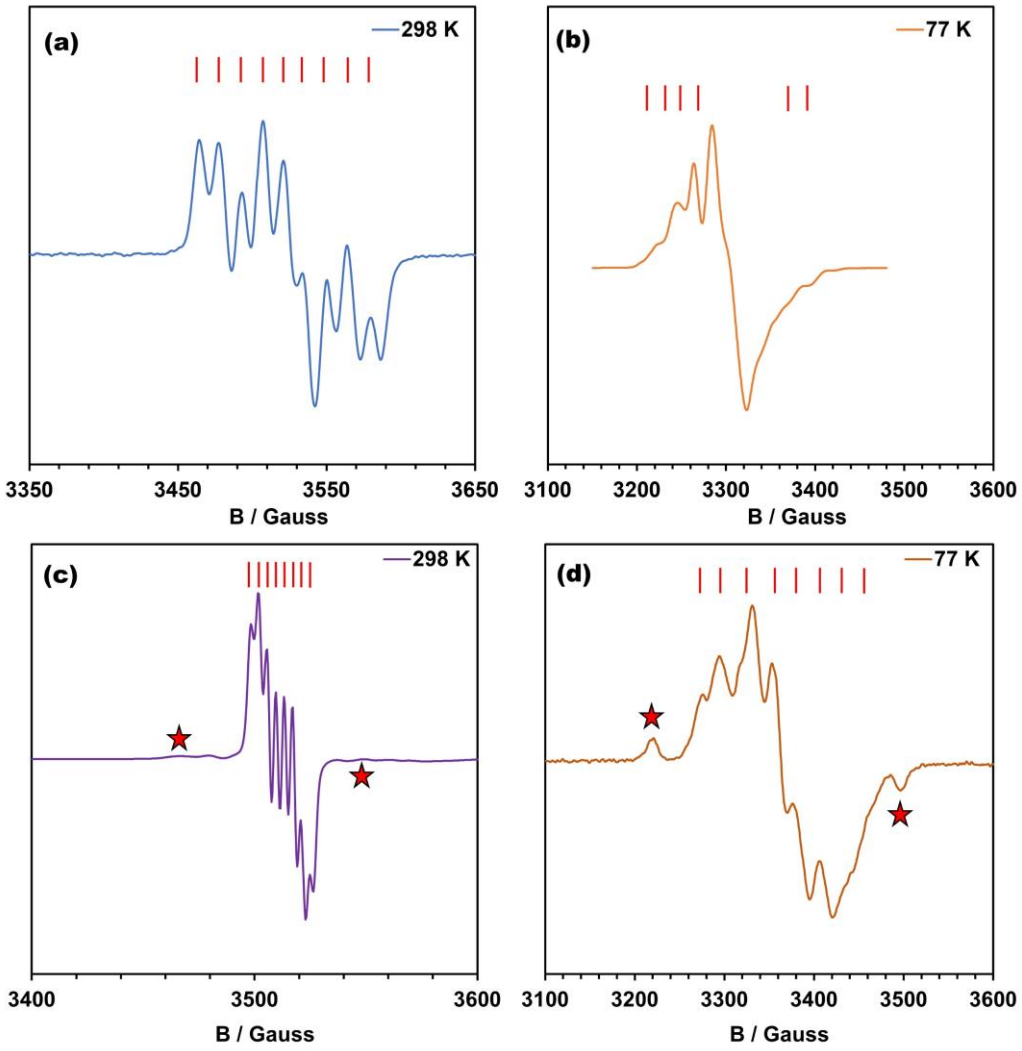

Figure 3.8. EPR spectra of cationic {[ONO]Co(L)$_3$}{PF_6} species in 1:1 THF:toluene solutions. Spectra taken for L = py at 298 K (a) and 77 K (b) exhibit a large shift in field. Spectra taken for L = DMAP at 298 K (c) and 77 K (d) show a more dramatic difference in field shift, with the room temperature solution yielding a narrower spectrum. Red stars and red bars indicate hyperfine features.

The product of the analogous oxidation when L = DMAP generated an EPR-active species with even more pronounced temperature-dependence. At 298 K (**Fig 3.8,** c), a sharp spectra is obtained over a narrow range of magnetic field strengths; upon closer inspection, not only are eight lines of hyperfine structure (A_{exp} ~ 78 MHz) observed, but also smaller features appear on either side of the resonance (**Fig 3.8,** c, red stars) with a separate A_{exp} ~ 208 MHz. At 77 K (**Fig 3.8,** d), the spectrum broadens and shifts; the eight-line hyperfine pattern is more difficult to detect, but the other features become somewhat more

Table 3.4. Experimentally observed parameters of the EPR spectra for {[ONO]Co(L)$_3$}{PF$_6$} cations.

Complex	Temp. / K	g	A
{[ONO]Co(py)$_3$}{PF$_6$}	77[a]	g = 1.99	20 MHz
	298	g_z = 2.03, g_y = 1.99, g_x = 1.96	40 MHz; 39 MHz; 38 MHz
{[ONO]Co(DMAP)$_n$}{PF$_6$}	77[a]	g_z = 2.07, g_y = 2.00; g_x = 1.93	208 MHz; 78 MHz; 78 MHz
	298	g = 2.00	11 MHz; 34 MHz

(a) Values are estimates due to broad experimental spectra.

distinguished (**Fig 3.8,** d**,** red stars). The presence of additional minor species has complicated efforts to simulate the dominant spin system in this complex.

3.2.5. Proton transfer reactivity.

Stoichiometric amounts of base were added to [ON(H)O]Co(L)$_2$ to deprotonate it and form the putative anion {[ONO]Co(L)$_2$}$^-$. However, no base (2,4,6-colllidine, py, NEt$_3$, and 2,3,4,6,7,8,9,10-octahydropyrimido[1,2-a]azepine (DBU)) could induce a change in the UV-visible spectra of [ON(H)O]Co(L)$_2$ at room temperature.

Attempts to isolate {[ONO]Co(DMAP)$_2$}$^-$ *via* deprotonation of [ON(H)O]Co(DMAP)$_2$ on a bulk scale showed no evidence of reaction, except in the case of DBU (pK_a = 24.4, MeCN).[40] Upon addition of one equivalent of DBU, no change in color was observed. However, addition of a second equivalent of DBU induced a faint purple tint to the solution. Upon cooling, a pale purple mother liquor was obtained, with purple crystals. While isolating and mounting these crystals for X-ray diffraction analysis, it was observed that the crystals became neon pink once more. The solid-state structure revealed these pink crystals to be [ON(H)O]Co(DMAP)(DBU). In addition, the purple mother liquor that produced these crystals became pink again upon warming. Subsequent cooling showed this color change process to be fully reversible. As DBU was not strong enough to stoichiometrically deprotonate the [ON(H)O]Co(DMAP)$_2$ complex, the strong base KH was used. Addition of one equivalent of KH to a THF solution of [ON(H)O]Co(DMAP)$_2$ did not immediately give

evidence of gas evolution or color change; stirring overnight afforded a brown paramagnetic solution.

In the presence of DMAP, the anionic $\{[ONO]Co(DMAP)\}^-$ complex reacted stoichiometrically with all proton sources to produce $[ON(H)O]Co(DMAP)_2$. The complex is so weakly acidic that no equilibria could be established even when thousands of equivalents of acid were added.

3.2.6. PCET reactivity.

The loss of one proton and one electron from $[ON(H)O]Co(L)_2$ should result in a neutral $[ONO]Co(L)_2$ species (**Scheme 3.1,** *vide supra*). Therefore, one equivalent of HAT acceptor TEMPO· was added to $[ON(H)O]Co(DMAP)_2$, resulting in the immediate formation of a deep blue-black solution that was consistent with $[ONO]Co(DMAP)_2$.

Attempts to establish an equilibrium and quantify the N–H bond strength by titration of TEMPO· into $[ON(H)O]Co(DMAP)_2$ were unsuccessful, in part due to the apparently large separation in BDFEs between the H-atom acceptor and the complex. Additionally, when $[ON(H)O]Co(DMAP)_2$ donated an H· to TEMPO·, a blue solution with a spectra similar to $[ONO]Co(DMAP)_2$ was produced, and the variations in intensity and peak position made it impossible to accurately measure how much $[ONO]Co(DMAP)_2$ was produced in these titrations. The addition of many equivalents of DMAP could somewhat stabilize the spectra, but because the species that was formed in the presence of excess ancillary ligand may not be the five-coordinate product of H-atom transfer from $[ON(H)O]Co(DMAP)_2$, casting uncertainty on the titrations. Therefore spectrophotometric measurement of the formation of $[ONO]Co(DMAP)_2$ in this reaction was not pursued.

Due to the uncertainty involved in direct BDFE measurement, an estimate was pursued by creating a ladder of reactivity with well-studied HAT acceptors. The quantitative reaction with TEMPO· indicated the BDFE of [ON(H)O]Co(DMAP)$_2$ lay well below 66.5 kcal mol^{-1}. Using half an equivalent of diphenylhydrazine as an H-atom acceptor (BDFE)[41] = 59.6 kcal mol^{-1}) likewise resulted in the formation of [ONO]Co(DMAP)$_2$. Diphenylhydrazine can accept two H-atoms, adding another degree of uncertainty to any equilibrium measurements that might attempt to measure the BDFE of a single HAT process. Thus it served primarily as a benchmark for the relative BDFE of [ON(H)O]Co(DMAP)$_2$.

Reaction of [ON(H)O]Co(L)$_2$ complexes with hydride acceptors should generate a putative {[ONO]Co(L)$_2$}$^+$ species (**Scheme 3.1,** *vide supra*). The addition of trityl cation to the protonated complex produced a purple product that was not characterized. The paramagnetic ^{1}H NMR spectra was too broad to detect any triphenylmethane that might have been produced. As the trityl cation is known to accomplish hydride transfer by several mechanisms, it was not deemed a suitable candidate for spectrophotometric titrations.

3.2.7. Density Functional Theory models of five-coordinate {[ONO]Co(DMAP)$_2$}^{y} isomers.

Unrestricted density functional theory (DFT) calculations carried out on the {[ONO]Co(L)$_n$}^{m} systems were performed with the B3LYP exchange-correlation functional, the LANL2DZ basis set, and tight SCF convergence criteria. Calculations began with geometry optimization from experimentally obtained crystal structures; calculated bond metrics were compared to those in the solid-state, and vibrational frequency calculations were performed to check for the absence of imaginary values. After all subsequent calculations, the stability of the wavefunction was tested to ensure minima had been reached. The process was repeated for high and low spin configurations of every complex modeled.

Atomic orbital contributions to the molecular orbitals (for closed-shell systems, **Table 3.4**) and spin density (for S = 0 complexes, **Table 3.5**) were extracted thereafter. Computed bond angles are also reported in **Table 3.5.**

Five-coordinate complexes were investigated first, according to the simplest PCET square scheme presented (**Scheme 3.1,** *vide supra*). A neutral protonated complex, a monoanionic deprotonated complex, a neutral oxidized complex, and the two-electron oxidized cation, were modeled in high- and low-spin states. In the case of five-coordinate [ON(H)O]Co(DMAP)$_2$ only the high-spin S = 3/2 calculation converged. For the low-spin S = 0 configuration of neutral [ONO]Co(DMAP)$_2$, Mulliken charge distributions and population analysis of the HOMO (**Table 3.4**) were obtained instead of spin density plots.

The singlet [ONO]Co(DMAP)$_2$ was strictly square pyramidal in the solid-state, and the geometry was maintained through the calculation steps. Population analysis indicates that the highest-occupied molecular orbital (HOMO, **Figure 3.9, b**) is formed from significant contributions of metal d_{z2} and [ONO] ligand-based π^*-orbitals (Co = ~ 24%, [ONO] = ~ 73%) in a non-bonding combination. The LUMO of the complex is a σ^* interaction with respect to d_{z2} and the apical DMAP, with a small non-bonding contribution from the p_z orbitals of the [ONO] oxygen and nitrogen atoms. Higher-lying orbitals are primarily DMAP-cobalt antibonding in nature, while [ONO]–Co π^*- and non-bonding molecular orbitals makeup the HOMO-1 to HOMO-5.

The singlet and triplet spin states of [ONO]Co(DMAP)$_2$ were calculated to be only kcal apart. The triplet S = 1 [ONO]Co(DMAP)$_2$ converged to a square-pyramidal system with the

Table 3.5. Mulliken charge distribution in [ONO]Co(DMAP)$_2$, and population analysis of the HOMO when S = 0.

Fragment	Charge / a.u.	Contribution / %
Co	0.371	24.6
[ONO]	−0.974	73.0
DMAP (total)	0.603	0

Table 3.6. Spin density, calculated bond angles, and τ_5 indices from calculated bond angles of complexes $\{[ONO]Co(DMAP)_2\}^m$ for m = 0, −1, +1, and $[ON(H)O]Co(DMAP)_2$, in both high- and low-spin configurations.

Complex	$[ON(H)O]Co(DMAP)_2$		$\{[ONO]Co(DMAP)_2\}^-$		$[ONO]Co(DMAP)_2$		$\{[ONO]Co(DMAP)_2\}^+$	
Spin	S = ½ (a)	S = 3/2	S = 1/2	S = 3/2	S = 0 (b)	S = 1	S = 1/2	S = 3/2
Fragment	**Spin Density / %**							
Co	-	89	98	86	-	57	92	49
O_{ONO} (total)	-	6.2	−1.8	3.8	-	3.3	−4.3	14
N_{ONO}	-	1.5	−0.48	5.3	-	18	2.3	9.9
C_{ONO} (total)	-	0.54	0.81	1.4	-	17	5.3	23
DMAP(total)	-	2.8	2.6	3.2	-	4.6	4.3	3.1
Bond	**Angle / °**							
O1-Co-O2	-	139	170	167	165	169	165	164
N1-Co-L1	-	89.8	99.2	123	103	96.9	96.9	169
N1-Co-L2	-	166	166	123	163	168	166	94.1
O1-Co-N1	-	80.8	86.0	83.7	86.0	85.5	84.4	85.2
O2-Co-N1	-	80.0	86.0	83.7	86.0	85.5	84.5	85.2
O1-Co-L1	-	109	93.4	94.3	96.5	93.7	95.5	96.5
O1-Co-L2	-	94.6	93.3	92.6	92.0	93.7	94.1	93.6
O2-Co-L1	-	107	93.4	92.6	97.8	93.7	94.5	96.5
O2-Co-L2	-	95.1	93.3	94.3	91.8	93.7	94.1	93.6
τ_5 (c)	-	0.5	0.07	0.7	0.03	0.02	0.02	0.08

(a) Calculation did not converge to listed spin state.
(b) Spin density does not apply to S = 0 molecules, see Atomic Orbital Contributions table.
(c) $\tau_5 = \frac{\beta-\alpha}{60^\circ}$ where α, ß are the largest angles about the M ion. τ_5 values of 0 indicate perfect square pyramidal geometry, and τ_5 values of 1 indicate trigonal bipyramidal.

(LS) = Low Spin; (HS) = High Spin

spin density split almost evenly between the metal center (Co = ~ 57%) and the redox-active ligand ([ONO] = ~38%). The two singly-occupied orbitals have significant Co and [ONO] character. A high-spin quartet did not converge.

From the closed-shell neutral complex, addition or removal of one electron should generate charged species with multiple possible electronic configurations. Assuming low-spin S = 1/2 configurations, both the $\{[ONO]Co(DMAP)_2\}^+$ cation and $\{[ONO]Co(DMAP)_2\}^-$ anion optimized to rigorously square-pyramidal (τ_5 ~ 0) species. The cobalt ion carries the majority (>90%) of the spin-density in both the cation and anionic complex.

High-spin quartet configurations for the cation and anion were also investigated. Optimization of the S = 3/2 systems resulted in delocalization of some spin onto the [ONO] ligand itself for both the anion and cation. The cation exhibits the most significant change in

Table 3.7. Spin density calculated for {[ONO]Co(DMAP)}$^-$ and {[ONO]Co(DMAP)$_3$}$^+$ and [ONO]Co(DMAP)$_3$

Complex	{[ONO]Co(DMAP)}$^-$		{[ONO]Co(DMAP)$_3$}$^+$	
Spin	S = 1/2	S = 3/2	S = 1/2	S = 3/2
Fragment	**Spin Density / %**			
Co	99	86	−1.2	53
O_{ONO} (total)	−3.4	6.2	14	17
N_{ONO}	0.47	4.4	37	10
C_{ONO} (total)	3.0	2.0	49	18
DMAP(total)	0.97	1.1	1.1	3

spin-density distribution between S = 1/2 and S = 3/2 calculations so that the high-spin complex carries ~ 47% of the spin-density on the [ONO] backbone overall. Despite the dramatic change in spin-density, the cation exhibits little change in bond angles between the low- and high-spin states, whereas the anionic {[ONO]Co(DMAP)$_2$}$^-$ complex distorts significantly from square pyramidal (τ_5 ~ 0) to almost trigonal bipyramidal (τ_5 = 0.7).

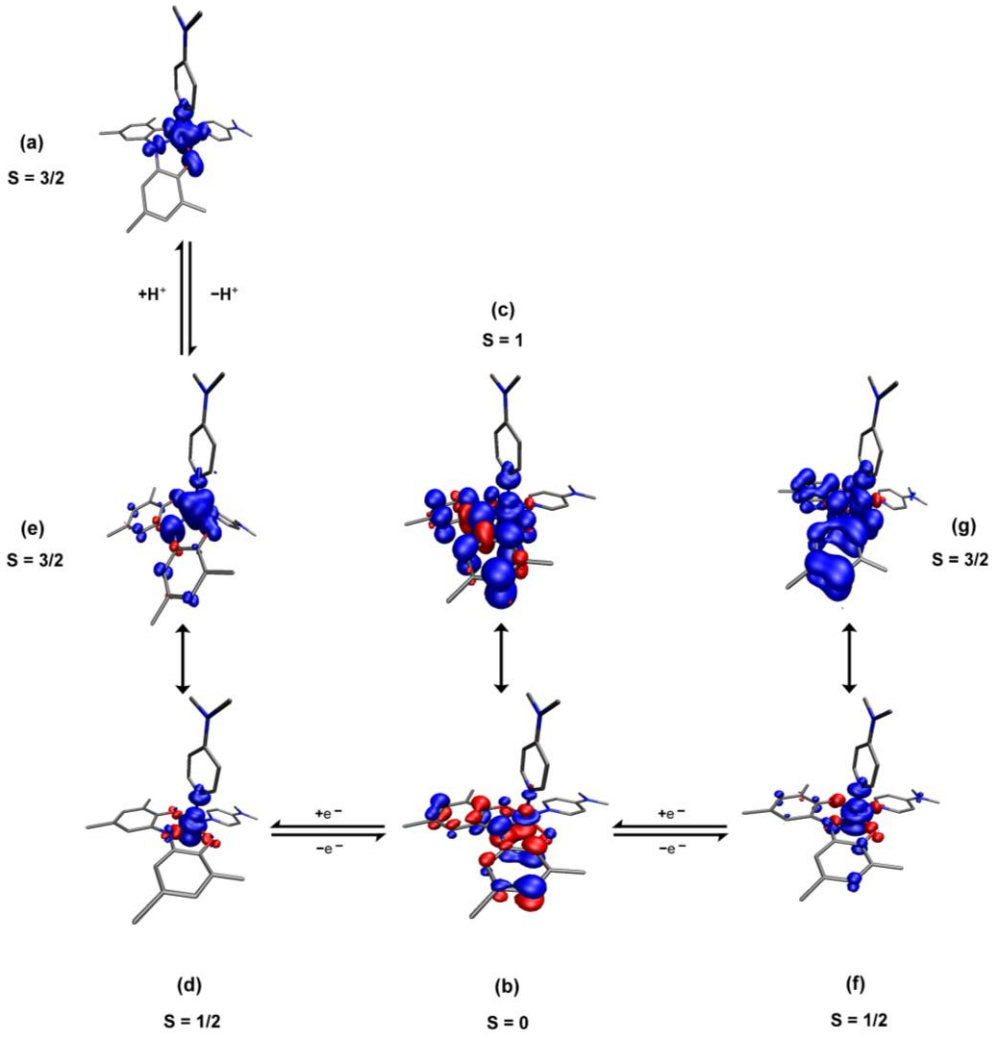

Figure 3.9. Spin-density plots (a, c-g) and Kohn-Sham highest-occupied molecular orbital (b) for five-coordinate $\{[ONO]Co(DMAP)_2\}^m$ (m = −1, 0, +1) and [ON(H)O]Co(DMAP)$_2$, in high- and low-spin configurations. Spin-density plots are shown with an iso = ± 0.0015, and the HOMO is shown with an iso = 0.045.

3.2.8. Computational models of $\{[ONO]Co(DMAP)_n\}^y$ isomers.

Of course, the $\{[ONO]Co(DMAP)\}^-$ anion had been isolated in a four-coordinate geometry, and the crystallographic and electrochemical evidence supports a six-coordinate geometry for the $\{[ONO]Co(L)_n\}^+$ cations (L = py, DMAP). Calculations were also performed on these structures for low-spin and high-spin isomers for spin states < 2 (quintet).

The anionic, square-planar complex converged as a stable doublet with the single unpaired electron residing primarily on the Co ion (98.9% of the spin-density). A four-coordinate quartet S = 3/2 state was also investigated, which saw ~ 12% of the spin density

shared across the [ONO] ligand backbone. Calculations performed on the six-coordinate $\{[ONO]Co(DMAP)_3\}^+$ species with an S = 1/2 configuration place only ~ 1% of the spin-density on Co; instead, almost 100% of the spin-density resides on the [ONO] ligand, with 37.3% on the central nitrogen and 48.6% on the aromatic backbone. Finally, a neutral six-coordinate $[ONO]Co(DMAP)_3$ complex was also investigated. The singlet S = 0 spin-state did not converge, but an S = 1 triplet.

3.3. Discussion.

3.3.1. Evidence of ligand lability.

The broad and variable spectral signatures seen in the neutral deprotonated species, and the solid-state analysis evidence of both the six-coordinate, oxidized complex, and a four-coordinate anion, indicated that the coordination environment around the Co ion may be fluxional. Titrations of excess DMAP were performed on this family of complexes and monitored by ^1H NMR, UV-visible spectroscopy, and cyclic voltammetry, to determine if the presence of additional ligand resulted in electronic changes. Excess DMAP was added to $[ON(H)O]Co(DMAP)_2$ and $\{[ONO]Co(DMAP)\}K$, but no electronic differences were observed in their UV-visible spectra. If the coordination of a fifth or sixth ligand were to induce a change in spin-state from low- to high-spin or an intravalent tautomerization (in which the ligand were effectively oxidized by the metal ion), some shift in the electronic absorption spectra might have been observed.

Both the electronic absorption spectra and the electrochemical data (**Figure 3.3, Figure 3.13**) obtained from dissolved samples of $[ONO]Co(DMAP)_2$ showed some initial concentrations of two equilibrium species. In the electronic absorption spectra of $[ONO]Co(DMAP)_n$, the spectral signatures of an $[ONO^{sq}]^{2-}$ ligand complex are always present

in general, but the molar extinction coefficients and λ_{max} shift from sample to sample; addition of 10 equivalents of DMAP could reproducibly stabilize the spectra toward one species, suggesting that ligand association may play a role in the variations. Therefore further ligand titrations were performed. Titrations were also performed *via* ^{1}H NMR on [ONO]Co(DMAP)$_n$ in C_6D_6, however, the results were inconclusive; while resonances associated with the aromatic and methyl protons of DMAP sharpened in the presence of excess ligand, on the NMR timescale it was not possible to observe an equilibrium between free and bound DMAP. Neither was it possible to assign DMAP and [ONO] aromatic resonances separately at any point.

The overlapping oxidative waves in the cyclic voltammetry of neutral [ONO]Co(L)$_n$ complexes further suggested that ligand equilibria might be occurring between complexes with different coordination numbers. The six-coordinate crystal structure of the cationic {[ONO]Co(py)$_3$}$^+$ complex suggested that the equilibrium in question might be between five- and six-coordinate members. Addition of excess DMAP should drive the formation of a species [ONO]Co(L)$_{(3)}$, which is then oxidized to {[ONO]Co(L)$_{(3)}$}$^+$ at a more negative potential than any remaining [ONO]Co(L)$_n$ in solution due to the increased ligand donation into the metal center. The binding strength of an additional equivalent of DMAP to [ONO]Co(L)$_2$ (L = DMAP) was therefore estimated based on the titrations shown in **Figure 3.3**, according to the following equilibrium relationships:

$$K_{eq} = \frac{[(ONO)CoL_3]}{[(ONO)CoL_2][L]} \qquad \textbf{(Eqn. 3.1)}$$

$$\frac{[(ONO)CoL_3]}{[(ONO)CoL_2]} = K_{eq}[L] + b \qquad \textbf{(Eqn. 3.2)}$$

When two redox species are both visible in solution, it is possible to use the Nernst equation in conjunction with these equilibria to relate the difference in peak potentials (ΔE) of two redox species—in this case, [ONO]Co(DMAP)$_2$ and [ONO]Co(DMAP)$_3$—to the

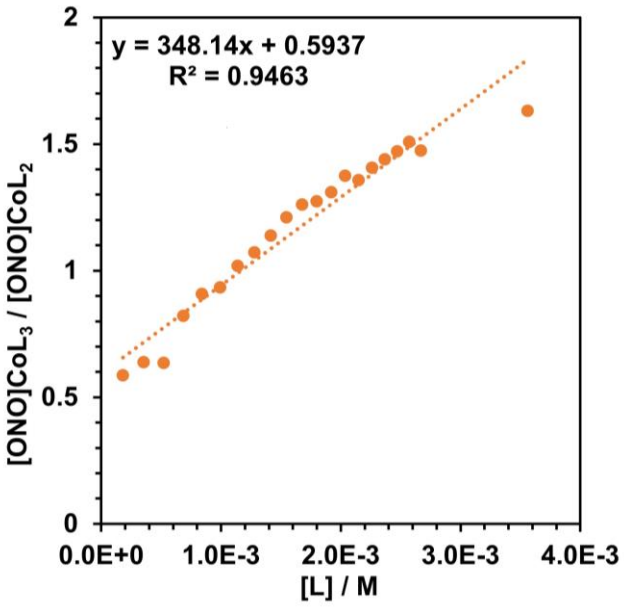

Figure 3.10. Plot of equilibrium measurements of $[ONO]Co(DMAP)_n$ in the presence of varying concentrations of DMAP ([L]). In lieu of equilibrium concentrations, the peak currents i_{pa} corresponding to −0.79 V and −0.63 V were used to measure $[(ONO)Co(L)_3]$ and $[(ONO)Co(L)_2]$.

concentration of an added ligand L. Previous studies have established that peak current (i_{pa} and i_{pc}) are directly proportional to solution concentrations of the species involved with electron transfer, resulting in a relationship that can be used to determine a ligand or substrate binding constant.[42-45] Plotting the concentration of L (DMAP) against the ratio of equilibrium species (**Figure 3.10**) yields a line whose slope is K_{eq}. From this value, a binding energy of −3.5 kcal mol^{-1} was determined.

The same logic should apply to the reduction of five- or six-coordinate $[ONO]Co(DMAP)_n$ to $\{[ONO]Co(DMAP)_n\}^-$ (n = 2, 3), which then becomes square planar in the solid state. Additional features are sometimes present in cyclic voltammograms of the $\{[ONO]Co(DMAP)_n\}^-$ anion that further support the possibility of ligand association and lability in the complex. However, the complex decomposes over the course of a few hours to an unidentified product with no reversible electrochemical features in coordinating solvents, precluding current efforts to measure an equilibrium constant for binding a fifth ligand.

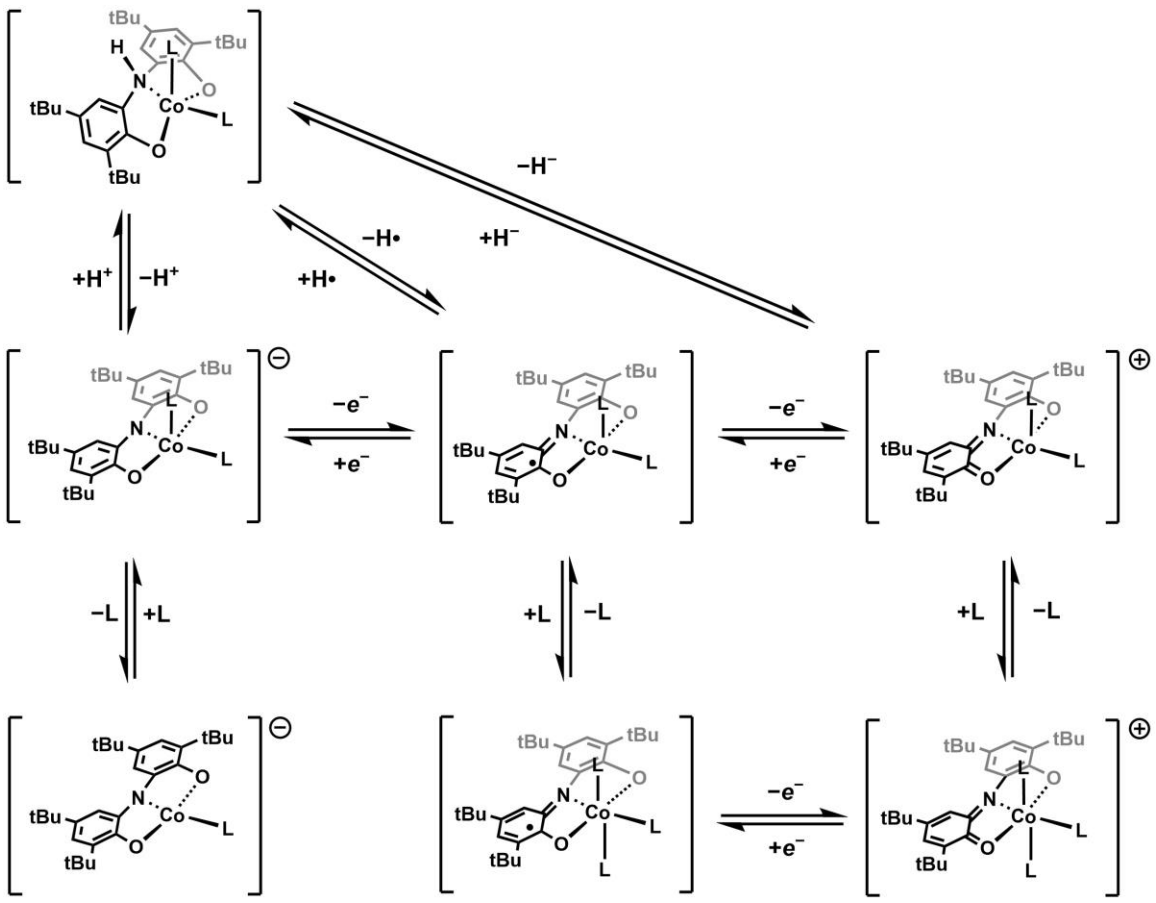

Scheme 3.3. Thermodynamic cycle relating $[ONO]Co(L)_n$ species by proton- and electon-transfer steps, amended to include experimentally-observed ligand equilibria.

Based on the different coordination numbers seen in the solid-state structures, and the electrochemical and spectroscopic data, it was concluded that PCET from $[ON(H)O]Co(L)_2$ generates five-coordinate products with labile ancillary ligands. In solution, the association (for neutral $[ONO]Co(L)_2$] and cationic $\{[ONO]Co(L)_2\}^+$) of a sixth ligand occurs readily at room temperature; likewise, ligand dissociation from the five-coordinate anion must also occur. Thus **Scheme 3.1** can be amended to include the proposed ligand equilibria in **Scheme 3.3**, below. The five-coordinate complexes are drawn with square-pyramidal geometry, but a flexible coordination environment is possible in solution.

$$\boldsymbol{BDFE}(X-H) = 1.37pK_a + 23.06E_1^\circ + C_G \quad \textbf{(Eqn. 3.3)}$$

$$\Delta\boldsymbol{G}_{\boldsymbol{H-}}^\circ = 1.37pK_a + 23.06E_1^\circ + 23.06E_2^\circ + \Delta G_{H+/H-} \quad \textbf{(Eqn. 3.4)}$$

3.3.2. Estimating pK_a, BDFE, and hydricity of [ON(H)O]Co(DMAP)$_2$.

To determine whether a transition metal complex is suitable as a donor or acceptor in a proposed PCET reaction, the X–H (BDFE) and thermodynamic hydricity (ΔG°_{H-}) can be measured directly, or the transfer of one proton and one electron for net HAT, and the transfer of one proton and two electrons to afford net hydride transfer, can be described using Hess's law as the sum of the pK_a and relevant reduction potentials to derive both the BDFE (**Equation 3.3**) and $\Delta G°_{H-}$ (**Equation 3.4**) from empirical values.[46-53]

Using the $E_{1/2}$ obtained from cyclic voltammetry performed in MeCN and the BDFEs of these HAT reagents, and the acetonitrile solvent factor C_G = 52.61 kcal mol^{-1}, it is possible to rearrange the Bordwell equation (**Equation 3.3**) to solve for the N–H pK_a in [ON(H)O]Co(DMAP)$_2$. The BDFE of the complex could lie at, or below, the 59 kcal mol (the BDFE of diphenylhydrazine), but it absolutely must lie below the BDFE of TEMPO (66 kcal mol). Therefore the pK_a may lie in the range of 28.1 < [ON(H)O]Co(DMAP)$_2$ < 33.1, though it may have a slightly lower pK_a (25<) based on the potential equilibrium with HDBU$^+$.

This estimated range of pK_a was corroborated by efforts to deprotonate the [ON(H)O]Co(DMAP)$_2$ complexes with bases of increasing strengths. From the isolated [ON(H)O]Co(DMAP)(DBU) crystal structure, it is apparent that the DBU–Co binding is more favorable than protonation to form H–DBU$^+$ (pK_a = 24.1, MeCN),[40] meaning that the complex is less acidic. Additionally, the incomplete reaction of 1.0 equivalent of KH with [ON(H)O]Co(DMAP)$_2$ in THF suggests that their pK_as may lie within a few units of one another, roughly bracketing the pK_a of ON(H)O]Co(DMAP)$_2$ ≤ 35. Working backwards from the pK_a of H–DBU$^+$ as a lower limit, an estimated BDFE of 59.8 kcal mol^{-1} is obtained.

By both methods, the BDFE of [ON(H)O]Co(DMAP)$_2$ lies below 60 kcal mol^{-1}, rendering it a potent H-atom donor. Combining the estimated pK_a limits and both ligand reduction potentials (**Equation 3.4**) results in an estimated thermodynamic hydricity (ΔG_{H^-}) between 59.9 and 72.0 kcal mol^{-1}. In comparison to previous examples of {[ENE]ML}$^-$ complexes, the {[ONO]Co(DMAP)}$^-$ anion ([Co]$^{1-}$) exhibits an $E_{1/2}$[Co]$^{0/1-}$ at −1.37 V vs. [FeCp$_2$]$^{+/0}$, a potential that is 100 mV more negative than the previously studied {[ONO]Ni(DMAP)}$^-$ complex ([Ni]$^{1-}$, $E_{1/2}$[Ni]$^{0/1-}$ = −1.28 V). While {[ONO]Co(DMAP)}$^-$ is apparently more reducing than the nickel congener, it is also likely a much weaker acid. A similar [ON(H)O]Ni(PPh$_3$) complex has a conjugate base that gets reduced at −0.95 V vs. [FeCp$_2$]$^{+/0}$ but has a pK_a of only 15.3 in acetonitrile.[36] However, the obvious structural changes this complex undergoes, losing an ancillary ligand to form a four-coordinate anion and gaining a ligand to form the oxidized octahedral complexes, render these values as mere estimates, as some amount of driving force in the PCET behavior of these complexes likely comes from ligand association/dissociation.

3.3.3. Charge distribution in {[ONO]Co(L)$_n$}^{y} complexes and geometry changes.

Tuning the electrochemistry of redox-active ligands such as the amidophenolate [ap]$^{2-}$, catecholate [cat]$^{2-}$, and both [ONO]$^{3-}$ and [SNS]$^{3-}$ bound to reactive late transition metal ions is of great interest. The tridentate [ONO] ligand is known to access three oxidation states reversibly, and the $E_{1/2}$[sq•/cat] and $E_{1/2}$[q/sq•] reduction potentials of this and similar ligands are sensitive to both metal ion and ancillary innocent ligand identities. However, as discussed previously, redox-active ligands bound to cobalt ions often deviate from of the well-segregated metal- and ligand-based reactivity that characterizes other redox-active ligand

complexes. Qualitative analysis of the cyclic voltammogram shown in **Figure 3.2** would suggest that the observed features are ligand-based, as they lie at relatively mild oxidative potentials for metal-based redox features.[54,55] However, the significant structural rearrangements observed for this family of complexes are often indicative of a metal-based electronic change. The electrochemistry of the py and DMAP complexes strongly suggested that they become six-coordinate upon one-electron oxidation from the neutral $[ONO]Co(L)_n$ species, a hypothesis that was supported by the six-coordinate crystal structure obtained for $\{[ONO]Co(py)_3\}^+$. In addition, the crystallographic evidence of a four-coordinate anion suggests that the reduction of $[ONO]Co(DMAP)_n$ may cause the dissociation of one or more ancillary ligands. The complexes can also access a third reversible electron transfer event at modest potential when only two ligand-based redox events were expected. Understanding the origin and effect of electron transfer, spin-crossover, and valence tautomerization on the $\{[ONO]Co(L)_n\}^y$ complexes therefore required further scrutiny.

Contradictions between solid-state structures and UV-Visible spectroscopy.

Generally, it is useful to assign formal oxidation states to the redox-active ligand and metal fragments in a complex using combined solution- and solid-state data, for the oxidation state designations can suggest whether a ligand- or metal-based redox event will occur first. Bond lengths in the [ONO] ligand backbone are sensitive to oxidation state changes,[56-59] and comparison to other transition metal complexes containing the ligand by MOS analysis can help determine whether the ligand is better described as $[ONO^{cat}]^{3-}$, $[ONO^{sq\cdot}]^{2-}$, or $[ONO^{q}]^{1-}$ in the solid-state. However, the intraligand structural metrics of the complexes studied in this work (**Table 3.1**) do not deviate much from one another, even when the complex overall

is oxidized. Other discrepancies between the solid-state bond metrics and solution spectroscopy made it difficult to assign formal oxidation states to the complexes.

In the [ONO]Co(L)$_2$ complexes, carbon-heteroatom bonds are not significantly shortened from typical single-bond lengths (C–N, 1.370-1.470 Å; C–O, 1.301-1.450 Å) and do not show double-bond character (C=N, 1.260-1.350 Å; C=O, 1.240-1.350 Å), as they would in a structure with the fully-oxidized [ONO^q] ligand.[56] The MOS of [ONO]Co(L)$_2$ falls between −2.0 and −2.5, which is consistent with an intermediate catecholato/semiquinonato oxidation state for the redox active ligand.

In comparing the cationic {[ONO]Co(py)$_3$}$^+$ to its five-coordinate, one-electron reduced congener, the MOS of both fall between −2.0 and −2.5. An oxidized [ONO^q]$^{1-}$ ligand would instead yield a value closer to −1. With the py cation, the spectroscopic oxidation state appears to contradict the solid-state evidence; {[ONO]Co(py)$_3$}$^+$ has a UV-visible spectrum (**Figure 3.5**) that is more in line with the low-energy [ONO^q]$^{1-}$ transitions seen in other complexes, while the MOS between neutral and cationic complexes are consistent with semiquinonate ligands. The transition between five-coordinate to six-coordinate species upon oxidation also suggested that the electron was removed from the metal, not the ligand, as a d^6 Co(III) ion would be expected to prefer an octahedral geometry.

Similarly, the ligand in anionic {[ONO]Co(DMAP}$^-$ is only somewhat reduced compared to the [ONO]Co(DMAP)$_2$ solid-state structure, though the anion's MOS of −2.75 ± 0.19 does fall within the range of other published [ONO^{cat}]$^{3-}$ ligand frameworks. UV-visible spectroscopy of the neutral [ONO]Co(L)$_2$ complexes gave spectra that were in line with prior examples of [ONO$^{sq\cdot}$]$^{2-}$ ligands, exhibiting characteristic π–π^* transitions ~ 600 nm. In contrast, the reduced and oxidized complexes of {[ONO]Co(DMAP)$_n$}^{y} (n = 0, y = −1; n = 3, y = +1) do not possess the usual features of [ONO^{cat}]$^{3-}$ or [ONO^q]$^{1-}$ ligands. In the case of a

metal-based reduction from [ONO]Co(DMAP)$_2$, the Co(I) ion produced would be stable in a d^8 square planar geometry.

Five-coordinate complexes are implicated as products of proton and hydride transfer from [ON(H)O]Co(DMAP)$_2$ (**Scheme 3.1**). The protonated complex itself is well-described as an S = 3/2, high-spin Co(II) ion with a coordinated $[ON(H)O]^{2-}$ ligand, assignments that are supported by intraligand bond order, solution magnetic and EPR measurements, and UV-visible spectroscopy. However, proton transfer, HAT, and hydride transfer may generate species that can each adopt multiple electronic configurations. The discrepancies between solution- and solid-state behavior for the anionic, neutral, and cationic complexes prompted computational study of the complexes in a variety of spin states, coordination environments, and oxidation states. It was hoped that understanding the electronic configurations or each complex might yield an understanding of their overall stability in solution.

Electronic configuration of [ON(H)O]Co(DMAP)$_2$.

Evan's method measurements of the solution in benzene (μ_{eff} = 2.96 μ_B) indicate the presence of two unpaired electrons, consistent with an S = 1 system. However, and S = 1 five-coordinate complex could largely be ruled out. In the solid-state, the $[ON(H)O]^{2-}$ ligand is unlikely to take on a radical configuration, and the lack of a counterion to the complex would indicate the metal center is in the Co(II) oxidation state with seven *d* electrons. A trigonal bipyramidal d^7 ion could be described as either an S = 1/2 or S = 3/2 spin system. An equilibrium between the two spin states might explain the solution average measurement of μ_{eff}.[60-64] An isostructural complex of the similar sulfur-based redox- and proton-active ligand [SN(H)S] was previously reported, with a high-spin S = 3/2 ground state.[65]

At room temperature, electron paramagnetic resonance (EPR) spectroscopy resulted in no detected signal, but upon cooling to 77 K, a broad EPR spectra was obtained with g_{eff} = 3.53 (**Figure 3.3**) with no visible hyperfine. The linewidth of the observed spectra is indicative of a wide distribution of zero-field splittings (D), and the general appearance of this asymmetric feature at low magnetic field strengths is characteristic of a high spin, axial, S = 3/2 Co(II) system in [ON(H)O]Co(DMAP)$_2$ at 77 K.. Other examples of five-coordinate, high spin Co(II) complexes have produced EPR spectra with $3 < g_{eff} < 9$.[66-70]

The aforementioned [SN(H)S] derivative species exhibits a near-identical spectrum visible at 4 K with g = 3.58, though [SN(H)S]Co(DMAP)$_2$ is formally four-coordinate (N_{SNS}–Co = 3.093 Å) and has been simulated as an S = 3/2 pseudo-tetrahedral system. In the case of [ON(H)O]Co(DMAP)$_2$, the complex is rigorously five-coordinate in the solid-state with a N_{ONO}–Co distance of 2.230(1) Å, well within the typical range for Co(II) complexes. A genuine S = 1 impurity in the sample cannot be ruled out, as integer spin systems cannot be observed in perpendicular mode. No features consistent with an S = 1/2 spin system were seen at either 77 K or 298 K, though it is not unusual for low-spin Co(II) signals to go unresolved due to relaxation effects.

Overall, magnetic and spectroscopic data suggest that [ON(H)O]Co(DMAP)$_2$ has a high-spin Co(II) electronic configuration. DFT calculations did not converge for a low-spin system. Thus theoretical approaches to proton and electron transfer from this complex began from an S = 3/2 starting point. However, protonation-induced spin-crossover is known to occur in cobalt-redox-active ligand complexes,[71] so both low- and high-spin anion, cation, and neutral precursor complexes were investigated.

Spin density distributions in cationic $\{[ONO]Co(DMAP)_n\}^+$ (n = 2, 3)

The five-coordinate cation converged to low- and high-spin isomers. When S = 1/2, more than 90% of the spin density lies on the Co ion, suggestive of a metalloradical with partial (<10%) delocalization to the [ONO] fragment (**Table 3.4**). The low-spin complex was rigorously square pyramidal, with the unpaired electron residing in a molecular orbital composed primarily of Co. The high-spin S = 3/2 complex shares dramatically more spin density with the [ONO] ligand, with only ~50% of the spin density remaining on Co while ~47% is placed on [ONO]. This electronic arrangement is strongly suggestive of a partially-reduced redox-active ligand that might resemble the $[ONO^{sq\cdot}]^{2-}$ radical state as opposed to the closed-shell $[ONO^{q}]^{1-}$ ligand.

The six-coordinate complex was also investigated. While the spin density of the high-spin S = 3/2 $\{[ONO]Co(DMAP)_3\}^+$ complex does not differ much from the five-coordinate high-spin complex, the low-spin complexes point to an explanation of what was observed in the solid-state. The low-spin five-coordinated complex has 92% of the spin density localized on the metal ion, but the addition of a sixth ligand induces an immediate change, with nearly 100% of the spin density transferring to the [ONO] ligand. As before, the delocalization of spin density onto the ligand backbone might resemble the $[ONO^{sq\cdot}]^{2-}$ radical state. A possible oxidation state assignment would therefore be $\{[ONO^{sq\cdot}]Co^{III}(DMAP)_3\}^+$, which would be consistent to the surprisingly high MOS obtained in the solid-state. In addition, the presence of a ligand radical would explain the presence of the third reversible electron transfer event observed in cyclic voltammetry. However, the UV-visible spectra of the complex does not bear evidence of the $[ONO^{sq\cdot}]^{2-}$ ligand.

The spin density distribution in low- and high-spin $\{[ONO]Co(DMAP)_n\}^+$ (n = 2, 3) complexes raised further questions about the electrochemistry and EPR and electronic absorption spectroscopy of the complex. The EPR spectra obtained for the cationic complexes

at 77 K (**Figure 3.5**) bears resemblance to an EPR obtained from a cobalt-verdazyl complex, $[Co(dipyvd)_2]^{2+}$ (dipyvd = 1- -isopropyl-3,5-dipyridyl-6-oxoverdazyl), which exists as a S = 1/2 radical ligand bound to a low-spin Co(III) species in solution, but in the solid-state or at lower temperatures exhibits valence tautomerization to an S = 3/2 high-spin Co(II) species.[72] Valence tautomerization is not unexpected in $\{[ONO]Co(L)_n\}^m$ species (n = 1, 2, 3) (m = −1, 0, +1), as it is frequently observed in cobalt complexes with catecholate and amidophenolate motif ligands. However, the presence of a valence tautomer may not fully explain the rest of the experimental evidence.

The OCP of $\{[ONO]Co(DMAP)_n\}^+$ lies at −0.64 V compared to −0.92 V in $[ONO]Co(DMAP)_n$. The shift in OCP indicates that the isolated species is indeed the product of one-electron oxidation of $[ONO]Co(DMAP)_n$. It has also been established that the neutral complex undergoes an equilibrium between five- and six-coordinate species, and that addition of excess ligand drives the formation of a putative $[ONO]Co(DMAP)_3$ complex. It may be possible that one-electron oxidation of $[ONO^{sq\cdot}]Co(L)_3$ results in electron transfer directly from the metal center, leaving a ligand radical in the cationic complex $\{[ONO^{sq\cdot}]Co(L)_3\}^+$. There remains a second possibility that the $\{[ONO^{q}]Co(L)_3\}^+$ species formed from oxidation of the ligand in $[ONO]Co(L)_3$ may quickly tautomerize to $\{[ONO^{sq\cdot}]Co(L)_3\}^+$, effectively oxidizing the metal center as seen in the solid-state. This system would then undergo the third reversible and ligand-based oxidation at +0.09 V, producing a putative $\{[ONO^{q}]Co(L)_3\}^{2+}$ complex.

Taken together, the spin density distributions of the five- and six-coordinate cations and their spin isomers suggests that an S = 3/2 five-coordinate $\{[ONO^{q}]Co^{II}(DMAP)_2\}^+$ species is produced when $[ON(H)O]Co(DMAP)_2$ loses a proton and two electrons. However, the five-coordinate quinonate complex quickly undergoes intravalent charge transfer to produce the d^6 $\{[ONO^{sq\cdot}]Co^{III}(DMAP)_2\}^+$ cation, which is then stabilized by the addition of a sixth ligand

to generate the low-spin S = 1/2 $\{[ONO^{sq\cdot}]Co^{III}(DMAP)_3\}^+$ in accordance with the $\{[ONO^{sq\cdot}]Co^{III}(py)_3\}^+$ structural metrics. The temperature dependent changes in the EPR spectra may be indicative of these equilibria.

Oxidation of the neutral $[ONO]Co(DMAP)_2$ must also produce a five-coordinate complex of the general form $\{[ONO]Co(DMAP)_2\}^+$, but determining the locus of electron transfer is more difficult. A closer look at the neutral species was therefore warranted.

Ligand equilibria and spin-crossover in neutral $[ONO]Co(L)_n$ (n = 2, 3).

The $[ONO]Co(DMAP)_2$ complex exhibited all the experimental features of a ligand radical complex, with rich electronic absorption spectra and a MOS ~ −2. It was EPR silent, suggesting either an S = 0 or S = 1 spin state at both 298 and 77 K. Ligand association to form a $[ONO]Co(DMAP)_3$ species was also observed spectroscopically and electrochemically. A broad ^1H NMR spectra could be due to the presence of paramagnetic impurities, but the inconsistent chemical shifts may also be indicative of the ligand equilibrium in solution. Therefore singlet and triplet configurations were modeled for both the five- and six-coordinate species. However, only calculations for the five-coordinate complexes converged.

The five-coordinate complex that is implicated in PCET from $[ON(H)O]Co(DMAP)_2$ converged to S = 0 and S = 1 solutions, with the metal adopting a low-spin configuration with respect to the *d* valence electrons. The HOMO of the singlet complex (**Table 3.4**) is comprised of roughly 1/3 Co to 2/3 [ONO] contributions, and it is rigorously square planar in accordance with the solid-state structure. Adopting a triplet S = 1 configuration does not cause significant change in geometry, and the spin density is distributed across both metal and ligand, with 57% on Co and 38.3% on the [ONO] ligand (**Table 3.5**). Both electronic configurations are therefore plausible based on the experimental evidence.

Theoretically, removal of a proton and electron from the $[ON(H)O]^{2-}$ ligand should produce a trigonal bipyramidal complex with the $[ONO^{sq\cdot}]^{2-}$ ligand coordinated to a high-spin d^7 Co(II); antiferromagnetic coupling with the ligand would result in an S = 1 overall spin state. In contrast, multi-site PCET, wherein the H^+ is supplied by the ligand and an electron is supplied by the metal, should produce an $[ONO^{cat}]^{3-}$ ligand bound to a Co(III) ion with two unpaired spins. While electronic absorption spectroscopy was not an adequate method to quantitatively measure HAT equilibrium concentrations of $[ON(H)O]Co(DMAP)_2$ and TEMPO·, it at least suggests that a product with the $[ONO^{sq\cdot}]^{2-}$ ligand is produced quickly at room temperature. However, both $[ONO^{cat}]Co^{III}(DMAP)_2$ and $[ONO^{sq}]Co^{II}(DMAP)_2$ may then undergo valence tautomerization to yield the observed square-pyramidal complexes with $[ONO^{sq\cdot}]^{2-}$ features. Computational evidence simply indicates that in the square-pyramidal geometry, the singlet and triplet complexes both exhibit substantial mixing between metal and ligand orbitals.

Formal oxidation state assignments are useful in predicting reactivity in many transition metal complexes that contain redox-active ligands, but from the extensive mixing of metal- and ligand-orbitals in $[ONO]Co(DMAP)_2$, it is difficult to conclude whether redox activity originates from one fragment or the other.

Spin density distributions in monoanionic $\{[ONO]Co(DMAP)_n\}^-$ (n = 1, 2)

Spin-crossover isomers of S = 1/2 and S = 3/2 were investigated for the anionic and cationic complexes, and it was immediately clear that reduction from the neutral five-coordinate $[ONO]Co(DMAP)_2$ induced significant perturbations on the Co–[ONO] system. The spin density on the metal dropped minimally from 98% to 86% upon spin-crossover from S = 1/2 to S = 3/2 in the $\{[ONO]Co(DMAP)_2\}^-$ complex (**Table 3.4**), but the change in spin state

resulted in a dramatic change in computed bond angles, approaching an almost trigonal bipyramidal geometry. The geometric and electronic resemblance between the S = 3/2 anion and the protonated [ON(H)O]Co(DMAP)$_2$ was difficult to ignore. The [ON(H)O]Co(DMAP)$_2$ complex converged to a high-spin S = 3/2 configuration with spin density distributions across the metal and ligand that were similar to the S = 3/2 monoanion. This may suggest that a high-spin, S = 3/2 trigonal bipyramidal anion is the species produced when [ON(H)O]Co(DMAP)$_2$ loses a proton.

In the low-spin S = 1/2 {[ONO]Co(DMAP)$_2$}$^-$ anion, more than 90% of the spin density lies on the metal center, and the geometry is rigorously square pyramidal. This complex was then compared to the S = 1/2 square-planar {[ONO]Co(DMAP)}$^-$ that was characterized in the solid-state. Calculations on four-coordinate species placed 99% of the spin density on the metal once again. These computational results are consistent with the UV-visible spectrum obtained for the anionic complex, which lacks visible [ONO$^{sq\cdot}$]$^{2-}$ features. While some spin density may be delocalized across the [ONO] ligand backbone when S = 3/2 in these complexes, there is no strong evidence to support valence tautomerization between Co^{II}/[ONO^{cat}] and Co^{I}/[ONO$^{sq\cdot}$] in solution. The weak isotropic EPR signal obtained for the monoanionic complex at 298 K was also not typical of a high-spin cobalt system, which often give spectra at much higher g values.

It is hypothesized that upon deprotonation of [ON(H)O]Co(DMAP)$_2$, the high-spin S = 3/2 {[ONO^{cat}]Co^{II}(DMAP)$_2$}$^-$ complex undergoes spin-crossover to low-spin S = 1/2 {[ONO^{cat}]Co^{II}(DMAP)}$^-$, which is substitutionally labile and in equilibrium with the anion observed in the solid-state and ESI-MS. The isolated species in **Figure 3.1** therefore may be described as a {[ONO^{cat}]Co^{II}(DMAP)}$^-$ anion. Likewise, reduction of the neutral [ONO]Co(DMAP)$_2$ may produce the low-spin five-coordinate {[ONO^{cat}]Co^{II}(DMAP)$_2$} species.

3.4. Conclusions.

The redox- and proton-active $[ON(H)O]^{2-}$ ligand was studied for its ability to perform PCET reactivity in a series of Co complexes. Several new complexes of the general form $\{[ONO]Co(L)_n\}^m$ (L = DMAP, py) (n = 1, 2, 3) (m = −1, 0, +1) were synthesized and characterized. While the $[ON(H)O]Co(DMAP)_2$ complex is well-described by a $[ON(H)O]^{2-}$ ligand coordinated to a high-spin Co(II), d^7 metal ion in a trigonal bipyramidal geometry, deprotonation and oxidation of this metal-ligand system appears to generate a host of valence tautomers, which then can undergo spin-crossover and adopt new geometries. Computational models of the five-coordinate anion, neutral, and oxidized species support the experimentally observed ligand lability and temperature-induced electronic changes.

Previous studies of [EN(H)E] ligands on late transition metals suggest that both the proton and electron originate from ligand-based orbitals; however, in the case of [ONO]–Co, it is difficult to say whether it is the ligand or metal that is oxidized. EPR data collected on the $\{[ONO]Co(L)_n\}^+$ (L = DMAP, py; n = 2, 3) species suggest that a ligand radical is present in each complex, but temperature-dependence of the g_{eff} factors indicates possible valence-tautomeric behavior. While it is not possible in this study to discern whether initial electron transfer occurs on metal or ligand, it is apparent that small changes in the electronic structure of the metal-ligand system overall induces changes in the coordination environment of the metal ion.

The measurable equilibria of spectator ligands can obscure the thermodynamic measurement of both PCET and the individual PC and ET steps that occur in a redox- and proton-active ligand complex. However, an estimate of the ligand-based N–H BDFE and hydricity was obtained, placing the BDFE of $[ON(H)O]Co(DMAP)_2$ *ca.* 59.8 kcal mol^{-1} and its pK_a between 28.1 and 33.1 in acetonitrile. Compared to other systems in which protons and reducing equivalents are sourced from a ligand, rather than a metal ion or from disparate

sites, $[ON(H)O]^{2-}$ is both a very weak acid and a potent reductant. Though this new Co(II) species is somewhat more basic and more reducing than our previously reported nickel (II) system, $[ON(H)O]Ni(PPh_3)$, their BDFEs seem to fall within ~ 5 kcal mol^{-1} of one another. Both systems, as well as the similar dithiolate complexes $[SN(H)S]Ni(PPh_3)$ (BDFE = 62.4 kcal mol^{-1}) and $[SN(H)S]Co(DMAP)_2$ (BDFE $\leq$ 65 kcal mol^{-1}) exhibit HAT reactivity that is more in line with traditional metal hydride complexes than what is usually seen in ligand-based or multi-site HAT systems.

It is apparent that judicious ligand design is necessary to mitigate the geometric and electronic rearrangements that may happen upon oxidation or reduction of the complex overall. The apparent stability of the five-coordinate $[ON(H)O]Co(L)_2$ congener suggests that a multidentate redox- and proton-active ligand with coordinatively fluxional arms may be able to stabilize both the protonated species as well as the products of deprotonation, and H-atom and hydride transfer, without the need for excess ligand in solution.

3.5. Experimental.

General considerations. All manipulations were carried out using standard Schlenk-line techniques or in a dry nitrogen glovebox, except where noted. Trifluoroacetic acid, concentrated ammonium hydroxide, and water were purged of dioxygen with a vigorous nitrogen stream (>1hr) before use in the synthesis of the $[ONO]H_3$ ligand. Hydrocarbon and ethereal solvents were sparged with argon and passed through activated Q5 and alumina Columns to remove dioxygen and water, as confirmed by dropwise addition of a solution of sodium benzophenone ketyl radical in THF. Such solvents were stored over activated molecular sieves in the glovebox. Cobalt (II) chloride (anhydrous), 4-dimethylaminopyridine, and 2.2.2-cryptand were used as-received from Sigma. Potassium hydride was obtained in mineral oil and washed with pentane prior to use. Pyridine was dried and distilled prior to use. Tetrabutylammonium hexafluorophosphate ($\{Bu_4N\}\{PF_6\}$) (Acros) was recrystallized from ethanol three times and dried under vacuum before use. Ferrocene and decamethylcobaltocene (Acros) were purified by vacuum sublimation.

Spectroscopic and electronic characterization. All NMR spectroscopy was performed on a Bruker Avance 400, 500, or 600 MHz spectrometer. ^1H spectra were referenced to residual proteo impurities of the solvents used (1.94 ppm, CD_3CN). Electronic absorption spectra were recorded using a Jasco V-670 absorption spectrometer using 10 mm quartz cuvettes at ambient temperatures, or on a Perkin-Elmer Lambda 800 UV/vis spectrophotometer in 1 cm path length cells at 25 °C. Electrospray ionization mass spectrometry (ESI-MS) was performed on a Waters LCT Premier mass spectrometer using dry, degassed toluene.

Cyclic voltammetry and differential pulse voltammetry experiments were performed on a Gamry G300 potentiostat/galvanostat/Zero Resistance Ammeter (Gamry Instruments, Warminster, PA) using a 3.0 mm glassy carbon working electrode, a platinum wire counter electrode, and a silver wire pseudo-reference electrode. Experiments were performed at ambient temperature in a dry nitrogen glovebox with 1 mM analyte and 100 mM $\{Bu_4N\}\{PF_6\}$ supporting electrolyte. All potentials have been referenced to $[FeCp_2]^{+/0}$ using ferrocene as an internal standard.

Crystallographic measurements. X-ray diffraction was performed on single crystals coated in Paratone oil and mounted on glass fibers. Data was acquired using a Bruker SMART APEX II diffractometer equipped with a CCD detector. A full sphere of data was collected for each crystal structure, and measurements were carried out using Mo Kα (λ = 0.71073 Å) radiation, which was wavelength selected with a single-crystal graphite monochromator. The SMART program package was used to determine unit-cell parameter and to collect data. The raw frame data were processed using SAINT36 and SADABS37 to yield the reflection data files. Subsequent calculations were carried out using the SHELXTL38 program suite. Structures were solved by direct methods and refined on F2 by full-matrix least-squares techniques to convergence. Analytical scattering factors for neutral atoms were used throughout the analyses.39 Hydrogen atoms, though visible in the difference Fourier map, were generated at calculated positions and their positions refined using the riding model. ORTEP diagrams were generated using ORTEP-3 for Windows. Bond distances used for metrical oxidation state analysis were extracted in Mercury for Windows.

Table 3.5. X-ray diffraction data collection and refinement parameters for [ON(H)O]Co(DMAP)$_2$, {K(2.2.2.-crypt)}{[ONO]Co(DMAP)}, [ONO]Co(DMAP)$_2$, [ONO]Co(py)$_2$, {[ONO]Co(py)$_3$}{PF_6}.

Complex	[ON(H)O]Co(DMAP)$_2$	{K(2.2.2.-crypt)}{[ONO]Co(DMAP)}	[ONO]Co(DMAP)$_2$	[ONO]Co(py)$_2$	{[ONO]Co(py)$_3$}{PF_6}
empirical form.	$C_{42}H_{61}CoN_5O_2$	$C_{53}H_{86}CoKN_5O_8$	$C_{42}H_{60}CoN_5O_2 \cdot 0.05(C_2H_3N)$	$C_{38}H_{50}CoN_3O_2 \cdot C_4H_8O$	$C_{57}H_{71}CoF_6N_4O_2P$
form. weight	726.88	1019.29	727.93	711.84	1048.08
crystal system	Monoclinic	Triclinic	Monoclinic	Monoclinic	Triclinic
space group	$P2_1/n$	P-1	$C2/c$	$P2_1/c$	P-1
T(K)	83(2)	93(2)	93(2)	143(2)	143(2)
a /Å	9.2728(4)	13.2318(4)	33.2477(11)	18.1528(11)	10.0465(6)
b /Å	20.0858(9)	19.5209(6)	10.5364(4)	28.2351(17)	16.9324(10)
c /Å	22.0694(9)	21.9215(7)	25.4948(9)	15.2540(9)	17.4104(10)
α /deg	90	91.1688(5)	90	90	74.7020(10)
β /deg	95.1108(6)	94.8071(6)	108.1905(18)	91.0390(10)	73.6470(10)
γ /deg	90	98.2485(5)	90	90	79.3910(10)
V /Å^3	4094.1(3)	5580.9(3)	8484.8(5)	7817.1(8)	2721.8(3)
Z	4	4	8	8	2
refl. collected	46643	127751	85493	88532	31185
indep. Refl.	9047	27709	7847	17231	11895
R1 ($I > 2\sigma$)[a]	0.0366	0.0448	0.0362	0.0434	0.0463
wR2 (all data)[b]	0.0917	0.1165	0.0882	0.1144	0.1232
GOF	1.017	1.029	1.040	1.020	1.029

[a] $R1 = \Sigma||F_o| - |F_c||/\Sigma|F_o|$; [b] $wR2 = [\Sigma[w(F_o^2 - F_c^2)^2]/\Sigma[w(F_o^2)^2]]^{1/2}$

Spectrophotometric titrations. Stock solutions were prepared in the glovebox by dissolving solid reagents in dry, spectroscopy-grade (sieve-free) acetonitrile and diluting to 10 mL in volumetric flasks. Stock solutions were stirred until homogenous (approx. 2 hours) and no solids were visible. To prepare a typical sample, ~2 mL of acetonitrile was added to a 5mL volumetric flask, followed by the appropriate aliquot of [Co] solution via a microliter syringe. Other reagents were added via separate microliter syringes when required. Then, the sample was diluted to the line with acetonitrile. Color changes associated with successful reactions were usually immediate. Samples were transferred to 25 mL scintillation vials equipped with stir bars and allowed to equilibrate for ~ 1 hr before being transferred to quartz cuvettes. Samples were then removed from the glovebox and brought to the spectrometer. Titrations were performed at least three times per concentration data point. Syringes for each reagent were rinsed three times with acetonitrile between samples to avoid dilution or contamination.

Electrochemical titrations. A 10 mL solution of [Co] analyte was prepared similarly to above, with added electrolyte, and allowed to stir for ~ 30 min before the experiment began. The open circuit potential and full window scans were performed first. Stock solutions of other reagents were prepared in the same manner and contained electrolyte to avoid dilution during the experiment. Aliquots were added to the electrochemical cell through holes in the top, then stirred ~ 1 minute, stopped, and allowed to fall still before cyclic voltammograms were taken. Ferrocene was added after titration was completed, and then scan rate dependence scans were performed.

^{1}H NMR titrations. Stock solutions of [Co], hexamethylbenzene, and TEMPO· were prepared similarly to above using dried CD_3CN. An aliquot of [Co] was added via microliter syringe to a 25 mL scintillation vial equipped with a stir bar, followed by an aliquot of TEMPO·, then hexamethylbenzene. The difference in CD_3CN was added to reach a total of 0.75 mL. The samples were allowed to stir for ~1 hr. Then 0.5 mL of each sample was added

to an NMR tube *via* fresh 1 mL syringes. NMR samples were taken immediately from the glovebox to the NMR spectrometer.

Synthesis of [ONO]Co(L)$_n$ complexes.

[ONO]H$_3$ was synthesized via a modified literature procedure. No water was added to the reaction at any point. **^{1}H NMR (400 MHz, CD$_3$CN):** 7.015 (d, 2H, aryl-H, J = 2.308 Hz), 6.71 (d, 2H, aryl-H, J = 2.308 Hz), 6.01 (s, 2H, -OH), 5.57 (s, 1H, -NH), 1.42 (s, 18H, -tBu), 1.20 (s, 18H, -tbu).

[ONO]Co(DMAP)$_2$. *From $CoCl_2$:* First, a clear green solution of [ONO]H$_3$ (342 mg, 0.803 mmol, 1 equiv.) in 30 mL of diethyl ether was frozen in a nitrogen coldwell, then combined with a frozen slurry of KH (96 mg, 1.147 mmol, 3 equiv.) in diethyl ether. The reaction was stirred for approximately 1 hour, when effervescence ceased and no solid KH was visible in the clear yellow solution. The reaction was then frozen, and PhI(OAc)$_2$ (129 mg, 0.400 mmol, 0.5 equiv.) was added, resulting in an immediate color change to dark green. The reaction was stirred for 2 hours, while $CoCl_2$(DMAP)$_2$ was prepared. In a separate 25 mL scintillation vial, DMAP (195 mg, 1.60 mmol, 2 equiv.) was added to as suspension of $CoCl_2$ (106 mg, 0.803 mmol, 1 equiv.) in diethyl ether. The suspension was stirred at room temperature for 2 hours until it became the characteristic neon blue of $CoCl_2$(DMAP)$_2$, at which point it was added to the cooled solution of [ONO$^{sq\cdot}$]K$_2$. The solution became blue-black and was allowed to stir for 3 days. The solvent was removed under vacuum and the dark residue was redissolved in toluene, filtered through celite, and washed with pentane. The filtrate was triturated with pentane until a blue-black solid was obtained. This solid was then redissolved in a 2:1 mixture of THF and pentane and stored at −35°C overnight. The product was isolated as a blue-black microcrystalline solid via filtration (359 mg, 70% yield). X-ray quality crystals were grown from a solution of THF layered beneath pentane and allowed to

diffuse at −35°C overnight. **^{1}H NMR (400 MHz, C_6D_6):** 9.28 (br s, 2H, DMAP aryl-H), 6.24 (br s, 4H, DMAP aryl-H), 2.89 (br s, DMAP N-CH_3), 2.43 (br s, 18H, -tBu), 1.63 (br s, 18H, -tBu). **MS (ESI+) (MeCN) m/z:** 725.2 (M+) (100%), 847.4 (M+DMAP) (95%). **Anal. Calcd (Found) for $C_{42}H_{60}N_5O_2Co \cdot \frac{1}{2}C_5H_{12}$ (%):** C, 70.14 (70.03); H, 8.73 (8.67); N, 9.19 (9.19). **UV-Vis (MeCN) λ_{max}/nm (ε $M^{-1}cm^{-1}$):** 355 (11,399), 478 (sh, 2,419), 631 (3,957).

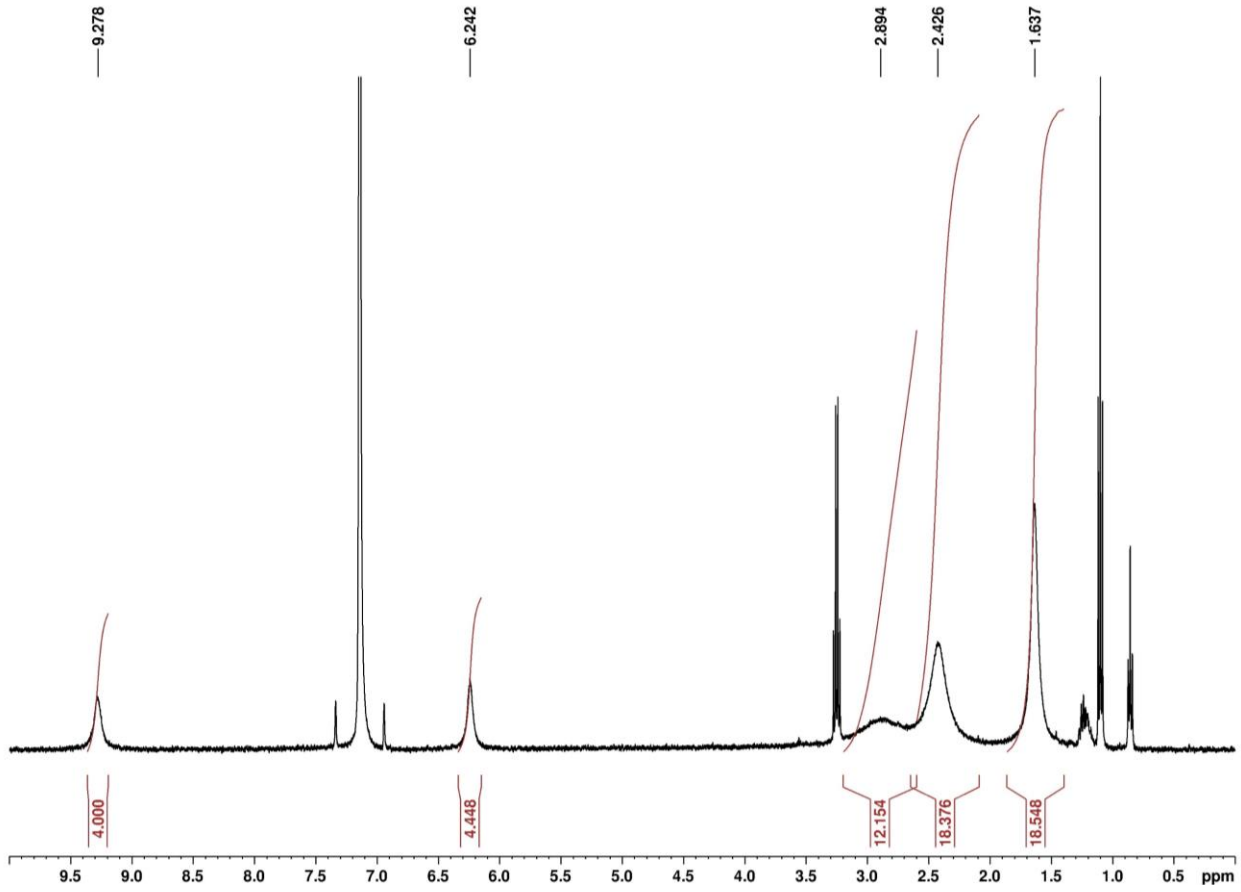

Figure 3.11. ^{1}H NMR of [ONO]Co(DMAP)$_n$ in C_6D_6 at 298 K, 400 MHz.

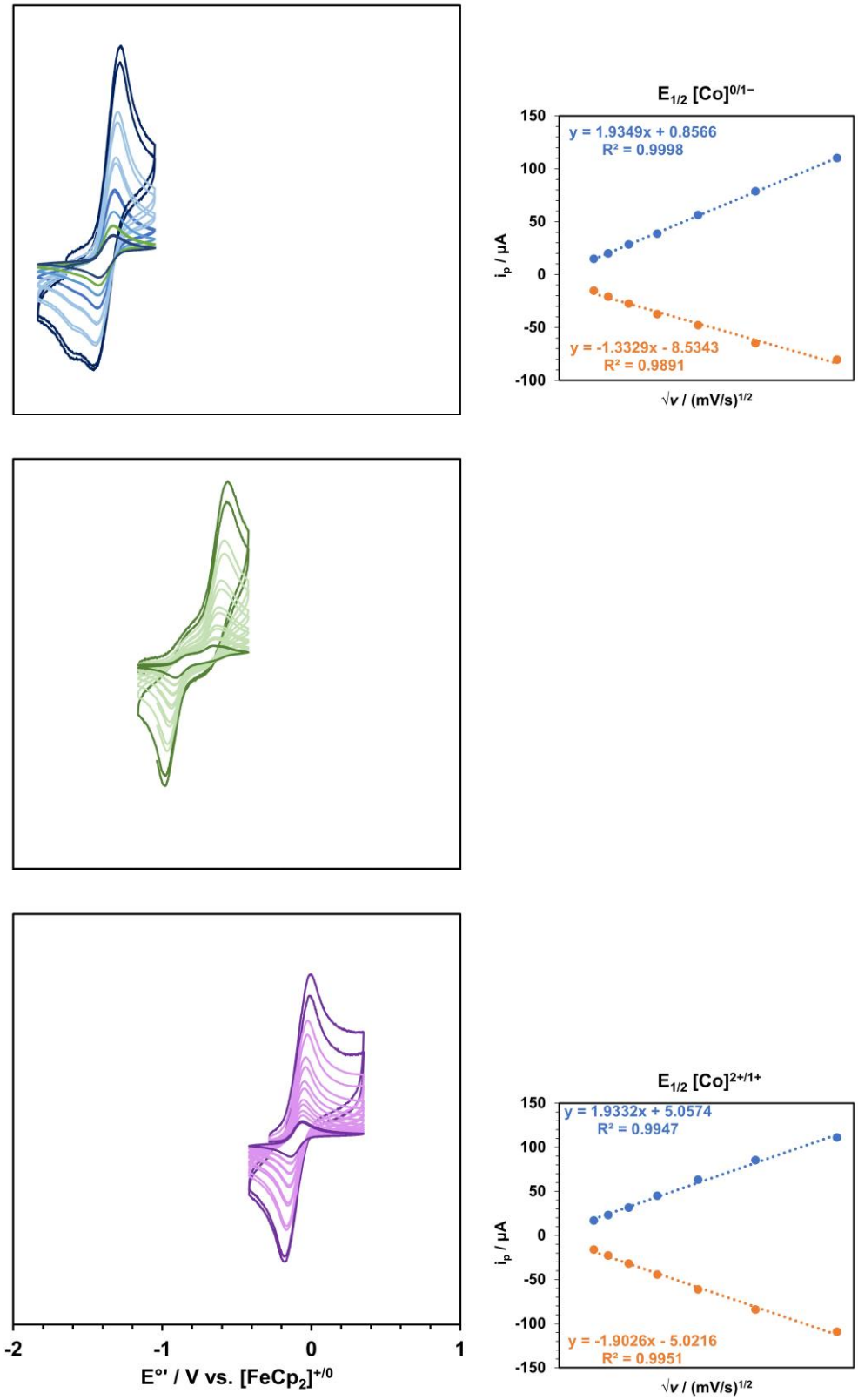

Figure 3.12. Scan rate dependence for putative ligand-based redox events in [ONO]Co(DMAP)$_2$.

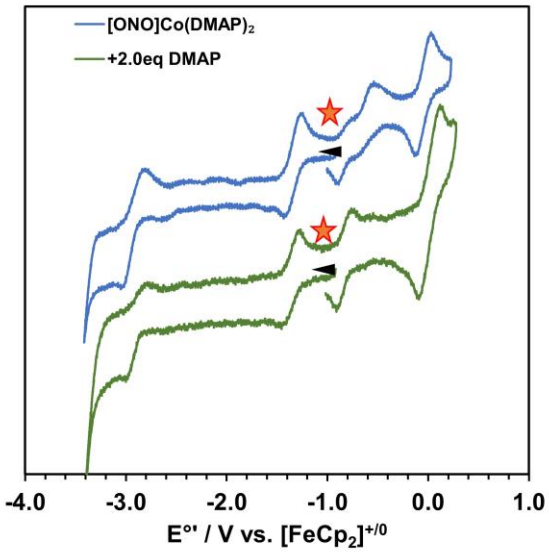

Figure 3.13. Cyclic voltammograms taken at 100 mV/s in acetonitrile of [ONO]Co(DMAP)n before (blue trace) and after (green trace) addition of 2.0 equivalents of excess DMAP.

[ON(H)O]Co(DMAP)$_2$. This synthesis proceeds faster (overnight) in THF, but yields and purity are improved when performed in diethyl ether. Pale purple [ONO]H$_3$ (399 mg, 1 equiv.) was dissolved in ~100mL of diethyl ether in a 250 mL round-bottom flask to yield a green solution, then frozen in a nitrogen coldwell. A suspension of KH (75 mg, 2 equiv.) was

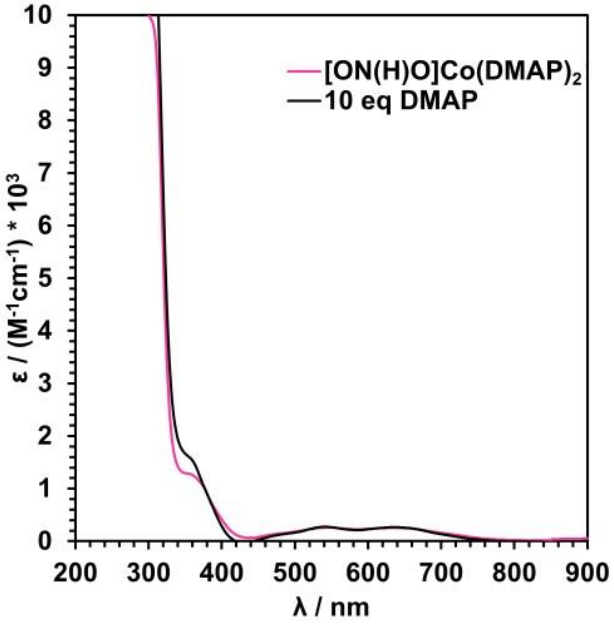

Figure 3.14. Electronic absorption spectra in acetonitrile of [ON(H)O]Co(DMAP)$_2$ in the absence and presence of 10 equivalents of DMAP.

also frozen, then combined with the [ONO]H_3 and allowed to warm to room temperature. The reaction was stirred for approximately 2 hours, when effervescence ceased and a clear yellow solution was obtained. Solid $CoCl_2(DMAP)_2$ (350 mg, 1 equiv.) was added, resulting in a red-purple solution, and the reaction was stirred until the product had precipitated as a bright pink solid and no neon blue $CoCl_2(DMAP)_2$ was visible (approx. 3 days). The reaction was filtered through a porous glass frit, resulting in a mixture of purple and pink solids and a brown filtrate. The filtrate was discarded, and the pink [ON(H)O]$Co(DMAP)_2$ was extracted from what $CoCl_2(DMAP)_2$ remained with several aliquots of toluene. The solvent was then removed under vacuum to result in a neon pink solid (588 mg, 98% yield). Crystals of X-ray quality were obtained from a saturated solution in MeCN stored at −35°C overnight. **MS (ESI+) (MeCN) m/z =** 725.2 (M). **UV-Vis (MeCN) λ_{max}/nm (ε $M^{-1}cm^{-1}$):** 364 (sh, 991), 575 (br).

{K}{[ONO]Co(DMAP)$_2$}. Solid [ONO]H_3 (109.4 mg, 0.2570 mmol, 1 equiv.) was dissolved in ~100 mL of diethyl ether in a 250 mL round-bottom flask, then frozen in a nitrogen coldwell. A suspension of KH (30.9 mg, 0.771 mmol, 3 equiv,) was also frozen, then

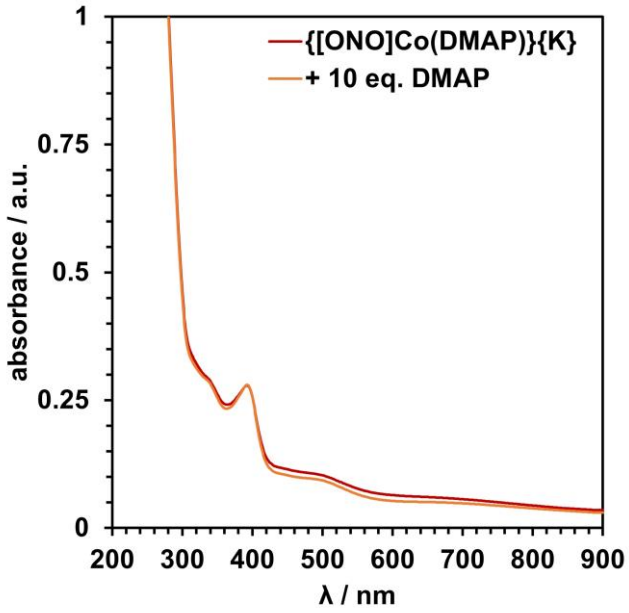

Figure 3.15. Electronic absorption spectra in acetonitrile of {K}{[ONO]Co(DMAP)} in the absence and presence of 10 equivalents of DMAP.

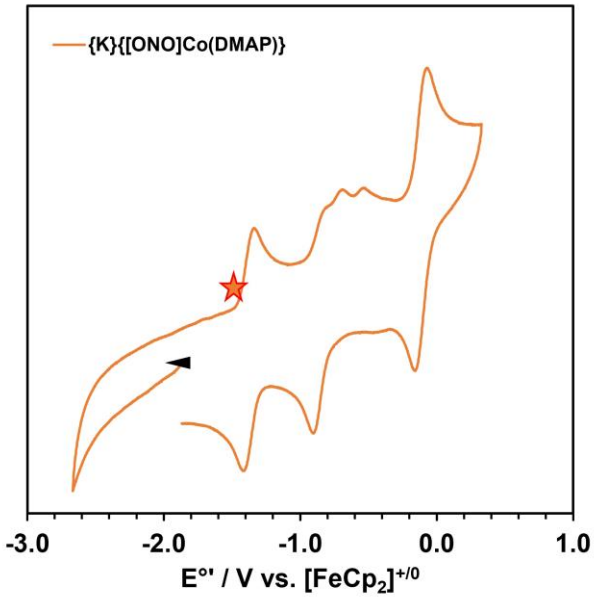

Figure 3.16. Cyclic voltammogram of {K}{[ONO]Co(DMAP)} dissolved in acetonitrile, recorded at 100 mV/s. Star indicates open circuit potential determined by a separate measurement, and arrow indicates scan direction.

added to [ONO]H_3 and stirred as a slurry for approximately 2 hours. The reaction was stirred for 2 hours, while $CoCl_2(DMAP)_2$ was prepared. In a separate 25 mL scintillation vial, DMAP (62.8 mg, 0.514 mmol, 2 equiv.) was added to as suspension of $CoCl_2$ (33.0 mg, 0.250 mmol, 1 equiv.) in diethyl ether. The suspension was stirred at room temperature for 2 hours until it became the characteristic neon blue of $CoCl_2(DMAP)_2$ and the excess DMAP was fully dissolved. It was then added to a frozen solution of [ONO]K_3 and the reaction immediately turned yellow-brown. The reaction was allowed to stir for 2 days until no unreacted $CoCl_2(DMAP)_2$ was visible. After filtration through a plug of celite on a porous glass frit, the filtrate was triturated with pentane to afford a dark brown powder. The solids were redissolved in ether and a few drops of THF and stored at −35°C overnight to crash out unreacted DMAP as white crystals. The complex itself was collected as a red-orange powder over two crops from saturated solutions in ether stored at −35°C overnight (151.1 mg, 92% yield for the four-coordinate complex). Crystals of the complex were obtained from a saturated solution in 2:1 ether:THF with 2.2.2.-cryptand added to sequester the potassium

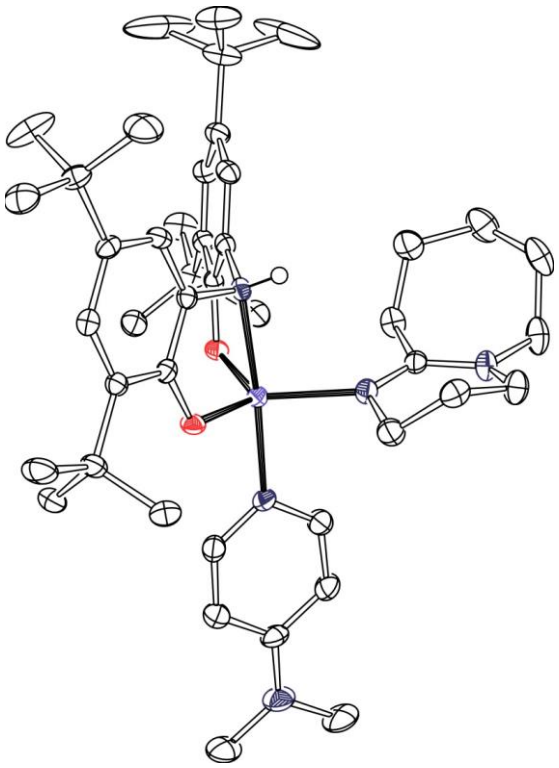

Figure 3.17. ORTEP diagram of [ON(H)O]Co(DMAP)(DBU). Hydrogen atoms, counter ions, chelating agents, and solvent molecules have been omitted for clarity.

counterion. **MS (ESI+) (MeCN) m/z:** 765 (M-K) (90%), 847 (M-K-2MeCN) (90%). **UV-Vis (MeCN) λ_{max}/nm (ε $M^{-1}cm^{-1}$):** 393 (5,419), 505 (sh, 2,037)

[ON(H)O]Co(DBU)(DMAP). DBU (20 µL, 1.8 equiv.) was added via syringe to a deep pink-red MeCN solution of [ON(H)O]Co(DMAP)$_2$. The solution was stirred for 24 hours at room temperature resulting in a purple-blue solution. When stirring ceased, visible pink, block-shaped crystals of the product began to form. These were suitable for X-ray diffraction.

{[ONO]Co(DMAP)$_n$}{PF_6}. To a solution of [ONO]Co(DMAP)$_3$ (456 mg, 0.714 mmol, 1 equiv.) and DMAP (175 mg, 1.434 mmol 2 equiv.) in ether $AgPF_6$ (182 mg, 0.719 mmol, 1 equiv.) was added, resulting in a color change from green/blue to purple. After stirring overnight, the solution was filtered through celite and solvent was removed under vacuum. The residue was co-evaporated with Et_2O, yielding 407 mg of crude product (57 % yield). **UV-**

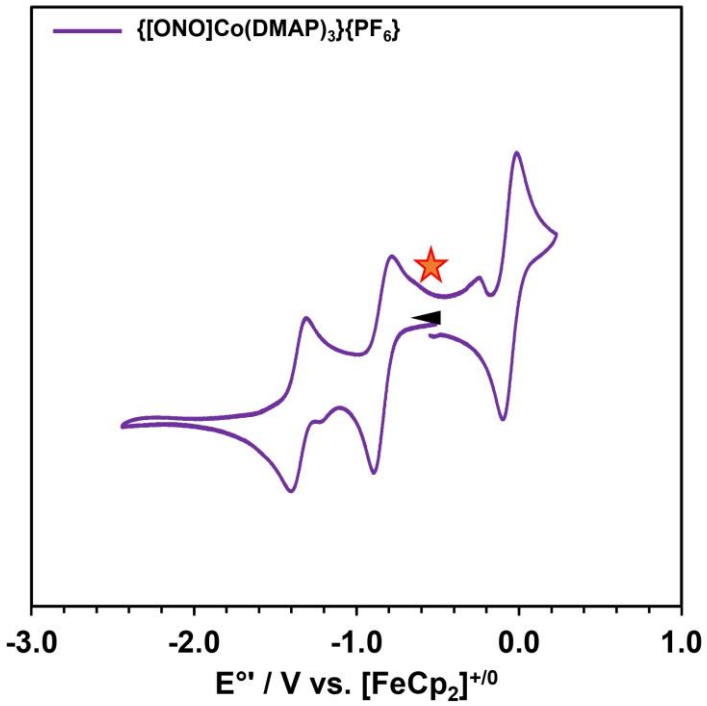

Figure 3.18. Cyclic voltammogram of {[ONO]Co(DMAP)$_3$}{PF_6} dissolved in acetonitrile, recorded at 100 mV/s. Star indicates open circuit potential determined by a separate measurement, and arrow indicates scan direction.

Vis (MeCN) λ_{max}/nm (ε $M^{-1}cm^{-1}$): 392 (5,862), 374 (4,625), 444 (sh, 1,269), 519 (1,396), 681 (1,323), 1023 (sh, 942).

[ONO]Co(py)$_2$. A mixture of [ONO]H_3 (1.18 g, 2.77 mmol, 1 equiv.) and KH (334 mg, 8.32 mmol, 3 equiv.) was stirred in THF at room temperature until the mixture became a yellow solution with a suspension of KH and bubbling had ceased. This mixture was partially frozen, and $PhI(OAc)_2$ (447 mg, 1.39 mmol, 0.5 equiv.) was added. The resultant green/black mixture was stirred at room temperature for 2 hours and subsequently cooled again. Separately, pyridine (450 µL, 5.58 mmol, 2 equiv.) was added to a suspension of $CoCl_2$ (360 mg, 2.77 mmol, 1 equiv.) in THF (20 mL). This suspension was stirred at room temperature for 2 hours during which time the purple $CoCl_2(py)_2$ precipitated from solution. This suspension was cooled and the cooled [ONO]K_2 mixture was added. The resultant dark green/black mixture was stirred at room temperature an additional 4 hours and then the

solvent was removed under vacuum. The residue was extracted with toluene (4 x 25 mL). Solvent was removed under vacuum. About 10 mL of pentane was added to the residue and stored at −35°C for 3 hours. The brown supernatant was removed by pipette and rinsed with 10 mL more of cold pentane. The solids were dried under vacuum to yield the product as a microcrystalline green/black solid as the mono-toluene adduct (1.70 g, 84% yield). Microcrystalline samples of the mono-THF solvate could be isolated by recrystallization from a mixture of saturated THF and pentane at −35°C. Either of these solids (thought to be outer-sphere co-crystallization materials) could be used in subsequent reactions. X-ray quality crystals were grown from a THF/pentane solution at −35°C.

{[ONO]Co(py)$_3$}{PF$_6$}. To a solution of [ONO]Co(py)$_2$ (200 mg, 0.282 mmol, 1 equiv.) and pyridine (115 µL, 1.42 mol, 5 equiv.) in THF, was added $AgPF_6$ (71.2 mg, 0.282 mmol, 1 equiv.), resulting in a color change from green/black to brown. After stirring overnight, the solution was filtered and solvent was removed under vacuum. The residue was co-evaporated with Et_2O and then pentane, yielding 222 mg of crude product. The crude product was recrystallized from layering THF solutions under pentane and allowing them to diffuse at room temperature, followed by cooling to –35°C, yielding 171 mg of the product as fine hairs over two crops (70%). X-ray quality crystals were grown by layering a toluene on a THF solution and allowing them to diffuse at room temperature overnight. **UV-Vis (MeCN) λ_{max}/nm (ε M^{-1}cm^{-1}):** 387 (3,352), 434 (4,685), 527 (2,447), 729 (6,269), 804 (6,838).

3.6. References.

1. Thomas-Colwell, J.; Arvin Sookezian; Kurtz, D. A.; Kallick, J.; Henling, L. M.; Stich, T. A.; Hill, M. D.; Hunter, B. M. Tuning Cobalt(II) Phosphine Complexes to Be Axially Ambivalent. **2022**, *61* (32), 12625–12634. *Inorg. Chem.* **2022,** *61*, 12625−12634
2. Lee, B.; Pabst, T. P.; Hierlmeier, G.; Chirik, P. J. Exploring the Effect of Pincer Rigidity on Oxidative Addition Reactions with Cobalt(I) Complexes. *Organometallics* **2023**, *42* (8), 708–718.
3. Gural'skiy, I. A.; Shylin, S.; Ksenofontov, V.; Tremel, W. Spin-State-Dependent Redox-Catalytic Activity of a Switchable Iron(II) Complex. *Eur. J. Inorg. Chem.* **2017,** *24,* 3125-3131.
4. Safaei, E.; Balaghi, S. E.; Chiang, L.; Clarke, R. M.; Martelino, D.; Webb, M. I.; Wong, E. W. Y.; Savard, D.; Walsby, C. J.; Storr, T. Stabilization of Different Redox Levels of a Tridentate Benzoxazole Amidophenoxide Ligand When Bound to Co(III) or V(V). *Dalton Trans.* **2019**, *48* (35), 13326–13336.
5. Harris, C. F.; Bayless, M.; Leest, van; Bruch, Q. J.; Livesay, B. N.; Bacsa, J.; Hardcastle, K. I.; Shores, M. P.; Bas de Bruin; Soper, J. D. Redox-Active Bis(Phenolate) N-Heterocyclic Carbene [OCO] Pincer Ligands Support Cobalt Electron Transfer Series Spanning Four Oxidation States. *Inorg. Chem.* **2017**, *56* (20), 12421–12435.
6. Lohmeyer, L.; Kaifer, E.; Enders, M.; Himmel, H. Switching from Metal- to Ligand-Based Oxidation in Cobalt Complexes with Redox-Active Bisguanidine Ligands. *Chem. Eur. J.* **2021**, *27* (46), 11852–11867.
7. Bill, E.; Bothe, E.; Chaudhuri, P.; Chlopek, K.; Herebian, D.; Kokatam, S.; Ray, K.; Weyhermüller, T.; Neese, F.; Wieghardt, K. Molecular and Electronic Structure of Four- and Five-Coordinate Cobalt Complexes Containing Two o-Phenylenediamine- or Two o-Aminophenol-Type Ligands at Various Oxidation Levels: An Experimental, Density Functional, and Correlated Ab Initio Study. *Chem. Eur. J.* **2004**, *11* (1), 204–224.
8. Bowman, A. C.; Carsten Milsmann; Bill, E.; Lobkovsky, E. B.; Weyhermüller, T.; Wieghardt, K.; Chirik, P. J. Reduced *N*-Alkyl Substituted Bis(Imino)Pyridine Cobalt Complexes: Molecular and Electronic Structures for Compounds Varying by Three Oxidation States. *Inorg. Chem.* **2010**, *49* (13), 6110–6123.
9. Sproules, S.; Kapre, R. R.; Roy, N.; Weyhermüller, T.; Wieghardt, K. The Molecular and Electronic Structures of Monomeric Cobalt Complexes Containing Redox Noninnocent O-Aminobenzenethiolate Ligands. *Inorganica Chim. Acta* **2010**, *363* (12), 2702–2714.
10. Alig, L.; Fritz, M.; Schneider, S. First-Row Transition Metal (De)Hydrogenation Catalysis Based on Functional Pincer Ligands. *Chem. Rev.* **2019**, *119* (4), 2681–2751
11. Pierpont, C.G. Studies on charge distribution and valence tautomerism in transition metal complexes of catecholate and semiquinonate ligands. *Coord. Chem. Rev.* **2001,** *216-217,* 99-125.

12. Stouffer, R. C.; Hadley, W. B.; Busch, D. H. Unusual magnetic properties of some six-coordinate cobalt(II) complexes – electronic isomers. *J. Am. Chem. Soc.* **1961**, 83, 3732-3724.
13. McNamara, W.; Han, Z.; Alperin, P. J.; Brennessel, W. W.; Holland, P. L.; Eisenberg, R. A Cobalt–Dithiolene Complex for the Photocatalytic and Electrocatalytic Reduction of Protons. **2011**, *133* (39), 15368–15371.
14. Storr, T.; Mukherjee, R. Preface for the Forum on Applications of Metal Complexes with Ligand-Centered Radicals. *Inorg. Chem.* **2018,** *57* (16), 9577-9579
15. Berning, D.E.; Noll, B. C.; Dubois, D.L. Relative Hydride, Proton, and Hydrogen Atom Transfer Abilities of $[HM(diphosphine)_2]PF_6$ Complexes (M = Pt, Ni). *J. Am. Chem. Soc.* **1999,** *121* (49), 11432-11447.
16. Semproni, S. P.; Atienza, C. C. H.; Chirik, P. J. Oxidative Addition and C–H Activation Chemistry with a PNP Pincer-Ligated Cobalt Complex. *Chemical Science* **2014**, *5* (5), 1956–1960.
17. Schevick, S.L.; Wilson, C.V. Kotesova, S.; Kim, D.; Holland, P.L.; Shenvi, R.A. Catalytic hydrogen atom transfer to alkenes: a roadmap for metal hydrides and radicals. *Chem. Sci.* **2020,** *11* (46), 12401-12422.
18. Bourrez, M.; Steinmetz, R.; Ott, S.; Gloaguen, F.; Hammarström, L. Concerted proton-coupled electron transfer from a metal-hydride complex. *Nature Chem.* **2015,** *7,* 140-145.\
19. Quist, D.A.; Ehudin, M.E.; Schaefer, A.W.; Schneider, G.L.; Solomon, E.I.; Karlin, K.D. Ligand Identity-Induced Generation of Enhanced Oxidative Hydrogen Atom Transfer Reactivity for a $Cu^{II}_2(O_2^{\cdot-})$ Complex Driven by Formation of a $Cu^{II}_2(\text{-OOH})$ Compound with a Strong O-H Bond. *J. Am. Chem. Soc.* **2019,** *141* (32), 12682-12696.
20. Ciancanelli, R.; Noll, B. C.; DuBois, D. L.; DuBois, M. R. Comprehensive Thermodynamic Characterization of the Metal−Hydrogen Bond in a Series of Cobalt-Hydride Complexes. *J. Am. Chem. Soc.* **2002**, *124* (12), 2984–2992.
21. Mock, M. B.; Potter, R. B.; Minako O'Hagan; Camaioni, D. M.; Dougherty, W. G.; W. Scott Kassel; DuBois, D. L. Synthesis and Hydride Transfer Reactions of Cobalt and Nickel Hydride Complexes to BX_3 Compounds. *Inorg. Chem.* 2011, *50* (23), 11914–11928
22. Khaskin, E.; Diskin-Posner, Y.; Weiner, L.; Leitus, G.; Milstein, D. Formal Loss of an H Radical by a Cobalt Complex via Metal–Ligand Cooperation. *ChemComm.* **2013**, *49* (27), 2771–2773.
23. Semproni, S. P.; Carsten Milsmann; Chirik, P. J. Four-Coordinate Cobalt Pincer Complexes: Electronic Structure Studies and Ligand Modification by Homolytic and Heterolytic Pathways. *J. Am. Chem. Soc.* **2014**, *136* (25), 9211–9224.
24. DuBois, D. L.; R. Morris Bullock. Molecular Electrocatalysts for the Oxidation of Hydrogen and the Production of Hydrogen – the Role of Pendant Amines as Proton Relays. *Eur. J. Inorg. Chem.* **2011**, *2011* (7), 1017–1027.
25. Henry, R.M.; Shoemaker, R.K.; DuBois, D.L.; Rakowski DuBois, M. Pendant Bases as Proton Relays in Iron Hydride and Dihydrogen Complexes. *J. Am. Chem. Soc.* **2006,** *128* (9), 3002-3010.

26. Wiedner, E. S.; Appel, A. M.; DuBois, D. L.; Bullock, R. M. Thermochemical and Mechanistic Studies of Electrocatalytic Hydrogen Production by Cobalt Complexes Containing Pendant Amines. *Inorg. Chem.* **2013**, *52* (24), 14391–14403.
27. Yang, J.; Li, P.; Li, X.; Xie, L.; Wang, N.; Lei, H.; Zhang, C.; Zhang, W.; Yong Rok Lee; Zhang, W.-Q.; Cao, R.; Shunichi Fukuzumi; Nam, W. Crucial Roles of a Pendant Imidazole Ligand of a Cobalt Porphyrin Complex in the Stoichiometric and Catalytic Reduction of Dioxygen. *Angew. Chem., Int. Ed.* **2022**, *61* (34).
28. Dolui, D.; Ghorai, S.; Dutta, A. Tuning the Reactivity of Cobalt-Based H2 Production Electrocatalysts via the Incorporation of the Peripheral Basic Functionalities. *Coord. Chem. Rev.* **2020**, *416*, 213335.
29. Darcy, J.W.; Koronkiewicz, B.; Parada, G.A.; Mayer, J.M. A Continuum of Proton-Coupled Electron Transfer Reactivity. *Acc. Chem. Res.* **2018,** *51* (10), 2391-2399.
30. McLoughlin, E.A.; Waldie, K.M.; Ramakrishnan, S.; Waymouth, R.M. Protonation of a Cobalt Phenylazopyridine Complex at the Ligand Yields a Proton, Hydride, and Hydrogen Atom Transfer Reagent. *J. Am. Chem. Soc.* **2018,** *140* (41), 13233-13241.
31. Henthorn, J.T.; Agapie, T. Modulation of Proton-Coupled Electron Transfer through Molybdenum–Quinonoid Interactions. *Inorg. Chem.* **2016,** *55* (11), 5337-5342.
32. Sherbow, T.J.; Fettinger, J.C.; Berben, L.A. Control of Ligand pKa Values Tunes the Electrocatalytic Dihydrogen Evolution Mechanism in a Redox-Active Aluminum(III) Complex. *Inorg. Chem.* **2017,** *56* (15), 8651-8660.
33. Blackmore, K.J.; Ziller, J.W.; Heyduk, A.F. "Oxidative Addition" to a Zirconium(IV) Redox-Active Ligand Complex. *Inorg. Chem.* **2005,** *44* (16), 5559-5561.
34. Haneline, M.R.; Heyduk, A.F. C–C Bond-Forming Reductive Elimination from a Zirconium(IV) Redox-Active Ligand Complex. *J. Am. Chem. Soc.* **2006,** *128* (26), 8410-8411.
35. Charette, B.J.; Ziller, J.W.; Heyduk, A.F. Metal-Ion Influence on Ligand-Centered Hydrogen-Atom Transfer *Inorg. Chem.* **2021,** *60* (3), 1579-1589.
36. Charette, B.J.; Ziller, J.W.; Heyduk, A.F. Exploring Ligand-Centered Hydride and H-Atom Transfer. *Inorg. Chem.* **2021,** *60* (7), 5367-5375.
37. Rosenkoetter, K.E.; Wojnar, M.K.; Charette, B.J.; Ziller, J.W.; Heyduk, A.F. Hydrogen-Atom Noninnocence of a Tridentate [SNS] Pincer Ligand. *Inorg. Chem.* **2018,** *57* (16), 9728-9737.
38. Szigethy, G.; Shaffer, D.W.; Heyduk, A.F. Coordination Effects on Electron Distributions for Rhodium Complexes of the Redox-Active Bis(3,5-di-tert-butyl-2-phenolate)amide Ligand. *Inorg. Chem.* **2012,** *51* (23), 12606-12618.
39. Ranis, L. G.; Kalpani Werellapatha; Pietrini, N. J.; Bunker, B. A.; Brown, S. N. Metal and Ligand Effects on Bonding in Group 6 Complexes of Redox-Active Amidodiphenoxides. *Inorg. Chem.,* **2014**, *53* (19), 10203–10216.
40. Tshepelevitsh, S.; Kütt, A.; Lõkov, M.; Kaljurand, I.; Saame, J.; Heering, A.; Plieger, P. G.; Vianello, R.; Leito, I. On the Basicity of Organic Bases in Different Media. European J. Org. Chem. 2019, 2019 (40), 6735–6748.
41. Conner, K. M.; Arostegui, A. C.; Swanson, D. R.; Brown, S. N. When Do Strongly Coupled Diradicals Show Strongly Coupled Reactivity? Thermodynamics and Kinetics of Hydrogen Atom Transfer Reactions of Palladium and Platinum Bis(Iminosemiquinone) Complexes. *Inorg. Chem.* **2018,** *57 (16), 9696–9707.*

42. Roubelakis, M. M.; Bediako, D. K.; Dogutan, D. K.; Nocera, D. G. Proton-Coupled Electron Transfer Kinetics for the Hydrogen Evolution Reaction of Hangman Porphyrins. *Energy Environ, Sci.* **2012,** *5*, 7737-7740.
43. Schmidt, M. H.; Miskelly, G. M.; Lewis, N. S. Effects of Redox Potential, Steric Configuration, Solvent, and Alkali Metal Cations on the Binding of Carbon Dioxide to Cobalt(I) and Nickel(I) Macrocycles. *J. Am. Chem. Soc.* **1990**, *112* (9), 3420–3426.
44. Spielvogel, K. D.; Stumme, N. C.; Fetrow, T. V.; Wang, L.; Luna, J. A.; Keith, J. M.; Shaw, S. K.; Daly, S. R. Quantifying Variations in Metal–Ligand Cooperative Binding Strength with Cyclic Voltammetry and Redox-Active Ligands. *Inorg. Chem.* **2022**, *61* (5), 2391–2401
45. Spielvogel, K. D.; Luna, J. A.; Loria, S. M.; Weisburn, L. P.; Stumme, N. C.; Ringenberg, M. R.; Durgaprasad, G.; Keith, J. M.; Shaw, S. K.; Daly, S. R. Influence of Multisite Metal-Ligand Cooperativity on the Redox Activity of Noninnocent N2S2 Ligands. *Inorg. Chem.* **2020**, 59, 10845-10853
46. Mayer, J.M. Understanding Hydrogen Atom Transfer: From Bond Strengths to Marcus Theory. *Acc. Chem. Res.* **2011,** *44* (1),36-46.
47. Warren, J.J.; Mayer, J.M. Predicting organic hydrogen atom transfer rate constants using the Marcus cross relation. *Proc. Natl. Acad. Sci. U.S.A.* **2010,** *107* (12), 5282-5287.
48. Bordwell, F.G.; Cheng, J.P.; Harrelson, J.A. Homolytic bond dissociation energies in solution from equilibrium acidity and electrochemical data. *J. Am. Chem. Soc.* **1988,** *110* (4), 1229-1231.
49. Wayner, D.D.M.; Parker, V.D. Bond energies in solution from electrode potentials and thermochemical cycles. A simplified and general approach. *Acc. Chem. Res.* **1993,** *26* (5), 287-294.
50. Parker, V.D.; Handoo, K.L.; Roness, F.; Tilset, M. Electrode Potentials and the Thermodynamics of Isodesmic Reactions. *J. Am. Chem. Soc.* **1991,** *113,* 7493-7498.
51. Tilset, M.; Parker, V.D. Solution homolytic bond dissociation energies of organotransition-metal hydrides. *J. Am. Chem. Soc.* **1989,** *111* (17), 6711-6717.
52. Wiedner, E.S.; Chambers, M.B.; Pitman, C.L.; Bullock, R.M.; Miller, A.J.M.; Appel, A.M. Thermodynamic Hydricity of Transition Metal Hydrides. *Chem. Rev.* **2016***, 116* (15), 8655-8692.
53. Warren, J.J.; Tronic, T.A.; Mayer, J.M. Thermochemistry of Proton-Coupled Electron Transfer Reagents and its Implications. *Chem. Rev.,* **2010,** *110* (12), 6961-7001.
54. Goetz, M. K.; Hill, E. A.; Filatov, A. S.; Anderson, J. S. Isolation of a Terminal Co(III)-Oxo Complex. *Journal of the American Chemical Society* **2018**, *140* (41), 13176–13180.
55. Piskunov, A. V.; Pashanova, K. I.; Bogomyakov, A. S.; Smolyaninov, I. V.; Starikov, A. G.; Fukin, G. K. Cobalt Complexes with Hemilabile O-Iminobenzoquinonate Ligands: A Novel Example of Redox-Induced Electron Transfer. *Dalton Transactions* **2018**, *47* (42), 15049–15060.
56. Chaudhuri, P.; Hess, M.; Müller, J. A.; Hildenbrand, K.; Bill, E.; and Thomas Weyhermüller; Wieghardt, K. Aerobic Oxidation of Primary Alcohols (Including Methanol) by Copper(II)− and Zinc(II)−Phenoxyl Radical Catalysts. *J. Am. Chem. Soc.* **1999**, *121* (41), 9599–9610.

57. Bruni, S.; Caneschi, A.; Franco Cariati; Delfs, C.; Dei, A.; Gatteschi, D. Ferromagnetic Coupling between Semiquinone Type Tridentate Radical Ligands Mediated by Metal Ions. J. Am. Chem. Soc. **1994,** *116 (4), 1388–1394.*
58. Chaudhuri, P.; Hess, M.; Hildenbrand, K.; Bill, E.; Weyhermüller, T.; Wieghardt, K. Ligand-Based Redox Isomers of [ZnII(C28H40NO2)2]: Molecular and Electronic Structures of a Diamagnetic Green and a Paramagnetic Red Form. *Inorg. Chem.* **1999**, *38* (12), 2781–2790.
59. Chaudhuri, P.; Verani, C. N.; Bill, E.; Bothe, E.; Weyhermüller, T.; Wieghardt, K. Electronic Structure of Bis(*O*-Iminobenzosemiquinonato)Metal Complexes (Cu, Ni, Pd). The Art of Establishing Physical Oxidation States in Transition-Metal Complexes Containing Radical Ligands. *J. Am. Chem. Soc.* **2001**, *123* (10), 2213–2223.
60. Rechkemmer, Y.; Breitgoff, F. D.; van der Meer, M.; Atanasov, M.; Hakl, M.; Orlita, M.; Neugebauer, P.; Neese, F.; Sarkar, B.; van Slageren, J. A Four-Coordinate Cobalt(II) Single-Ion Magnet with Coercivity and a Very High Energy Barrier. *Nat. Commun.* **2016**, *7* (1), 10467.
61. Ribeiro, M. A.; Lanznaster, M.; Silva, M. M. P.; Resende, J. A. L. C.; Pinheiro, M. V. B.; Krambrock, K.; Stumpf, H. O.; Pinheiro, C. B. Cobalt Lawsone Complexes: Searching for New Valence Tautomers. *Dalton Trans.* **2013**, *42* (15), 5462–5470.
62. Dori, Z.; Gray, H. B. High-Spin, Five-Coordinate Cobalt(II) Complexes. *Inorg. Chem.* **1968**, 7, 889–892.
63. Ray, M.; Hammes, B. S.; Glenn; Rheingold, A. L.; Borovik, A. S. Structure and Physical Properties of Trigonal Monopyramidal Iron(II), Cobalt(II), Nickel(II), and Zinc(II) Complexes. *Inorg. Chem.* **1998**, *37* (7), 1527–1532.
64. Ciampolini, M.; Nardi, N.; Speroni, G. P. Five-Coordinated Complexes of 3d Bivalent Metal Ions with Polyamines. Coord. Chem. Rev. 1966, 1, 222–233.
65. Charette, B.J. Investigations into the Reactivity of Transition Metal Complexes with Redox-Active Ligands for Proton Coupled Electron Transfer and Nitrene Transfer. Ph.D. Dissertation, University of California Irvine, Irvine, CA, **2021.**
66. Fukui, K.; Hiroaki Ohya-Nishiguchi; Hirota, N. ESR and Magnetic Susceptibility Studies on High-Spin Tetrahedral Cobalt(II)–Thiolate Complexes: An Approach to Rubredoxin-Type Active Sites. *Chem. Soc. Jpn.,* **1991**, *64* (4), 1205–1212.
67. Goetz, M. K.; Hill, E. A.; Filatov, A. S.; Anderson, J. S. Isolation of a Terminal Co(III)-Oxo Complex. *J. Am. Chem. Soc.* **2018**, *140* (41), 13176–13180.
68. Jenkins, D. M.; Di Bilio, A. J.; Allen, M. J.; Betley, T. A.; Peters, J. C. Elucidation of a Low Spin Cobalt(II) System in a Distorted Tetrahedral Geometry. *J. Am. Chem. Soc.* 2002, *124* (51), 15336–15350.
69. Cockle, S. A.; Lindskog, S.; Grell, E. Electron-Paramagnetic-Resonance Studies on Cobalt(II) Carbonic Anhydrase–Sulphonamide Complexes. *Biochem. J.,* **1974,** *143,* 703–715.
70. Miecznikowski, J. R.; Zygmont, S. E.; Jasinski, J. P.; Kaur, M.; Almanza, E. M.; Kharbouch, R. M.; Bonitatibus, S. C.; Mircovich, E. E.; Pierre Le Magueres; Reinheimer, E. W.; Weitz, A. C. Synthesis, Characterization, and Electrochemistry of SNS Cobalt(II) Tridentate Complexes. *Transit Met Chem* **2022,** *47*, 127-137.

71. Zhao, J., Peng, Q., Wang, Z. *et al.* Proton mediated spin state transition of cobalt heme analogs. *Nat. Commun.* **10**, 2303 (2019).
72. Fleming, C.; Chung, D.; Ponce, S.; Brook, D. J. R.; DaRos, J.; Das, R.; Ozarowski, A.; Stoian, S. A. Valence Tautomerism in a Cobalt-Verdazyl Coordination Compound. *Chem. Comm.* **2020**, *56* (32), 4400–4403.

CHAPTER 4: Attempts to protonate a {[ONO]$TaCl_3$}$^-$ monomer

4.1. Introduction.

Transition metal reagents for proton-coupled electron transfer (PCET) are primarily based on metal ions from Groups 9 and 10, such as Pd, Rh, and Ir. Late metals are favored due to their ability to undergo both one- and two-electron redox processes reversibly, and changes in coordination geometries upon oxidation or reduction of these metal centers are often predictable. Electron-deficient metal hydrides of Groups 3-7 remain understudied. Early transition metal complexes can support formal hydride ligands and perform net hydride-transfer, such as ketone and aldehyde reduction to alcohols, and they often exhibit higher thermodynamic hydricities than later metal ions.[1] However, metal hydride complexes of Zr, Ta, W, Mo, V, and Hf, often form dimers or polymetallic clusters, or participate in other undesired reactions, due to the ability of electropositive metal ions to support an unusual number of ligands beyond the traditional four-, five-, and six-coordinate geometries of later metals. Examples of non-metallocene hydride complexes are still uncommon in the literature, and their applications to catalytic hydrogenation, C–H functionalization, and polymerization remains limited.

Multidentate ligands have emerged as suitable platforms for mononuclear early transition metal ions, such as the tetrapodal triamidoamine ligand reported by Okuda,[2] and pyridine-linked pincer ligands with phenolate[3] and pyrrolide[4] motifs (**Figure 4.1**) have likewise been used to study stable Ta, Zr, and Hf systems in high oxidation states. In addition, studies of tridentate pincer ligands such as bis(3,5-di-tert-butyl-2-phenoxy)amide ([ONO]) and bis(2-isopropylamino-4-methoxyphenylamine ([NNN]) on formally d^0 Zr(IV)[5,6] and Ta(V)[7-11], ions have widened the scope of early transition metal reagents capable of multi-electron reactions such as nitrene transfer, oxidative addition, and reductive elimination.[12]

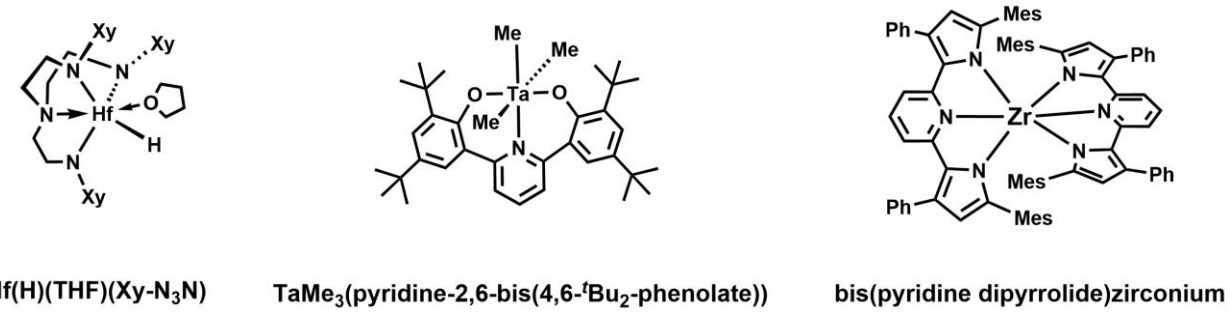

Hf(H)(THF)(Xy-N_3N) **$TaMe_3$(pyridine-2,6-bis(4,6-^{t}Bu_2-phenolate))** **bis(pyridine dipyrrolide)zirconium**

Figure 4.1. Multidentate ligands have been shown to stabilize early transition metal ions in high oxidation states. From left to right: a hafnium (IV) hydride stabilized by a tetradentate ligand; a tantalum (V) trialkyl complex with a tridentate ligand with phenol- and pyridine- motifs; a zirconium (IV) complex supported by two tridentate ligands with pyridine dipyrrolide backbones.

In these complexes, electrons are provided strictly from the bound pincer ligands, though substrates are coordinated directly to the metal. Despite the ligand-localized redox activity, the metal ion modulates the reduction potentials of the ligand significantly. The first oxidation of the $[ONO^{cat}]^{3-}$ ligand shifts by 430 mV in acetonitrile depending on whether it is coordinated to the electropositive Ta(V) ion ($E_{1/2}$ = −0.074 V vs. $[FeCp_2]^{+/0}$) or Pt(II) ($E_{1/2}$ = −0.51 V).[12] While the $\{[ONO]TaCl_3\}^-$ and $\{[ONO]Pt(PPh_3)\}^-$ complexes have differing coordination environments and ancillary ligands, other studies have likewise shown that metal ion identity can tune the reduction potential of bound redox-active ligands.[11] Additionally, the central basic site in the [ONO] ligand can store and deliver protons independent of the metal it is bound to, whether the metal is a late-transition metal like Ni or an early-transition metal.[6] Redox- and proton-active ligands have granted late-metal reactivity to early-transition metals, thus making elements such as Ta viable candidates for stable PCET reactivity. For example, The $[ON(H)O]ZrCl_2(THF)$ complex readily reduced O_2, forming a hydroxide-bridged dimer (**Scheme 4.1**) in a $2H^+/4e^-$ process.[6]

The redox- and proton-activity of the $[ON(H)O]^{2-}$ ligand was observed in another complex of an early transition metal, Ta(V). Addition of hydrazine to $[ONO]TaMe_2$ resulted in the formation of a half-protonated dimer, $[ONO^{cat}]TaMe(\mu\text{-}\eta^2\text{:}\eta^2\text{–}N_2H_2)(\mu\text{-}\eta^2\text{:}\eta^1\text{–}$

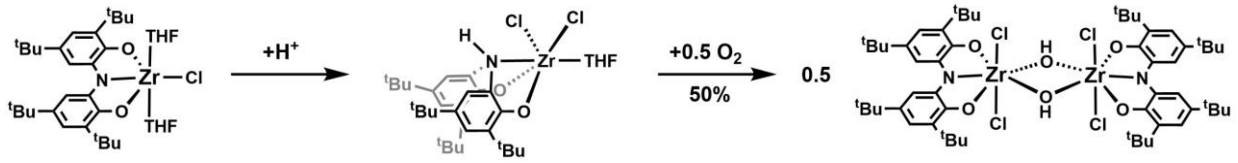

Scheme 4.1. Protonation of [ONO]ZrCl(THF)$_2$ results in a dichloride complex capable of 2H$^+$/4e$^-$ reduction of O_2, forming a hydroxide-bridged dimer.

N_2H_3)TaMe[ON(H)O] (**Scheme 4.2**).[7] The redox activity of the [ONO]$^{3-}$ ligand on tantalum(V) had already been characterized and catalytic multi-electron reactivity such as nitrene transfer was observed. Complexes of the [ONO^{cat}]$^{3-}$, [ONO^{sq}]$^{2-}$, and [ONO^{q}]$^{1-}$ ligand on tantalum had also been isolated and studied, but no further acid-base studies had been reported. Therefore the details of its acidity and homolytic bond dissociation free energy (BDFE) were unknown.

In the published studies, it was observed that as is oxidized from, effectively, 3 X-type donors in the [ONO^{cat}]$^{3-}$ oxidation state, to 1 X- and 2 L-type donors as the [ONO^{q}]$^{1-}$ state, the Ta(V) ion preferentially binds additional ligands (**Scheme 4.3**) to produce a family of neutral complexes with different coordination numbers: [ONO^{cat}]TaCl$_2$(OEt$_2$), [ONO^{sq}]TaCl$_3$, and [ONO^{q}]TaCl$_4$. The structural changes were evident in the irreversible electrochemistry as observed in cyclic voltammetry. Changes in coordination environment represent equilibria that can compete with and obscure the electron- and proton-transfer reactivity of these complexes, making individual measurement of their pK_a, BDFE, and thermodynamic hydricity (ΔG_{H^-}) difficult. However, if a monoanionic trichloride {[ONO^{cat}]TaCl$_3$}$^-$ derivative

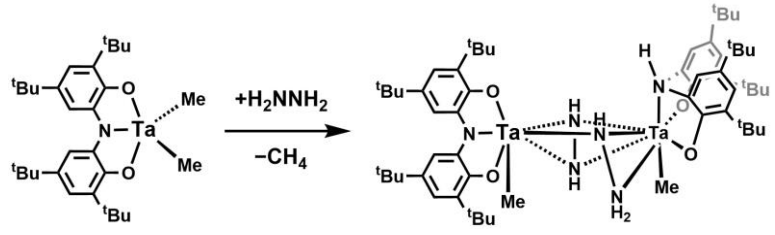

Scheme 4.2. Addition of hydrazine to [ONO]TaMe$_2$ results in the formation of a half-protonated dimer, [ONO^{cat}]TaMe(μ-η^2:η^2–N_2H_2)(μ-η^2:η^1–N_2H_3)TaMe[ON(H)O].

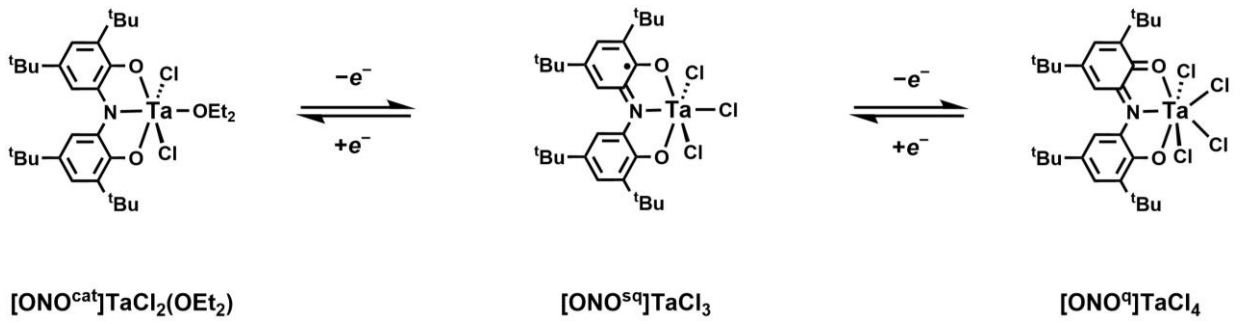

Scheme 4.3. Published [ONO]$TaCl_n$ (n = 2, 3, 4) complexes with the [ONO] ligand bound in the cat, sq, and q states. As the ligand is oxidized, the Ta(V) ion coordinates X-type ligands to maintain a net neutral charge.

could be obtained, one-electron oxidation to [ONO^{sq}]$TaCl_3$ should become reversible. The isolation of a protonated species, such as [ON(H)O]$TaCl_3$, would then allow for the measurement of PCET from the complex (**Scheme 4.4**), to compare it with other examples of the [ON(H)O] ligand bound to late transition metal ions. The pK_a and reduction potentials, if measured separately, would provide the BDFE[14-21] of [ON(H)O] on Ta(V) according to **Equation 4.1**:

$$\boldsymbol{BDFE}(X\text{–}H) = 1.37pK_a + 23.06E_1^\circ + C_G \qquad \textbf{(Eqn. 4.1)}$$

Therefore, a more detailed study of the protonated ligand on early transition metal ions was warranted.

The protonated [ON(H)O] ligand has been previously observed in the aforementioned [ONO^{cat}]TaMe(μ-η^2:η^2–N_2H_2)(μ-η^2:η^1–N_2H_3)TaMe[ON(H)O] dimer, which provided a benchmark of the ligand's BDFE.[22] Reaction of [ONO]$TaMe_2$ with any amount (i.e. fractional, stoichiometric, or excess) of H_2NNH_2 (hydrazine) produced the unusual asymmetric dimer. While one Ta center can be described as a seven-coordinate Ta(V) ion, with a *mer*-[ONO^{cat}]$^{3-}$ ligand taking up three sites of the base in a pentagonal bipyramid geometry, the second metal ion is an eight-coordinate Ta(V), with a *fac*-[ON(H)O] ligand; the buckling of the redox-active ligand when the central nitrogen becomes sp^3 hybridized has been seen in late transition

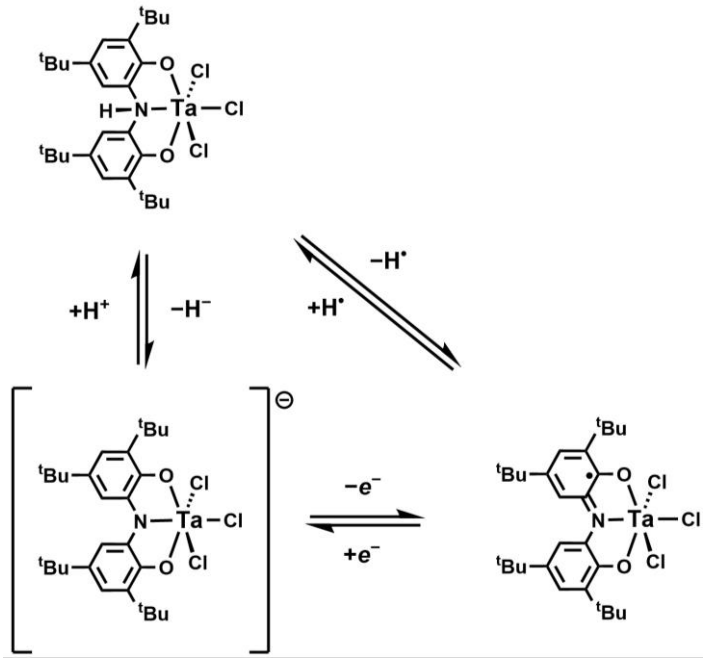

Scheme 4.4. Proposed thermodynamic scheme of a [ON(H)O]$TaCl_3$ species. Direct measurement of ligand reduction potential and pK_a would afford the bond dissociation free energy of the N–H bond.

metal complexes. The N–H proton of the [ON(H)O] ligand was observed in both the ^{1}H NMR spectrum as well as in the crystal structure. The presence of one doubly protonated –NH_2 moiety (bond dissociation enthalpy (BDE)[23] = 80.8 kcal mol^{-1}) of a hydrazine bound to the same Ta(V) center suggests that the [ON(H)O] N–H bond must be very strong (BDE > 80 kcal mol^{-1}) and much less acidic than those of hydrazine. Likewise, the methyl ligand bound to the same metal ion would seemingly indicate that the H–CH_3 bond[24-26] (BDE *c.a.* 103 kcal mol^{-1}) is also weaker than the N–H bond in [ON(H)O].

The suggestion that the [ON(H)O] bond strength may be greater than 100 kcal mol^{-1} was surprising when compared to the behavior of the monomeric Group IV [ON(H)O]$ZrCl_2$(THF) complex. No direct measurements of the BDE or BDFE, or the reduction potential and pK_a of the Zr complex have been obtained. However, the overall reaction to produce the hydroxy-bridged dimer from O_2 requires the [ON(H)O] to have a weaker bond strength than (M)O–H. Such (M)O–H bond[24-27] strengths vary depending on the

identity and oxidation state of the metal center it is bound to. In late metal complexes featuring bridging hydroxyl ions, BDFE's between 70-85 kcal mol^{-1} have been reported,[28-29] and the O–H BDE of high-valent manganese III/IV dimers bridged by hydroxides[30,31] have been reported in the same general range. The hydroxo-vanadium complexes $[V^{IV}O(OH)(R_2bpy)_2]BF_4$ and $[V^{V}O_2(R_2bpy)_2]BF_4$ (bpy = 2,2'-bipyridine, R = tBu, Me, H)[32] have also been studied and possess O–H BDFEs ~ 70 kcal mol^{-1}. Thus, in order to form a (M)OH species, $[ON(H)O]ZrCl_2$ likely has an N–H BDFE < 85 kcal mol^{-1}, far lower than those suspected for the $\{Ta\}_2$ species.

Despite the comparison to previous examples of early-metal hydrides, hydroxides, and proton-active ligand complexes, the [ON(H)O] in the tantalum dimer seemed to be strangely stable. Efforts to prevent the formation of the dimeric product by inclusion of strongly coordinating pyridine ligands and bases such as triethylamine were unsuccessful, and likewise the dimer was stable to heating and attempts at deprotonation. An independent route to a monomeric $[ON(H)O]TaX_n$ species was pursued, in the hopes of studying a very weakly acidic, strongly reducing redox- and proton-active ligand on an early transition metal ion. To that end, an $\{[ONO^{cat}]TaCl_3\}^-$ monoanion was isolated and characterized as a robust monomer. The complex was studied for its electrochemistry and pK_a, which were compared to the previous studies of the ligand on Ta and other transition metal ions.

4.2. Results and discussion.

4.2.1. Attempted synthesis of $[ON(H)O]TaCl_3$.

Direct synthesis of a protonated $[ON(H)O]TaCl_3$ species was attempted, following an analogous procedure to $[ON(H)O]ZrCl_2(THF)$. The $[ONO]H_3$ ligand was doubly deprotonated in diethyl ether with *n*-BuLi, followed by metalation with $TaCl_5$. Tetrahydrofuran was not

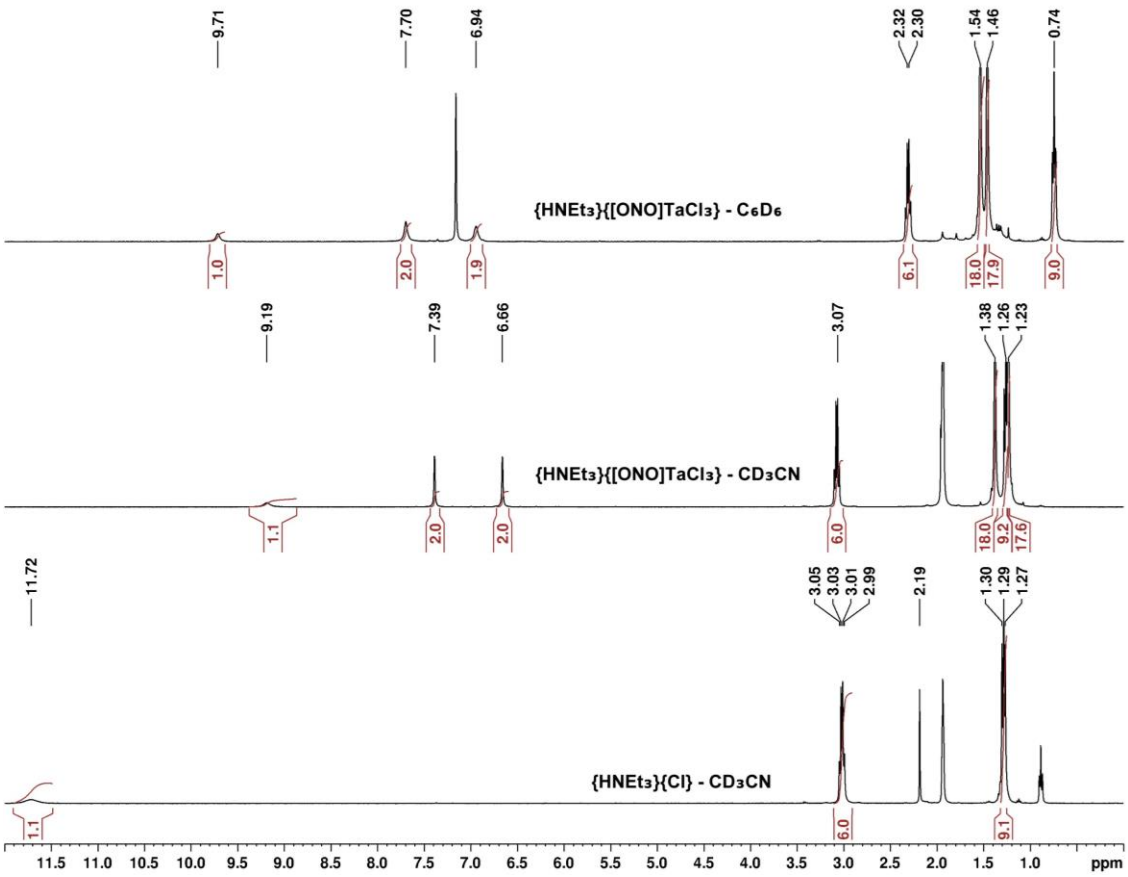

Figure 4.2. Stacked ^{1}H NMRs comparing triethylammonium chloride (bottom, CD_3CN; peak at 2.19 ppm is a hexamethylbenzene standard) to the putative $\{HNEt_3\}\{[ONO]TaCl_3\}$ in both CD_3CN and C_6D_6 for comparison.

used for the tantalum synthesis, as $TaCl_5$ is known to polymerize the solvent.[33] A red-brown solution was obtained with visible precipitation of LiCl, and workup produced a red crystalline solid. However, this product did not produce any recognizable resonances in ^{1}H NMR, and other synthetic approaches were investigated.

Deprotonation of the $[ONO]H_3$ ligand was attempted with other bases previously used to successfully generate $[ON(H)O]ML_n$ (M = Ni, Pd, Pt) species. Reaction with two equivalents of triethylamine did not form $[ON(H)O]TaCl_3$, but rather a non-stoichiometric amount of triethylammonium chloride and a yellow product whose ^{1}H NMR (**Figure 4.2**) did not match previously-reported tantalum complexes of the [ONO] ligand. In C_6D_6, the aromatic protons of the [ONO] ligand (7.70 and 6.94 ppm) were shifted downfield of the

neutral [ONO]$TaCl_2(OEt_2)$ species (7.32 and 6.91 ppm). One equivalent of $\{HNEt_3\}^+$ was present in the ^1H NMRs, but the alkyl resonances were not significantly shifted from free $\{HNEt_3\}^+$ (**Figure 4.2**). A broad peak at chemical shifts greater than 9 ppm appeared in the spectra of the tantalum complex in both C_6D_6 and CD_3CN; this peak was assigned to an $\{HNEt_3\}^+$ cation rather than a protonated [ON(H)O]. The N–H proton of the ligand usually appears upfield between 5-6 ppm, regardless of the metal it is bound to; for example, in the previously reported Zr(IV) complex, the N–H resonance appeared at 5.82 ppm in C_6D_6. In the case of the $[ONO^{cat}]TaMe(\mu\text{-}\eta^2\text{:}\eta^2\text{–}N_2H_2)(\mu\text{-}\eta^2\text{:}\eta^1\text{–}N_2H_3)TaMe$[ON(H)O] dimer, the NH proton was observed at 6.94 ppm, in addition to the observed aromatic protons. However, the signal at 9.19 ppm in Figure 5.2 is significantly shifted from free triethylammonium, despite the alkyl region remaining largely unchanged; it is possible that the $\{HNEt_3\}^+$ cation is associating and dissociating rapidly in solution, or that the proton exchanges between triethylamine and [ONO] on a timescale that is not captured by the ^1H NMR measurement.

The presence of protonated triethylamine in the ^1H NMR of the complex had implications for its stoichiometry and acidity; the single equivalent of $\{HNEt_3\}^+$ suggests that the tantalum species has a monoanionic charge. To accomplish this, the complex could be made up of a Ta(V) center with three X-type ligands and a fully-reduced $[ONO^{cat}]^{3-}$ ligand, or a $[ONO^{cat}]^{3-}$ ligand, two X-type ligands, and a Ta(IV) ion. However, it is unlikely that the $\{[ONO]TaCl_n\}^-$ anion has a Ta(IV) ion. In the previous examples of [ONO]–Ta complexes, the metal ion appeared to remain in a stable d^0 Ta(V) oxidation state no matter the oxidation state of the [ONO] ligand itself. The electrochemistry of the complex is also consistent with a fully-reduced $[ONO^{cat}]^{3-}$ ligand; the open-circuit potential (OCP) lies negative of the two redox events (**Figure 4.3**), indicating the complex can be oxidized twice (**Table 4.1**). However, the differences between the ^1H NMR of this complex and the previously reported $[ONO]TaCl_2(OEt_2)$ would indicate that the Ta(V) centers are not equivalent, suggesting

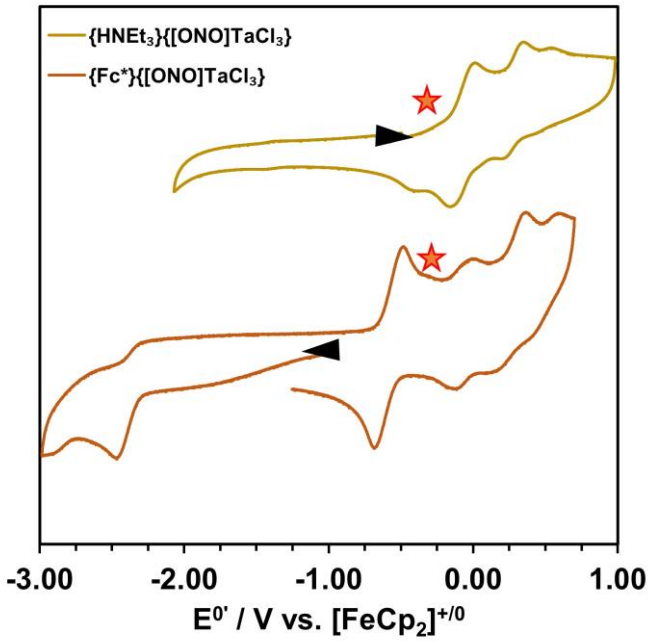

Figure 4.3. Cyclic voltammograms of tantalum complexes (yellow trace = {HNEt$_3$}{[ONO]TaCl$_3$}; orange trace = {Fc*}{[ONO]TaCl$_3$})dissolved in acetonitrile, recorded at 3200 mV/s. Star indicates open circuit potential determined by a separate measurement, and black arrows indicates scan direction. Voltammetry was performed in solutions containing 0.1 M {Bu$_4$N}{Cl} using a glassy carbon working electrode, Pt-wire counter electrode, an Ag$^{+/0}$ pseudo-reference electrode, and [FeCp$_2$]$^{+/0}$ as an internal standard.

Table 4.1. Reduction potentials of {X}{[ONO]TaCl$_3$} complexes in acetonitrile reported at 100 mV/s scan rates.

X	E°' / V vs. [FeCp$_2$]$^{+/0}$ (i_{pa}/i_{pc})				
	[Ta]$^{2-/3-}$	[Ta]$^{1-/2-}$	[Ta]$^{0/1-}$	[Ta]$^{1+/0}$	[Ta]$^{2+/+1}$
HNEt$_3^+$	–	–	−0.0739 (1.81)	0.280 (1.26)	0.557[a]
Fc*$^+$	−2.39[a]	−0.590	−0.0744	0.252a	0.596[a]

(#) – i_{pa}/i_{pc}. [a] Completely irreversible.

coordinated a third X-type ligand (n = 3). Thus, while no solid-state structure was obtained, it seems likely that a trichloride {[ONO]TaCl$_3$}$^-$ species was synthesized. That triethylamine was present as a free, protonated cation in MeCN also provided a benchmark for the pK_a of the [ON(H)O] ligand when bound to Ta(V). Triethylammonium has a pK_a of 18.83 in MeCN, meaning that {[ON(H)O]TaCl$_n$}$^-$ must be more acidic (have a lower pK_a).

4.2.2. Isolation of a $\{[ONO]TaCl_3\}^-$ anion.

As the protonated species was not isolated by direct synthesis, protonation of a complex containing the fully reduced $[ONO^{cat}]^{3-}$ ligand was attempted, beginning with the previously-isolated $[ONO]TaCl_2(OEt_2)$ species. Typically, the potential-pK_a measurements used to determine X–H BDFEs requires the use of solvent-dependent acidity data, most of which is measured in MeCN, DMSO, and water, as well as a solvent-dependent correction factor (C_G for BDFE calculations). Unfortunately, $[ONO]TaCl_2(OEt_2)$ was discovered to react irreversibly in MeCN. The signature aromatic and *tert*-butyl peaks of the [ONO] ligand protons are not present in NMRs taken in CD_3CN and do not reform if the complex is dissolved in acetonitrile, dried, and redissolved in C_6D_6 or other solvents.

In contrast, the anionic $\{[ONO]TaCl_3\}^-$ was stable in all solvents tested. Thus, protonation of this species was pursued instead. Cation exchange of the triethylammonium cation was attempted first to avoid competing acid-base equilibria. However, stirring the complex with tetrabutylammonium chloride $\{Bu_4N\}\{Cl\}$ did not result in the precipitation of $\{HNEt_3\}\{Cl\}$ or changes to the ^1H NMR. Other attempts to replace the cation were likewise unsuccessful. Synthesis of the trichloride anion from fully-deprotonated $[ONO^{cat}]^{3-}$ and $TaCl_5$ by salt metathesis did not produce either $\{[ONO]TaCl_3\}^-$ or $[ONO]TaCl_2(OEt_2)$. An alternate synthetic route was investigated.

It was hypothesized that chemical reduction of the neutral, trichloride $[ONO^{sq}]TaCl_3$ complex might yield a stable trichloride $\{[ONO]TaCl_3\}^-$ anion. The semiquinonate complex was therefore obtained *via* oxidation of $[ONO]TaCl_2(OEt_2)$ following the published literature procedure, modified to use half an equivalent of $PhI(OAc)_2$ instead of $PhICl_2$. The purity of $[ONO]TaCl_3$ was confirmed by electrochemistry in dichloromethane and compared to known reduction potentials. Subsequent one-electron reduction of this complex with decamethylferrocene (Fc*) resulted in an immediate color change from violet to brown, and a

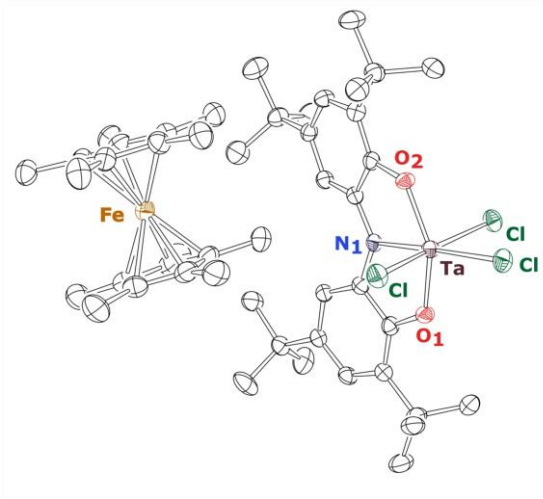

Figure 4.4. ORTEP diagram of {Fc*}{[ONO]$TaCl_3$}. Co-crystallized solvent molecules have been removed for clarity.

Table 4.2. Selected bond distances (Å) of solid-state structures obtained for {Fc*}{[ONO]$TaCl_3$}, [ONO]$TaCl_2(OH_2)$, and previously-reported [ONO]$TaCl_2(OEt_2)$.

Complex	{Fc*}{[ONO]$TaCl_3$}	[ONO]$TaCl_2(OH_2)$	[ONO[$TaCl_2(OEt_2)$
Bond		**Distance / Å**	
O1-C1	1.352(5)	1.3655(18)	1.359(10)
O2-C7	1.360(5)	1.3655(18)	1.423(11)
O1-Ta	1.934(3)	1.9068(11)	1.877(6)
O2-Ta	1.923(3)	1.9069(11)	1.894(6)
N1-Ta	2.088(3)	2.0643(17)	2.040(7)
C6-N1	1.415(5)	1.4113(16)	1.405(13)
C12-N1	1.410(5)	1.4114(16)	1.431(12)
MOS[a]	− 2.93 ± 0.131	−3.03 ± 0.103	−2.85 ± 0.084

(a) This molecule was symmetric across the central mirror plane.
(b) MOS are averaged between two sides of one molecule. In crystals with multiple molecules in the unit cell, MOS is reported for just one.

fine brown powder precipitated overnight. The complex was found to be insoluble in aromatic solvents, and the ^1H NMR in CD_3CN showed evidence of a new species. The aromatic peaks attributed to the [ONO] ligand appeared at 7.08 and 6.71 ppm, upfield from {$HNEt_3$}{[ONO]$TaCl_3$} (7.39 and 6.66 ppm). The *tert*-butyl protons of the [ONO] ligand are known to be sensitive to changes in the ligand coordination environment and the overall charge of the complex, and in the new anionic species, they appear at 1.35 and 1.31 ppm compared to 1.38 and 1.24 ppm in {$HNEt_3$}{[ONO]$TaCl_3$}.

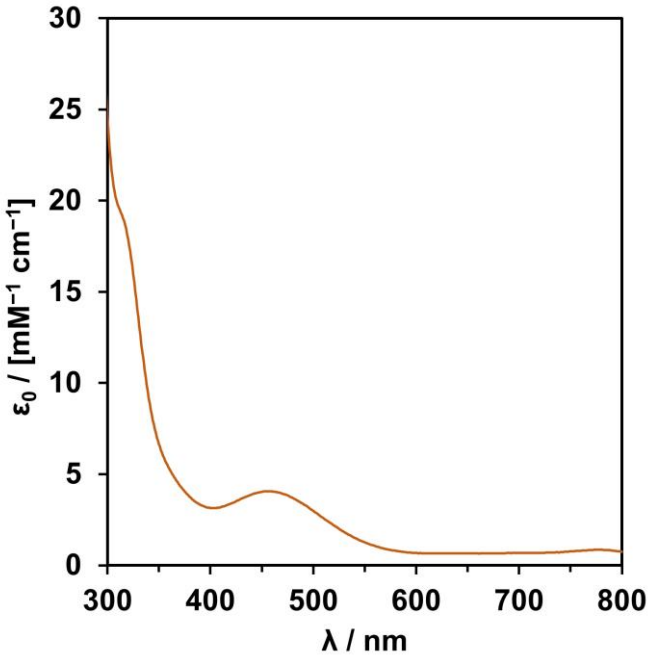

Figure 4.5. Electronic absorption spectra of {Fc*}{[ONO]TaCl$_3$} in acetonitrile.

The brown solid was identified as {Fc*}{[ONO]TaCl$_3$} by single-crystal X-ray crystallography (**Figure 4.4**). The complex is six-coordinate, with the [ONO] ligand bound *mer* to the Ta center, as seen in previously-isolated [ONO]–Ta complexes. Intraligand bond lengths within the [ONO] backbone are sensitive to oxidation state, and examination of the C–O and C–N bond lengths shows distinct single-bond character (**Table 4.2**). Single-bonded sp^2-sp^2 atoms are quite long (1.370-1.470 Å), whereas in the singly- and doubly-oxidized species these bonds would contract significantly toward double-bonded C=N (1.260-1.350 Å). In {Fc*}{[ONO]TaCl$_3$}, the C–N bond lengths are greater than 1.4 Å, consistent with a fully-reduced ligand. The Brown group developed a metrical oxidation state (MOS) calculator to evaluate oxidation states in well-studied redox active ligands, such as [ONO], by comparing the C–C, C–N, and C–O bond lengths to previously reported complexes.[34] The MOS of this complex is likewise consistent with a [ONO^{cat}]$^{3-}$ ligand.

Both the electrochemistry (**Figure 4.3, Table 4.1**) and the electronic absorption spectrum of {Fc*}{[ONO]TaCl$_3$} indicate that the [ONO] ligand may be fully reduced. The

OCP lies between the reduction of $\{Fc^*\}^+$ and the first oxidation of the complex, and the reduction potentials of the first and second oxidations are in agreement with both the putative $\{HNEt_3\}\{[ONO]TaCl_3\}$ and previous electrochemistry of $[ONO^{sq}]TaCl_3$. With a vast excess of Cl^- in the electrolyte, the ligand-based redox events are more reversible than they appear in previous work, but the ratio of peak currents and scan rate dependence studies show that they are still not completely reversible. The likely [sq•/cat] reduction at −0.074 V vs. $[FeCp_2]^{+/0}$ becomes completely irreversible at slow scan rates, and the [q/sq•] redox event is almost completely irreversible, consistent with the complex binding a fourth Cl^- ligand as was seen in $[ONO^q]TaCl_4$.

4.2.3. Attempted protonation of the $\{[ONO]TaCl_3\}^-$ anion.

Protonation studies of the isolated anionic complex were monitored by ^1H NMR in CD_3CN with an internal standard of hexamethylbenzene (2.19 ppm). As a control experiment, 1 and 10 equivalents of $\{HNEt_3\}\{Cl\}$ were added to the $\{Fc^*\}\{[ONO]TaCl_3\}$ complex; no changes in the ^1H NMR spectra were observed (**Figure 4.6**) even after several days, consistent with the [ONO] ligand having a much lower pK_a than triethylamine. Other acids were investigated in the same manner. Addition of 2,4,6-trimethylpyridininium chloride (pK_a = 15.00, MeCN),[34] 2,6-dimethylpyridine (pK_a = 14.16, MeCN),[35] and *para*-cyanoanilinium tetrafluoroborate (pKa = 7.0, MeCN)[34] likewise produced no changes in the spectra. The lack of protonation indicated that the pK_a of the $\{[ONO]TaCl_3\}^-$ species remained lower than any of the acids tested.

Numerous studies of inorganic superacids have shown that the pK_a of hydrochloric acid (HCl) varies dramatically in different solvents. While it is highly acidic (pK_a < 2) in aqueous solvents, in MeCN the pK_a of HCl has been experimentally determined to be 10.30.

Stoichiometric addition of a dilute HCl solution to $\{[ONO]TaCl_3\}^-$ on the Schlenk line gave no

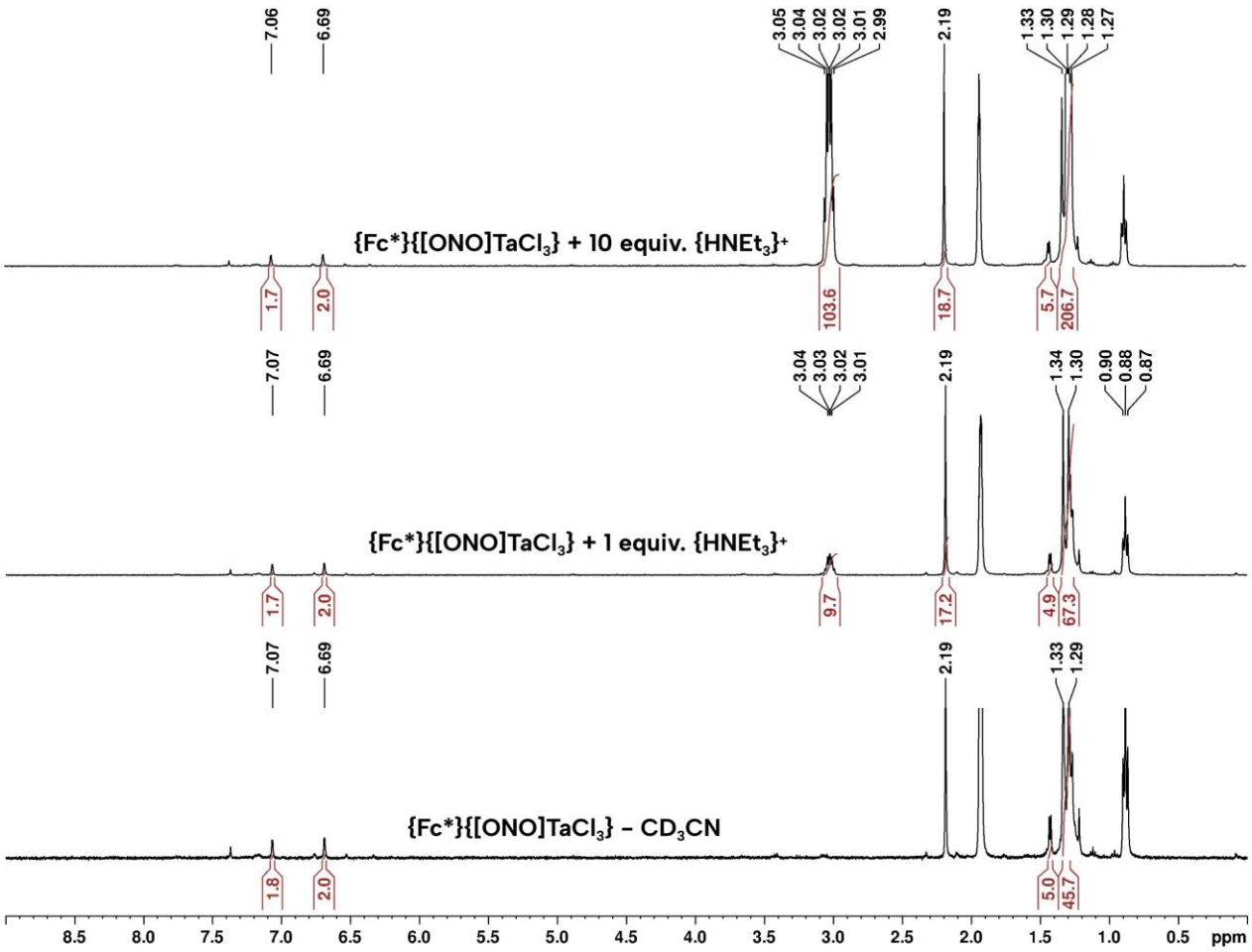

Figure 4.6. Addition of one (middle) and ten (top) equivalents of $\{HNEt_3\}^+$ to a solution of $\{Fc^*\}\{[ONO]TaCl_3\}$ was monitored by ^1H NMR in CD_3CN. No protonation of the redox-active ligand was observed, and peaks corresponding with the anion did not shift even after several days.

observable reaction, and $\{Fc^*\}\{[ONO]TaCl_3\}$ was recovered from the reaction mixture. Thus it seemed apparent that $\{Fc^*\}\{[ONO]TaCl_3\}$ is the stronger acid.

It was apparent that the $\{[ONO]TaCl_3\}^-$ complex was unlikely to be protonated even by strong acids. The superacidity of $\{[ONO]TaCl_3\}^-$ was confirmed when a $[ONO^{cat}]TaCl_2(OH_2)$ crystal structure was obtained from wet solvent (**Figure 4.7**). The [ONO] ligand is fully-reduced in the solid-state, and the water molecule remains doubly protonated. Computational studies of water bound to various Lewis acids in aprotic solvents indicate that

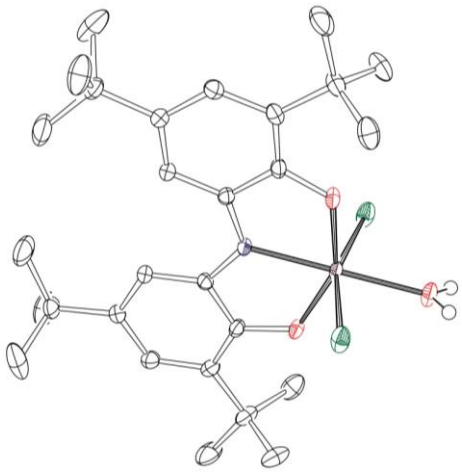

Figure 4.7. ORTEP diagram of [ONO]$TaCl_2(OH_2)$. Co-crystallized solvent molecules have been removed for clarity. Protons on the aqua ligand were located in the difference map.

its pK_a can vary substantially depending on what it is coordinated to, but the acidity of the hydronium ion in acetonitrile has been experimentally and computationally determined.[36-40] Treating the Ta(V) center as a very simple Lewis acid bound to a water molecule, such as the case in the hydronium ion, the pK_a of H_3O^+ in acetonitrile (2.2) serves as another benchmark for the acidity of the $[ONO^{cat}]^{3-}$ ligand bound to a Ta(V) center.

With the electrochemistry measurements of a tricholoride $\{[ONO]TaCl_3\}^-$ complete and an upper ceiling for the pK_a of [ON(H)O]$TaCl_3$ obtained, it was possible to estimate the BDFE of the N–H bond. According to Equation 5.1 and assuming the pK_a of a [ON(H)O]$TaCl_3$ lies below 2 in acetonitrile, a maximum BDFE of 55.0 kcal mol^{-1} is obtained. Given the uncertain nature of this pK_a estimate, the BDFE was also calculated using the pK_a of HCl (10.30), resulting in a calculated BDFE of 70.0 kcal mol^{-1}. Even this highly inflated BDFE is in stark disagreement with the observation of a protonated ligand in $[ONO^{cat}]TaMe(\mu\text{-}\eta^2\text{:}\eta^2\text{–}N_2H_2)(\mu\text{-}\eta^2\text{:}\eta^1\text{–}N_2H_3)TaMe[ON(H)O]$ dimer (*vide supra*). To remain protonated while Me remains bound in an adjacent position on the metal center, the [ON(H)O] ligand must have an extraordinarily high BDFE and a very weakly acidic (pK_a > 20) proton, unless the kinetic barrier to the deprotonated complex is exceedingly high.

It was clear that the protonated [ON(H)O] ligand in the [ONO^{cat}]TaMe(μ-η^2:η^2–N_2H_2)(μ-η^2:η^1–N_2H_3)TaMe[ON(H)O] dimer required deeper scrutiny. In its deprotonated form, the [ONO] redox-active ligand has behaved similarly across many studies, regardless of the metal it is bound to. Compared to other examples of the [EN(H)E] ligand family (E = O, S) on late transition metals, one stark difference from the protonated {Ta} dimer emerged. When protonated, the [ON(H)O] ligand was observed to bend as a result of the *sp*^{3} hybridization of the central nitrogen in [ON(H)O]Ni(PPh_3) and [ON(H)O]Co$(DMAP)_2$ (∠O1-M-O2 = 170.62(9)° and 119.13(5)°, respectively). However, in the {Ta} dimer, the ligand was bent entirely from a *mer* to *fac* coordination mode, decreasing ∠O1-M-O2 to only 96.38(10)°. The difference between a *mer* (~180°) and *fac* [ONO] ligand may represent a structural rearrangement significant enough to serve as an intrinsic barrier to its protonation.

Structural reorganization and changes in *d*-orbital occupancy have been demonstrated to affect the rate of HAT in certain compounds, illustrating the importance of not only thermochemical but also kinetic barriers in studying PCET. In the case of an oxo-hydroxo-vanadium(IV) compound,[32] HAT transfer occurred a million times more slowly than similar oxo-ruthenium(IV) complexes. Experimental rate measurements and computational analysis indicated that the dramatic difference in rate between the two systems was due to a larger inner-sphere reorganization energy, associated with a greater change in bond order between the vanadium and oxo fragments (**Scheme 4.5**). Redox changes in the {[ONO]$TaCl_n$}^{y} series (n = 3, y = −1, 0; n = 4, y = 0) have been shown to originate from orbitals localized on the redox-active ligand, but as [ONO] is successively oxidized from a 3-X type, trianionic

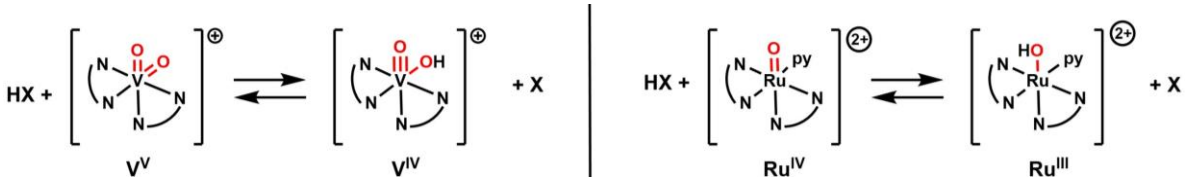

Scheme 4.5. Bond order changes in ruthenium and vanadium oxo complexes in response to HAT.

donor ligand to a dianionic, then monoanionic ligand, the Ta(V) center compensates for the loss by binding more X-type ligands. However, the $\{[ONO^{cat}]TaCl_3\}^-$ complex should be charge-balanced to accommodate the electronic needs of the Ta(V) center, even as the $[ONO^{cat}]^{3-}$ trianion is protonated to become a dianion. When protonation of the complex was attempted in the presence of excess Cl^- ions from a $\{Bu_4N\}\{Cl\}$ buffer, no reaction was observed over the course of several days or after heating to 70°C , suggesting a different origin for the observed barriers. However, without isolation of a monomeric $[ON(H)O]TaCl_3$ species, it was not possible to make rate measurements to investigate the activation barriers.

4.2.4. Isolation of a monomeric tantalum complex containing the *fac*-[ON(H)O] ligand.

When $[ONO]H_3$ and $TaCl_5$ were stirred in diethyl ether under a nitrogen atmosphere, two products were obtained. The first, a yellow species insoluble in pentane, produced a ^1H NMR (**Figure 4.8**, **top**) that did not exactly match the ^1H NMRs of $[ONO]TaCl_2(OEt_2)$ or $\{X\}\{[ONO]TaCl_3\}$ (X = Fc*, $HNEt_3^+$). A singlet resonance at 6.94 ppm integrated for ~ 1H and was first thought to be evidence of an [ON(H)O] species; in the $[ONO^{cat}]TaMe(\mu\text{-}\eta^2\text{:}\eta^2\text{–}N_2H_2)(\mu\text{-}\eta^2\text{:}\eta^1\text{–}N_2H_3)TaMe[ON(H)O]$ dimer, the suspected N–H proton of the [ON(H)O] ligand produced a resonance at 6.94 ppm in C_6D_6 as well. However, concentrated solution of the yellow product in diethyl ether, stored at −40°C for several weeks, produced blocky red crystals that were identified as $[ONO]TaCl_2(OEt_2)$ by single-crystal X-ray analysis as well as by ^1H NMR, suggesting that the ^1H NMR may be produced by a putative $[ONO]TaCl_2$ species rather than an $[ON(H)O]TaCl_n$ complex, and the signal at 6.94 ppm may be an unknown impurity. Like $[ONO]TaCl_2(OEt_2)$, the complex decomposed in MeCN. This complex was also unreactive toward either acid sources or bases, consistent with the behavior observed in *mer*-$\{[ONO^{cat}]TaCl_n\}^y$ (n = 2, y = 0; n = 3, y = −1). Additionally, the yellow complex produced

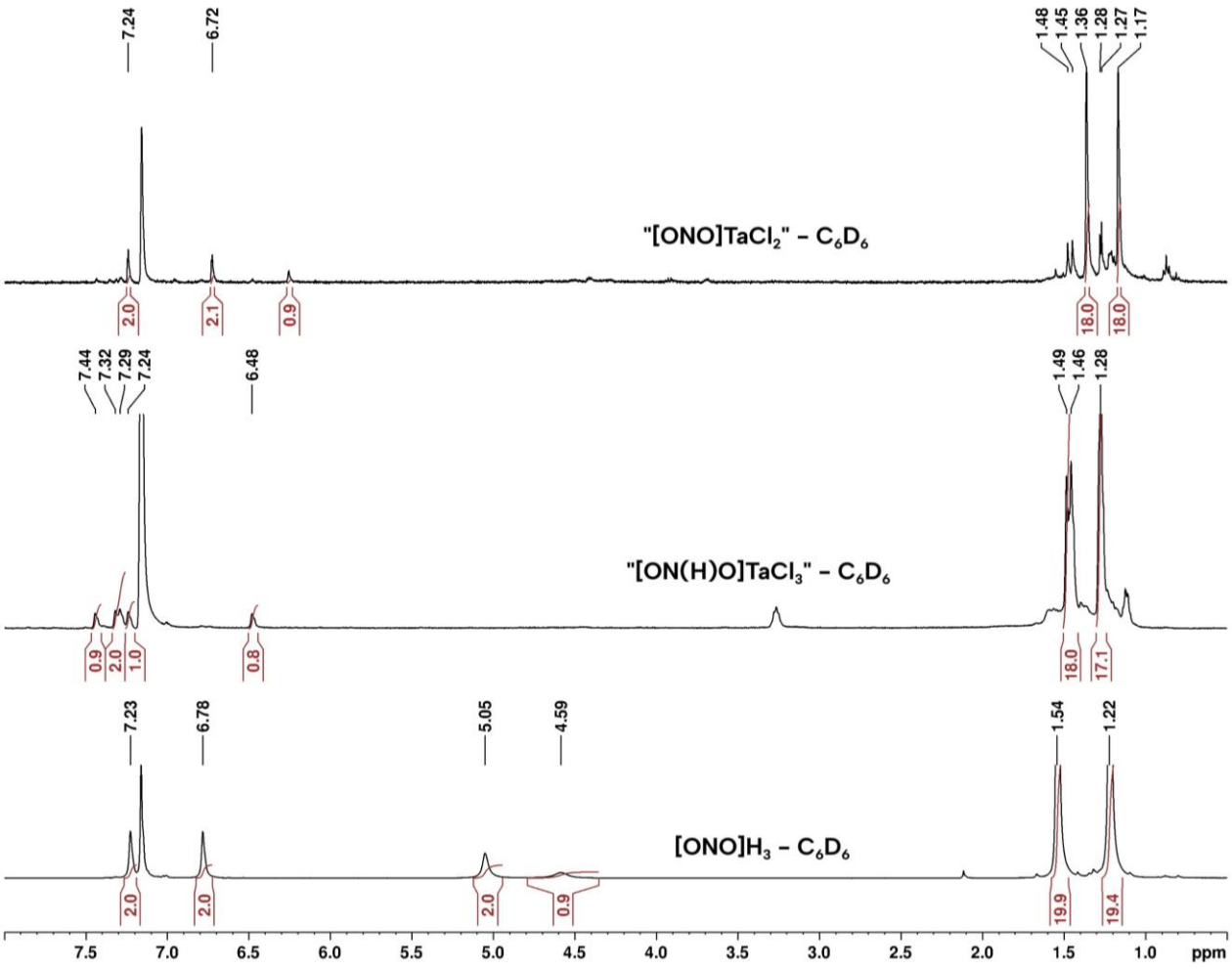

Figure 4.8. Comparison of ^{1}H NMR spectra obtained from the reaction of $[ONO]H_3$ and $TaCl_5$. Spectra taken in C_6D_6. Top: suspected $[ONO]TaCl_2$ complex with an impurity of suspected $[ON(H)O]TaCl_3$ (middle). The free $[ONO]H_3$ ligand is included (bottom) for comparison.

$[ONO^{sq}]TaCl_3$ upon chemical oxidation, as confirmed by electrochemical measurement of the reduction potentials and open circuit potentials, further supporting the formation of a neutral $[ONO^{cat}]TaCl_2$ species.

The second product, an orange solid soluble in many organic solvents, produced a ^{1}H NMR spectrum (**Figure 4.8, middle**) that did not bear any resemblance to previously-isolated complexes of the [ONO] ligand on Ta(V). In addition to the prominent singlet (~1H) that appeared at 6.49 ppm, the *tert*-butyl region did not exhibit the two singlets typical of the redox-active ligand, but rather four singlets at 1.48, 1.45, 1.28, and 1.27 ppm, each

integrating to 9H. The aromatic region likewise featured more peaks than expected, with four singlets of ~ 1H each appearing between 7.24-7.43 ppm (the peaks at 7.31 and 7.29 partially overlap). Notably, the asymmetric ligand environment of the protonated [ON(H)O] in the [Ta] dimer exhibited four aromatic proton resonances at 7.88, 7.66, 7.42, and 7.25 ppm, each integrating for 1H, and four *tert*-butyl resonances of 9H each. Thus it was suspected that a *fac*-$\{[ON(H)O]TaCl_n\}_y$ (n and y unknown) had been isolated.

The overall reaction stoichiometry that produced the two species discussed above is uncertain. If the singlet at 6.94 ppm in the yellow complex was indeed evidence of a protonated ligand, then it is possible that the reaction according to **Scheme 5.5:**

$$2[ONO]H_3 + 2TaCl_5 \xrightarrow[-4HCl]{} \textit{mer}\text{-}[ON(H)O]TaCl_3 + \textit{fac}\text{-}[ON(H)O]TaCl_3$$

Scheme 4.6. Proposed reaction to produce the *mer* and *fac* isomers of $[ON(H)O]TaCl_3$.

Reaction of one mole of $[ONO]H_3$ with one mole of $TaCl_5$ would result in the formation of both *mer*- and *fac*-$[ON(H)O]TaCl_3$. However, based on the previous experiments with *mer*-$\{[ONO]TaCl_3\}^-$ in the presence of acid, the *mer*-isomer may be acidic enough to result in the eventual loss of another equivalent of HCl. This disproportionation would produce the observed mixture of *mer*-$[ONO]TaCl_2(OEt_2)$ and *fac*-$[ON(H)O]TaCl_3$. It is also possible that the products may be a mixture of charged species, such as $\{[ON(H)O]TaCl_2\}^+$ and $\{[ON(H)O]TaCl_4\}^-$, given that the *fac*-monomeric unit in the hydrazine-bridged dimer exhibited an eight-coordinate geometry. In the absence of further evidence, however, the neutral *fac*-$[ON(H)O]TaCl_3$ was suspected to be the stable product.

The putative *fac* isomer was vigorously heated to attempt conversion to the *mer* isomer, and the complex was monitored by variable temperature ^1H NMR and UV-visible spectroscopy. However, the purported *fac*-$[ON(H)O]TaCl_3$ complex bears great similarity to the $\{[ONO]TaCl_3\}^-$ anion in its electronic absorption spectrum, shown in **Figure 4.9**, and no

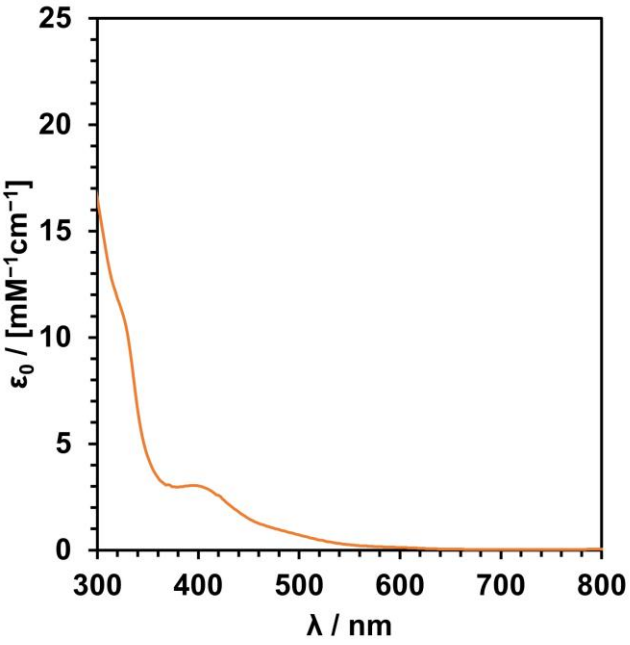

Figure 4.9. Electronic absorption spectra of the suspected *fac*-[ON(H)O]$TaCl_3$ isomer, produced from the reaction of [ONO]H_3 and $TaCl_5$. Spectra taken in acetonitrile.

change was noticed. The ^1H spectra showed no sign of reaction either. The presence of {Bu_4N}{Cl} during heating likewise did not facilitate isomerization.

Due to the similarities between the UV-visible spectra of the protonated and deprotonated complexes, it was suspected that monitoring deprotonation in spectrophotometric titrations would be difficult. Therefore deprotonation studies were monitored by ^1H NMR rather than by UV-visible spectroscopy. The complex is stable in CD_3CN, and the chemical shifts were sufficiently distinct from previous [ONO]–Ta compounds, that the titration's endpoint would be easily distinguished. In CD_3CN, the asymmetric environment of the ligand backbone in the [ON(H)O]$TaCl_3$ complex is more apparent (**Figure 4.10, a**). Stoichiometric addition of the base 2,4,6-collidine (2,4,6-trimethylpyridininium pK_a = 15.00, MeCN) to the orange complex produced a red-brown

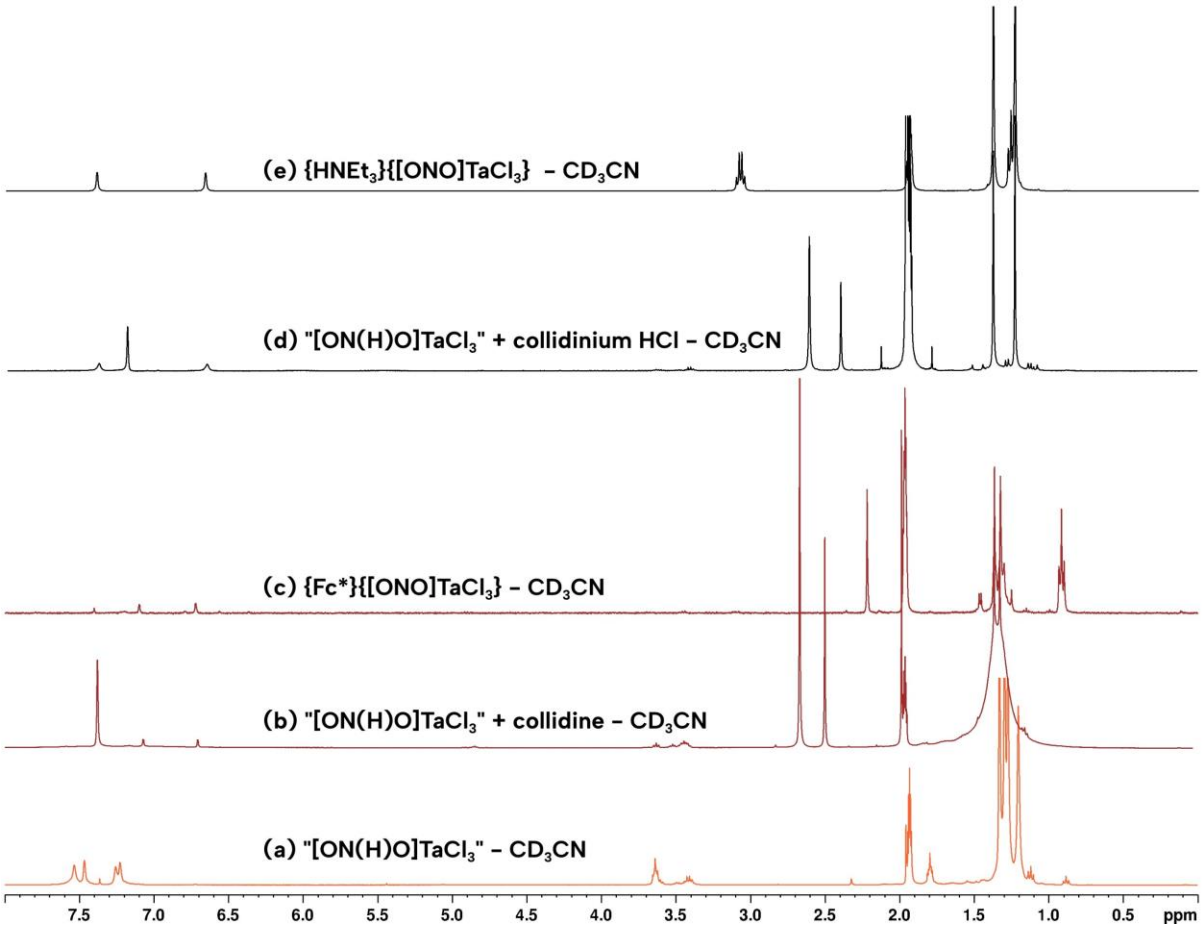

Figure 4.10. Addition of acid (green spectra, d) and base (red spectra, b) to the putative *fac*-[ON(H)O]TaCl3 (orange spectra, a) resulted in the formation of species similar to {Fc*}{[ONO]$TaCl_3$} (brown spectra, c), and {$HNEt_3$}{[ONO]$TaCl_3$} (black spectra, e). Peak labels were excluded for clarity.

solution whose ^{1}H spectrum (**Fig. 4.10, b**) has two narrowly spaced narrow *tert*-butyl resonances, and two sharp singlets in the aromatic region. The product closely matched the spectrum of {Fc*}{[ONO]$TaCl_3$} (**Fig 4.10, c**). Conversely, addition of one equivalent of 2,4,6-trimethylpyridinium chloride to the [ON(H)O]$TaCl_3$ complex yielded a bright yellow solution with a ^{1}H NMR spectrum (**Fig. 4.10, d**) that resembled {$HNEt_3$}{[ONO]$TaCl_3$} (**Fig. 4.10, e**). This set of reactions indicated that the *fac*-[ON(H)O]$TaCl_3$ may have an acidity lower than 15.00 in acetonitrile.

The presence of potential *mer* and *fac* isomers with differing acidities presented a challenge for further acidity measurements and brought into question the structure of the

yet-unknown {$HNEt_3$}{[ONO]$TaCl_3$} complex. The putative *fac*-[ON(H)O]$TaCl_3$ complex may become a *mer*-{[ONO]$TaCl_3$}$^-$ anion when deprotonated, as suggested by the close resemblance of the product's ^{1}H NMR to the crystallographically characterized {Fc*}{[ONO]$TaCl_3$}. It was not clear if the *fac*-[ON(H)O]$TaCl_3$ complex's reactivity with collidinium chloride was indicative of reactivity with H^+ *via* the protonated collidine or the Cl^- counteranion; HAT or hydride transfer from an [ON(H)O]$TaCl_n$ complex should not produce an anion, but rather the distinctive, previously-characterized [ONO^{sq}]$TaCl_3$ or [ONO^{q}]$TaCl_4$. However, the product of that reaction resembles the {$HNEt_3$}{[ONO]$TaCl_3$} complex by ^{1}H NMR; that suspected anion has been studied for its electronic absorption and electrochemical features (*vide supra*), and it appears to be a complex of [ONO^{cat}]$^{3-}$ similar to {Fc*}{[ONO]$TaCl_3$}. There is thus far no concrete evidence that the *mer* and *fac* isomers interconvert in solution. Thus it is difficult to discern the mechanism of the acid-base reactivity in this system. Additionally, the proton transfer behavior of the suspected *fac*-[ON(H)O]$TaCl_3$ and *mer*-{[ONO]$TaCl_3$}$^-$ complexes still do not explain the stability of the [ONO^{cat}]TaMe(μ-η^2:η^2–N_2H_2)(μ-η^2:η^1–N_2H_3)TaMe[ON(H)O] dimer. Further studies into that HAT reactivity of [ON(H)O]$TaCl_3$ with substrates may shed more light onto the observed thermochemical differences.

4.3. Conclusion.

A monomeric {[ONO]$TaCl_3$}$^-$ anion was isolated and characterized for its proton- and electron-transfer behavior. The complex is well-described as a fully-reduced, [ONO^{cat}]$^{3-}$ ligand on a Ta(V) metal center, and undergoes one quasireversible one-electron transfer in acetonitrile solution, while a second oxidation requires the coordination of an additional X-type ligand. The redox chemistry is localized on the [ONO] ligand, consistent with previous

studies of the ligand coordinated to Ta(V). Attempts to protonate the *mer*-$[ONO^{cat}]^{3-}$ ligand complex with acids of varying strengths failed, indicating that the $[ON(H)O]TaCl_3$ species may have a $pK_a < 10$ in acetonitrile. Evidence was presented that *mer*- and *fac*-$[ON(H)O]TaCl_3$ may have differing acidities, with *mer*-$[ON(H)O]TaCl_3$ being more acidic, preventing its protonation under the conditions studied. A neutral *mer*-$[ONO]TaCl_2(OH_2)$ complex was examined by X-ray crystallography, and its stability suggested that *mer*-$[ON(H)O]TaCl_3$ may indeed be a superacid. A putative *fac*-$[ON(H)O]TaCl_3$ species was investigated, and preliminary studies likewise indicate its acidity may be comparable to or below the pK_a of HCl in acetonitrile.

4.4. Experimental.

General considerations. All manipulations were carried out using standard Schlenk-line techniques or in a dry nitrogen glovebox, except where noted. Trifluoroacetic acid, concentrated ammonium hydroxide, and water were purged of dioxygen with a vigorous nitrogen stream (>1hr) before use in the synthesis of the [ONO]H_3 ligand. Hydrocarbon and ethereal solvents were sparged with argon and passed through activated Q5 and alumina Columns to remove dioxygen and water, as confirmed by dropwise addition of a solution of sodium benzophenone ketyl radical in THF. Such solvents were stored over activated molecular sieves in the glovebox. $TaCl_5$ (Aldrich), 4-dimethylaminopyridine, and 2.2.2-cryptand were used as-received from Sigma. Potassium hydride was obtained in mineral oil and washed with pentane prior to use. 2,4,6-trimethylpyridine and 2,6-dimethylpyridine were dried and distilled prior to use. Tetrabutylammonium hexafluorophosphate ({Bu_4N}{PF_6}) (Acros) was recrystallized from ethanol three times and dried under vacuum before use. Ferrocene and decamethylcobaltocene (Acros) were purified by vacuum sublimation.

Spectroscopic and electronic characterization. All NMR spectroscopy was performed on a Bruker Avance 400 MHz spectrometer. ^1H spectra were referenced to residual proteo impurities of the solvents used (1.94 ppm, CD_3CN; 7.16 ppm, C_6D_6). Electronic absorption spectra were recorded using a Jasco V-670 absorption spectrometer using 10 mm quartz cuvettes at ambient temperatures, or on a Perkin-Elmer Lambda 800 UV/vis spectrophotometer in 1 cm path length cells at 25 °C.

Cyclic voltammetry and differential pulse voltammetry experiments were performed on a Gamry G300 potentiostat/galvanostat/Zero Resistance Ammeter (Gamry Instruments,

Warminster, PA) using a 3.0 mm glassy carbon working electrode, a platinum wire counter electrode, and a silver wire pseudo-reference electrode. Experiments were performed at ambient temperature in a dry nitrogen glovebox with 1 mM analyte and 100 mM $\{Bu_4N\}\{PF_6\}$ or $\{Bu_4N\}\{Cl\}$supporting electrolyte. All potentials have been referenced to $[FeCp_2]^{+/0}$ using ferrocene or cobaltocene as an internal standard.

Crystallographic measurements. X-ray diffraction was performed on single crystals coated in Paratone oil and mounted on glass fibers. Data was acquired using a Bruker SMART APEX II diffractometer equipped with a CCD detector. A full sphere of data was collected for each crystal structure, and measurements were carried out using Mo Kα (λ = 0.71073 Å) radiation, which was wavelength selected with a single-crystal graphite monochromator. The SMART program package was used to determine unit-cell parameter and to collect data. The raw frame data were processed using SAINT36 and SADABS37 to yield the reflection data files. Subsequent calculations were carried out using the SHELXTL38 program suite. Structures were solved by direct methods and refined on F2 by full-matrix least-squares techniques to convergence. Analytical scattering factors for neutral atoms were used throughout the analyses. Hydrogen atoms, though visible in the difference Fourier map, were generated at calculated positions and their positions refined using the riding model. ORTEP diagrams were generated using ORTEP-3 for Windows. Bond distances used for metrical oxidation state analysis were extracted in Mercury for Windows.

Table 4.3. X-ray diffraction data collection and refinement parameters for [ONO]Ta(OH_2) and {Fc*}{[ONO]$TaCl_3$}.

Complex	[ONO]Ta(OH_2)	{Fc*}{[ONO]$TaCl_3$}
empirical formula	C_{28} H_{42} Cl_2 N O_3 Ta · 2($C_4H_{10}O$)	C_{48} H_{70} Cl_3 Fe N O_2 Ta · ½($C_4H_{10}O$)
formula weight	840.71	1073.26
crystal system	Monoclinic	Monoclinic
space group	*C*2/*c*	$P2_1/n$
T(K)	133(2)	92(2)
a /Å	12.2681(5)	11.9104(3)
b /Å	14.2440(6)	21.0149(5)
c /Å	23.9627(11)	21.1627(5)
α /deg	90	90
β /deg	101.1600(7)	96.3165(14)
γ /deg	90	90
V /Å^3	4108.2(3)	5264.8(2)
Z	4	4
refl. collected	50377	59163
indep. Refl.	6306	9744
R1 ($I > 2\sigma$)[a]	0.0191	0.0399
*w*R2 (all data)[b]	0.0442	0.0999
GOF	1.090	1.076

Spectrophotometric titrations. Stock solutions were prepared in the glovebox by dissolving solid reagents in dry, spectroscopy-grade (sieve-free) acetonitrile and diluting to 10 mL in volumetric flasks. Stock solutions were stirred until homogenous (approx. 2 hours) and no solids were visible. To prepare a typical sample, ~2 mL of acetonitrile was added to a 5mL volumetric flask, followed by the appropriate aliquot of [Ta] solution via a microliter syringe. Other reagents were added via separate microliter syringes when required. Then, the sample was diluted to the line with acetonitrile. Color changes associated with successful reactions were usually immediate. Samples were transferred to 25 mL scintillation vials equipped with stir bars and allowed to equilibrate for ~ 1 hr before being transferred to quartz cuvettes. Samples were then removed from the glovebox and brought to the spectrometer. Titrations were performed at least three times per concentration data point. Syringes for each reagent were rinsed three times with acetonitrile between samples to avoid dilution or contamination.

^{1}H NMR titrations. Stock solutions of [Ta], hexamethylbenzene, and B or {H}{B} (B = triethylamine; 2,4,6-trimethylpyridine; 2,6-dimethylypyridine; diphenylamine; *para*-cyanoaniline) were prepared similarly to above using dried CD_3CN. An aliquot of [Ta] was added *via* microliter syringe to a 25 mL scintillation vial equipped with a stir bar, followed by an aliquot of acid or base, then hexamethylbenzene. The difference in CD_3CN was added to reach a total of 0.75 mL. The samples were allowed to stir for ~1 hr. Then 0.5 mL of each sample was added to an NMR tube *via* fresh 1 mL syringes. NMR samples were taken immediately from the glovebox to the NMR spectrometer.

Synthesis of tantalum complexes.

[ONO]$TaCl_2(OEt_2)$. The synthesis of this complex has been previously reported using an "internal base" complex. Due to the thermal instability of the $TaMe_3Cl_2$ starting material,

an alternate synthesis using 3 equivalents of *n*-BuLi was also previously developed. Both methods were used to synthesize this complex.

[ONO]TaCl$_3$. The synthesis of this complex has been previously reported. A modified oxidation of [ONO]TaCl$_2$(OEt$_2$) was used, substituting PhI(OAc)$_2$ for PhICl$_2$ due to the thermal stability of the reagent, and the desired insolubility of the byproducts.

{Fc*}{[ONO]TaCl$_3$}. A solution of [ONO]TaCl$_3$ (179.4 mg, 0.2529 mmol, 1.0 equiv.) in a 25 mL scintillation vial was frozen in a liquid nitrogen Coldwell in the glovebox. A solution of decamethylferrocene (Fc*) (82.5 mg, 0.2528 mmol, 1.0 equiv.) in 9:1 diethyl ether:toluene was also cooled. When the tantalum solution was frozen, the Fc* was added dropwise and the reaction was stirred. A gradual color change from deep purple to orange-brown was observed. The reaction was allowed to stir to room temperature overnight, and a brown product precipitated from solution. The reaction was concentrated to induce further precipitation, and the solids were collected (187.2 mg, 71.45%) by filtration. Crystals suitable for X-ray analysis could be grown by layering a toluene solution of Fc* and a diethyl ether solution of [ONO]TaCl$_3$, separated by a layer of ether, and allowing the reaction to progress without stirring over the course of two days. They could also be obtained from concentrated solutions in diethyl ether. **^{1}H NMR (400 MHz, CD$_3$CN):** 7.08 ppm (s, 2H, [ONO] aryl-H), 6.71 ppm (s, 2H, [ONO] aryl-H), 1.35 ppm (s, 18H, [ONO] *t*-Bu), 1.31 ppm (s, 18H, [ONO] *t*-Bu). **UV-Vis (MeCN) λ_{max}/nm (ε M^{-1}cm^{-1}):** 318 (sh), 458 (4,000)

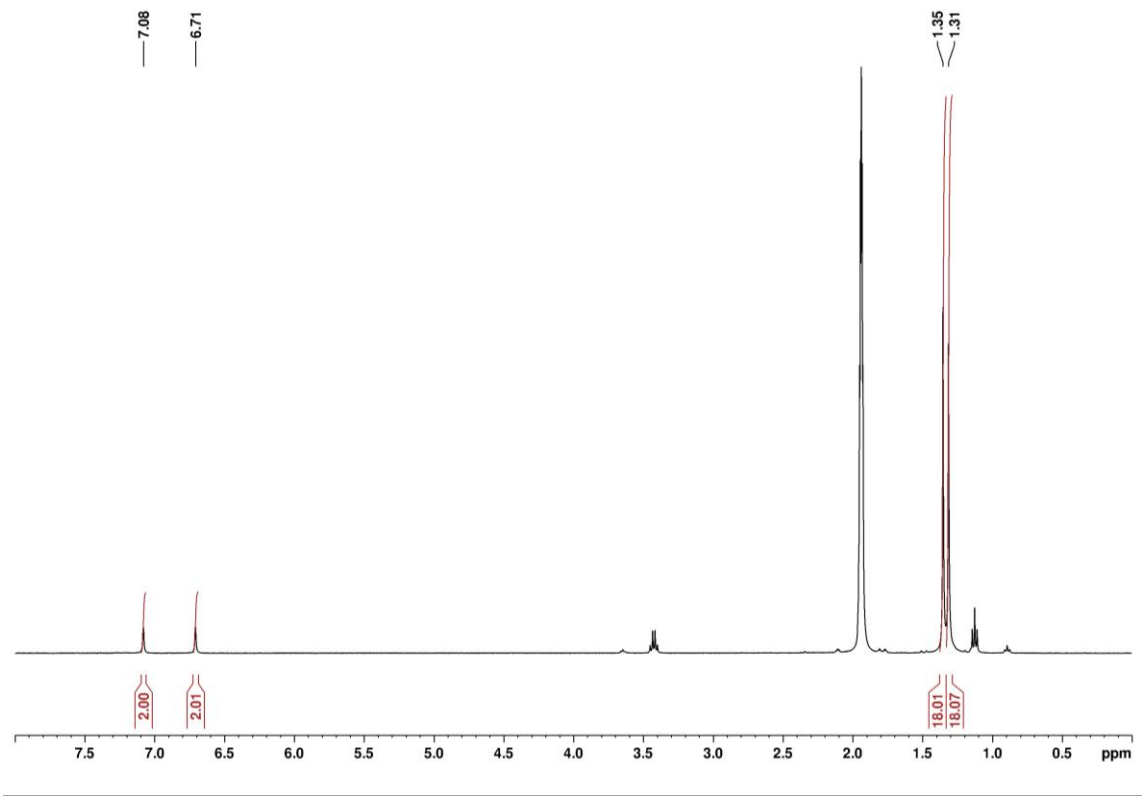

Figure 4.11. ^{1}H NMR of {Fc*}{[ONO]TaCl$_3$} taken in CD_3CN at 298 K

{HNEt$_3$}{[ONO]TaCl$_3$}. The [ONO]H$_3$ ligand was stirred in diethyl ether with two equivalents of triethlyammine for 30 minutes. The solution was then frozen in a nitrogen coldwell. A separate solution of $TaCl_5$ in diethyl ether was frozen in a 25 mL scintillation vial equipped with a stir bar. Once both solutions were frozen, they were combined and allowed to thaw while stirring for 3 hours. A bright yellow solution was obtained with slight cloudiness. The reaction was filtered through celite, and the filtrate was stripped of solvent under vacuum to yield a flakey yellow solid. **^{1}H NMR (400 MHz, CD_3CN):** 9.19 ppm (s, 1H, {HNEt$_3$}$^+$ N–H), 7.39 ppm (s, 2H, [ONO] aryl-H), 6.66 ppm (s, 2H, [ONO] aryl-H), 3.07 (q, 6H, {HNEt$_3$}$^+$ C–H$_2$), 1.38 ppm (s, 18H, [ONO] *t*-Bu), 1.26 ppm (t, 9H, {HNEt$_3$}$^+$ C–H$_3$), 1.23 ppm (s, 18H, [ONO] *t*-Bu). **^{1}H NMR (400 MHz, C_6D_6):** 9.71 ppm (s, 1H, {HNEt$_3$}$^+$ N–H), 7.70 ppm (s, 2H, [ONO] aryl-H), 6.94 ppm (s, 2H, [ONO] aryl-H), 2.32 ppm (q, 6H, {HNEt$_3$}$^+$ C–H$_2$), 1.54

ppm (s, 18H, [ONO] *t*-Bu), 1.46 (s, 18H, [ONO] *t*-Bu), 0.74 ppm (t, 9H, $\{HNEt_3\}^+$ C–H_3}. **UV-Vis (MeCN) λ_{max}/nm (ε / $M^{-1}cm^{-1}$):** 302 (sh)

"*fac*-[ON(H)O]$TaCl_3$". A solution of [ONO]H_3 (995.9 mg, 2.340 mmol, 1.0 equiv.) in diethyl ether was prepared in a 100 mL Schlenk flask in the glovebox and brought out to the Schlenk line under a nitrogen atmosphere. The ligand solution was cooled using a liquid nitrogen/acetone cold bath. A second solution of $TaCl_5$ (839.3 mg, 2.343 mmol, 1.0 equiv.) in diethyl ether was prepared in the glovebox similarly in a 250 mL Schlenk flask equipped with a stir bar and likewise cooled on the Schlenk line. Once both solutions were cooled, and the $TaCl_5$ was fully-dissolved, the ligand was transferred by cannula onto the stirring $TaCl_5$ solution. The reaction was allowed to slowly warm to room temperature, turning pale orange, and stirred overnight. The reaction was cannula filtered to remove unreacted $TaCl_5$ and yielding a dark orange filtrate. The solvent was stripped from the filtrate and the vessel was brought into the glovebox for further workup. In the glovebox, the red-orange residue was dissolved in pentane to yield an orange solution with a yellow precipitate. The solution was placed in the freezer for 3 hours to collect more yellow solid, which was then separated from the orange solution by filtration. Solvent was stripped from the filtrate to yield a microcrystalline orange solid. A total of 1.2930 g of orange solid ("*fac*-[ON(H)O]$TaCl_3$") and 695.2 mg of yellow solid were collected. **"*fac*-[ON(H)O]$TaCl_3$" ^{1}H NMR (400 MHz, C_6D_6):** 7.44 (s, 1H, [ONO] aryl-H), 7.32 ppm (s, 1H, [ONO] aryl-H), 7.29 ppm (s, 1H, [ONO] aryl-H), 7.24 ppm (s, 1H, [ONO] aryl-H), 6.49 ppm (s, 1H, [ONO] N–H), 1.49 ppm (s, 9H, [ONO] *t*-Bu), 1.46 ppm (s, 9H, [ONO] *t*-Bu), 1.28 ppm (s, 9H, [ONO] *t*-Bu), 1.27 ppm (s, 9H, [ONO] *t*-Bu). **^{1}H NMR (400 MHz, CD_3CN):** 7.53 (s, 1H, [ONO] aryl-H), 7.47 ppm (s, 1H, [ONO] aryl-H), 7.26 ppm (s, 1H, [ONO] aryl-H), 7.23 ppm (s, 1H, [ONO] aryl-H), 6.73 ppm (s, 1H, [ONO] N–H), 1.33 ppm (s, 9H, [ONO] *t*-Bu), 1.30 ppm (s, 9H, [ONO] *t*-Bu), 1.28 ppm (s, 9H, [ONO] *t*-Bu), 1.21 ppm (s, 9H, [ONO] *t*-Bu). **UV-Vis (MeCN) λ_{max}/nm (ε / $M^{-1}cm^{-1}$):** 322 (sh), 400 (3,039).

4.5. References.

1. Labinger, J. A.; Komadina, K. H. Hydridic character of early transition metal hydride complexes. *J. Organomet. Chem.* **1978,** *155* (2), C25-C28.
2. Schrader, S.; Ghana, P.; Hoffmann, A.; Spaniol, T. P.; Okuda, J. A Terminal Hydride of Hafnium Supported by a Triamidoamine Ligand. *Organometallics* **2023**, *42* (11), 1106—1114.
3. Tonks, I. A.; Henling, L. M.; Day, M. W.; Bercaw, J. E. Amine, Amido, and Imido Complexes of Tantalum Supported by a Pyridine-Linked Bis(phenolate) Pincer Ligand: Ta−N π-Bonding Influences Pincer Ligand Geometry. *Inorg. Chem.* **2009**, *48* (12), 5096-5105.
4. Leary, D. C.; Zhang, Y.; Rodriguez, J. G.; Akhmedov, N. G.; Peterson, J. L.; Dolinar, B. S.; Milsmann, C. *Organometallics* **2023**, *42* (11), 1220-1231.
5. Nguyen, A. I.; Zarkesh, R. A.; Lacy, D. C.; Thorson, M. K.; Heyduk, A. F. Catalytic nitrene transfer by a zirconium(iv) redox-active ligand complex. *Chem Soc.* **2011,** *2,* 166-169.
6. Lu, F.; Zarkesh, R. A.; Heyduk, A.F. A Redox-Active Ligand as a Reservoir for Protons and Electrons: O2 Reduction at Zirconium(IV). *Eur. J. Inorg. Chem.* **2011**, *2012* (3), 467-470.
7. Zarkesh, R. A.; Ziller, J. W.; Heyduk, A. F. Four-Electron Oxidative Formation of Aryl Diazenes Using a Tantalum Redox-Active Ligand Complex. *Angew. Chem., Int. Ed.* **2008,** *47* (25), 4715-4718.
8. Zarkesh, R. A.; Heyduk, A. F. Reactivity of Organometallic Tantalum Complexes Containing a Bis(phenoxy)amide (ONO)3– Ligand with Aryl Azides and 1,2-Diphenylhydrazine. *Organometallics* **2011,** *30* (18), 4890-4898.
9. Zarkesh, R. A.; Heyduk, A. F. Reactivity of Diazoalkanes with Tantalum(V) Complexes of a Tridentate Amido-Bis(phenolate) Ligand. *Organometallics* **2009**, *28* (23), 6629-6631.
10. Nguyen, A. I. Blackmore, K. J.; Carter, S. M.; Zarkesh, R. A.; Heyduk, A. F. One- and Two-Electron Reactivity of a Tantalum(V) Complex with a Redox-Active Tris(amido) Ligand. *J. Am. Chem. Soc.* **2009**, *131* (9), 3307-3316.
11. Hananouchi, S.; Krull, B. T.; Ziller, J. W.; Furche, F.; Heyduk, A. F. Metal effects on ligand non-innocence in Group 5 complexes of the redox-active [ONO] pincer ligand. *Dalton Trans.* **2014,** *48* (43), 17991-18000.
12. Heyduk, A.F.; Zarkesh, R. A.; Nguyen, A. I. Designing Catalysts for Nitrene Transfer Using Early Transition Metals and Redox-Active Ligands. *Inorg. Chem.* **2011,** *50* (20), 9849-9863.
13. Charette, B. J.; Ziller, J. W.; Heyduk, A. F. Metal-Ion Influence on Ligand-Centered Hydrogen-Atom Transfer. *Inorg. Chem.* **2021,** *60* (3), 1579-1589.
14. Mayer, J.M. Understanding Hydrogen Atom Transfer: From Bond Strengths to Marcus Theory. *Acc. Chem. Res.* **2011,** *44* (1),36-46.

15. Warren, J.J.; Mayer, J.M. Predicting organic hydrogen atom transfer rate constants using the Marcus cross relation. *Proc. Natl. Acad. Sci. U.S.A.* **2010,** *107* (12), 5282-5287.
16. Bordwell, F.G.; Cheng, J.P.; Harrelson, J.A. Homolytic bond dissociation energies in solution from equilibrium acidity and electrochemical data. *J. Am. Chem. Soc.* **1988,** *110* (4), 1229-1231.
17. Wayner, D.D.M.; Parker, V.D. Bond energies in solution from electrode potentials and thermochemical cycles. A simplified and general approach. *Acc. Chem. Res.* **1993,** *26* (5), 287-294.
18. Parker, V.D.; Handoo, K.L.; Roness, F.; Tilset, M. Electrode Potentials and the Thermodynamics of Isodesmic Reactions. *J. Am. Chem. Soc.* **1991,** *113,* 7493-7498.
19. Tilset, M.; Parker, V.D. Solution homolytic bond dissociation energies of organotransition-metal hydrides. *J. Am. Chem. Soc.* **1989,** *111* (17), 6711-6717.
20. Wiedner, E.S.; Chambers, M.B.; Pitman, C.L.; Bullock, R.M.; Miller, A.J.M.; Appel, A.M. Thermodynamic Hydricity of Transition Metal Hydrides. *Chem. Rev.* **2016***, 116* (15), 8655-8692.
21. Warren, J.J.; Tronic, T.A.; Mayer, J.M. Thermochemistry of Proton-Coupled Electron Transfer Reagents and its Implications. *Chem. Rev.,* **2010,** *110* (12), 6961-7001.
22. Zarkesh, R. A. Synthesis, Reactivity, and Multi-Electron Redox Behavior of a Bis(phenoxy)amide. Ligand Coordinated to a Tantalum Metal Center. Ph.D. Dissertation, University of California Irvine, Irvine, CA, **2012**.
23. Zhao, Y.; Bordwell, F. G.; Cheng, J. P.; Wang, D. Equilibrium Acidities and Homolytic Bond Dissociation Energies (BDEs) of the Acidic H-N Bonds in Hydrazines and Hydrazides. *J. Am. Chem. Soc.* **1997**, *119*, 9125-9129.
24. Cottrell, T. L. *The Strengths of Chemical Bonds*. Butterworth, London, 1958.
25. Darwent, B. deB. *Bond Dissociation Energies in Simple Molecules*. National Standard Reference Data Series, NationalBureau of Standards, no. 31, Washington, 1970.
26. Benson, S. W. III – Bond Energies. *J. Chem. Educ.* **1965,** *45* (9), 502.
27. Kerr, J. A. Bond Dissociation Energies by Kinetic Methods. **1966,** *66* (5), 465-500.
28. VanNatta, P. E.; Ramirez, D. A.; Velarde, A. R.; Ali, G.; Kieber-Emmons, M. T. Exceptionally High O–H Bond Dissociation Free Energy of a Dicopper(II) μ-Hydroxo Complex and Insights into the Geometric and Electronic Structure Origins Thereof. *J. Am. Chem. Soc.* **2020**, *142* (38), 16292-16312.
29. Brines, L. M.; Coggins, M. K.; Chaau Yan Poon, P.; Toledo, S.; Werner, K.; Kirk, M. L.; Kovacs, J. A. Water-Soluble Fe(II)–H2O Complex with a Weak O–H Bond Transfers a Hydrogen Atom via an Observable Monomeric Fe(III)–OH. *J. Am. Chem. Soc.* **2015,** *137* (6), 2253-2264.
30. Baldwin, M. J.; Pecoraro, V. L.; Energetics of Proton-Coupled Electron Transfer in High-Valent Mn2(μ-O)2 Systems: Models for Water Oxidation by the Oxygen-Evolving Complex of Photosystem II. *J. Am. Chem. Soc.* **1996**, *118* (45), 11325-11326.
31. Larsen, A. S.; Wang, K.; Lockwood, M. A.; Rice, G. L.; Won, T. J.; Lovell, S.; Sadilek, M.; Turecek, F.; Mayer, J. M. Hydrocarbon Oxidation by Bis-μ-oxo Manganese Dimers: Electron Transfer, Hydride Transfer, and Hydrogen Atom Transfer Mechanisms. *J. Am. Chem. Soc.* **2002**, *124* (34), 10112-10123.

32. Waidmann, C. R.; Zhou, X.; Tsai, E. A.; Kaminsky, W.; Hrovat, D. A.; Borden, W. T.; Mayer, J. M. Slow Hydrogen Atom Transfer Reactions of Oxo- and Hydroxo-Vanadium Compounds: The Importance of Intrinsic Barriers. **2009,** *131* (13), 4729-4743.
33. Marchetti, F.; Pampaloni, G.; Repo, T. The polymerization of Tetrahydrofuran Initiated by Niobium(V) and Tantalum(V) Halides. *Eur. J. Inorg. Chem.* **2008,** *12*, 2107-2112.
34. Brown, S.N. Metrical Oxidation States of 2-Amidophenoxide and Catecholate Ligands: Structural Signatures of Metal–Ligand π Bonding in Potentially Noninnocent Ligands. *Inorg. Chem.* **2012,** *51* (3), 1251-1260.
35. Tshepelevitsh, S.; Kütt, A.; Lõkov, M.; Kaljurand, I.; Saame, J.; Heering, A.; Plieger, P. G.; Vianello, R.; Leito, I. On the Basicity of Organic Bases in Different Media. European J. Org. Chem. 2019, 2019 (40), 6735–6748.
36. Lathem, A. P.; Heiden, Z. M. Quantification of Lewis acid induced Brønsted acidity of protogenic Lewis bases. *Dalton Trans.* **2017,** *46* (48), 5976-5985.
37. Paenurk, E.; Kaupmees, K.; Himmel, D.; Kutt, A.; Kaljurand, I.; Koppel, I. A.; Krossing, I.; Leito, I. A unified view to Brønsted acidity scales: do we need solvated protons? *Chem. Sci.* **2017**, *10* (8), 6964-6973.
38. Ramaat, E.; Kaupmees, K.; Ovsjannikov, G.; Trummal, A.; Kutt, A.; Saame, J.; Koppel, I.; Kaljurand, I.; Lipping, L.; Rodima, T.; Pihl, V.; Koppel, I. A.; Leito, I. Acidities of strong neutral Brønsted acids in different media. *J. Phys. Org. Chem.* **2012,** *26* (2), 162-170.
39. Trummal, A.; Lipping, L.; Kaljurand, I.; Koppel, I. A.; Leito, I. Acidity of Strong Acids in Water and Dimethyl Sulfoxide. *J. Phys. Chem. A.* **2016,** *120* (20), 3663-3669.
40. Kutt, A.; Rodima, T.; Saame, J.; Ramaat, E.; Maemets, V.; Kaljurand, I.; Koppel, I. A; Garlyauskayte, R. Y.; Yagupolskii, Y. L.; Yagupolskii, L. M.; Bernhardt, E.; Willner, H.; Leito, I. Equilibrium Acidities of Superacids. *J. Org. Chem.* **2011,** *76* (2), 391-395.
41. Roth, J. P.; Yoder, J. C.; Won, T. J.; Mayer, J. M. Application of the Marcus cross relation to hydrogen atom transfer reactions. *Science* **2001**, *294* (5551); 2524-2526.

Appendix I

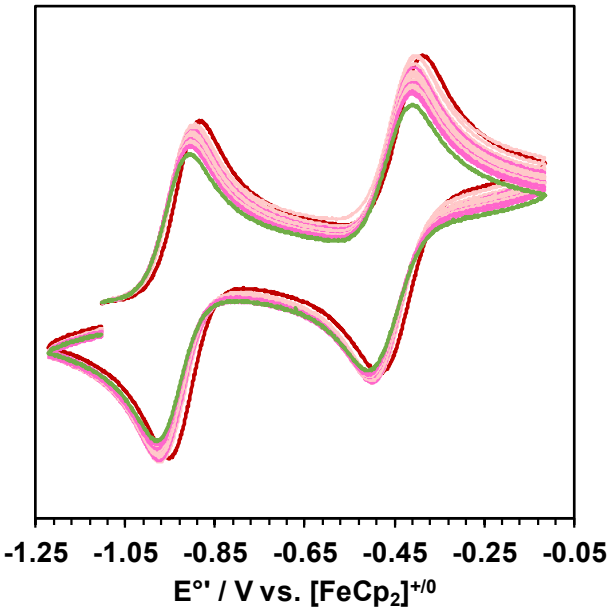

Figure A1.1. Cyclic voltammograms at 200 mV/s showing shift in reduction potentials as PPh_3 is titrated into {[ONO]Ni(py)}K (red trace) until {[ONO]Ni(PPh_3)}K is formed (green trace) at 2.0 equivalents.. Equilibrium study performed in MeCN solutions containing 0.1 M {Bu_4N}{PF_6} electrolyte and using a glassy carbon working electrode, Pt-wire counter electrode, an $Ag^{+/0}$ pseudo-reference electrode, and $[FeCp_2]^{+/0}$ as an internal standard.

The ligand substitution reaction to form {K}{[ONO]Ni(py)} from {K}{[ONO]Ni(PPh_3)} could not be studied using ^1H or ^{31}P NMR, as the relaxation time of nuclei in the complexes made it difficult to see both free and bound species. Instead, titrations were performed and monitored with CV (**Figure A1.1.**) in acetonitrile. Aliquots of a PPh_3 stock solution, with electrolyte, were added to {[ONO]Ni(py)}K prepared as described for standard CV experiments. After addition of every 0.1 equivalent of PPh_3, the solution was stirred, allowed to settle, and a scan was taken at 200 mV/s. The shift in the first redox event (~ 1.0 V vs. $[FeCp_2]^{+/0}$) was monitored, as this peak has been shown to be insensitive to PPh_3 concentration, while the peak ~ −0.4 V shifts anodically in the presence of excess ligand due to the formation of a five-coordinate species. The shift in peak potential was monitored from the pure {K}{[ONO]Ni(py)} −0.92 V starting point until the potentials ceased moving at 2.0

equivalents of PPh_3, which coincided with reaching the {[ONO]Ni(PPh_3)}K potential of −0.95 V.

A triphenylphosphine derivative was previously synthesized in our lab and has been studied for proton, hydrogen-atom, hydride-, and nitrene-transfer reactivity.[32,33] Its spectroscopic, electrochemical, and solid-state characterization is used as a basis of comparison for the {[ONO^{cat}]Ni(L)}K complexes presented herein. Formation of these pyridine derivatives from the PPh_3 complex is facile, and electrochemical measurements of both the forward and reverse reaction enabled the calculation of the binding constant K for both L = py and L = PPh_3. According to **Equation 2.2**:

$$\Delta E = q\frac{RT}{nF}\ln[L] + \frac{RT}{nF}\ln K \qquad \textbf{(EQN A1.1)}$$

if the number of ligands binding to the metal center (q) in the observed associative step is known, then the measured change in reduction potential can be used to determine K_L. The binding constant K_{PPh3} obtained from this analysis is 723 M^{-1}, and an analogous study of {K}{[ONO]Ni(PPh_3)} + py yielded a K_{py} of 1690 M^{-1}. The binding affinities calculated from CV are in general agreement with the stoichiometric equivalents added to each complex to afford complete ligand replacement: it requires 2.0 equivalents of PPh_3 to fully displace py from {K}{[ONO]Ni(py)}, and the reverse reaction is 1:1. The association of py is highly favored and is accompanied by a shift in [ONO] $E_{1/2}$[sq•/cat] reduction potential, albeit small compared to K_{eq}.